UNIVERSIDAD COMPLUTENSE DE MADRID
FACULTAD DE CIENCIAS FÍSICAS

TESIS DOCTORAL

Modelos con anyones en códigos cuánticos y superconductores topológicos

Anyon models in quantum codes and topological superconductors

MEMORIA PARA OPTAR AL GRADO DE DOCTOR

PRESENTADA POR

Santiago Varona Angulo

Director

Miguel Ángel Martín-Delgado Alcántara

Madrid

UNIVERSIDAD COMPLUTENSE DE MADRID
FACULTAD DE CIENCIAS FÍSICAS

TESIS DOCTORAL

Modelos con anyones en códigos cuánticos y superconductores topológicos

Anyon models in quantum codes and topological superconductors

MEMORIA PARA OPTAR AL GRADO DE DOCTOR

PRESENTADA POR

Santiago Varona Angulo

DIRECTOR

Miguel Ángel Martín-Delgado Alcántara

Modelos con anyones en códigos cuánticos y superconductores topológicos

---

Anyon models in quantum codes and topological superconductors

por

Santiago Varona Angulo

bajo la supervisión de

Miguel Ángel Martín-Delgado Alcántara

UNIVERSIDAD
COMPLUTENSE
MADRID

Tesis presentada en la
Universidad Complutense de Madrid
para el grado de Doctor en Física

Departamento de Física Teórica
Facultad de Ciencias Físicas

Septiembre 2020

Abstract

In this thesis we study two main topics related to the interplay between quantum information and topology: topological superconductors and topological quantum error correction.

Topological superconductors have been extensively studied, partly motivated by the search of a condensed-matter realization of Majorana fermions. These quasiparticles are non-Abelian anyons and can be used for quantum information processing. There have been several proposals and experiments where topological superconductors are realized by building heterostructures. These heterostructures usually consist of an s-wave superconductor proximity-coupled to a semiconductor. In publication [P1] we explore the possibility of engineering a topological superconductor using a d-wave parent superconductor coupled to a two-dimensional electron gas with spin-orbit coupling and a Zeeman field. We determine an analytical expression of the Majorana states and compare these results to the ones obtained using a conventional s-wave superconductor. We observe that, despite the angular dependence of the d-wave pairing, the localization of the Majorana fermions is very similar for equal superconducting pairing constant. Since d-wave superconductors correspond in general to high-temperature superconductors (with much larger superconducting pairing), we may expect sharper localization for this kind of setups. In addition, we employ a topological invariant to show the topological nature of the superconductor and check the robustness of the Majorana zero-energy modes against static disorder. Publication [P2] investigates other more exotic superconducting pairings: nodeless pairings compatible with tetragonal crystal symmetry. We compute the topological phase diagram in the presence of a Zeeman field and spin-orbit coupling, and analyze in detail the high Chern numbers obtained, the massive edge modes and the zero-energy modes.

Quantum error correction is an essential piece in order to obtain fault-tolerant quantum computers. Topological quantum error correcting codes stand out as one of the most efficient and promising candidates to achieve fault-tolerant quantum computation. Publication [P3] makes use of the connection between topological orders and topological error correcting codes to define a new topological code, the semion code, based on the double semion model. We use a modified version of the plaquette operators of the double semion model to construct the string operators and logical operators necessary to build a quantum memory. The resulting code

fits into the stabilizer formalism but it is not a Pauli nor a CSS code. In publication [P4] we further explore the semion code and obtain the error threshold for independent bit- and phase-flip noise, and for depolarizing noise. While this task is usually addressed resorting to a mapping into a statistical mechanical model, the structure of plaquette operators makes this mapping too involved. Instead, we take advantage of the near-optimal performance of some neural decoders to compute the threshold values. We also make a comparison with the Kitaev toric code and observe some differences as a consequence of the non-Pauli nature of the semion code. Additionally, we compare the performance of multilayer perceptrons and convolutional neural networks for the decoding task, finding that convolutional neural networks are better suited.

Resumen

En esta tesis estudiamos dos temas relacionados con la información cuántica y la topología: los superconductores topológicos y la corrección cuántica topológica de errores.

Los superconductores topológicos han sido ampliamente estudiados, hecho parcialmente motivado por la búsqueda de fermiones de Majorana en sistemas de materia condensada. Estas cuasipartículas son anyones no abelianos y se pueden utilizar para el procesamiento de información cuántica. Recientemente se han presentado varias propuestas y experimentos en los que se obtienen superconductores topológicos mediante la construcción de heteroestructuras. Dichas heteroestructuras generalmente consisten en un superconductor de onda s acoplado a un semiconductor. En la publicación [P1] exploramos la posibilidad de diseñar un superconductor topológico utilizando un superconductor padre de onda d acoplado a un gas de electrones bidimensional con interacción de espín-órbita y un campo Zeeman. Hallamos una expresión analítica de los estados de Majorana y comparamos estos resultados con los obtenidos cuando se usa un superconductor de onda s convencional. Observamos que, a pesar de la dependencia angular del acoplo de onda d, la localización de los fermiones de Majorana es muy similar para el mismo valor de la constante de acoplo superconductora. Puesto que los superconductores de onda d corresponden en general a superconductores de alta temperatura y, por consiguiente, con un valor mucho mayor para el acoplo superconductor, podemos esperar una localización más pronunciada para este tipo de configuraciones. Además, empleamos un invariante topológico que muestra la naturaleza topológica del superconductor y verificamos la robustez de los modos de energía cero frente el ruido estático. La publicación [P2] investiga otras interacciones superconductoras más exóticas: acoplamientos sin nodos compatibles con la simetría de un cristal tetragonal. Calculamos el diagrama de fases topológicas en presencia de un campo Zeeman y acoplamiento espín-órbita. Asimismo, analizamos en detalle los altos números de Chern obtenidos, los modos de borde masivo y los modos de energía cero.

La corrección cuántica de errores es una elemento esencial en la consecución ordenadores cuánticos tolerantes a fallos. Los códigos topológicos de corrección cuántica de errores se destacan como uno de los candidatos más eficientes y prometedores para lograr este último fin. La publicación [P3] utiliza la conexión entre

los órdenes topológicos y los códigos topológicos de corrección de errores para definir un nuevo código topológico, basado en el modelo del doble semión. Usamos una versión modificada de los operadores de plaqueta del modelo del doble semión para construir los operadores de cadena y los operadores lógicos necesarios para una memoria cuántica. El código resultante se ajusta al formalismo del estabilizador, pero no es un código formado por operadores de Pauli ni CSS. En la publicación [P4] exploramos más a fondo el código desarrollado en [P3] y obtenemos el umbral de error para dos tipos de ruido: el ruido independiente de inversión de bits y fases, y el ruido de despolarización. Si bien esta tarea generalmente se aborda realizando un mapeo a un modelo mecánico estadístico, la estructura de los operadores de plaquetas hace que éste sea demasiado complejo. En su lugar, aprovechamos el rendimiento casi óptimo de algunos decodificadores neuronales para calcular los valores de umbral. También hacemos una comparación con el código tórico de Kitaev y constatamos la presencia de algunas diferencias como consecuencia de que el código semiónico no está compuesto únicamente de operadores de Pauli. Por último, comparamos el rendimiento de perceptrones multicapa y redes neuronales convolucionales para la tarea de decodificación, encontrando que las segundas son más apropiadas para efectuar esta tarea.

La virtud intelectual de abstraer que semejante idioma postula, me sugiere que los Yahoos, pese a su barbarie, no son una nación primitiva sino degenerada.

Jorge Luis Borges, *El informe de Brodie*

List of publications

[P1] L. Ortiz, S. Varona, O. Viyuela, M. A. Martin-Delgado, *Localization and oscillations of Majorana fermions in a two-dimensional electron gas coupled with d-wave superconductors*, Physical Review B **97** (2018), 064501.

[P2] S. Varona, L. Ortiz, O. Viyuela, and M. A. Martin-Delgado, *Topological phases in nodeless tetragonal superconductors*, Journal of Physics: Condensed Matter **30** (2018), no. 39, 395602.

[P3] G. Dauphinais, L. Ortiz, S. Varona, M. A. Martin-Delgado, *Quantum error correction with the semion code*, New Journal of Physics **21** (2019), no. 5, 053035.

[P4] S. Varona, M. A. Martin-Delgado, *Determination of the semion code threshold using neural decoders*, Physical Review A **102** (2020), 032411.

Contents

Introduction

Quantum technologies have experienced a great progress in the last two decades. In the field of quantum computation, we now have small devices capable of performing small quantum computations. These devices are still very noisy and of modest size. Nevertheless, quantum supremacy [Pre12], a term that designates a task performed by a quantum device which no classical existing computer could do, was achieved in one of these small devices in an experiment that sampled the output of random quantum circuits [Aru+19]. We may now start to think of producing useful quantum computations in these noisy intermediate-scale quantum (NISQ) devices emerging in the near future [Pre18]. The new quantum computers should be able to execute shallow circuits with reasonable fidelity.

Some potential NISQ algorithms with shallow circuits are the variational quantum eigensolver [McC+16] and the quantum approximate optimization algorithm [FGG14], which can be applied to quantum problems (such as quantum chemistry) and optimization problems respectively. These two algorithms use both quantum and classical resources. First, a quantum circuit is executed and some observables are measured. The result is then fed into a classical optimization algorithm which slightly modifies the parameters of the quantum circuit, starting the process all over again. This is iteratively repeated till we reach a quantum state which should provide us with the solution of the problem. It is still an open question whether these algorithms can produce a quantum advantage over their classical counterparts.

Despite the possible existence of some early applications, we cannot ignore that many useful ones require fault-tolerant quantum computation, and we need to build much better devices with longer coherence times, higher gate fidelities and many more physical qubits to reach that goal. Qubits in quantum computers must be isolated from exterior noise in order to keep the stored information undamaged and avoid decoherence. Nevertheless, we must be able to measure the qubits and initialize them and they need to interact strongly with each other to process information. All these requisites are quite difficult to satisfy at the same time and, as a consequence, it has taken many years of research to take quantum technologies to their current status.

Nowadays, quantum processors are implemented using several physical systems, each of them with its corresponding advantages and disadvantages. Among the most popular and advanced we have superconducting circuits [DS13, Wen17b]

and trapped ions [Ber+17, Bru+19]. Superconducting circuits use the intrinsic coherence of superconductors to build electrical circuits with different elements, such as Josephson junctions, and obtain quantum mechanical devices. It was precisely in a superconducting quantum chip where quantum supremacy was recently achieved [Aru+19]. Trapped ion quantum computing use ions confined in Paul traps. Each qubit is formed by two electronic states of the ion and it can be manipulated by laser fields. Many other candidates exist. One of the most promising, but still in an early research phase when compared to superconducting circuits or trapped ions, are topological qubits [Kit03, Nay+08]. The approach is based on certain quasiparticle excitations appearing in some condensed matter systems, such as topological superconductors. These excitations behave as non-Abelian anyons in two-dimensions, meaning that exchanging them modifies non-trivially the quantum state of the system. The trajectory of the quasiparticles defines a braid, which corresponds to a unitary operation. Small fluctuations in the trajectory do not modify the braid. Besides, a single degree of freedom (a qubit) is formed by several of these excitations,[1] while the excitations can be arbitrarily far apart, endowing the system with a non-local nature. As a consequence, this system should be much more robust than other physical implementations.

There are many different exotic non-Abelian excitations, each of them with different braiding rules. Majorana fermions hosted in topological superconductors have been the main experimental goal in recent years [Lut+18]. Topological superconductors can be experimentally realized by forming superconductor-semiconductor heterostructures. Signatures of Majorana fermions have been measured in several studies using nanowires, for instance [Mou+12, Alb+16, Zha+18], providing strong evidence of their existence. In the near future, the attention is focused on measuring the non-Abelian statistics of these excitations and the validation of a topological qubit with long coherence time, which are key aspects when it comes to quantum information processing. In the long term, there are already some proposals for scalable implementations of this technology [Kar+17].

Although topological qubits should provide a much stronger resistance to decoherence, we cannot forget that fault-tolerance is necessary to unlock all the power of quantum computation. This in turn requires quantum error correction. The field of quantum error correction was born more than twenty years ago with Shor's code [Sho95] and has become a cornerstone in the theory of quantum computation to the extent that, without this discipline, large scale quantum computation would remain in the realm of pure mathematics without any chance to be realizable in experiments. Fault-tolerant quantum computation based on quantum error correcting codes is a crucial step to scalability of quantum computers, leaving the small scale that we are achieving nowadays with machines built by Google, IBM and others.

[1] Two excitations in the case of Majorana fermions.

Topology has also played a very significant role in the development of quantum error correction. Among quantum error correcting codes, topological codes stand out as the most efficient and promising candidates to realize the above-mentioned fault-tolerant quantum computation. The most significant example of topological codes is the Kitaev toric code [Kit97, Kit03]. Its simplicity and superb features have made the Kitaev model a very fruitful area of research. Also other topological codes have been studied, such as the color code [BM06]. Research in the field of topological quantum error correcting codes continues in many different directions, such as finding protocols to carry out universal fault-tolerant quantum computation in two-dimensional topological codes [BK05, Bro20], reducing the required overheads of these protocols [Lit19], large-scale implementations [Fow+12] or developing new topological codes [FTE20].

These two fields, topological superconductors and topological codes, are related by topological phases of matter. These phases cannot be described by the conventional Ginzburg-Landau theory based on symmetry breaking and local order parameters [Kit03, LW05, Sta16, Wen17a]. Instead, they are characterized by global order parameters capturing the topological nature of the system. We can distinguish two main groups here: topological orders and symmetry protected topological phases.

Topological orders have degenerate ground states that are protected from any type of local perturbations and exhibit long-range entanglement. They are also characterized by excitations with fractional statistics, i.e., anyons, which under exchange pick up a $e^{i\theta}$ phase and are neither fermions nor bosons. More generally, they can be non-Abelian anyons, which under exchange take the system to a different state. The standard example of this kind of phases is the fractional quantum Hall effect. Topological stabilizer codes are also examples of this category, since, as we will see, we can define a topological order from a topological stabilizer code. The main example of this correspondence is the Kitaev toric code and the Kitaev model. On the other hand, symmetry protected topological phases do not have anyons in the bulk, have short-range entanglement and require the presence of symmetries. The ground state is not degenerate unless the system has boundaries. It is precisely at these boundaries where we find edge states which may exhibit non-Abelian statistics. These states are only robust against perturbations that respect the symmetry of the Hamiltonian. Examples of symmetry protected topological phases are topological superconductors and topological insulators.

Along this thesis we explore different aspects of topological phases applied to quantum information. The thesis is divided into two main chapters. Chapter 1 deals with topological superconductors and the possibility of engineering this kind of systems using d-wave superconducting pairing and other more exotic pairings. A general review of the field and the motivation of publications [P1] and [P2] is given at the beginning. Some introductory concepts are explained in sections 1-3. Afterwards, publications [P1] and [P2] are summarized and presented. Chapter 2

is devoted to topological quantum error correction and analyzes a new topological code coming from a topological order, the double semion model. Similarly to what is done in chapter 1, a general review of the field and some motivation of publications [P3] and [P4] is given initially. Sections 1-3 contain some important concepts to understand publications [P3] and [P4], which are summarized and presented next.

CHAPTER 1

Majorana fermions in topological superconductors

Topological superconductors have aroused great interest in recent years, partly motivated by the search for a condensed-matter realization of Majorana fermions and their potential application to quantum information [Ali12, LF12]. Majorana initially introduced these fermions as elementary particles and, over the years, neutrinos and some supersymmetric particles were proposed as possible candidates. However, it is now possible to find Majoranas as emerging quasiparticles in condensed matter systems.

Interest in Majorana fermions stems from their unconventional exchange statistics, they are non-Abelian anyons. Exchange statistics describe the way wave functions behave when identical particles are swapped. The wave function picks up a -1 phase under the exchange of two identical (conventional) fermions, and a $+1$ for bosons. However, for topological reasons, we can have a much richer behavior in two dimensions. The particles that are neither bosons nor fermions are called anyons. For Abelian anyons, the wave function picks up a complex phase $e^{i\theta}$. In the case of non-Abelian anyons, by exchanging two identical particles we obtain a different quantum state. This means we can manipulate the ground state of a system hosting Majorana fermions by adiabatically exchanging them to perform unitary operations. The world lines of the Majorana fermions form a braid in 2+1 dimensions, which corresponds to a certain unitary. In this way, we can achieve fault-tolerant topological quantum computation [Kit03, Nay+08].

In addition to their exotic exchange statistics, Majorana fermions have other prominent characteristics. They are their own antiparticles: if γ_i is the operator corresponding to one of these modes, we have $\gamma_i = \gamma_i^\dagger$ and $\{\gamma_i, \gamma_j\} = 2\delta_{ij}$. This implies that we do not have an occupation number operator for a single mode, since $\gamma_i^\dagger \gamma_i = 1$. However, if we consider two Majorana modes γ_1 and γ_2, we can define a fermion as $c^\dagger = (\gamma_1 + \mathrm{i}\gamma_2)/2$, satisfying the conventional fermionic relation $\{c^\dagger, c\} = 1$. Hence, a Majorana mode can be regarded as *half* of a usual fermion. The fermionic mode c has now a number operator and quantum information can be encoded by filling or emptying the mode with the creation and annihilation operators. This fermionic mode has two interesting characteristics. First, since γ_1 and γ_2 can be arbitrarily far apart from each other, c may be a highly non-local operator. Besides, Majoranas are zero-energy modes due to the particle-hole symmetry of the superconductor. The corresponding antiparticle of a given excitation of energy E is an excitation of energy $-E$, therefore condition $\gamma = \gamma^\dagger$

is not satisfied unless $E = 0$. Thus, we can create or annihilate fermion c at no energy cost.

The great variety of quasiparticles emerging in condensed matter make it an ideal area to look for Majorana fermions. In a semiconductor or a metal, electrons and holes are oppositely charged, therefore particles and antiparticles are not related in the sense that their field operators are not Hermitian. However, in a superconductor, $U(1)$ symmetry is spontaneously broken and charge is no longer observable. The excitations of a superconductor superpose electrons and holes, making these materials good candidates for the search of Majorana fermions. Early theoretical studies by Read and Green [RG00] and Kitaev [Kit01] found topologically non-trivial superconductors in two and one dimensions respectively. Both works considered time-reversal breaking p-wave superconductors and spinless fermions. Nevertheless, experimental realizations of topological superconductors seemed to be challenging. In fact, p-wave pairing emerges intrinsically very rarely, as is the case of Sr_2RuO_4, which is only conjectured to be topological [Mae+12].

Few years later, new studies on topological insulators led to a ground-breaking work by Fu and Kane [FK08] where Majorana fermions are realized in the surface states of a topological insulator with proximity-induced s-wave superconductivity. This proposal paved the way to the engineering of heterostructures realizing topological superconductors and Majorana fermions. A semiconducting nanowire with spin-orbit coupling in proximity to an s-wave superconductor and a magnetic field were cleverly combined in [ORO10, LSD10] to obtain an effective p-wave superconducting wire. These proposals have been carried out in the laboratory and we already have experimental evidence of the existence of Majorana fermions in this type of setups. The zero-bias peak in the differential conductance, which is the consequence of the existence of a Majorana zero mode in the density of states, was measured in [Mou+12, Chu+13]. The exponential decay of Majorana fermions into the bulk was observed in [Alb+16]. More recently, the quantized $2e^2/h$ zero-bias conductance peak [Zha+18] and the 4π-periodic Josephson effect [Lar+19] were also observed, strongly supporting the existence of Majorana fermions. Similar proposals exist to engineer two-dimensional topological superconductors, see for instance [Ali10]. Another setup where signatures of Majorana fermions have been measured is [Nad+13, Nad+14], which involves depositing ferromagnetic iron atoms on top of superconducting lead to form a topological superconducting chain.

All these proposals and experiments use s-wave parent superconductors to induce a superconducting gap. However, much less has been done regarding d-wave superconductors. Sato and Fujimoto [SF10] showed the existence of Majorana fermions in two-dimensional d-wave superconductors with spin-orbit coupling and magnetic field. Takei *et al.* [Tak+13] studied the possibility of inducing topological superconductivity with high-temperature superconductors for various heterostructures. Since d-wave superconductors are in general high-temperature superconductors, they offer bigger gaps and work at higher temperatures. The d-wave gap

is also qualitatively different. It depends on the angle and has nodal lines, i.e., points in the Brillouin zone where the gap vanishes. This contrasts with the constant value of the s-wave pairing. In publication [P1], we investigate the possibility of engineering a topological superconductor with a d-wave parent superconductor and compare in detail the differences with the s-wave alternative. Continuing our study of new pairing symmetries, in publication [P2] we analyze the phase diagrams and edge states of all possible nodeless mixed pairings compatible with tetragonal crystal symmetry.

This chapter is organized as follows. Sections 1-3 contain introductory concepts to the field of topological superconductors. Section 1 is devoted to the Kitaev chain, a simple toy model showing non-trivial topology. Section 2 discusses an experimental realization of the Kitaev chain. In section 3, the role of topological invariants is outlined. Finally, sections 4 and 5 contain a summary and the main results of publications [P1] and [P2].

1. The Kitaev chain

A very simple one-dimensional model of topological superconductivity is the Kitaev chain [Kit01]. We start by introducing the Hamiltonian of a spinless p-wave superconductor,

$$\mathcal{H} = -\mu \sum_{i=1}^{N} c_i^\dagger c_i - \sum_{i=1}^{N-1} \left(t\, c_i^\dagger c_{i+1} + \Delta c_i c_{i+1} + \text{H.c.} \right), \tag{1}$$

where c_i ($c_i^\dagger$) is the fermion annihilation (creation) operator at site i, μ is the chemical potential, t the hopping and Δ the superconducting pairing. Note that p-wave pairing couples neighboring sites, unlike s-wave pairing which couples fermions on the same site (and opposite spin). We will now rewrite equation (1) in terms of Majorana operators, i.e., we will divide each fermion into two Majorana modes with

$$c_i = \frac{1}{2} \left(\gamma_{B,i} + \mathrm{i} \gamma_{A,i} \right). \tag{2}$$

At each fermionic site i, we have two Majorana modes, A and B. If we find the inverse relations of equation (2), we obtain $\gamma_{A,i} = \mathrm{i} \left(c_i^\dagger - c_i \right)$ and $\gamma_{B,i} = c_i^\dagger + c_i$, which clearly fulfill the Majorana relation $\gamma_{\alpha,i} = \gamma_{\alpha,i}^\dagger$. In general, this is purely a mathematical transformation without physical effects, since these Majorana operators are close to each other and cannot be addressed individually. However, under certain circumstances, we might discover some surprising consequences. Substituting into (1), we have

$$\mathcal{H} = -\frac{\mu}{2} \sum_{i=1}^{N} (1 + \gamma_{B,i} \gamma_{A,i}) - \frac{\mathrm{i}}{2} \sum_{i=1}^{N-1} \left[(\Delta + t)\, \gamma_{B,i} \gamma_{A,i+1} + (\Delta - t)\, \gamma_{A,i} \gamma_{B,i+1} \right]. \tag{3}$$

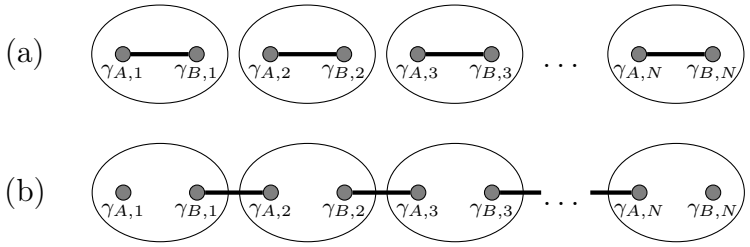

Figure 1. Representation of the Majorana operators in the Kitaev chain. (a) Hamiltonian (3) with $\mu \neq 0$ and $t = \Delta = 0$. Every Majorana is coupled to its neighbor on the same site. (b) After setting $\mu = 0$ and $t = \Delta \neq 0$ in Hamiltonian (3), we obtain equation (4). The two Majorana operators at the edges are not coupled to the rest of the system.

There are two cases where the behavior of the system is particularly clear, as illustrated in figure 1. First, if we choose $\mu \neq 0$ and $t = \Delta = 0$, the second term in equation (3) vanishes and only the first term remains. The Majorana modes at each site are coupled with each other and nothing specially interesting happens. This is the topologically trivial phase. However, there is a non-trivial phase when we take the limit $\mu = 0$ and $t = \Delta \neq 0$, where we obtain

$$\mathcal{H} = -\mathrm{i} \sum_{i=1}^{N-1} t \gamma_{B,i} \gamma_{A,i+1}. \tag{4}$$

We now see that the two Majoranas at the edges of the chain, $\gamma_{A,1}$ and $\gamma_{B,N}$, uncouple from the rest of the system and do not appear in Hamiltonian (4). Thus, they are Majorana zero-energy modes of the Hamiltonian. We can define new fermion operators by summing Majorana modes at neighboring sites, $\tilde{c}_i = (\gamma_{B,i} + \mathrm{i}\gamma_{A,i+1})/2$, which yields $\mathcal{H} = -\mathrm{i} \sum_{i=1}^{N-1} t \tilde{c}_i^\dagger \tilde{c}_i$. There is one missing fermion operator in this Hamiltonian, $\tilde{c}_N = (\gamma_{B,N} + \mathrm{i}\gamma_{A,1})/2$, which is a highly non-local fermion operator composed of the two Majorana zero modes at the edges. The ground state of the system is two-fold degenerate, corresponding to the 0 or 1 occupation number of this fermion.

It is important to note that the behavior we found for $\mu = 0$ and $t = \Delta \neq 0$, also occurs if $|\mu| < 2t$. The only difference is that, in general, the Majorana edge modes are not perfectly localized at the edges but they exponentially decay into the bulk. This produces an overlap between the two Majorana modes, lifting the ground state degeneracy. Nevertheless, since the decay scales as $e^{-L/\xi}$, where L is the length of the chain and ξ the coherence length of the superconductor (which is inversely proportional to the superconducting gap), this effect should be negligible if L is large enough. Therefore, there is no need to fine tune the parameters of the Hamiltonian to get to the non-trivial phase.

Considering periodic boundary conditions, we can Fourier transform Hamiltonian (1) to momentum space and take the $k \to 0$ limit. This yields

$$\mathcal{H} = \frac{1}{2}\int dk\, \boldsymbol{c}_k^\dagger H \boldsymbol{c}_k = \frac{1}{2}\int dk \begin{pmatrix} c_k^\dagger, c_{-k} \end{pmatrix} \begin{pmatrix} \frac{k^2}{2m} - \tilde{\mu} & \Delta k \\ \Delta k & -\frac{k^2}{2m} + \tilde{\mu} \end{pmatrix} \begin{pmatrix} c_k \\ c_{-k}^\dagger \end{pmatrix}. \tag{5}$$

Here, $m = 1/(2t)$ and $\tilde{\mu} = \mu + 2t$. Note that the superconducting coupling has a linear momentum dependence, since we are dealing with a p-wave superconductor. Diagonalizing H, we obtain the energy bands $E_\pm(k) = \pm\sqrt{\epsilon^2(k) + \Delta^2 k^2}$, with $\epsilon(k) = k^2/2m + \tilde{\mu}$. The bulk is always gapped except when $\tilde{\mu} = 0$. We want to study the Majorana zero energy solutions at the edge of the system. Thus, we consider a semi-infinite wire ($x > 0$) and look for solutions of the equation

$$\begin{pmatrix} \frac{-1}{2m}\partial_x^2 - \tilde{\mu} & -\mathrm{i}\Delta\partial_x \\ -\mathrm{i}\Delta\partial_x & \frac{1}{2m}\partial_x^2 + \tilde{\mu} \end{pmatrix} \begin{pmatrix} \psi_1 \\ \psi_2 \end{pmatrix} = E \begin{pmatrix} \psi_1 \\ \psi_2 \end{pmatrix}, \tag{6}$$

where we have transformed H back to real space, and we set $E = 0$. Since the system is particle-hole symmetric we have $\psi_2 = -\mathrm{i}\psi_1$. Solving the differential equation

$$\frac{1}{2m}\partial_x^2\psi_1 + \Delta\partial_x\psi_1 + \tilde{\mu}\psi_1 = 0, \tag{7}$$

and imposing boundary conditions $\psi_1(0) = 0$ and $\lim_{x\to\infty}\psi_1(x) = 0$, we observe that it is only possible to find zero-energy solutions when $\tilde{\mu} > 0$. Finally, the zero-energy solution reads

$$\boldsymbol{\psi} = Ne^{-\Delta m x}\sin\left(\sqrt{2m\tilde{\mu} - m^2\Delta^2}\, x\right)\begin{pmatrix} 1 \\ -\mathrm{i} \end{pmatrix}, \tag{8}$$

where N is a normalization factor, and the corresponding field operator

$$\gamma = N\int dx\; e^{-\Delta m x}\sin\left(\sqrt{2m\tilde{\mu} - m^2\Delta^2}\, x\right)\left(c(x) - \mathrm{i}c^\dagger(x)\right). \tag{9}$$

As expected, the Majorana mode exponentially decays into the bulk due to the $e^{-\Delta m x}$ factor. Multiplying by a global phase, $\tilde{\gamma} = e^{\mathrm{i}\pi/4}\gamma$, we clearly see $\tilde{\gamma} = \tilde{\gamma}^\dagger$.

Since we can only find these zero-energy solutions for $\tilde{\mu} > 0$, $\tilde{\mu} = 0$ separates the trivial from the non-trivial phase, and, as we saw earlier, this is exactly the point where the bulk spectrum is not gapped. These gap closings signal topological phase transitions. It is not possible to smoothly deform the Hamiltonian to join both regimes (trivial and non-trivial phase) without closing the gap. As a consequence, when we have an edge where the system is topological on one side and trivial on the other, the gap closes producing a Majorana edge mode. This is precisely what happens here, on the left side ($x < 0$) we have the vacuum, while on the right ($x > 0$) we have a topological superconductor.

A similar analysis can be done for a spinless $p + ip$ superconductor in two dimensions, whose Hamiltonian is

$$H = \begin{pmatrix} \frac{k^2}{2m} - \mu & i\Delta(k_x + ik_y) \\ -i\Delta(k_x - ik_y) & -\frac{k^2}{2m} + \mu \end{pmatrix}, \tag{10}$$

where $k^2 = k_x^2 + k_y^2$. The energy bands are $E_\pm(\boldsymbol{k}) = \pm\sqrt{\epsilon^2(\boldsymbol{k}) + \Delta^2 k^2}$ and the system is topologically non-trivial for $\mu > 0$. If we place the system on a cylinder, i.e., periodic boundary conditions in one direction and open boundary conditions in the other, we can find, analogously to what we did in one dimension, Majorana edge modes at the edges of the cylinder. It is also possible to find Majorana fermions in other type of geometries, such as a vortex core [GS11, Ali12], where we have a trivial phase inside a circular region and a non-trivial phase outside. Several of this vortex cores can be moved in a two-dimensional plane to braid the Majorana fermions.

2. Experimental realization

The Kitaev chain studied in the previous section has very particular characteristics. It is a one-dimensional system of spinless fermions with superconducting pairing. Now it is time to explore how this can be realized with the ingredients we have in the laboratory. We will need to overcome several problems to finally obtain a system with the same characteristics as the Kitaev chain. First, superconductivity in nature has in general even-parity pairing (s-wave or d-wave), coupling electrons and holes with opposite spin. Bogolons in an s-wave superconductor take the form $b = uc_\uparrow^\dagger + vc_\downarrow$ and therefore we cannot have a spinless regime in order to obtain $b = b^\dagger$, as Majorana particles require. Despite these difficulties, it is still possible to engineer a system that effectively resembles a Kitaev chain by combining different materials and joining them to create a heterostructure [ORO10, LSD10].

The necessary ingredients are a semiconducting wire with spin-orbit coupling, a magnetic field, and an s-wave superconductor (see figure 2). The Hamiltonian of the wire reads

$$\mathcal{H}_{\text{wire}} = \frac{1}{2}\int dk_x\, \boldsymbol{\Psi}^\dagger(k_x) H_{\text{wire}}(k_x) \boldsymbol{\Psi}(k_x), \tag{11}$$

where

$$H_{\text{wire}}(k_x) = \epsilon(k_x)\tau_z \otimes \mathbb{I}_\sigma + \alpha k_x\, \tau_z \otimes \sigma_y + V\, \mathbb{I}_\tau \otimes \sigma_z, \tag{12}$$

with $\epsilon(k_x) = k_x^2/(2m) - \mu$. Each term, from left to right, corresponds to kinetic energy, spin-orbit coupling and magnetic field along the z-axis. We have used the Nambu spinor $\boldsymbol{\Psi}^\dagger(k_x) = (\psi_\uparrow^\dagger(k_x), \psi_\downarrow^\dagger(k_x), \psi_\downarrow(-k_x), -\psi_\uparrow(-k_x))$, anticipating the introduction of superconductivity, and τ_i and σ_i denote Pauli matrices acting on particle-hole and spin space, respectively. The energy bands are

$$E_{\text{wire},\pm}(k_x) = \epsilon(k_x) \pm \sqrt{V^2 + \alpha^2 k_x^2}. \tag{13}$$

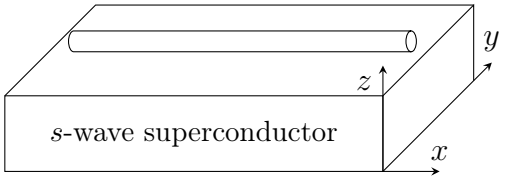

Figure 2. Semiconducting nanowire on top of an s-wave superconductor.

Superconductivity can be induced on the semiconducting one-dimensional wire by placing it in the proximity of an s-wave superconductor. In this way, superconductor and semiconductor couple and electrons can tunnel between both systems. The wire inherits the pairing of the superconductor and effectively produces a superconducting wire thanks to the proximity effect. The resulting Hamiltonian in the wire reads

$$H(k_x) = H_{\text{wire}}(k_x) + H_\Delta, \tag{14}$$

with $H_\Delta = \Delta\, \tau_x \otimes \mathbb{I}_\sigma$. We choose Δ to be a real positive value. More explicitly, in matrix form,

$$H(k_x) = \begin{pmatrix} \epsilon(k_x) + V & -\mathrm{i}\alpha k_x & \Delta & 0 \\ \mathrm{i}\alpha k_x & \epsilon(k_x) - V & 0 & \Delta \\ \Delta & 0 & -\epsilon(k_x) + V & \mathrm{i}\alpha k_x \\ 0 & \Delta & -\mathrm{i}\alpha k_x & -\epsilon(k_x) - V \end{pmatrix}. \tag{15}$$

The energy bands are given by

$$E_\pm^2(k_x) = V^2 + \Delta^2 + \epsilon^2(k_x) + \alpha^2 k_x^2 \pm 2\sqrt{V^2\Delta^2 + V^2\epsilon^2(k_x) + \alpha^2\epsilon^2(k_x)}. \tag{16}$$

The gap at $k_x = 0$ is $E_\pm(k_x = 0) = |V| \pm \sqrt{\Delta^2 + \mu^2}$ and vanishes for $\mu^2 = V^2 - \Delta^2$. The values where the gap vanishes indicate a topological phase transition, and, as we will see, the superconducting wire is topologically non-trivial if $|\mu| < \sqrt{V^2 - \Delta^2}$.

To understand what purpose each term in the Hamiltonian serves, let us consider first equation (13) with $\alpha = 0$. By introducing a magnetic field in the nanowire we have removed the spin degeneracy. If we place μ inside the gap between these two bands, $|\mu| < |V|$, only the lower band is occupied and we obtain a 'spinless' regime similar to the Kitaev chain. However, the magnetic field alone, without spin-orbit coupling, is not enough to produce a gapped spectrum when the superconducting pairing is introduced. This can be seen when considering the spectrum of the superconducting wire in equation (16) with $\alpha = 0$, which reduces to

$$E_\pm = V \pm \sqrt{\Delta^2 + \epsilon^2(k_x)}. \tag{17}$$

When the magnetic field is higher than the superconducting gap, $|V| > \Delta$, the spectrum is not gapped. This reflects the fact that s-wave pairing inherited from the parent superconductor couples fermions with opposite spin, while the wire is polarized under the magnetic field. A spin-orbit coupling perpendicular to the

magnetic field solves this by making the spin no longer a good quantum number, allowing for some superconducting pairing and opening the gap.

The relation of equation (15) to the Kitaev chain becomes clear by partially diagonalizing H into the basis where H_{wire} is diagonal. This yields

$$H = \begin{pmatrix} E_{\text{wire},+} & 0 & \Delta_{+-} & \Delta_{++} \\ 0 & E_{\text{wire},-} & \Delta_{--} & \Delta_{+-} \\ \Delta_{+-}^* & \Delta_{--}^* & -E_{\text{wire},-} & 0 \\ \Delta_{++}^* & \Delta_{+-}^* & 0 & -E_{\text{wire},+} \end{pmatrix}, \tag{18}$$

where

$$\Delta_{--}(k_x) = \frac{\mathrm{i}\Delta\alpha k_x}{\sqrt{V^2+\alpha^2 k_x^2}}, \tag{19}$$

$$\Delta_{++}(k_x) = \frac{-\mathrm{i}\Delta\alpha k_x}{\sqrt{V^2+\alpha^2 k_x^2}}, \tag{20}$$

$$\Delta_{+-}(k_x) = \frac{-V\Delta}{\sqrt{V^2+\alpha^2 k_x^2}}. \tag{21}$$

We can already see intraband p-wave pairing (Δ_{--} and Δ_{++}) and interband s-wave pairing between upper and lower band (Δ_{+-}). In the limit where the magnetic field is much larger than the spin-orbit energy and the superconducting pairing, $|V| \gg m\alpha^2, \Delta$, we can ignore the upper band, which plays essentially no role, and do $\psi_+ \to 0$. We keep only the lower band, where the operator $\psi_-^\dagger(k_x)$ adds an electron with energy $E_{\text{wire},-}(k_x)$. This finally yields the effective Hamiltonian

$$\mathcal{H}_{\text{eff}} = \int dk_x \, \mathbf{\Psi}_-^\dagger(k_x) H_{\text{eff}}(k_x) \mathbf{\Psi}_-(k_x) \ , \tag{22}$$

with $\mathbf{\Psi}_-^\dagger(k_x) = (\psi_-^\dagger(k_x), \psi_-(-k_x))$ and

$$H_{\text{eff}} = \begin{pmatrix} \frac{k_x^2}{2m} - \mu_{\text{eff}} & \mathrm{i}\Delta_{\text{eff}} k_x \\ -\mathrm{i}\Delta_{\text{eff}} k_x & -\frac{k_x^2}{2m} + \mu_{\text{eff}} \end{pmatrix}. \tag{23}$$

We have approximated $E_{\text{wire},-} \simeq \frac{k^2}{2m} - \mu - |V| = \frac{k_x^2}{2m} - \mu_{\text{eff}}$ and $\Delta_{--} \simeq \mathrm{i}\Delta\alpha k_x/|V| = \mathrm{i}\Delta_{\text{eff}} k_x$. This effective Hamiltonian clearly resembles the Hamiltonian of the Kitaev chain in equation (5) and, as we found for the Kitaev chain, it is non-trivial if $\mu_{\text{eff}} > 0$, i.e., $\mu > -|V|$. Comparing this result with the points where the gap vanishes in the full Hamiltonian (15) and taking into account the range of validity of the effective model ($|V| \gg m\alpha^2, \Delta$; $|\mu| < |V|$), we conclude that (15) has a non-trivial phase for

$$|\mu| < \sqrt{V^2 - \Delta^2}. \tag{24}$$

While exchange statistics are not well-defined in one-dimensional systems (since particles would need to pass through one another), it is still possible to braid the Majorana fermions of these wires by building a network of connected wires

[Ali+11]. The Majorana fermions can then be moved by locally tuning μ and driving certain parts of the wire in and out of the non-trivial phase at will.

3. Topological invariants

In previous sections, we have determined the trivial and non-trivial phases of the superconductor by considering open-boundary conditions to explicitly check whether Majorana zero-energy modes were present at the edges. However, it is possible to infer the existence of zero-energy edge states in terms of the properties of the bulk. This can be done by simply computing a topological invariant associated with the bulk Hamiltonian. The topological invariant is an integer taking non-zero values in the non-trivial phase. The specific topological invariant that needs to be computed depends on the symmetries and the dimension of the model [BH13, Chi+16]. Since we will be dealing with time-reversal breaking superconductors in two dimensions, we focus here on the Chern number. The Chern number can be related to the number of zero-energy modes at defects or boundaries of the system. This relation is called the bulk-boundary correspondence.

For the one-dimensional Kitaev chain and the two-dimensional $p + \mathrm{i}p$ superconductor, we can rewrite Hamiltonians (5) and (10) as

$$H(\boldsymbol{k}) = \boldsymbol{h}(\boldsymbol{k}) \cdot \boldsymbol{\sigma}, \tag{25}$$

with $\boldsymbol{\sigma} = (\sigma_x, \sigma_y, \sigma_z)$. In case of the $p + \mathrm{i}p$ superconductor we have $\boldsymbol{h} = (-\Delta k_y, -\Delta k_x, \epsilon(\boldsymbol{k}))$. The normalized vector $\hat{\boldsymbol{h}}(\boldsymbol{k}) = \boldsymbol{h}(\boldsymbol{k})/|\boldsymbol{h}(\boldsymbol{k})|$ defines a map from the two-dimensional Brillouin zone to the unit sphere. If we have $\mu > 0$ and $k = |\boldsymbol{k}| = 0$, $\hat{\boldsymbol{h}}$ is at the south pole of the sphere. As k grows, $\hat{\boldsymbol{h}}$ passes the equator when k equals the Fermi momentum and ends up in the north pole when $k \to \infty$. In case of $\mu < 0$, we start from the north pole and, as k grows, we descend towards the equator. However, we turn back before reaching the equator and return to the starting point as $k \to \infty$. Hence, the sphere is swapped once if $\mu > 0$ and none if $\mu < 0$. The total number of times that the sphere is swept by $\hat{\boldsymbol{h}}(\boldsymbol{k})$ is given by

$$\nu_{\mathrm{Ch}} = \frac{1}{4\pi} \int d^2\boldsymbol{k}\ \hat{\boldsymbol{h}} \cdot (\partial_{k_x} \hat{\boldsymbol{h}} \times \partial_{k_y} \hat{\boldsymbol{h}}), \tag{26}$$

which is the Chern number. Thus, the Chern number shows to which topological class the map $\hat{\boldsymbol{h}}(\boldsymbol{k})$ belongs. Since this map belongs to one class if $\mu > 0$ and another if $\mu < 0$, we cannot smoothly transform the Hamiltonian between the two phases. In order to do so, we need to close the gap.

More formally, the Chern number can be defined as the integral of the Berry curvature in the Brillouin zone [SA17]. A Bloch Hamiltonian with n energy bands has eigenstates $|u_n(\boldsymbol{k})\rangle$ given by the equation $H(\boldsymbol{k})|u_n(\boldsymbol{k})\rangle = E_n(\boldsymbol{k})|u_n(\boldsymbol{k})\rangle$. The Berry connection is defined by $\boldsymbol{\mathcal{A}}^{(n)}(\boldsymbol{k}) = \mathrm{i}\langle u_n(\boldsymbol{k})|\boldsymbol{\nabla}_{\boldsymbol{k}} u_n(\boldsymbol{k})\rangle$, and can be understood as the rate of change of $|u_n(\boldsymbol{k})\rangle$ in momentum space. This quantity has some ambiguity, since we can perform a gauge transformation $|u_n(\boldsymbol{k})\rangle \to e^{\mathrm{i}\phi_n(\boldsymbol{k})}|u_n(\boldsymbol{k})\rangle$,

which transforms the Berry connection as $\boldsymbol{\mathcal{A}}^{(n)}(\boldsymbol{k}) \to \boldsymbol{\mathcal{A}}^{(n)}(\boldsymbol{k}) - \boldsymbol{\nabla}_{\boldsymbol{k}}\phi_n(\boldsymbol{k})$. A gauge invariant quantity, the Berry curvature, can be defined as

$$\mathcal{F}_{ij}^{(n)} = \partial_{k_i}\mathcal{A}_{k_j}^{(n)}(\boldsymbol{k}) - \partial_{k_j}\mathcal{A}_{k_i}^{(n)}(\boldsymbol{k}). \tag{27}$$

The Chern number of the n-th band in two dimensions can be computed via

$$\nu_{\mathrm{Ch}}^{(n)} = \frac{1}{2\pi}\int_{\mathrm{BZ}} d^2\boldsymbol{k}\, \mathcal{F}_{xy}^{(n)}(\boldsymbol{k}). \tag{28}$$

Superconductors have particle-hole symmetry and, as a consequence, the total Chern number of the occupied bands equals the total Chern number of the unoccupied bands with opposite sign. Thus, only the Chern number of the occupied bands is computed.

Using the Stokes theorem, equation (28) can be reduced to an integral along the border of the Brillouin zone. Since the Brillouin zone has periodic boundary conditions, it is a torus and has no border. Therefore, unless the Berry connection has some singular points, the Chern number vanishes and the topology is trivial. A non-zero Chern number reflects the fact that it is not possible to find a smooth gauge for $|u_n(\boldsymbol{k})\rangle$ in the whole Brillouin zone. This is exactly what happens for the $p + \mathrm{i}p$ superconductor. For the occupied band, we can make the choice

$$|u_-\rangle = \frac{1}{\sqrt{2h(h+h_3)}}\begin{pmatrix} h_1 - \mathrm{i}h_2 \\ -h - h_3 \end{pmatrix}, \tag{29}$$

where $\boldsymbol{h} = (h_1, h_2, h_3)$ and $h = |\boldsymbol{h}|$. $|u_-\rangle$ is singular for $\boldsymbol{h} = (0, 0, -h)$. This means $|u_-\rangle$ has a singularity at the point $\boldsymbol{k} = (0, 0)$ of the Brillouin zone when $\mu > 0$. We can remove this singular point by making a gauge transformation, but the new wave function will have a singular point elsewhere in the Brillouin zone. Since the map $\hat{\boldsymbol{h}}(\boldsymbol{k})$ covers the whole unit sphere if $\mu > 0$, we cannot find a smooth gauge for $|u_-\rangle$ in the whole Brillouin zone and the Chern number is non-zero.

4. Summary and main results of publication 1

Most of the proposals to realize Majorana fermions consist of heterostructures where superconductivity is induced by proximity effect with an s-wave superconductor. This raises the question of what would happen if s-wave parent superconductors are replaced with d-wave superconductors. High-temperature superconductors have in general d-wave pairing. Therefore, the pairing gap of these superconductors is much larger. In addition, d-wave pairing has angular dependence, while s-wave pairing is constant. We have $\Delta_d(\boldsymbol{k}) \propto k_x^2 - k_y^2 = k^2\cos(2\theta_{\boldsymbol{k}})$. Interestingly, the pairing gap vanishes for some directions ($\theta = \pm\frac{\pi}{4}$), producing the so called nodal lines. As a consequence, we may have bulk nodal zero-energy states in addition to Majorana zero-energy states. Below we have presented the main results obtained in publication [P1].

1. **Analytical expression of Majorana states coming from d-wave superconductors.** In this work, we construct an effective model for a two-dimensional electron gas with spin-orbit coupling and subject to a Zeeman field coupled with a d-wave superconductor. High-temperature superconductors represent a possible instance of d-wave superconductors in addition to promising quantum simulation proposals. We derive a two-band effective Hamiltonian that allows us to obtain an analytical expression for wave function of the Majorana states, i.e., their decay and their frequency of oscillations.
2. **Comparison between Majorana states coming from d-wave and s-wave parent superconductors.** Having the analytical expression of the decay and oscillation frequency of the Majorana bound states, we compare the decay and oscillations profiles of Majorana quasiparticles induced by a d-wave superconductor to the ones induced by an s-wave superconductor as a function of the parameters in the Hamiltonian. It is important to highlight that d-wave pairing has an angular dependence whereas s-wave pairing is constant. We find that, despite angular dependence, ratios for decay and frequency seem to be very similar for equal values of the superconducting gap. However, since d-wave superconductors have larger superconducting pairing amplitudes, we may expect Majorana zero modes to be more localized than in the s-wave parent superconductor case.
3. **Lattice model: a topological invariant and Majorana robustness against disorder.** We define a microscopic lattice model that comprises the effective Hamiltonian previously mentioned. Within this model, we calculate the parity of the Chern number, which is a well-defined topological invariant for nodal superconductors. Moreover, we prove the stability of the new Majorana fermions against static disorder due to their topological character.

Localization and oscillations of Majorana fermions in a two-dimensional electron gas coupled with *d*-wave superconductors

L. Ortiz,[1] S. Varona,[1] O. Viyuela,[2,3] and M. A. Martin-Delgado[1]
[1]*Departamento de Física Teórica I, Universidad Complutense, 28040 Madrid, Spain*
[2]*Department of Physics, Harvard University, Cambridge, Massachusetts 02318, USA*
[3]*Department of Physics, Massachusetts Institute of Technology, Cambridge, Massachusetts 02139, USA*

(Received 27 September 2017; published 1 February 2018)

We study the localization and oscillation properties of the Majorana fermions that arise in a two-dimensional electron gas (2DEG) with spin-orbit coupling (SOC) and a Zeeman field coupled with a d-wave superconductor. Despite the angular dependence of the d-wave pairing, localization and oscillation properties are found to be similar to the ones seen in conventional s-wave superconductors. In addition, we study a microscopic lattice version of the previous system that can be characterized by a topological invariant. We derive its real space representation that involves nearest and next-to-nearest-neighbors pairing. Finally, we show that the emerging chiral Majorana fermions are indeed robust against static disorder. This analysis has potential applications to quantum simulations and experiments in high-T_c superconductors.

DOI: 10.1103/PhysRevB.97.064501

I. INTRODUCTION

The idea of a fermionic particle being precisely its own antiparticle has been puzzling physicists for generations. These exotic particles were hypothesized by Majorana [1] and have been thoroughly studied in high energy physics as a possible solution to the intriguing nature of neutrinos and dark matter [2]. However, the detection of Majorana fermions had remained elusive until they were introduced as quasiparticles in certain condensed matter systems. A series of experiments has claimed the observation of signatures of Majorana states [3–8].

Roughly, the condensed matter version of Majorana fermions constitutes *half* of a usual fermion, i.e., an ordinary fermion is a superposition of two Majorana modes which can be separated by arbitrary distance. The resulting state is highly delocalized and robust against local perturbations. Moreover, Majorana states exhibit novel statistics: They are non-Abelian anyons. The two latter features draw the attention of the quantum computation community. Braiding Majorana fermions provides a method for realizing topological quantum computation [9–12]. Novel methods combining Majorana physics with topological error correction have also appeared recently [13–17].

Correspondingly to these unusual properties, an increasing interest on how to get and manipulate Majorana fermions has grown up. The appearance of Majorana states was predicted in a system with odd superconducting pairing [18]. Since odd superconducting pairing has not been found in nature, the proposal seemed to be unrealistic. A few years later, a remarkable idea to induce topological superconductivity at the surface of a topological insulator by means of proximity effect made it feasible [19].

Alternatively, approaching a semiconductor nanowire, with spin-orbit coupling and subject to a magnetic field, to the surface of a superconductor induces an odd superconducting pairing among the electrons in the semiconductor [20,21]. The resulting phase is topological and has Majorana quasiparticles.

Initially, various experimental setups using s-wave superconductors were proposed to host Majorana fermions [22,23]. Recent experiments confirm the success of the experimental proposal [24,25]. It is also possible to obtain topological superconductivity by depositing magnetic adatoms on top of a conventional s-wave superconductor [26–33], where signatures of Majorana modes have been seen.

Additionally, high-T_c superconductors were suggested to induce topological superconductivity [34–36]. The motivation to study these types of superconductors comes in two directions. First, the induced superconducting gap is proportional to the gap in the original superconductor but reduced by a factor, as a consequence of proximity effect. Since the superconducting gap is larger for high-T_c superconductors, the induced gap becomes wider. Second, high-T_c superconductors show anisotropic pairing. Therefore, they induce different pairing depending on the orientation of the sample.

Since high-T_c superconductors are an instance of a d-wave pairing, one may wonder what would happen when a d-wave superconductor induces a superconducting gap in a two-dimensional electron gas (2DEG) with spin-orbit coupling and a Zeeman field. A realization of a 2DEG could be a semiconductor even though the aim of this work is to provide a general framework which can be applied also to other schemes [37] and include quantum simulation in the pathway.

Considering a host d-wave superconductor, we analyze the interesting features of the new Majorana fermions comparing them to the Majorana bound states induced by s-wave superconductors. To accomplish this task, we develop a phenomenological model using a d-wave superconductor as a parent Hamiltonian to induce superconductivity. As a result, we get an effective pairing which has f-wave symmetry ($l = 3$), in contrast to the effective p-wave symmetry ($l = 1$) that appears for a parent s-wave superconductor.

d-wave superconductors act differently from s-wave superconductors in two fundamental ways: (1) d-wave pairing shows an angular dependence. As a consequence, d-wave superconductors present a richer phenomenology with respect to s-wave superconductors. They can induce a p-wave pairing and also a novel f-wave pairing depending on the orientation of the superconductor [34]. We focus our study on the latter case. Majorana fermions created present clearly defined edge localization, despite the angular dependence of d-wave pairing and its expected larger correlation length. We also show that the frequency of oscillations of Majorana fermions for d-wave and s-wave superconductors are indeed very similar for a wide range of parameters. (2) Since d-wave pairing has nodal lines, where the superconducting gap is zero [38–40], Majorana and nodal states coexist. As a consequence, nodal states appear in the system where the gap in the effective model closes, similarly to what happens for Majorana states.

Furthermore, we study a microscopic lattice Hamiltonian that comprises the previous effective model. We characterize the phase diagram using the parity of the Chern number, which is a well-defined topological invariant even for nodal systems. In addition, we consider the effect of static disorder to prove the robustness of the propagating Majorana modes.

The paper is organized as follows: In Sec. II, a superconducting Hamiltonian with effective f-wave pairing is derived. We use this simplified Hamiltonian model to calculate analytically the wave function of Majorana fermions in Sec. II B. Moreover, we exhaustively study the properties of Majorana fermions arising from this induced f-wave pairing. In Sec. III, we study a lattice version of the previous effective model. In particular, we obtain a microscopic model in real space and define the topological invariant for this nodal system. The robustness of Majorana states against disorder is also discussed. Detailed analytic calculations on how to obtain the wave function of the Majorana bound states are explained in Appendix A.

II. PHENOMENOLOGICAL HAMILTONIAN

In this section, we study the problem of a 2DEG with strong spin-orbit interaction and Zeeman field, as well as an induced d-wave superconducting pairing mechanism. There are several physical platforms that can realize this model such as: (i) a planar semiconductor approximated to a high-T_c superconductor [22], (ii) a d-wave superconductor with intrinsically strong spin-orbit interaction [38], (iii) cold atoms simulation of d-wave superconductors [41], where the spin-orbit interaction can be also induced by laser [42].

Any of the above proposals requires three key ingredients: spin-orbit coupling (SOC), a strong Zeeman field, and a parent superconductor. The Zeeman field is introduced perpendicular to the semiconductor plane, as shown in Fig. 1. In certain parameter regimes, the Hamiltonian presents an effective spin-triplet pairing symmetry with propagating Majorana states at edges, similar to s-wave parent superconductors. However, we show that the localization, oscillation, and stability properties of these Majorana modes are very similar when the underlying parent symmetry of the superconductor is d wave, despite the angular dependence that the superconducting pairing exhibits.

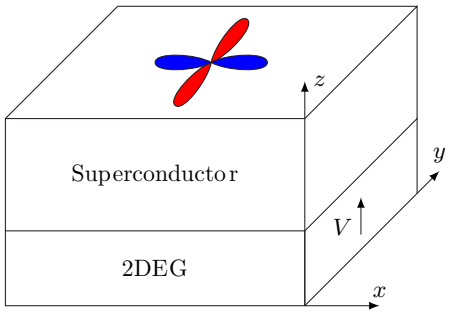

FIG. 1. Orientation of the d-wave superconductor with respect to the 2DEG with SOC and Zeeman field.

In what follows we present both analytic and numerical results supporting these claims.

A. Derivation of the Hamiltonian

We begin by considering a 2DEG with SOC [23]. Crucially, the SOC breaks the spin degeneracy of the 2DEG bands. Since we will eventually include superconductivity, we already embed the particle-hole structure in the Hamiltonian. To this end, we use the following Nambu spinor basis in momentum space, $\Psi^\dagger(\boldsymbol{k}) = (\psi^\dagger_\uparrow(\boldsymbol{k}), \psi^\dagger_\downarrow(\boldsymbol{k}), \psi_\downarrow(-\boldsymbol{k}), -\psi_\uparrow(-\boldsymbol{k}))$, where $\psi(\psi^\dagger)$ are annihilation (creation) operators satisfying the fermionic anticommutation relations. The Hamiltonian reads

$$\mathcal{H}_\alpha = \frac{1}{2}\int \mathrm{d}^2\boldsymbol{k}\ \ \Psi^\dagger(\boldsymbol{k}) H_\alpha(\boldsymbol{k}) \Psi(\boldsymbol{k}), \tag{1}$$

with

$$H_\alpha(\boldsymbol{k}) = \left(\frac{k^2}{2m} - \mu\right)\tau_z \otimes \mathbb{I}_\sigma + \alpha\ \tau_z \otimes (k_y\ \sigma_x - k_x\ \sigma_y), \tag{2}$$

where $k_x(k_y)$ is the crystalline momentum in the $x(y)$ direction, $k^2 = k_x^2 + k_y^2$, m is the effective mass of the electron in the material, μ is the chemical potential, α is the Rashba SOC strength, and σ_i and τ_i are Pauli matrices acting on spin and particle-hole space, respectively. As a result, Hamiltonian $H_\alpha(\boldsymbol{k})$ is a 4×4 matrix.

Next, we include a Zeeman field perpendicular to the 2DEG plane to open a gap between the spin-up and the spin-down bands:

$$H_V = V\ \mathbb{I}_\tau \otimes \sigma_z. \tag{3}$$

The Zeeman field could be generated by a ferromagnetic insulator or by a magnetic field. Since the field was chosen to be perpendicular to the plane, using a magnetic field would cause orbital effects which are neglected in Eq. (3).

The corresponding energy dispersion relations for the particle bands are

$$E_\pm(\boldsymbol{k}) = \frac{k^2}{2m} - \mu \pm \sqrt{V^2 + \alpha^2 k^2}, \tag{4}$$

where $\pm$ denotes the upper and lower bands, respectively. At $\boldsymbol{k} = 0$ the separation between the two is $2|V|$. If μ is placed inside the gap, $|\mu| < |V|$, only the lower band is occupied. This is necessary to reach the spinless regime.

By placing a superconductor on top of the 2DEG, it is possible to induce superconductivity through proximity effect. Provided we assume spin-singlet pairing, the induced Hamiltonian is given by

$$H_\Delta(\boldsymbol{k}) = \Delta(\boldsymbol{k})\,\tau_x \otimes \mathbb{I}_\sigma, \tag{5}$$

where $\Delta(\boldsymbol{k})$ is the induced pairing amplitude, considered real throughout the paper.

Combining all terms from Eqs. (2), (3), and (5), we find the final Hamiltonian with induced superconducting pairing

$$H = H_\alpha(\boldsymbol{k}) + H_V + H_\Delta(\boldsymbol{k}). \tag{6}$$

In order to further simplify the above Hamiltonian, let us express it in the diagonal basis of $H_\alpha(\boldsymbol{k}) + H_V$ with Rashba coupling and Zeeman field only:

$$H = \begin{pmatrix} E_+ & 0 & \Delta_{+-} & \Delta_{++} \\ 0 & E_- & \Delta_{--} & \Delta_{+-} \\ \Delta^*_{+-} & \Delta^*_{--} & -E_- & 0 \\ \Delta^*_{++} & \Delta^*_{+-} & 0 & -E_+ \end{pmatrix}, \tag{7}$$

where

$$\Delta_{--}(\boldsymbol{k}) = \frac{-\alpha k \Delta(\boldsymbol{k})}{\sqrt{V^2+\alpha^2k^2}}\frac{-ik_x+k_y}{k}, \tag{8}$$

$$\Delta_{++}(\boldsymbol{k}) = \frac{-\alpha k \Delta(\boldsymbol{k})}{\sqrt{V^2+\alpha^2k^2}}\frac{ik_x+k_y}{k}, \tag{9}$$

$$\Delta_{+-}(\boldsymbol{k}) = \frac{-V\Delta(\boldsymbol{k})}{\sqrt{V^2+\alpha^2k^2}}. \tag{10}$$

Therefore, the originally parent pairing $\Delta(\boldsymbol{k})$ has generated an effective intraband Δ_{++}, Δ_{--} and interband Δ_{+-} pairing. If the interband coupling Δ_{+-}, which is of the order of $\Delta(\boldsymbol{k})$, is much smaller than the separation between the two particle bands $\approx|V|$, i.e., $|V| \gg \Delta(\boldsymbol{k})$, we can neglect the upper unoccupied band. As a result, we focus on the 2×2 effective Hamiltonian given by the lower bands. In this limit, the intraband terms couple electrons with the same spin, i.e., spin-triplet pairing, reaching the spinless regime. This is essential to have Majorana bound states, since creation and annihilation operators for Majorana quasiparticles must be equal to each other in order to fulfill the condition that Majorana fermions are their own antiparticles.

For d-wave pairing symmetry, the amplitude is given by

$$\Delta(\boldsymbol{k}) = \frac{\Delta_d}{k_F^2}\left(k_x^2 - k_y^2\right), \tag{11}$$

where k_F is the Fermi momentum in the 2DEG. It is important to highlight that the d-wave pairing amplitude, unlike the constant s-wave pairing, depends on the azimuth angle, $\theta_{\boldsymbol{k}}$, since $k_x^2 - k_y^2 = k^2\cos(2\theta_{\boldsymbol{k}})$. The momentum parallel to the interface is conserved and therefore, the induced pairing for d superconductors takes the form given in Eq. (11) [34,43–46]. Note that for an s-wave parent superconductor where $\Delta(\boldsymbol{k}) = \Delta_s$ is constant, the above condition, $|V| \gg \Delta(\boldsymbol{k})$, is more restrictive than for a d-wave parent superconductor, where $|V| \gg \Delta(\boldsymbol{k})$ is automatically satisfied for $\boldsymbol{k} \sim 0$, unlike the s-wave case. We stress that the continuum theory given by Hamiltonian (6) is strictly valid in the vicinity of the Γ point $\boldsymbol{k} \approx 0$. In this case, the d-wave superconductor is itself a gapless system and supports flat bands at the edge. The effect of these modes on the 2DEG depends on the particular details of the setup and are considered negligible for the present study.

Assuming that the Zeeman field is also much larger than the spin-orbit energy, $|V| \gg E_{SO} = \frac{1}{2}m\alpha^2$, and that we have a parent d-wave superconductor, we arrive at the following effective Hamiltonian:

$$H_{\text{eff}}(\boldsymbol{k}) = \begin{pmatrix} \frac{k^2}{2m} - \mu - |V| & \Delta_f(\boldsymbol{k}) \\ \Delta_f^*(\boldsymbol{k}) & -\frac{k^2}{2m} + \mu + |V| \end{pmatrix}, \tag{12}$$

with an induced pairing

$$\Delta_f = \frac{-\alpha\Delta_d}{|V|}(-ik_x + k_y)\frac{\left(k_x^2 - k_y^2\right)}{k_F^2}, \tag{13}$$

where $k_F = \sqrt{2m(\mu+|V|)}$. If we expand the above equation in polar coordinates to study the orbital symmetries of the pairing, we have: $\Delta_f \sim k^3(e^{3i\theta_k} - e^{-i\theta_k})$. Thus, the resulting pairing has both orbital p-wave and f-wave symmetries and both form a spin triplet that allows the existence of Majorana states. From now on, we call the mentioned pairing f-wave pairing for simplicity.

We note that the energy gap closes when $\mu + |V| = 0$ signaling a phase transition. For $\mu > -|V|$ the superconductor is in a topological phase and in a trivial phase otherwise. Additionally, the energy gap also closes at four nodal points at the Fermi surface when $k_x = \pm k_y = \pm k_F$ [47].

It is worth mentioning that the effective f-wave pairing in Eq. (13) is obtained when the crystallographic orientation of the d-wave parent superconductor with respect to the 2DEG plane is the one shown in Fig. 1. Otherwise a different pairing symmetry would be induced [34].

B. Majorana wave function from d-wave superconductors

So far we have derived an effective two-band Hamiltonian, which is simple enough to analytically compute the localization and oscillation properties of the induced Majorana modes. In particular, we would like to study how the wave function of the Majorana fermions is modified due to the inclusion of a parent d-wave superconductor, instead of the more commonly studied case with s-wave pairing symmetry.

Starting from Hamiltonian in Eq. (12), we assume semi-infinite boundary conditions in the x direction and periodic boundary conditions in the y direction. As mentioned before, we take the pairing amplitude $\Delta(\boldsymbol{k})$ to be real. Majorana zero modes (MZMs) have to fulfill the zero energy condition $H_{\text{eff}}\,\boldsymbol{\psi} = E\boldsymbol{\psi} = 0$ at $k_y = 0$, giving rise to the following system of differential equations

$$\begin{aligned} \frac{1}{2m}\partial_x^2\psi_1 + \frac{\alpha\Delta_0}{|V|}\partial_x^3\psi_2 + (\mu+|V|)\psi_1 &= 0 \\ \frac{1}{2m}\partial_x^2\psi_2 + \frac{\alpha\Delta_0}{|V|}\partial_x^3\psi_1 + (\mu+|V|)\psi_2 &= 0. \end{aligned} \tag{14}$$

The equation above can be easily decoupled using particle-hole symmetry, since ψ_1 and ψ_2 are related by $\psi_1 = -\psi_2$. We are left with a single independent linear differential equation where the third order term comes from the f-wave pairing in Eq. (13). Subsequently, a third degree characteristic polynomial is solved to find the solutions. Since we consider a semi-infinite system and we are looking for localized states at

the edge, we enforce the boundary conditions: $\psi(x=0)=0$ and $\psi(x=\infty)=0$. The only possible solution for Eq. (14) with these constraints casts the form

$$\psi_1(x) = Ne^{-ux}\sin vx, \tag{15}$$

where u and v are, respectively, the real and imaginary parts of one of the roots of the characteristic polynomial. Since u and v are the solutions for a d-wave parent Hamiltonian, henceforth we will add the subindex u_d and v_d to denote these solutions. For an s-wave parent Hamiltonian, the solution for MZMs also takes the form in Eq. (15). In this case, the solutions are called u_s and v_s. We study first the properties of Majorana wave function coming from a d-wave superconductor, and we compare the results with the MZMs induced by an s-wave superconductor.

The decay of the MZMs into the bulk is given by u_d, and the amplitude of the oscillation of the wave function by v_d. The third order differential equation for ψ_1 leads to a third order algebraic equation for u_d. Making use of the relations between the coefficients of a third order polynomial and its roots, it is possible to find an explicit expression for u_d:

$$u_d = -\frac{|q|}{q}\sqrt{\frac{p}{3}}\cosh\left(\frac{1}{3}\operatorname{arccosh}\left(\frac{3|q|}{2p}\sqrt{\frac{3}{p}}\right)\right) - \frac{1}{3}\left|\frac{|V|(\mu+|V|)}{\alpha\Delta_d}\right|, \tag{16}$$

where p and q are defined as

$$p := \frac{1}{3}\left|\frac{V}{2m\alpha\Delta_d}\right|^2, \tag{17}$$

$$q := -\frac{2}{27}\left|\frac{V}{2m\alpha\Delta_d}\right|^3 - (\mu+|V|)\left|\frac{V}{\alpha\Delta_d}\right|. \tag{18}$$

The detailed calculation of these expressions is specified in Appendix A.

Having the analytic expression of the decay of the MZMs, one may wonder why it is important that Majorana fermions remain localized. This is crucial for instance from the point of view of quantum computation, since one reason for the protection of the MZMs is due to their nonlocal character that result into protection against local perturbations.

The coherence length of the superconductor ξ is inversely proportional to the superconducting gap. Consequently, the larger the gap, the more localized we may expect the MZMs to be. This is true regardless of whether the underlying pairing symmetry is s wave or d wave. The angular dependence for d-wave superconductors, Eq. (11), leads to an effective reduction of the superconducting gap, which implies a larger coherence length ξ on average in the superconductor. As a result, we may intuitively expect a stronger interaction between Majorana fermions at the edges due to this larger coherence length. An exponentially small gap in the length of the sample opens because of the interaction of the two edge Majoranas. Therefore, edge localization constitutes a figure of merit for the usefulness of MZMs.

Remarkably, we show that for a wide range of values in the system parameters, the effect of the angular dependence of the d-wave pairing symmetry is irrelevant and MZMs are as isolated as for an underlying s-wave pairing. Furthermore, since experiments show a larger pairing gap for d-wave superconductors $\Delta_d \gg \Delta_s$ [48–52], the localization of MZMs should be even more pronounced in that case.

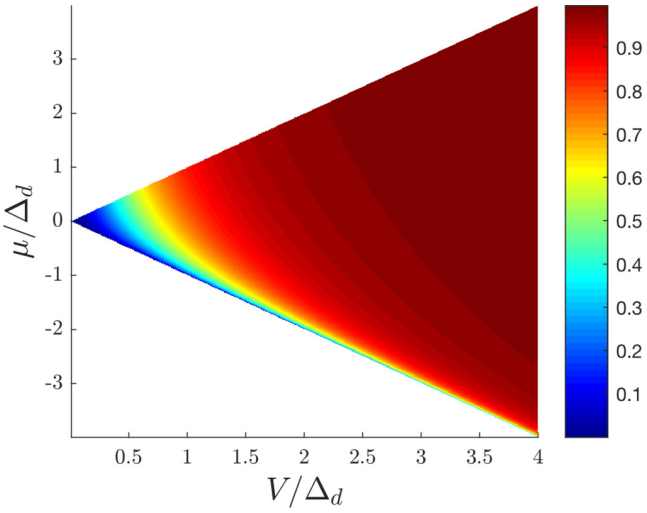

FIG. 2. Ratio between the exponential decays, u_d/u_s, of Majoranas coming from d- and s-wave superconductors, respectively, as a function of V and μ. Only the area with $|\mu| < |V|$ is shown. Parameters: $\Delta_s = \Delta_d$ and $E_{SO} = 0.05\Delta_d$.

Larger values of u_d mean that MZMs are more localized and decay faster into the bulk. We compare the decay u_d with $u_s = |\frac{\alpha\Delta_s}{V}|m$, where $|V| \gg \Delta_s, E_{SO}$, in Figs. 2 and 3. Figure 2 shows the ratio u_d/u_s as a function of V and μ considering the underlying s-wave superconducting gap equal to the d-wave one, $\Delta_s = \Delta_d$ in order to isolate and study the influence of the angular dependence solely. Figure 3 shows this same ratio as a function of E_{SO} and μ. The ratios between the Hamiltonian parameters are taken to resemble experimental values in semiconductors such as InAs or InSb [49,51,52].

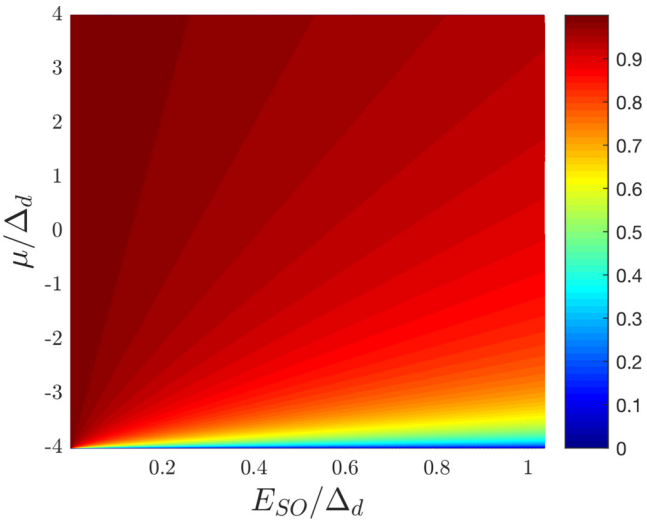

FIG. 3. Ratio between the localization of MZMs induced by d and s-wave superconductivity, u_d/u_s, as a function of E_{SO} and μ. Parameters: $\Delta_s = \Delta_d$ and $V = 4\Delta_d$.

In Fig. 2 it can be seen that provided the Zeeman energy V is large with respect to Δ_d, the ratio u_d/u_s is nearly equal to 1. This implies that the larger V the more similar the s-wave and the d-wave case become, regardless of the angular dependence of the d-wave pairing.

Nevertheless, there are certain areas where the ratio u_d/u_s decreases, where the localization of MZMs coming from s-wave superconductor is much greater than the localization of Majoranas induced by a d-wave superconductor. This can be seen in a small band in the lower part of Fig. 3 where $\mu \sim -V$. Also, in Fig. 2 the ratio decreases for low values of V. However, this latter area is outside the valid regime of our effective model. In Fig. 2, we need to have $|V| \gg \Delta_s$ for u_s [and $|V| \gg \Delta(\boldsymbol{k})$ for u_d] and $|V| \gg E_{SO}$ in Fig. 3.

A possible instance of d-wave superconductors corresponds to high-T_c superconductors, where the superconducting gap is one or two orders of magnitude greater than a conventional s-wave superconductor [44,48]. This means that Δ_s would be much smaller than Δ_d. Considering realistic Δ_s values, the ratios in Figs. 2 and 3 are multiplied by the relation Δ_d/Δ_s. Thus, MZMs arising from d-wave superconductors should be much more localized for high V than their counterparts, induced by s-wave superconductors.

Additionally, the wave function of MZMs, see Eq. (15), oscillates at a frequency v_d,

$$v_d^2 = \frac{2(s_1 + 2u)}{u}, \tag{19}$$

where $s_1 = \frac{(\mu+|V|)|V|}{\alpha\Delta_d}$. A detailed derivation of Eq. (19) can be found in Appendix A. The equivalent expression for Majoranas coming from an s-wave superconductor is $v_s = \sqrt{2m(\mu+|V|) - m^2|\frac{\alpha\Delta_s}{V}|^2}$. It is important to remark that v_s can take imaginary values. For $2m(\mu+|B|) < m^2|\frac{\alpha\Delta}{B}|^2$ the square root is imaginary and the sine of v_s turns into a hyperbolic sine. Therefore, in order to compare v_s and v_d, we should consider $v_s = 0$ for the range mentioned before. Nevertheless, this occurs when V/Δ_s is small. Therefore this region with $v_s = 0$ is outside the scope of our calculations, since we require $|V| \gg \Delta_s$. Outside these regions, when $|V| \gg \Delta_s, E_{SO}$ we have $v_s \simeq \sqrt{2m(\mu+|V|)} = k_F$. The resulting ratios v_d/v_s have very similar behavior to u_d/u_s, taking values close to 1 but always smaller. The larger the Zeeman energy, V, the closer this ratio gets to 1. It was mentioned previously that the ratio u_d/u_s is multiplied by a factor Δ_d/Δ_s when $\Delta_d \neq \Delta_s$. Contrary to what happens with the decay ratio, u_d/u_s, the oscillation ratio does not appreciably change with Δ_d/Δ_s and keeps always values close to 1.

In summary, we have proven that the angular dependence of an underlying d-wave superconductor has little effect on the localization and oscillation properties of MZMs induced on a 2DEG. Moreover, since d-wave superconductors have larger superconducting pairing amplitudes, we may expect MZMs to be more localized than in the s-wave parent superconductor case. This fact could have positive implications in current proposals for topological quantum computation using MZMs, since the robustness of the Majorana quasiparticles partly relies on their nonlocal and edge-localized character.

III. MICROSCOPIC HAMILTONIAN

In Sec. II we have derived an effective model to study the low energy physics around $\boldsymbol{k} \sim 0$. In this section, we define a microscopic lattice model that comprises the effective Hamiltonian previously described in Eq. (12). Moreover, we calculate a topological invariant which distinguishes between topological and trivial phases, i.e. whether Majorana states exist or not. This microscopic model corresponds to the exotic pairing phenomenologically derived in Sec. II.

A. Lattice Hamiltonian

Assuming that k and k^2 terms in Eq. (12) correspond to the lowest order expansion of the trigonometric functions $\sin k$ and $\cos k$, we can write a lattice Hamiltonian in momentum space that casts the form

$$\mathcal{H}_{\text{micro}} = \frac{1}{2}\sum_{\boldsymbol{k}} (c_{\boldsymbol{k}}^\dagger,\, c_{-\boldsymbol{k}}) H_{\text{m}}(\boldsymbol{k}) \begin{pmatrix} c_{\boldsymbol{k}} \\ c_{-\boldsymbol{k}}^\dagger \end{pmatrix}, \tag{20}$$

where

$$H_{\text{m}}(\boldsymbol{k}) = \begin{pmatrix} \epsilon(\boldsymbol{k}) & d(\boldsymbol{k}) \\ d^*(\boldsymbol{k}) & -\epsilon(\boldsymbol{k}) \end{pmatrix}, \tag{21}$$

with $\epsilon(\boldsymbol{k}) = -2t(\cos k_x + \cos k_y) - \tilde{\mu} + 4t$, $d(\boldsymbol{k}) = 4i\tilde{\Delta}$ $(\sin k_x + i \sin k_y)(\cos k_y - \cos k_x)$, $t = 1/2m$, $\tilde{\mu} = \mu + |V|$ and $\tilde{\Delta} = \frac{\alpha\Delta_d}{2|V|k_F^2}$. We recover Eq. (12) in the $\boldsymbol{k} \to 0$ limit. The energy bands for the lattice model are given by $E(\boldsymbol{k}) = \pm\sqrt{\epsilon^2(\boldsymbol{k}) + |d(\boldsymbol{k})|^2}$. The gap vanishes at the points $(k_x, k_y, \tilde{\mu}) = (0,0,0)$, $(0,\pi,4t)$, $(\pi,0,4t)$, and $(\pi,\pi,8t)$, suggesting phase transitions. Additionally, there are nodal lines, placed at $k_x = \pm k_y = \pm k_F$.

Despite the existence of nodal lines that render the system gapless, it is possible to define a topological invariant that distinguishes between nontrivial and trivial phases. The Chern number [53] calculated for nodeless superconductors is no longer well defined [38,54]. To define the Chern number in a system with gapless lines like ours, it is necessary to remove the nodal states by adding a small perturbation. Nevertheless, the value of the Chern number is not independent of the perturbation introduced, and only the parity of the Chern number is uniquely defined by this procedure. Thus, this is a well-defined topological invariant even in the presence of bulk gapless excitations. The parity of the Chern number can be computed as

$$(-1)^{\nu_{\text{Ch}}} = \prod_{\alpha, i=1,2,3,4} \text{sgn}\, E_\alpha(\Gamma_i), \tag{22}$$

where $E_\alpha(\boldsymbol{k})$ is the eigenvalue of Hamiltonian (21) for each band α. In our particular case, α only takes one single value because the model only has one independent band, due to particle-hole symmetry. Γ_i are the time-reversal-invariant momenta $(0,0)$, $(0,\pi)$, $(\pi,0)$, and (π,π). Since $d(\boldsymbol{k})$ vanishes at time-reversal-invariant momenta we have

$$E_1(\Gamma_i) = \epsilon(\Gamma_i) = -2t(\cos\Gamma_{i,x} + \cos\Gamma_{i,y}) - \tilde{\mu} + 4t. \tag{23}$$

Applying the definition, the following expression is obtained:

$$(-1)^{\nu_{\text{Ch}}} = \text{sgn}[(-\tilde{\mu})(-\tilde{\mu}+4t)^2(-\tilde{\mu}+8t)], \tag{24}$$

and the parity of the Chern number is -1 in the interval $0 < \tilde{\mu} < 8t$, where the system is in a topological phase. The lower phase boundary $\tilde{\mu} = 0$ is in agreement with the results shown in Sec. II B, where there was a topological phase transition at $\tilde{\mu} = 0$. Additionally, the lattice model presents an upper bound for the topological phase at $\tilde{\mu} = 8t$ arising from the gap closing at the M point $(k_x,k_y) = (\pi,\pi)$. This feature was not captured in the phenomenological analysis around the Γ point $\boldsymbol{k} = 0$.

In order to obtain a microscopic model in real space, we employ the inverse Fourier transform:

$$c_{k_x,k_y} = \frac{1}{L}\sum_{n,m} e^{ink_x} e^{imk_y} c_{n,m}, \tag{25}$$

where $n(m)$ runs over all sites in the $x(y)$ direction and the result of this calculation is:

$$\begin{aligned}\mathcal{H}_{\text{micro}} = \sum\nolimits_{m,n}\{&-(\tilde{\mu}-4t)c^{\dagger}_{m,n}c_{m,n} - t(c^{\dagger}_{m+1,n}c_{m,n}\\ &+c^{\dagger}_{m,n}c_{m+1,n} + c^{\dagger}_{m,n+1}c_{m,n} + c^{\dagger}_{m,n}c_{m,n+1})\\ &+\tilde{\Delta}(c^{\dagger}_{m+1,n+1}c^{\dagger}_{m,n} + c^{\dagger}_{m+1,n}c^{\dagger}_{m,n+1}) + \text{H.c.}\\ &-i\tilde{\Delta}(c^{\dagger}_{m+1,n+1}c^{\dagger}_{m,n} + c^{\dagger}_{m,n+1}c^{\dagger}_{m+1,n}) + \text{H.c.}\\ &-\tilde{\Delta}(c^{\dagger}_{m+2,n}c^{\dagger}_{m,n}) + i\tilde{\Delta}(c^{\dagger}_{m,n+2}c^{\dagger}_{m,n}) + \text{H.c.}\}.\end{aligned} \tag{26}$$

Notably, the pairing in Eq. (21), when transformed from momentum to real space as is done in Eq. (26), involves nearest and next-to-nearest-neighbors interactions. This is in marked contrast to the microscopic model coming from a host s-wave superconductor, since the latter involves only nearest-neighbors interactions.

We want to study the properties of propagating Majorana states hosted by (26). Thus, we consider a cylindrical geometry with periodic boundary conditions in the y direction and open boundary conditions in the x direction. In Fig. 4 we depict the energy spectrum for this particular geometry. The propagating Majorana states cross linearly at $k_y = 0$ and are separated by a gap from the bulk states. At $k_y = \pm k_F$ the gap closes again at the Fermi momentum k_F, due to the nodal character of the superconducting pairing.

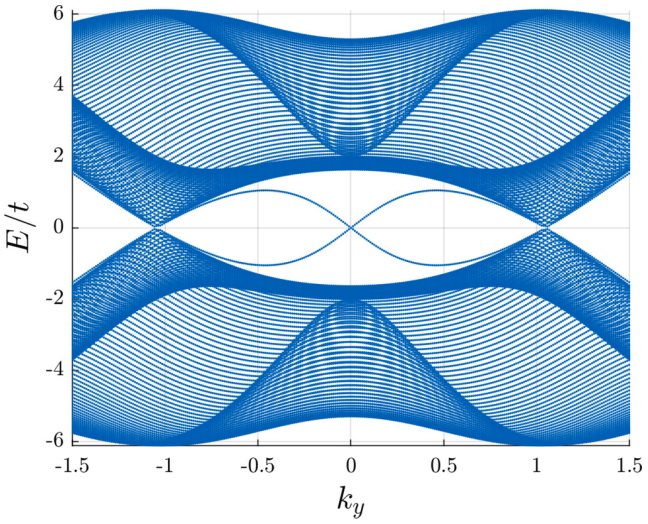

FIG. 4. Energy spectra for the f-wave lattice model (21) on a cylindrical geometry. Parameters: $\tilde{\mu} = 2t$, $\tilde{\Delta} = t$. Lattice sites in the x direction $N = 100$. Chiral gapless edge modes can be seen, since the system is topological for these parameters.

B. Disorder analysis

We observe the stability of Majorana fermions under static disorder in our lattice model. A random perturbation which depends on the site position modifies slightly the chemical potential. In order to introduce this perturbation, we add a new term to the Hamiltonian in (26), namely:

$$\mathcal{H}_{\delta\tilde{\mu}} = \sum_{m,n} \delta\tilde{\mu}_{m,n} c^{\dagger}_{m,n} c_{m,n}. \tag{27}$$

The coefficients $\delta\tilde{\mu}_{m,n} \in [-\sigma_{\mu},\sigma_{\mu}]$ are picked from a random uniform distribution with zero mean value and width $2\sigma_{\mu}$. We seek to probe the edge localization of the zero modes. Results show that even in the presence of a random potential, the propagating Majorana modes are robust. Similar studies in odd-frequency s-wave pairing show that Majorana fermions are also robust against disorder [55,56].

We introduce static disorder in both the x and y direction, considering a cylindrical geometry for our system. Neither k_x nor k_y are good quantum numbers now, since we are breaking translational symmetry. Thus, we calculate the spectrum of the perturbed Hamiltonian and focus on the low energy states. We plot the wave function of zero energy modes to check the localization of MZMs in Fig. 5. The results obtained show that even in the presence of weak static disorder, the edge states remain localized. Moreover, the exponential decay that characterizes MZMs is preserved up to a scale of energies where the static disorder could be treated as a perturbation with respect to the other energies in the system (see Fig. 6 in Appendix B). Majorana fermions may interact with nodal states under certain conditions making the Majoranas less robust [38].

On the other hand, nodal states exposed to static disorder may change their position in momentum space but cannot be removed. These states appear when the gap closes, $E = \sqrt{\epsilon^2(\boldsymbol{k}) + |d(\boldsymbol{k})|^2} = 0$, which can only happen if $\epsilon(\boldsymbol{k}) = d(\boldsymbol{k}) = 0$. $\epsilon(\boldsymbol{k}) = 0$ is the Fermi surface, while $d(\boldsymbol{k}) = 0$ yields the nodal lines $k_x = \pm k_y$. The intersection of the nodal lines and the Fermi surface results in the nodal states. Static disorder introduces a perturbation $\delta\tilde{\mu}$, which consequently alters the Fermi surface, $\epsilon + \delta\epsilon$, changing the point at which nodal lines cross the surface [57].

IV. CONCLUSIONS AND OUTLOOK

The purpose of this work is to study the properties of emerging Majorana modes in a 2DEG with strong spin-orbit coupling, a Zeeman field, and proximity induced d-wave superconductivity. Although the angular dependence of d-wave superconducting pairing would intuitively increase the superconducting coherence length, we have remarkably shown that Majorana modes are almost as localized as the ones obtained with a constant s-wave pairing amplitude. Moreover, since realistic values of the d-wave gap are much greater than

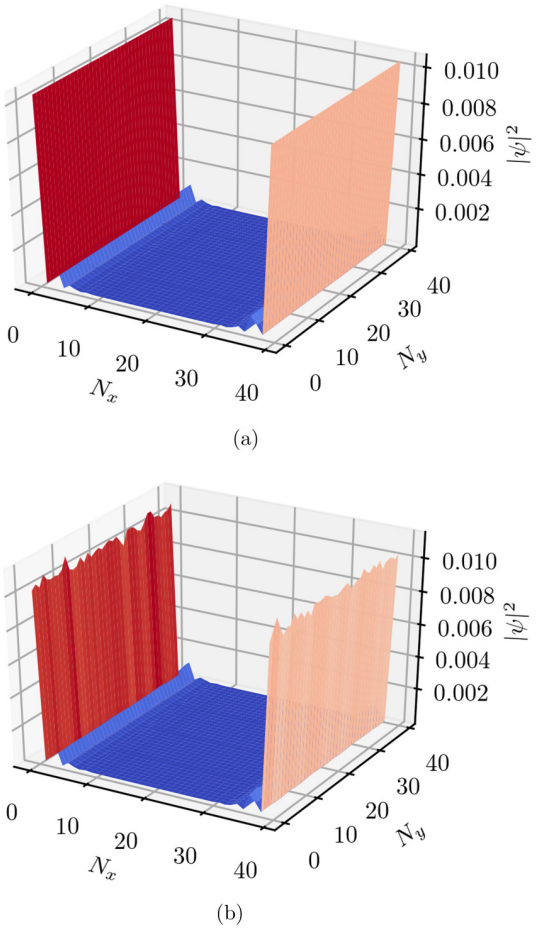

FIG. 5. Wave functions of the zero energy edge modes on a cylindrical geometry. (a) Shows the wave function of the zero-energy state with no disorder in the system. (b) Depicts the same state with $\sigma_\mu = 0.1$. Parameters: $\tilde{\mu} = 2t$, $\tilde{\Delta} = t = 1$. Lattice size is $N_x \times N_y = 40 \times 40$.

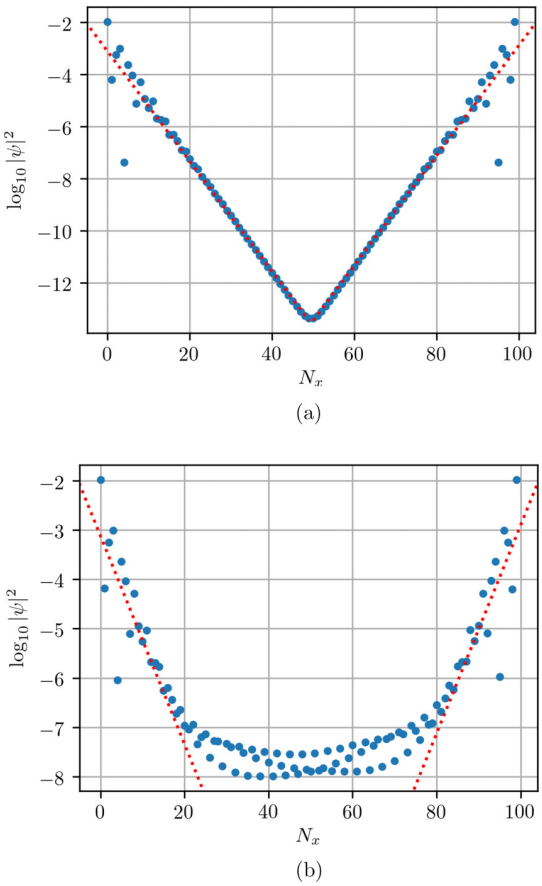

FIG. 6. Wave function probabilities of the zero energy edge modes on a plane in a logarithmic scale. (a) Shows the wave function of the zero-energy state with no disorder in the system. (b) Depicts the same state with $\sigma_\mu = 0.1$. Parameters: $\tilde{\mu} = 2t$, $\tilde{\Delta} = t$. Lattice size is $N_x \times N_y = 100 \times 40$. An average of 15 possible realizations for every 40 possible sections in the y direction was performed.

the s-wave superconducting gap, a sharper localization profile is expected for Majorana states induced by the former.

We have also studied a microscopic lattice version of the previous model with an effective f-wave pairing. In real space this model involves nearest and next-to-nearest-neighbors interactions. We have computed the phase diagram of this model by means of the parity of the Chern number, a topological invariant that is well defined even for nodal systems. In addition, we have proven the stability of the propagating Majorana modes against static disorder. This analysis has direct implications in experiments and proposals with high-T_c superconductors [9], as well as in cold atoms simulation of d-wave superconductors [41], with Raman-induced spin-orbit coupling [28].

ACKNOWLEDGMENTS

We thank D. Chowdhury and L. Fu for helpful discussions. We acknowledge financial support from the Spanish MINECO Grants No. FIS2012-33152, No. FIS2015-67411, and the CAM research consortium QUITEMAD+, Grant No. S2013/ICE-2801. The research of M.A.M.-D. has been supported in part by the US Army Research Office through Grant No. W911N F-14-1-0103. O.V. thanks Fundación Rafael del Pino, Fundación Ramón Areces and RCC Harvard. S.V. thanks FPU-MECD Grant.

APPENDIX A: DERIVATION OF MAJORANA STATES FROM AN EFFECTIVE f-WAVE PAIRING

Given a cylindrical geometry for Hamiltonian (12), we look for MZMs solutions that satisfy the equation $H_{\text{eff}}\,\boldsymbol{\psi} = 0$ at $k_y = 0$. This yields the system of differential equations in Eq. (14). Using particle-hole symmetry we can decouple these equations and obtain a single differential equation:

$$\frac{\alpha\Delta_d}{|V|k_F^2}\partial_x^3\psi_1 - \frac{\partial_x^2}{2m}\psi_1 - (\mu + |V|)\psi_1 = 0, \qquad \text{(A1)}$$

which has a third derivative instead of the first derivative we would find in the p-wave case. Using the ansatz e^{kx} we obtain the associated characteristic polynomial of (A1):

$$k^3 - \frac{(\mu + |V|)|V|}{\alpha\Delta_d}k^2 - \frac{2m(\mu + |V|)^2|V|}{\alpha\Delta_d} = 0. \qquad \text{(A2)}$$

We will now discuss when Eq. (A1) has Majorana solutions with boundary conditions $\psi(0) = \psi(\infty) = 0$. Polynomial (A2) may be rewritten as $(k-k_1)(k-k_2)(k-k_3) = k^3 - s_1k^2 + s_2k - s_3$, where k_1, k_2, and k_3 are the roots of the cubic polynomial and $s_1 = k_1 + k_2 + k_3 = \frac{(\mu+|V|)|V|}{\alpha\Delta_0}$, $s_2 = k_1k_2 + k_2k_3 + k_1k_3 = 0$, and $s_3 = k_1k_2k_3 = \frac{2m(\mu+|V|)^2|V|}{\alpha\Delta_0}$. The discriminant of the cubic equation reads

$$D = -4s_1^3s_3 - 27s_3^2. \tag{A3}$$

D vanishes for $(\mu + |V|) = 0$, $V = 0$ and $(\mu + |V|)|V|^2 = -\frac{27}{2}m\alpha^2\Delta_0^2$. Considering $\alpha, m, \Delta_0 \in \mathbb{R}^+$ and $\mu, V \in \mathbb{R}$; we have $D > 0$ when $(\mu + |V|)|V|^2 < -\frac{27}{2}m\alpha^2\Delta_0^2$ and negative D otherwise. If $D \geqslant 0$ we have three real roots, otherwise we have one real and two complex roots. A general solution for differential equation (A1) is $\psi_1 = C_1e^{k_1x} + C_2e^{k_2x} + C_3e^{k_3x}$, where we need to enforce the boundary conditions $\psi(0) = 0$ and $\psi(\infty) = 0$. We are working under the constraint $|\mu| < |V|$, thus we have that our solutions satisfy $D < 0$. If $D < 0$ there is one real root, k_1, and two complex, k_2 and k_3. Since s_1 and s_3 are real, one finds that $k_2, k_3 = -u \pm iv$, thus $s_1 = k_1 - 2u$, $s_2 = -2k_1u + (u^2 + v^2) = 0$ and $s_3 = k_1(u^2 + v^2)$. Therefore:

(i) $k_1, u > 0$ or $k_1, u < 0$ are not possible since $s_2 = 0$.

(ii) $k_1 < 0$ and $u < 0$: We have $C_2 = C_3 = 0$ to satisfy the boundary conditions at infinity and $C_1 = 0$ to satisfy them at $z = 0$. No solution.

(iii) $k_1 > 0$ and $u > 0$: $C_1 = 0$ to satisfy boundary conditions at infinity and $C_2 = -C_3$ to satisfy them at $x = 0$. Therefore $\psi_1 = C_2(e^{k_2x} - e^{k_3x}) = C_2e^{-ux} \sin vx$.

Summing up, if there are any Majoranas for $k_y = 0$, Eq. (A2) needs to have a positive real root and two complex roots with negative real part.

For the cubic polynomial (A2) there is a hyperbolic solution for the real root, k_1, given by

$$k_1 = -2\frac{|q|}{q}\sqrt{\frac{p}{3}}\cosh\left(\frac{1}{3}\operatorname{arccosh}\left(\frac{3|q|}{2p}\sqrt{\frac{3}{p}}\right)\right) + \frac{s_1}{3}, \tag{A4}$$

where p and q are defined in the main text, in Eqs. (17) and (18). From this equation we can immediately find equations for $u = \frac{-s_1+k_1}{2}$ and for $v^2 = \frac{2k_1}{u}$. These variables are called u_d and v_d in the main text.

APPENDIX B: EXPONENTIAL DECAY OF MZMS WITH STATIC DISORDER

This Appendix is devoted to provide a detailed description of the exponential decay of the MZMs. To this end, we plot the wave function of the zero energy modes in logarithmic scale. If the decay were purely exponential, the wave function would be a straight line. However, we know that there are natural oscillations due to the ansatz of the wave function, Eq. (15) in the paper. Figure 6(a) shows the decay of a Majorana state without disorder. The red dashed line represents a linear fitting of the results obtained from the lattice model. As it can be concluded from the figure, it is a clearly exponential decay. The same linear fitting is plotted in Fig. 6(b), i.e., the gradient of the red dashed line is the same in both graphics. For weak disorder, the exponential decay remains unaltered. The fluctuations around the linear fitting shown in Fig. 6(b) come not only from the disorder introduced in the system but also from the oscillations of the wave function itself [Eq. (15)].

We can conclude that the decay of the Majorana modes coming from d-wave superconductors remains roughly exponential even when weak static disorder is introduced in the system.

[1] E. Majorana, Il Nuovo Cimento **14**, 171 (1937).
[2] F. Wilczek, Nat. Phys. **5**, 614 (2009).
[3] A. Das, Y. Ronen, Y. Most, Y. Oreg, M. Heiblum, and H. Shtrikman, Nat. Phys. **8**, 887 (2012).
[4] V. Mourik, K. Zuo, S. M. Frolov, S. R. Plissard, E. P. A. M. Bakkers, and L. P. Kouwenhoven, Science **336**, 1003 (2012).
[5] M. T. Deng, C. L. Yu, G. Y. Huang, M. Larsson, P. Caroff, and H. Q. Xu, Nano Lett. **12**, 6414 (2012).
[6] S. M. Albrecht, A. P. Higginbotham, M. Madsen, F. Kuemmeth, T. S. Jespersen, J. Nygård, P. Krogstrup, and C. M. Marcus, Nature (London) **531**, 206 (2016).
[7] Q. L. He, L. Pan, A. L. Stern, E. C. Burks, X. Che, G. Yin, J. Wang, B. Lian, Q. Zhou, E. S. Choi, K. Murata, X. Kou, Z. Chen, T. Nie, Q. Shao, Y. Fan, S.-C. Zhang, K. Liu, J. Xia, and K. L. Wang, Science **357**, 294 (2017).
[8] H.-H. Sun, K.-W. Zhang, L.-H. Hu, C. Li, G.-Y. Wang, H.-Y. Ma, Z.-A. Xu, C.-L. Gao, D.-D. Guan, Y.-Y. Li, C. Liu, D. Qian, Y. Zhou, L. Fu, S.-C. Li, F.-C. Zhang, and J.-F. Jia, Phys. Rev. Lett. **116**, 257003 (2016).
[9] A. Kitaev, Ann. Phys. **303**, 2 (2003).
[10] S. Bravyi, B. M. Terhal, and B. Leemhuis, New J. Phys. **12**, 083039 (2010).
[11] J. Alicea, Y. Oreg, G. Refael, F. von Oppen, and M. Fisher, Nat. Phys. **7**, 412 (2011).
[12] C. Nayak, S. H. Simon, A. Stern, M. Freedman, and S. D. Sarma, Rev. Mod. Phys. **80**, 1083 (2008).
[13] D. Litinski, M. S. Kesselring, J. Eisert, and F. von Oppen, Phys. Rev. X **7**, 031048 (2017).
[14] D. Litinski and F. von Oppen, Phys. Rev. B **96**, 205413 (2017).
[15] D. Litinski and F. von Oppen, arXiv:1709.02318.
[16] H. Bombin and M. A. Martin-Delgado, Phys. Rev. Lett. **97**, 180501 (2006).
[17] H. Bombin and M. A. Martin-Delgado, Phys. Rev. Lett. **98**, 160502 (2007).
[18] A. Y. Kitaev, Phys. Usp. **44**, 131 (2001).
[19] L. Fu and C. L. Kane, Phys. Rev. Lett. **100**, 096407 (2008).
[20] R. M. Lutchyn, J. D. Sau, and S. D. Sarma, Phys. Rev. Lett. **105**, 077001 (2010).
[21] Y. Oreg, G. Refael, and F. von Oppen, Phys. Rev. Lett. **105**, 177002 (2010).
[22] J. D. Sau, R. M. Lutchyn, S. Tewari, and S. D. Sarma, Phys. Rev. Lett. **104**, 040502 (2010).
[23] J. Alicea, Phys. Rev. B **81**, 125318 (2010).

[24] P. Zhang, K. Yaji, T. Hashimoto, Y. Ota, T. Kondo, K. Okazaki, Z. Wang, J. Wen, G. D. Gu, H. Ding, and S. Shin, arXiv:1706.05163.
[25] C.-X. Liu, F. Setiawan, J. D. Sau, and S. D. Sarma, Phys. Rev. B **96**, 054520 (2017).
[26] F. Pientka, L. I. Glazman, and F. von Oppen, Phys. Rev. B **88**, 155420 (2013).
[27] F. Pientka, L. I. Glazman, and F. von Oppen, Phys. Rev. B **89**, 180505 (2014).
[28] S. Nadj-Perge, I. K. Drozdov, J. Li, H. Chen, S. Jeon, J. Seo, A. H. MacDonald, B. A. Bernevig, and A. Yazdani, Science **346**, 602 (2014).
[29] T. Neupert, A. Yazdani, and B. A. Bernevig, Phys. Rev. B **93**, 094508 (2016).
[30] O. Viyuela, D. Vodola, G. Pupillo, and M. A. Martin-Delgado, Phys. Rev. B **94**, 125121 (2016).
[31] J. Li, T. Neupert, Z. Wang, A. H. MacDonald, A. Yazdani, and B. A. Bernevig, Nat. Commun. **7**, 12297 (2016).
[32] V. Kaladzhyan, J. Röntynen, P. Simon, and T. Ojanen, Phys. Rev. B **94**, 060505 (2016).
[33] O. Viyuela, L. Fu, and M. A. Martin-Delgado, Phys. Rev. Lett. **120**, 017001 (2018).
[34] S. Takei, B. M. Fregoso, V. Galitski, and S. D. Sarma, Phys. Rev. B **87**, 014504 (2013).
[35] J. Linder, Y. Tanaka, T. Yokoyama, A. Sudbø, and N. Nagaosa, Phys. Rev. Lett. **104**, 067001 (2010).
[36] Y. Tanaka, M. Sato, and N. Nagaosa, J. Phys. Soc. Jpn. **81**, 011013 (2012).
[37] Y. Levine, A. Haim, and Y. Oreg, Phys. Rev. B **96**, 165147 (2017).
[38] M. Sato and S. Fujimoto, Phys. Rev. Lett. **105**, 217001 (2010).
[39] B. T. Zhou, N. F. Q. Yuan, H.-L. Jiang, and K. T. Law, Phys. Rev. B **93**, 180501 (2016).
[40] A. P. Schnyder and P. M. R. Brydon, J. Phys.: Condens. Matter **27**, 243201 (2015).
[41] S. Trebst, U. Schollwöck, M. Troyer, and P. Zoller, Phys. Rev. Lett. **96**, 250402 (2006).
[42] L. Jiang, T. Kitagawa, J. Alicea, A. R. Akhmerov, D. Pekker, G. Refael, J. I. Cirac, E. Demler, M. D. Lukin, and P. Zoller, Phys. Rev. Lett. **106**, 220402 (2011).
[43] P. Zareapour, J. Xu, S. Y. F. Zhao, A. Jain, Z. Xu, T. S. Liu, G. D. Gu, and K. S. Burch, Supercond. Sci. Technol. **29**, 125006 (2016).
[44] P. Zareapour, A. Hayat, S. Y. F. Zhao, M. Kreshchuk, A. Jain, D. C. Kwok, N. Lee, S.-W. Cheong, Z. Xu, A. Yang, G. Gu, S. Jia, R. J. Cava, and K. S. Burch, Nat. Commun. **3**, 1056 (2012).
[45] S. Kashiwaya and Y. Tanaka, Rep. Prog. Phys. **63**, 1641 (2000).
[46] Y. Tanaka and S. Kashiwaya, Phys. Rev. Lett. **74**, 3451 (1995).
[47] M. Leijnse and K. Flensberg, Semicond. Sci. Technol. **27**, 124003 (2012).
[48] M. Hashimoto, I. M. Vishik, R.-H. He, T. P. Devereaux, and Z.-X. Shen, Nat. Phys. **10**, 483 (2014).
[49] T. D. Stanescu, R. M. Lutchyn, and S. D. Sarma, Phys. Rev. B **84**, 144522 (2011).
[50] H. J. Suominen, M. Kjaergaard, A. R. Hamilton, J. Shabani, C. J. Palmstrøm, C. M. Marcus, and F. Nichele, Phys. Rev. Lett. **119**, 176805 (2017).
[51] J. S. Lee, B. Shojaei, M. Pendharkar, A. P. McFadden, Y. Kim, H. J. Suominen, M. Kjaergaard, F. Nichele, C. M. Marcus, and C. J. Palmstrøm, arXiv:1705.05049.
[52] J. Shabani, M. Kjaergaard, H. J. Suominen, Y. Kim, F. Nichele, K. Pakrouski, T. Stankevic, R. M. Lutchyn, P. Krogstrup, R. Feidenhans'l, S. Kraemer, C. Nayak, M. Troyer, C. M. Marcus, and C. J. Palmstrøm, Phys. Rev. B **93**, 155402 (2016).
[53] M. Kohmoto, Ann. Phys. **160**, 343 (1985).
[54] M. Sato, Phys. Rev. B **81**, 220504 (2010).
[55] Y. Asano and Y. Tanaka, Phys. Rev. B **87**, 104513 (2013).
[56] Y. Tanaka and A. A. Golubov, Phys. Rev. Lett. **98**, 037003 (2007).
[57] M. Sato, Phys. Rev. B **73**, 214502 (2006).

5. Summary and main results of publication 2

The search for new topological phases of matter has been especially intense in superconductors, which can host the long-sought-after Majorana fermions that can be used as building blocks for topological quantum computers. The most representative example of this topological phases is triplet p-wave superconductivity. However, a rich topological behavior can also appear in singlet superconductors when subject to spin-orbit coupling and a Zeeman field. Therefore, exhausting the analysis of all possible superconducting pairing channels of these materials is a fundamental question. In this work, we study all possible mixed nodeless pairings compatible with tetragonal crystal symmetry. These pairings are obtained by combining the one-dimensional irreducible representations of the crystal symmetry group D_{4h}. The one-dimensional representations are s-wave, g-wave and the two d-wave possibilities, d_{xy} and $d_{x^2-y^2}$. These are then combined to form the four nodeless pairings $s + \mathrm{i}g$, $s + \mathrm{i}d_{xy}$, $s + \mathrm{i}d_{x^2-y^2}$ and $d_{x^2-y^2} + \mathrm{i}d_{xy}$. Below, the main results obtained in publication [P2] are presented.

1. **Chern number and zero-energy modes.** In this work, we analyze the four possible nodeless superconducting pairings compatible with tetragonal crystal symmetry. We compute the phase diagrams for each one of these pairings, obtaining high Chern numbers for some phases. The bulk-edge correspondence establishes that the Chern number coincides with the number of edge states. However, we show that the number of zero-energy modes is not necessarily the same as the Chern number, since some of these zero-energy modes are not topologically robust.
2. **Massive edge states.** For a particular case of these nodeless superconducting pairings, $d+\mathrm{i}d$, we have observed topologically protected massive edge modes which are associated with the partial Chern number of the upper band.
3. **Zero energy modes away from highly symmetric points.** The $d+\mathrm{i}d$ pairing shows another interesting property: it presents zero-energy modes out of the time-reversal-invariant momenta. Based on the bulk-edge correspondence, we explain why this happens for certain regions of the topological phase diagram and show that these zero-modes are topologically robust.

IOP Publishing Journal of Physics: Condensed Matter
J. Phys.: Condens. Matter **30** (2018) 395602 (7pp) https://doi.org/10.1088/1361-648X/aadc71

Topological phases in nodeless tetragonal superconductors

S Varona[1], L Ortiz[1], O Viyuela[2,3] and M A Martin-Delgado[1]

[1] Departamento de Física Teórica, Universidad Complutense, 28040 Madrid, Spain
[2] Department of Physics, Harvard University, Cambridge, MA 02318, United States of America
[3] Department of Physics, Massachusetts Institute of Technology, Cambridge, MA 02139, United States of America

E-mail: svarona@ucm.es

Received 3 July 2018, revised 20 August 2018
Accepted for publication 23 August 2018
Published 10 September 2018

Abstract

We compute the topological phase diagram of 2D tetragonal superconductors for the only possible nodeless pairing channels compatible with that crystal symmetry. Subject to a Zeeman field and spin–orbit coupling, we demonstrate that these superconductors show surprising topological features: non-trivial high Chern numbers, massive edge states, and zero-energy modes out of high symmetry points, even though the edge states remain topologically protected. Interestingly, one of these pairing symmetries, $d + id$, has been proposed to describe materials such as water-intercalated sodium cobaltates, bilayer silicene or highly doped monolayer graphene, which opens the way for further applications of our results.

Keywords: topological superconductors, topological phases of matter, edge states, bulk-edge correspondence

(Some figures may appear in colour only in the online journal)

1. Introduction

Topological phases of matter have acquired a prominent role in condensed matter physics and quantum computation since the most outstanding examples were proposed [1–3].

Developments on 2D superconductors have led to great interest in investigating novel quantum phenomena. There is an increasing body of experimental evidence that superconductivity can be remarkably robust in the two-dimensional (2D) limit, both in conventional and in high-T_c superconductors [4].

Particularly, topological superconductors have gained additional interest since they host Majorana fermions, that could be used as building blocks of future topological quantum computers [5–7]. The odd superconducting pairing mechanism required to display topological features has not being found in Nature, except for the B phase of superfluid ^{3}He [8] and probably ruthenates [9]. However, it can be synthesized in different experimental platforms: topological insulators [10, 11] and semiconductors [12–14] proximity coupled to superconductors, diluted magnetic impurities in superconducting lead [15], iron-based superconductors [16], quantum anomalous Hall insulator [17], etc. These experiments make use of underlying superconductors to eventually observe Majorana fermions. Most of these proposals use conventional superconductors [10, 18, 19], although there are some for high-T_c superconductors [20–23] as well.

Likewise, describing the more exotic high-T_c superconductors has motivated a lot of research since they were experimentally discovered [24]. Shortly after, the resonating valence bond theory came up as the first theoretical proposal to describe these materials [25]. Despite the microscopic origin of high-T_c superconductors is still unknown, these materials were shown to present d-wave pairing symmetry, tetragonal crystal symmetry and singlet pairing [26]. The question of understanding what generic properties might be expected of singlet-paired tetragonal superconductors gave rise to a systematic symmetry classification of all possible pairing channels [27].

Singlet pairing in tetragonal superconductors can take the well-known forms of s-wave and d-wave states. However, it is also possible to have alternative singlet pairings which are compatible with the symmetry group of tetragonal crystals D_{4h}. A complementary analysis of the D_{6h} group would allow

us to extend these results for the case of hexagonal lattices. Even though the results would be qualitatively different, the analytic procedure and numerical methods developed in this work still hold. These pairings might have some interesting implications regarding topological phases and the appearance of Majorana fermions. Of particular interest are the four different mixed nodeless pairings that can be formed by summing 1D irreducible representations of D_{4h}. One instance of these nodeless pairings is $d+\mathrm{i}d$ pairing [28–33], which has potential applications and has been proposed in materials such as water-intercalated sodium cobaltates, bilayer silicene, epitaxial bilayer films of bismuth and nickel [32, 34–38], or highly doped monolayer graphene [39]. Thus, in this paper we wonder about the role of these less-studied nodeless pairing channels in the search for distinct topological phases of matter.

Superconductors have a particularly rich topological behavior in the presence of spin–orbit coupling (SOC) and a Zeeman field [40, 41]. When also considering d-wave superconductors, the presence of nodal lines gives rise to bulk states at zero energy and cause two main undesired effects: (i) the Chern number is ill-defined since the gap closes at the nodal points. (ii) Although the parity of the Chern number is a well-defined topological invariant and Majorana states are topologically protected, these may interact with nodal states in disordered systems [42, 43]. Remarkably, some of the tetragonal pairings previosly mentioned are nodeless. Thus, there are no nearby zero energy modes that may spoil the topological protection of the edge states. Since the gap does not close, the Chern number is well defined and related to the number of edge states via the bulk-edge correspondence [44–46].

In this work we analyse the four possible nodeless superconducting pairings (compatible with D_{4h} symmetry) thoroughly, using the Chern number and the bulk-edge correspondence, finding the following results: (i) despite the Chern number coincides with the number of edge states, the number of zero-energy modes is not necessarily the same as the Chern number. (ii) Massive edge states can be found for $d+\mathrm{i}d$ pairing when the upper band Chern number takes non-zero values. (iii) $d+\mathrm{i}d$ also presents zero energy modes out of the time-reversal-invariant momenta of the Brillouin Zone. This is quite remarkable, since in most cases the zero modes are naturally placed a these highly symmetric points. We explicitly show how the edge states satisfy the bulk-edge correspondence and test their robustness to weak disorder perturbations. Edge states appearing for $d+\mathrm{i}d$ pairing have been previously observed [28–32]. However, a detailed construction and explanation of their existence was still missing, to best of our knowledge.

The article is organized as follows. In section 2 we introduce the four different pairings we want to study with tetragonal symmetry D_{4h}. In section 3, we study their induced topological phases. In section 4 we compute the topological edge states and zero-energy modes. Section 5 is devoted to conclusions.

2. Formalism

In this section, we introduce a Hamiltonian on a square lattice to study the topological phases arising from 2D singlet superconductors with tetragonal D_{4h} symmetry. The necessary ingredients to have topological behavior are SOC, Zeeman field and superconducting pairing. Concretely, we analyze all possible nodeless pairing compatible with tetragonal symmetry. As it is mentioned in the introduction, nodeless pairings are particularly interesting. The Hamiltonian for these systems reads

$$\mathcal{H}=\frac{1}{2}\sum_{\boldsymbol{k},\sigma,\sigma'}\left(c^{\dagger}_{\boldsymbol{k},\sigma},c_{-\boldsymbol{k},\sigma}\right)H\left(\boldsymbol{k}\right)\begin{pmatrix}c_{\boldsymbol{k},\sigma'}\\ c^{\dagger}_{-\boldsymbol{k},\sigma'}\end{pmatrix}, \tag{1}$$

where

$$H\left(\boldsymbol{k}\right)=\begin{pmatrix}\epsilon\left(\boldsymbol{k}\right)-V\sigma_z+\boldsymbol{g}\left(\boldsymbol{k}\right)\cdot\boldsymbol{\sigma} & \mathrm{i}\Delta\left(\boldsymbol{k}\right)\sigma_y\\ -\mathrm{i}\Delta^{*}\left(\boldsymbol{k}\right)\sigma_y & -\epsilon\left(\boldsymbol{k}\right)+V\sigma_z+\boldsymbol{g}\left(\boldsymbol{k}\right)\cdot\boldsymbol{\sigma}^{*}\end{pmatrix}, \tag{2}$$

with $\epsilon\left(\boldsymbol{k}\right)=-2t\left(\cos k_x+\cos k_y\right)-\mu$, $\boldsymbol{g}\left(\boldsymbol{k}\right)=\alpha\left(\sin k_y,-\sin k_x,0\right)$ is the SOC, V is the Zeeman field, $\Delta\left(\boldsymbol{k}\right)$ is the superconducting pairing and $\boldsymbol{\sigma}$ are the Pauli matrices. $\Delta\left(\boldsymbol{k}\right)$ is an even function $\Delta\left(-\boldsymbol{k}\right)=\Delta\left(\boldsymbol{k}\right)$ as required by singlet pairing. The Hamiltonian is particle-hole symmetric, i.e. $\Gamma H\left(\boldsymbol{k}\right)\Gamma^{\dagger}=-H^{*}\left(-\boldsymbol{k}\right)$, with $\Gamma=\sigma_x\otimes\mathbb{I}$. The energy bands for this Hamiltonian take the form

$$\begin{aligned}E^2_{\pm}\left(\boldsymbol{k}\right)=&\epsilon^2\left(\boldsymbol{k}\right)+\left|\boldsymbol{g}\left(\boldsymbol{k}\right)\right|^2+V^2+\left|\Delta\left(\boldsymbol{k}\right)\right|^2\\&\pm2\sqrt{\epsilon^2\left(\boldsymbol{k}\right)\left|\boldsymbol{g}\left(\boldsymbol{k}\right)\right|^2+\epsilon^2\left(\boldsymbol{k}\right)V^2+\left|\Delta\left(\boldsymbol{k}\right)\right|^2V^2},\end{aligned} \tag{3}$$

where E_+ is the upper band and E_- the lower. Due to particle-hole symmetry we also have the hole-like solutions $-E_+$ and $-E_-$. It is important to obtain the conditions for which the energy gap closes, since these will signal a topological phase transition. From equation (3) one can obtain the conditions that must be satisfied for the lower band gap, $E_-\left(\boldsymbol{k}\right)$, to close

$$\epsilon^2\left(\boldsymbol{k}\right)+\left|\Delta\left(\boldsymbol{k}\right)\right|^2-V^2-\left|\boldsymbol{g}\left(\boldsymbol{k}\right)\right|^2=0, \tag{4}$$

$$\left|\Delta\left(\boldsymbol{k}\right)\right|\left|\boldsymbol{g}\left(\boldsymbol{k}\right)\right|=0. \tag{5}$$

We can also calculate the conditions for which the upper band gap, $E_+\left(\boldsymbol{k}\right)-E_-\left(\boldsymbol{k}\right)$, closes, i.e. $E_+\left(\boldsymbol{k}\right)=E_-\left(\boldsymbol{k}\right)$. We find

$$\epsilon\left(\boldsymbol{k}\right)=0, \tag{6}$$

$$\left|\Delta\left(\boldsymbol{k}\right)\right|=0. \tag{7}$$

To characterize completely the phase diagram in these systems we need a topological invariant. The topological invariant associated with the different topological phases for 2D superconductors with no time-reversal symmetry is the Chern number [47]. The bulk-edge correspondence relates the Chern number to the number of topological edge states at the boundary of the system [44, 48]. We will numerically

compute the Chern number by discretizing the Brillouin zone, using the expression [49, 50]

$$\nu_{\mathrm{Ch}} = \frac{1}{2\pi}\sum_j \mathrm{Im}\left(\log\prod_i \langle\psi_{\boldsymbol{k}_i}|\psi_{\boldsymbol{k}_{i+1}}\rangle\right)_j, \tag{8}$$

where $|\psi_{\boldsymbol{k}_i}\rangle$ is an eigenvector of the Hamiltonian evaluated at $\boldsymbol{k}_i$, j labels the different cells of the mesh that discretizes the Brillouin zone and i runs over the four vertices of each cell. The expression in equation (8) is derived by integrating the Berry curvature over the 2D Brillouin zone. The Berry curvature can be approximated as $\frac{-1}{\delta A_j}\mathrm{Im}\left(\log\prod_i\langle\psi_{\boldsymbol{k}_i}\psi_{\boldsymbol{k}_{i+1}}\rangle\right)_j$ at cell j, where δA_j is the area of the cell and the value of Im is restricted to the principle branch of the logarithm. This definition yields a quantity which is manifestly gauge invariant.

We are interested in the singlet nodeless pairings compatible with point-group symmetry D_{4h} of a tetragonal superconductor. They are given by the s-wave pairing and by four mixed pairings obtained by combining a real part from a 1D representation of the point group and an imaginary part from another 1D representation [27]. These 1D representations (neglecting higher order terms) are

$$\Delta_s(\boldsymbol{k}) = \Delta_s^0, \tag{9}$$

$$\Delta_g(\boldsymbol{k}) = \Delta_g^0(\sin 2k_x \sin k_y - \sin 2k_y \sin k_x), \tag{10}$$

$$\Delta_{d_{xy}}(\boldsymbol{k}) = \Delta_{d_{xy}}^0 \sin k_x \sin k_y, \tag{11}$$

$$\Delta_{d_{x^2-y^2}}(\boldsymbol{k}) = \Delta_{d_{x^2-y^2}}^0(\cos k_x - \cos k_y). \tag{12}$$

Combining these representations we get the four possible mixed nodeless pairings

$$\Delta_s(\boldsymbol{k}) + \mathrm{i}\Delta_g(\boldsymbol{k}), \tag{13}$$

$$\Delta_s(\boldsymbol{k}) + \mathrm{i}\Delta_{d_{xy}}(\boldsymbol{k}), \tag{14}$$

$$\Delta_s(\boldsymbol{k}) + \mathrm{i}\Delta_{d_{x^2-y^2}}(\boldsymbol{k}), \tag{15}$$

$$\Delta_{d_{x^2-y^2}}(\boldsymbol{k}) + \mathrm{i}\Delta_{d_{xy}}(\boldsymbol{k}). \tag{16}$$

In the following, they will be referred to as $s+\mathrm{i}g$, $s+\mathrm{i}d_{xy}$, $s+\mathrm{i}d_{x^2-y^2}$ and $d+\mathrm{i}d$ respectively. All of them have various properties in common: they break time-reversal symmetry, they are nodeless and consequently they are characterized by the Chern number. Equation (13) mixes s-wave and g-wave pairings and equation (16) is completely d-wave but not nodal. Equations (14) and (15) mix d-wave and s-wave pairings.

3. Phase diagrams

This section is devoted to study the properties of the superconducting pairings shown in the previous section using phase diagrams. Each topological phase has a Chern number associated with it. Therefore, the following phase diagrams display the trivial and non-trivial phases which can be found upon varying the parameters of the Hamiltonian. By means of equation (8) we compute the topological phase diagrams depicted in figure 1 for the four possible pairings, where the total Chern number of the occupied bands, $\nu_{\mathrm{Ch}} = \nu_{\mathrm{Ch}}^- + \nu_{\mathrm{Ch}}^+$, is shown as a function of μ and V. $\nu_{\mathrm{Ch}}^{\pm}$ is computed by substituting in equation (8) the eigenvectors of the corresponding band. The pairings $s+\mathrm{i}g$ and $s+\mathrm{i}d_{xy}$ share the same diagram. The Chern number value changes at points where the gap closes. Therefore we will solve equations (4) and (5) to determine these gap-closing points. In particular, equation (5) is only satisfied when $|\boldsymbol{g}(\boldsymbol{k})| = 0$, since $|\Delta(\boldsymbol{k})| = 0$ is not possible for our nodeless pairings (except for the $d+\mathrm{i}d$ case at $\boldsymbol{k} = (0,0)$). The condition $|\boldsymbol{g}(\boldsymbol{k})| = 0$ implies that the momentum must be equal to $\boldsymbol{k} = (0,0), (0,\pi), (\pi,0), (\pi,\pi)$, which are the time-reversal invariant momenta. These four values for the momentum are then substituted in equation (4) yielding four gap-closing equations. Since $\boldsymbol{k} = (0,\pi)$ and $\boldsymbol{k} = (\pi,0)$ yield the same equation we effectively have three independent equations.

In the following, we describe in detail the phase diagram for each nodeless pairing channel. The mixed pairing amplitudes $s+\mathrm{i}g$ and $s+\mathrm{i}d_{xy}$ are analyzed within the same subsection since they are found to be topologically equivalent.

3.1. $s+\mathrm{i}g$ and $s+\mathrm{i}d_{xy}$

We consider first the pairing $\Delta(\boldsymbol{k}) = \Delta_s^0 + \mathrm{i}\Delta_g^0(\sin 2k_x \sin k_y - \sin 2k_y \sin k_x)$. From equations (4) and (5) we find the three equations where the gap closes, which are given by

$$V^2 = (4t+\mu)^2 + \left(\Delta_s^0\right)^2, \tag{17}$$

$$V^2 = \mu^2 + \left(\Delta_s^0\right)^2, \tag{18}$$

$$V^2 = (4t-\mu)^2 + \left(\Delta_s^0\right)^2. \tag{19}$$

The upper gap between the upper and lower bands, $E_+(\boldsymbol{k}) - E_-(\boldsymbol{k})$, does not close since the condition $|\Delta(\boldsymbol{k})| = 0$ given in equation (7) cannot be satisfied. Δ_g^0 does not appear in equations (17)–(19) because $\Delta_g(\boldsymbol{k})$ vanishes at the time-reversal invariant momenta. A continuous deformation of the Hamiltonian taking $\Delta_g^0 \to 0$ does not close the gap. Thus, the $\Delta_s(\boldsymbol{k}) + \mathrm{i}\Delta_g(\boldsymbol{k})$ superconductor and a conventional s-wave superconductor are topologically equivalent.

For the $s+\mathrm{i}d_{xy}$ case, $\Delta(\boldsymbol{k}) = \Delta_s^0 + \mathrm{i}\Delta_{d_{xy}}^0 \sin k_x \sin k_y$, we obtain the same gap closing equations that we had for the $s+\mathrm{i}g$ case, since $\Delta_{d_{xy}}(\boldsymbol{k})$ vanishes at $\boldsymbol{k} = (0,0), (0,\pi), (\pi,0), (\pi,\pi)$. This means we can also take $\Delta_{d_{xy}}^0 \to 0$ without closing the gap. In the phase diagram of figure 1(a) we depict the different transition points given by equations (17)–(19). The Chern number takes values between -2 and 2, which, by means of the bulk-edge correspondence, implies that the system can host up to two edge states.

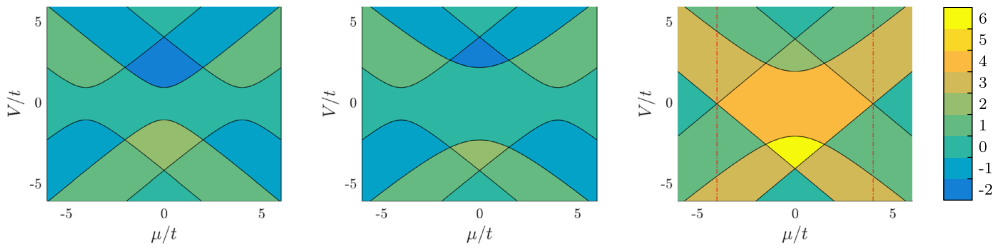

Figure 1. Total Chern number of the occupied bands, $\nu_{\mathrm{Ch}} = \nu^{-}_{\mathrm{Ch}} + \nu^{+}_{\mathrm{Ch}}$, following the definition of equation (8). (a) Phase diagram for $s + \mathrm{i}g$ pairing. Parameters $\alpha = \Delta^0_s = \Delta^0_g = t$. Same diagram for s-wave and $s + \mathrm{i}d_{xy}$ cases. (b) Phase diagram for $s + \mathrm{i}d_{x^2-y^2}$ superconductor. Parameters $\alpha = \Delta^0_s = \Delta^0_{d_{x^2-y^2}} = t$. Parabola at the middle is shifted by $4\Delta^0_{d_{x^2-y^2}}$, in contrast to $s + \mathrm{i}g$ case. (c) Phase diagram for $d + \mathrm{i}d$ superconductor. For $|\mu| < 4t$, between the red dashed lines, we have two massive edge modes. This can be observed by computing the Chern number of just one of the bands. Parameters $\alpha = \Delta^0_{d_{x^2-y^2}} = \Delta^0_{d_{xy}} = t$.

3.2. $s + \mathrm{i}d_{x^2-y^2}$

Considering the $s + \mathrm{i}d_{x^2-y^2}$ pairing, $\Delta(\boldsymbol{k}) = \Delta^0_s + \mathrm{i}\Delta^0_{d_{x^2-y^2}}(\cos k_x - \cos k_y)$, we can compute the gap closing points as we did for $s + \mathrm{i}g$. We obtain the same equations as we had in section 3.1 (equations (17) and (19)) but instead of equation (18) we now obtain

$$V^2 = \mu^2 + \left(\Delta^0_s\right)^2 + 4\left(\Delta^0_{d_{x^2-y^2}}\right)^2. \tag{20}$$

In contrast to $s + \mathrm{i}g$ or $s + \mathrm{i}d_{xy}$, where neither Δ^0_g nor $\Delta^0_{d_{xy}}$ played any role, the pairing amplitude $\Delta^0_{d_{x^2-y^2}}$ appears in equation (20). The upper gap does not close. Notably, the Chern number takes the same values as $s + \mathrm{i}g$, see phase diagram in figure 1(b). However, now we have that the middle parabola given by equation (20) is shifted because of $\Delta^0_{d_{x^2-y^2}}$, in contrast to $s + \mathrm{i}g$ and $s + \mathrm{i}d_{xy}$.

3.3. $d + \mathrm{i}d$

For $d + \mathrm{i}d$ pairing, $\Delta(\boldsymbol{k}) = \Delta^0_{d_{x^2-y^2}}(\cos k_x - \cos k_y) + \mathrm{i}\Delta^0_{d_{xy}} \sin k_x \sin k_y$, substituting in equations (4) and (5) one finds the gap-closing conditions

$$V^2 = (4t + \mu)^2, \tag{21}$$

$$V^2 = \mu^2 + 4\left(\Delta^0_{d_{x^2-y^2}}\right)^2, \tag{22}$$

$$V^2 = (4t - \mu)^2. \tag{23}$$

Remarkably in this case, the upper gap between the two particle bands closes, unlike what happens for the other pairing channels. The condition $|\Delta(\boldsymbol{k})| = 0$ of equation (7) implies $\boldsymbol{k} = (0,0), (\pi,\pi)$. Substituting these values into equation (6), $\epsilon(\boldsymbol{k}) = 0$, we get $\mu = \pm 4t$. Therefore the Chern number of the upper band takes non-zero values for $-4t < \mu < 4t$, in particular we have $\nu^{+}_{\mathrm{Ch}} = 2$ (the Chern number of the upper band for other pairings was zero). The Chern number of the occupied bands is plotted in figure 1(c), taking values between 0 and 6, in contrast to what we found in previous cases where we had values between -2 and 2.

4. Edge states and spectra

In this section, we investigate the connection between the Chern number and the physics of the edge states, when considering our previous system with open boundary conditions. Therefore, we place our model Hamiltonian on a cylindrical geometry with open boundary conditions in the x-direction and periodic boundary conditions in the y-direction. In this way, k_y remains a good quantum number and we can observe the edge states appearing at the boundaries of the cylinder. In section 4.1 we study the connection between the Chern number, the edge states and the zero-energy modes. In section 4.2 we show particularly interesting features of the $d + \mathrm{i}d$ spectrum.

4.1. Chern number and zero-energy modes

The bulk-boundary correspondence establishes a relation between the bulk Chern number and the edge states at the boundary of the system. This is given explicitly by the equation [44, 45]

$$\nu_{\mathrm{Ch}} = N_+ - N_-, \tag{24}$$

where N_+ (N_-) is the number of forward (backward) propagating edge states. The above formula relates the Chern number with the spectral flow, i.e. the difference between the number of edge states connecting the negative energy band with the positive energy band (forward propagating N_+) and the number of edge states going the other way around (backward propagating N_-). In general, we will expect for our model that the number of edge states at one boundary equals the Chern number.

One may be tempted to equate the number of edge states to the number of zero-energy modes, since the edge states cross the zero-energy level on their way across the gap. Although this is usually true, we have found some exceptions in the $s + \mathrm{i}g$ and $d + \mathrm{i}d$ cases where one of the edge states crosses the zero-energy level more than once, producing three zero-energy modes. These three zero-energy modes cannot be expected to be topologically robust, since a smooth deformation of the Hamiltonian, such as the introduction of weak disorder, can reduce the number of crossings to one. Thus, only one of the zero-modes can be qualified as topologically

robust. A particular example of this can be seen in figure 2 for the case of $s + ig$, where only the crossing at $k_y = 0$ is topologically robust. By tuning Δ_g^0 the number of zero modes is reduced to one.

As a consequence of the bulk-boundary correspondence, the edge states are topologically protected and are robust under weak static disorder. If disorder is weak and respects particle-hole symmetry, the gap does not close and the topological states propagating at the edge of the system remain, since equation (24) still holds. This has been tested by introducing weak disorder perturbations to the parameters of the Hamiltonian and diagonalising numerically to obtain the edge states.

4.2. Edge states in $d + id$

In this section, we study the $d + id$ pairing channel in detail. One noteworthy characteristic of the $d + id$ spectrum is the presence of zero-energy modes away of the time-reversal invariant momenta $k_y = 0, \pi$, where they appear for the other pairings considered. This new phenomena occur for regions of the topological phase diagram with $\nu_{\text{Ch}} = 3, 4, 6$. We will now explain why this happens for $\nu_{\text{Ch}} = 4$ and small Zeeman field (central part of figure 1(c)), by applying some ideas of bulk-boundary correspondence [51, 52]. In this region we have four edge states with four zero-energy modes at $k_y \neq 0, \pi$, even in the absence of Zeeman field or SOC.

We start by considering the $d + id$ pairing without SOC nor Zeeman field. Hamiltonian (1) can be separated in two independent subsystems, $\mathcal{H} = \mathcal{H}_\uparrow + \mathcal{H}_\downarrow$. Thus we have

$$\mathcal{H}_\uparrow = \frac{1}{2}\sum_{\boldsymbol{k}} \left(c^\dagger_{\boldsymbol{k},\uparrow}, c_{-\boldsymbol{k},\downarrow}\right) H_\uparrow(\boldsymbol{k}) \begin{pmatrix} c_{\boldsymbol{k},\uparrow} \\ c^\dagger_{-\boldsymbol{k},\downarrow} \end{pmatrix}, \tag{25}$$

with

$$H_\uparrow(\boldsymbol{k}) = \begin{pmatrix} \epsilon(\boldsymbol{k}) & \Delta(\boldsymbol{k}) \\ \Delta^*(\boldsymbol{k}) & -\epsilon(\boldsymbol{k}) \end{pmatrix}. \tag{26}$$

$\mathcal{H}_\downarrow$ can be obtained by turning the spins upside down and yields the same spectrum as $\mathcal{H}_\uparrow$, i.e. the bands of $\mathcal{H}$ are now degenerate. We will now drop the $\uparrow$ and $\downarrow$ symbols for simplicity. Equation (26) can be recast into the form $H = \boldsymbol{h}\cdot\boldsymbol{\sigma}$, where $\boldsymbol{h} = \left(\Delta_{d_{x^2-y^2}}(\boldsymbol{k}), -\Delta_{d_{xy}}(\boldsymbol{k}), \epsilon(\boldsymbol{k})\right)$ and $\boldsymbol{\sigma}$ are the Pauli matrices. Since we are interested in the spectrum on a cylindrical geometry with periodic boundary conditions in y-direction and open boundary conditions in x-direction, we will express H as a family of one-dimensional Hamiltonians labeled by k_y, i.e. $H_{k_y}(k_x)$. Thereby, $\boldsymbol{h}_{k_y}(k_x)$ defines a map from the 1D Brillouin zone to a loop in $\mathbb{R}^3$. Note that the origin of $\mathbb{R}^3$ corresponds to the closing of the gap. It is straightforward to see that the loop defined by $\boldsymbol{h}_{k_y}(k_x)$ is an ellipse contained in a plane by reexpressing $\boldsymbol{h}_{k_y}(k_x)$ as

$$\boldsymbol{h}_{k_y}(k_x) = \boldsymbol{b}_0 + \boldsymbol{b}_1\cos k_x + \boldsymbol{b}_2 \sin k_x, \tag{27}$$

where $\boldsymbol{b}_1\cos k_x$ and $\boldsymbol{b}_2\sin k_x$ span the ellipse on a plane with normal vector $\boldsymbol{n}_\perp = \boldsymbol{b}_1\times\boldsymbol{b}_2/|\boldsymbol{b}_1\times\boldsymbol{b}_2|$ and $\boldsymbol{b}_0$ shifts the center of the ellipse from the origin. These vectors are given by

$$\boldsymbol{b}_0 = \left(-\Delta^0_{d_{x^2-y^2}}\cos k_y, 0, -2t\cos k_y - \mu\right), \tag{28}$$

$$\boldsymbol{b}_1\cos k_x = \left(\Delta^0_{d_{x^2-y^2}}, 0, -2t\right)\cos k_x, \tag{29}$$

$$\boldsymbol{b}_2\sin k_x = \left(0, -\Delta^0_{d_{xy}}\sin k_y, 0\right)\sin k_x. \tag{30}$$

The vector $\boldsymbol{b}_0$ can be divided into two contributions. The first one shifts the ellipse from the origin in direction parallel to the plane containing the loop, $\boldsymbol{b}_0^{\parallel}$. The other contribution shifts it perpendicularly, $\boldsymbol{b}_0^{\perp}$.

It can be proven that if the loop defined by $\boldsymbol{h}_{k_y}(k_x)$ contains the origin, the Hamiltonian (25) has a zero-energy mode when placed on a chain with open boundary conditions. To show this, we first move the loop to the xy-plane in $\mathbb{R}^3$ by making a simple rotation. This is equivalent to performing a SU(2) transformation to our Nambu basis, $\boldsymbol{d}_{k_x} = U\left(c_{k_x,\uparrow}, c^\dagger_{-k_x,\downarrow}\right)^T$. Next, we can smoothly deform the loop into a circle without crossing the origin (since this would close the gap). After this smooth deformation, we obtain $\boldsymbol{h}_{k_y}(k_x) = (\cos k_x, \sin k_x, 0)$. Fourier transforming this Hamiltonian back to real space we find that for an open chain

$$\mathcal{H}' = \sum_{n=1}^{N_x-1} d^\dagger_{n,\uparrow} d^\dagger_{n+1,\downarrow} + \text{H.c.}, \tag{31}$$

where we can immediately see that $d^\dagger_{1,\downarrow}$, $d_{1,\downarrow}$, $d^\dagger_{N_x,\uparrow}$, and $d_{N_x,\uparrow}$ do not appear, so that we have zero-energy modes localized at the edges.

One can also prove [51] that even if the loop does not contain the origin, we have edge states with non-zero energy if the projection of the loop in the perpendicular direction, $\boldsymbol{n}_\perp$,

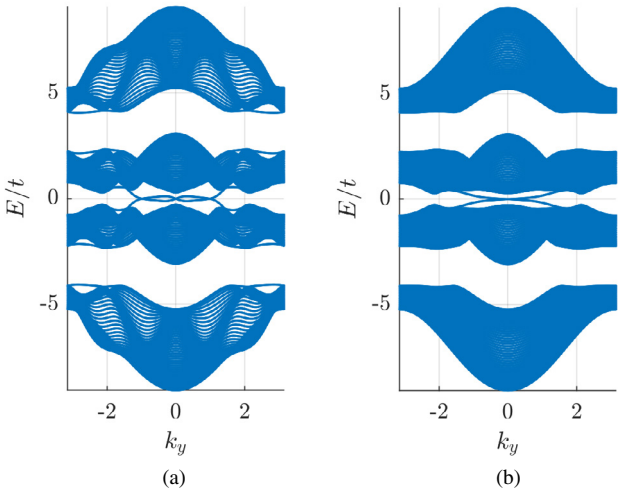

Figure 2. $s + ig$ spectrum on a cylindrical geometry. Chern number is 1. The edge states in (a) cross zero energy three times. By taking Δ_g^0 from $2t$ to $0.5t$, which is a smooth deformation, we see how the zero-energy modes at $k_y \neq 0$ disappear in (b). Parameters: $\mu = 2t$, $V = 3t$, $\alpha = \Delta_s^0 = t$, lattice sites $N_x = 50$.

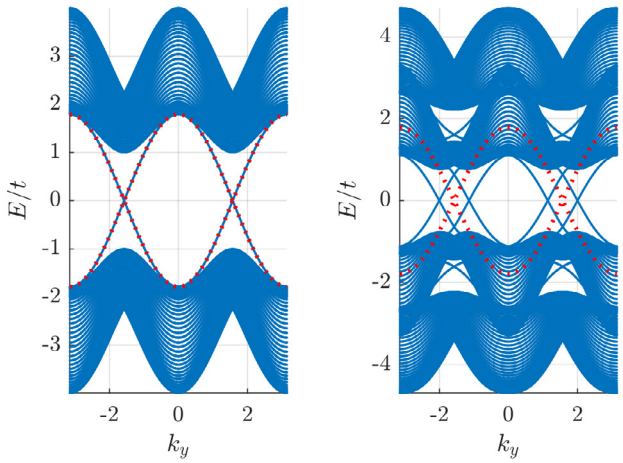

Figure 3. $d + \mathrm{i}d$ spectra on a cylindrical geometry. Chern number is 4, which corresponds to the four edge states that cross zero energy at each boundary of the cylinder. (a) No SOC nor Zeeman field, bands are degenerate. The dotted line are the edge states given by equation (32). (b) SOC and Zeeman field are non-zero ($\alpha = t$, $V = 0.7t$). The bands and the edge modes move with respect to the original ones, still depicted in red. Note the two massive edge modes between the upper and the lower band. Parameters: $\mu = 0$, $\Delta^0_{d_{x^2-y^2}} = \Delta^0_{d_{xy}} = t$, $N_x = 50$.

does contain it. The energy of these edge states is given by the perpendicular distance to the origin $E = \pm|\boldsymbol{b}_0 \cdot \boldsymbol{n}^{\perp}|$. For the $d + \mathrm{i}d$ case we have

$$E(k_y) = \pm \frac{4t\cos k_y + \mu}{\sqrt{4t^2 + \left(\Delta^0_{d_{x^2-y^2}}\right)^2}} \Delta^0_{d_{x^2-y^2}}. \tag{32}$$

This implies the existence of zero-energy modes at $\cos k_y = \pm\frac{\mu}{4t}$, which shows that we have solutions at $k_y \neq 0, \pi$.

The results we have obtained are valid for $d + \mathrm{i}d$ paring without SOC nor Zeeman field. The spectrum for this particular setting can be seen in figure 3(a). When a small Zeeman field is turned on, $\mathcal{H}_\uparrow$ and $\mathcal{H}_\downarrow$ no longer have the same spectrum and the degeneracy breaks down. One band moves up in energy and the other one moves down doubling the number of Dirac cones. This can be accounted for in equation (32) by adding a term $\pm V$. The effect of SOC is rather complicated but it can be roughly described as a horizontal displacement of the bands with respect to one another, that also doubles the number of Dirac cones. Combining the Zeeman field and the SOC, the zero-energy states are placed further apart from each other in momentum space. The final result is four zero-energy modes away from $k_y = 0, \pi$, see figure 3(b). Remarkably, even with no Zeeman field or SOC the Chern number is non-zero and there are are topologically protected edge states. Note that in this case, weak disorder can slightly displace the momentum k_y at which the edge states cross the zero-energy level. However, these edge states cannot be smoothly connected to the bulk, since they are topologically robust. Hence, these edge states always cross the zero-energy level and connect two bulk bands, despite the crossing point might be slightly shifted due to disorder, as described in section 4.1.

Another interesting feature of the $d + \mathrm{i}d$ spectrum appears when we have a non-zero Chern number for the upper band. In the region $|\mu| < 4t$ we have $\nu^+_{\mathrm{Ch}} = 2$, and we can observe two massive edge modes in addition to the zero-energy modes that may appear, as can be seen in figure 3(b). This effect is something unique of the $d + \mathrm{i}d$ pairing symmetry.

5. Conclusions

We have studied four 2D tetragonal superconductors with SOC and Zeeman field. The four possible mixed nodeless pairings compatible with the point-group symmetry of tetragonal superconductors have been considered. For these systems we are able to obtain the phase diagrams by numerically computing the Chern number and calculating the gap closing conditions. The phase diagrams for $s + \mathrm{i}g$ and $s + \mathrm{i}d_{xy}$ are found to be equivalent to the s-wave case, since we can continuously deform the Hamiltonian without closing the gap. The $d + \mathrm{i}d$ pairing channel shows rich behavior, with the Chern number taking values up to 6.

Computing the energy spectra for the different pairing amplitudes, we have found that for certain cases the number of zero-energy modes is higher than the Chern number. These extra zero-energy modes are shown to be topologically unprotected and disappear in the presence of disorder. For the $d + \mathrm{i}d$ case we have explained why zero-modes appearing at $k \neq 0, \pi$ are possible, in contrast to what occurs for other cases, where we have $k = 0, \pi$. Finally, we have also seen how massive edge modes appear associated to the non-trivial topology of the upper band. This is proven by calculating the Chern number of the upper band.

Potential applications of anysotropic $d + \mathrm{i}d$ superconducting pairings have been proposed in materials such as water-intercalated sodium cobaltates, bilayer silicene, epitaxial bilayer films of bismuth and nickel or FeAs-based superconductors [32, 34–38].

Our results could also be applied to a broaden context: the new physics emerging in multicomponent superconducting systems, with a multicomponent superconducting order parameter as a consequence of particular pairing symmetry [53].

Interestingly, the ultra-highly doped monolayer graphene [39] was proposed to support $d + \mathrm{i}d$ superconductivity originated from repulsive electron–electron interactions. This begs the question of whether a similar analysis to the one performed in this paper, but for the corresponding dihedral symmetry group, could shed some light over the recently discovered superconducting twisted bilayer graphene [54, 55].

Acknowledgments

We acknowledge financial support from the Spanish MINECO grants FIS2012-33152, FIS2015-67411, and the CAM research consortium QUITEMAD + , Grant No. S2013/ICE-2801. The research of MAM-D has been supported in part by the US. Army Research Office through Grant No. W911N F-14-1-0103. OV thanks Hiroki Isobe for interesting

discussions, Fundación Ramón Areces and RCC Harvard. SV thanks FPU MECD Grant.

References

[1] Thouless D J, Kohmoto M, Nightingale M P and den Nijs M 1982 *Phys. Rev. Lett.* **49** 405
[2] Haldane F 1983 *Phys. Lett.* A **93** 464
[3] Wen X G 1992 *Int. J. Mod. Phys.* B **06** 1711
[4] Gonzalez J, Martin-Delgado M, Sierra G and Vozmediano A H 1995 *Quantum Electron Liquids and High-T_c Superconductivity* (Berlin: Springer) (https://doi.org/10.1007/978-3-540-47678-8)
[5] Nayak C, Simon S H, Stern A, Freedman M and Das Sarma S 2008 *Rev. Mod. Phys.* **80** 1083
[6] Alicea J 2012 *Rep. Prog. Phys.* **75** 076501
[7] Litinski D, Kesselring M S, Eisert J and von Oppen F 2017 *Phys. Rev.* X **7** 031048
[8] Volovik G 1988 *Sov. Phys.—JETP* **67** 1804
[9] Maeno Y, Hashimoto H, Yoshida K, Nishizaki S, Fujita T, Bednorz J G and Lichtenberg F 1994 *Nature* **372** 532
[10] Fu L and Kane C L 2008 *Phys. Rev. Lett.* **100** 096407
[11] Xu J P *et al* 2015 *Phys. Rev. Lett.* **114** 017001
[12] Mourik V, Zuo K, Frolov S M, Plissard S R, Bakkers E P A M and Kouwenhoven L P 2012 *Science* **336** 1003
[13] Deng M T, Yu C L, Huang G Y, Larsson M, Caroff P and Xu H Q 2012 *Nano Lett.* **12** 6414
[14] Albrecht S M, Higginbotham A P, Madsen M, Kuemmeth F, Jespersen T S, Nygård J, Krogstrup P and Marcus C M 2016 *Nature* **531** 206
[15] Nadj-Perge S, Drozdov I K, Li J, Chen H, Jeon S, Seo J, MacDonald A H, Bernevig B A and Yazdani A 2014 *Science* **346** 602
[16] Wang D *et al* 2017 *Science* (https://doi.org/10.1126/science.aao1797)
[17] He Q L *et al* 2017 *Science* **357** 294
[18] Alicea J 2010 *Phys. Rev.* B **81** 125318
[19] Lutchyn R M, Sau J D and Das Sarma S 2010 *Phys. Rev. Lett.* **105** 077001
[20] Zareapour P *et al* 2012 *Nat. Commun.* **3** 1056
[21] Trani F, Campagnano G, Tagliacozzo A and Lucignano P 2016 *Phys. Rev.* B **94** 134518
[22] Li Z X, Chan C and Yao H 2015 *Phys. Rev.* B **91** 235143
[23] Yan Z, Song F and Wang Z 2018 *Phys. Rev. Lett.* **121** 096803
[24] Bednorz J G and Müller K A 1986 *Z. Phys.* B **64** 189
[25] Anderson P W 1987 *Science* **235** 1196
[26] Tsuei C C and Kirtley J R 2000 *Rev. Mod. Phys.* **72** 969
[27] Wenger F and Östlund S 1993 *Phys. Rev.* B **47** 5977
[28] Senthil T, Marston J B and Fisher M P A 1999 *Phys. Rev.* B **60** 4245
[29] Morita Y and Hatsugai Y 2000 *Phys. Rev.* B **62** 99
[30] Read N and Green D 2000 *Phys. Rev.* B **61** 10267
[31] Sato M, Takahashi Y and Fujimoto S 2010 *Phys. Rev.* B **82** 134521
[32] Chern T 2016 *AIP Adv.* **6** 085211
[33] Awoga O A, Bouhon A and Black-Schaffer A M 2017 *Phys. Rev.* B **96** 014521
[34] Kiesel M L, Platt C, Hanke W and Thomale R 2013 *Phys. Rev. Lett.* **111** 097001
[35] Liu F, Liu C C, Wu K, Yang F and Yao Y 2013 *Phys. Rev. Lett.* **111** 066804
[36] Lin S Z, Maiti S and Chubukov A 2016 *Phys. Rev.* B **94** 064519
[37] Zhou S and Wang Z 2008 *Phys. Rev. Lett.* **100** 217002
[38] Gong X, Kargarian M, Stern A, Yue D, Zhou H, Jin X, Galitski V M, Yakovenko V M and Xia J 2017 *Sci. Adv.* **3** e1602579
[39] Nandkishore R, Levitov L S and Chubukov A V 2014 *Nat. Phys.* **8** 1804
[40] Zhang L F, Covaci L and Milošević M V 2017 *Phys. Rev.* B **96** 224512
[41] Becerra V F and Milošević M V 2016 *Phys. Rev.* B **94** 184517
[42] Sato M and Fujimoto S 2010 *Phys. Rev. Lett.* **105** 217001
[43] Ortiz L, Varona S, Viyuela O and Martin-Delgado M A 2018 *Phys. Rev.* B **97** 064501
[44] Fukui T, Shiozaki K, Fujiwara T and Fujimoto S 2012 *J. Phys. Soc. Japan* **81** 114602
[45] Chiu C K, Teo J C Y, Schnyder A P and Ryu S 2016 *Rev. Mod. Phys.* **88** 035005
[46] Sedlmayr N, Kaladzhyan V, Dutreix C and Bena C 2017 *Phys. Rev.* B **96** 184516
[47] Sato M and Ando Y 2017 *Rep. Prog. Phys.* **80** 076501
[48] Teo J C Y and Kane C L 2010 *Phys. Rev.* B **82** 115120
[49] Fukui T, Hatsugai Y and Suzuki H 2005 *J. Phys. Soc. Japan* **74** 1674
[50] Resta R 2000 *J. Phys.: Condens. Matter* **12** R107
[51] Mong R S K and Shivamoggi V 2011 *Phys. Rev.* B **83** 125109
[52] Ryu S and Hatsugai Y 2002 *Phys. Rev. Lett.* **89** 077002
[53] Miloevi M V and Perali A 2015 *Supercond. Sci. Technol.* **28** 060201
[54] Cao Y, Fatemi V, Fang S, Watanabe K, Taniguchi T, Kaxiras E and Jarillo-Herrero P 2018 *Nature* **556** 43
[55] Isobe N, Yuan H and Fu L 2018 arXiv:1805.06449

CHAPTER 2

Topological quantum error correction

The most important handicap in the way to the realization of practical quantum computers is the high level of noise suffered by the physical qubits. As a consequence, quantum error correction is essential to achieve fault-tolerant quantum computation. In the search for scalable and efficient quantum error correcting codes, topological properties of quantum systems have proven to be very useful tools. These tools have resulted in topological codes such as the toric code [Kit97, Kit03], the color code [BM06] and higher-dimensional versions [HZW05, BM07]. Topological codes encode quantum information in global degrees of freedom of the system, while the measurements required to extract the error syndromes are local. Additionally, they tolerate much higher error rates than other error correcting codes [Svo+06, Ter15].

The Kitaev toric code has become a seminal work not only in the field of topological quantum computation, where it was originally conceived, but also in strongly correlated systems, in which it has played a fundamental role as the paradigmatic quantum phase exhibiting topological order. This relation becomes explicit by defining the Hamiltonian $H = -\sum_v Q_v - \sum_p B_p$, where Q_v and B_p are the vertex and plaquette stabilizer operators[1] of the Kitaev code. The ground state space of this Hamiltonian is the same as the code space of the Kitaev code, and defines a topologically ordered system. Likewise, it is possible to relate in general topological stabilizer codes with topological orders. Given a topological stabilizer code, one can define a topological order with Hamiltonian $H = -\Delta \sum_i S_i$, where S_i are the stabilizers of the code [BDP12, Ter15, Fuj15]. The code space of topological stabilizer codes coincides with the ground state space of the corresponding topological order.

Although topological codes have plenty of advantages (high error thresholds, local stabilizer measurements, simple structure), they also have some caveats, for instance, the lack of a universal gate set [EK09, BK13]. This has been solved in the toric code by introducing techniques such as magic state distillation [BK05, Lit19] or just-in-time gauge fixing [Bom18, Bro20], allowing us to do universal

[1] The stabilizer operators are a set of commuting operators which square to one. Thus, their eigenvalues are ± 1 [Got97, Bac13]. These operators are periodically measured to detect errors. If the code is topological, as is the case of the toric code, the stabilizer operators must satisfy some locality conditions: the number of qubits in the support of each stabilizer is bounded and the number of stabilizers with support containing any given qubit is bounded [Bom13].

quantum computation. However, these methods come at the cost of some additional overhead in terms of space-time costs and qubit footprint. Therefore, finding new topological codes more suitable for practical implementation and with reduced overhead seems necessary. In order to discover these new topological codes, one can exploit the connection between topological codes and topological orders. While this connection has been mainly explored in one direction, i.e., from the quantum information perspective of error correcting codes to the condensed matter perspective of quantum phases, it is interesting to make this connection in the opposite direction. We may begin from a topological order and develop a topological error correcting code. This is what is done in [P3], where the double semion model is transformed into a topological code.

The double semion model is a relative of the Kitaev model that appeared as another new and inequivalent topological phase of matter corresponding to a lattice gauge theory with the same gauge group $\mathbb{Z}_2$ [Fre+04, LW05]. However, the application of the double semion model and other topological phases to topological quantum computation has remained an open problem. In publication [P3], we remedy this situation by introducing a new formulation of the double semion model suitable for a complete treatment as a quantum memory with topological properties. The resulting code is a topological stabilizer code, but it is non-Pauli and non-CSS,[2] since plaquette operators are no longer made of simple Pauli operators. The results and new tools developed in [P3] open the door to a new way of constructing quantum codes. We believe that the tools introduced here for models like the double semion based on Abelian lattice gauge theories can be generalized to other Levin-Wen models [LW05]. In fact, very recently similar ideas where applied to twisted quantum doubles [FTE20].

Following our conversion of the double semion model into a topological code (the semion code) in [P3], we determine the error threshold of this new code in [P4]. The threshold value separates two different regimes. When the noise error rate is below threshold, increasing the distance of the code increases the lifetime of the encoded logical information and reduces the logical error rate. In other words, increasing the number of physical qubits that encode each logical qubit (and therefore increasing the redundancy of data), makes the code more resistant against noise. For error rates above threshold, this is no longer true. Thus, it only makes sense to use error correction when our error rate is below threshold. This value is one of the most significant quantities characterizing the performance of an error correcting code.

In case of topological codes, the threshold is usually determined by mapping the system into a statistical mechanical model. For example, the Kitaev toric code is mapped into a two-dimensional random bond Ising model [Den+02] and

[2]CSS stands for Calderbank, Shor and Steane. It denotes a class of quantum error correcting codes that treat independently bit-flip (X) and phase-flip (Z) errors [CS96, Ste96]. The stabilizer operators of these codes can be written as a product of all X- or all Z-Pauli operators.

the color code into a two-dimensional random three-body Ising model [KBM09]. These methods yield an optimal threshold, i.e., they assume one always applies an optimal recovery operation for a given error syndrome.[3] Nevertheless, given the complex structure of plaquette operators in the semion code, doing these kind of statistical mechanical mappings becomes a very difficult task. Hence, instead of using this approach, we obtain the error threshold by taking advantage of the near-optimal performance of some decoders based on neural networks [Dav+18, MKJ19]. This kind of decoders where recently proposed to solve the decoding problem of error correcting codes [TM17, KJ17, VCB17, Bai+18], since neural networks can be run efficiently and, in principle, replicate an optimal decoding strategy. However, this solution has some scalability issues, given that larger codes require longer training times and more resources. Some steps have already been taken to address these problems [Ni18, BN18, VBA19].

This chapter is organized as follows. Section 1 is devoted to the Kitaev toric code, the simplest topological quantum error correcting code. Section 2 presents some general aspects of the semion code of publication [P3]. In section 3, we introduce the decoding problem and discuss decoders based on machine learning techniques. Sections 4 and 5 contain a summary and the main results of publications [P3] and [P4].

1. The toric code

Kitaev's toric code [Kit97, Kit03] can be defined on a square lattice with opposite edges identified, i.e., forming a torus.[4] Qubits are placed at the edges of the lattice. The stabilizer operators, namely, the set of commuting operators that are periodically measured looking for errors, are given by plaquette and vertex operators. Vertex operators are defined as $Q_v = \prod_{i\in v} Z_i$, the multiplication of Z-Pauli operators acting at each of the edges connected to vertex v. Similarly for plaquette operators, we have $B_p = \prod_{i\in\partial p} X_i$, the multiplication of X-Pauli operators acting on the edges at the border of plaquette p (see figure 1a). All the states belonging to the code space satisfy

$$Q_v|\psi\rangle = |\psi\rangle, \quad B_p|\psi\rangle = |\psi\rangle, \tag{30}$$

they are the simultaneous $+1$ eigenstate of all the stabilizer operators.

In an $L \times L$ periodic lattice, we have $2L^2$ qubits, L^2 vertex operators and L^2 plaquette operators. Equation (30) sets $2L^2$ constraints on the code space. However, since the lattice is placed on a torus, we have that $\prod_v Q_v = 1$ and

[3] Choosing a recovery operation given an error syndrome is called decoding. An optimal decoder (yielding an optimal recovery operation) chooses the operation which most likely takes the code successfully to its initial state. This is in general a computationally hard problem [Pou06].

[4] It is also possible to place the lattice on a planar surface with boundaries, what is sometimes referred to as surface code instead of toric code [BK98].

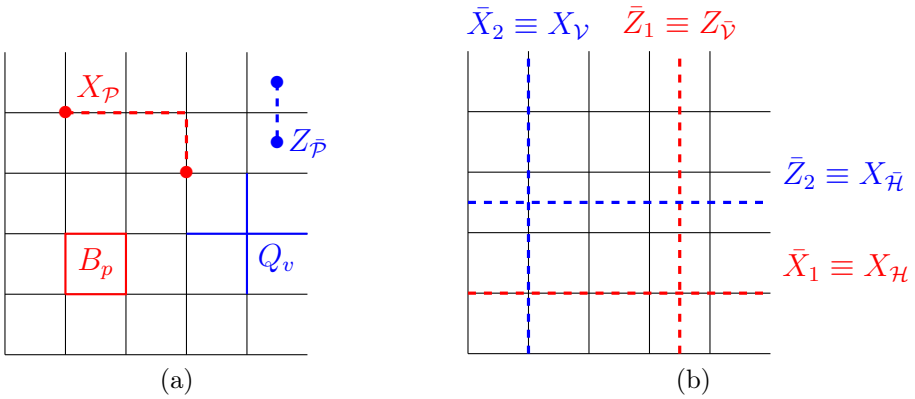

Figure 1. Square lattices with periodic boundary conditions and $L = 5$. (a) The support of a plaquette operator (B_p), a vertex operator (Q_v) and two string operators ($X_{\mathcal{P}}$ and $Z_{\bar{\mathcal{P}}}$) is shown. The bullet points at the endpoints of the string signal the stabilizers that anticommute with the strings. Note that strings of Z live on the dual lattice and paths on the dual lattice are denoted with a bar. (b) Two pairs of logical operators on the torus. The distance of the code is 5.

$\prod_p B_p = 1$, the product of all vertex and plaquette operators equals 1. Thus, the total number of constraints is $2(L^2-1)$ and the number of logical qubits is given by the difference between the number of physical qubits and the number of constraints: $2L^2 - 2(L^2-1) = 2$. Therefore, the dimension of the code space is $2^2 = 4$. This number does not depend on the size of the lattice, but on the genus, g, of the surface where the lattice is embedded (i.e., the number of *holes* of the surface). The genus can be related to the Euler characteristic, a topological invariant given by $\chi = -E + V + P = 2 - 2g$. Here, E, V and P are, respectively, the number of edges, vertices and plaquettes of the lattice. The code space dimension is 4^g, with $g = 1$ for the torus. This denotes the topological nature of the code.

Alternatively, we can look at the toric code from the perspective of topological orders with the Hamiltonian

$$H = -\sum_v Q_v - \sum_p B_p. \tag{31}$$

The ground state of this Hamiltonian is four-fold degenerate and coincides with the code space, since the conditions in equation (30) minimize the energy. In a lattice with N qubits, if the system is initialized in state $|0\rangle^{\otimes N}$, which is a $+1$ eigenstate of all vertex operators, the ground state can be obtained by projecting

to the +1 subspace of plaquette operators,

$$|\Omega_0\rangle = \prod_p \frac{1+B_p}{2} \, |0\rangle^{\otimes N}. \tag{32}$$

In this basis ($|0\rangle$ for the +1 eigenstate of Z and $|1\rangle$ for the -1 eigenstate), we can picture each edge of the lattice as being empty if in state $|0\rangle$ and occupied if in state $|1\rangle$, analogously to the approach taken in string-net models [LW05, KBS13]. Each B_p acting on $|0\rangle^{\otimes N}$ flips the edges at the boundary of plaquette p, creating a loop. Expanding (32),

$$|\Omega_0\rangle = \frac{1}{2^P}(1 + B_1 + B_2 + B_3 + \cdots + B_1B_2 + B_1B_3 + B_2B_3 + \dots)|0\rangle^{\otimes N}, \tag{33}$$

we can see that the multiplication of plaquette projectors acting on the empty state, yields a linear combination of (nearly) all possible loops in the lattice. However, there are some loops that cannot be generated by a multiplication of plaquettes. These are the non-trivial curves of the torus, which go around the whole system and cannot be smoothly contracted to a point.[5] If instead of the empty state $|0\rangle^{\otimes N}$, we use another state in which a non-trivial loop in the torus is occupied, equation (32) yields a different ground state. Since there are two non-trivial loops in the torus, the ground state is four-fold degenerate, as we derived earlier counting the number of constraints and degrees of freedom.

When an X error occurs on a given qubit, the two vertex operators with support on that qubit flip, i.e., their eigenvalue changes to -1, since the X-Pauli operator anticommutes with Z. From the perspective of Hamiltonian (31), an X error acting on the ground state, can be seen as an operator creating a pair of quasiparticle excitations. These excitations correspond to the two vertices that have been flipped. We can move around the excitations by concatenating several X operators, forming strings. A string along a path $\mathcal{P}$, a sequence of concatenated edges, can be defined as $X_\mathcal{P} = \prod_{i\in\mathcal{P}} X_i$. Since along the bulk of the string operator, every vertex shares two qubits with the string, the string commutes in the bulk, but anticommutes at its endpoints, as depicted in figure 1a.

In order to correct the errors, we need to annihilate the quasiparticle excitations. We can do this by applying a string operator, $X_\mathcal{R}$, where $\mathcal{R}$ is a path with the same endpoints as $\mathcal{P}$. Thus, the string $X_\mathcal{R}$ brings the excitations back together. $\mathcal{R}+\mathcal{P}$, defined as the symmetric difference of $\mathcal{R}$ and $\mathcal{P}$,[6] forms a loop. If this loop is trivial, i.e., if it can be expressed as a multiplication of plaquette operators, the recovery operation is successful and the code returns to its original state. We have $X_\mathcal{R}X_\mathcal{P}|\Omega\rangle = \prod_{p\in C} B_p|\Omega\rangle = |\Omega\rangle$, where $|\Omega\rangle$ belongs to the code

[5] In other words, they cannot be expressed as a boundary of a region, while trivial loops can be expressed as the boundary of the region they enclose.

[6] The set $\mathcal{R}+\mathcal{P}$ contains edges that are either in $\mathcal{R}$ or $\mathcal{P}$, but not both. Namely, the union of two sets minus their intersection: $\mathcal{R}+\mathcal{P} \equiv (\mathcal{R}\cup\mathcal{P}) \setminus (\mathcal{R}\cap\mathcal{P})$

space and C is a set of plaquette operators whose multiplication equals $X_{\mathcal{R}}X_{\mathcal{P}}$. The last equality follows from the fact that the ground state satisfies (30).

When $\mathcal{R}+\mathcal{P}$ is a non-trivial loop, the recovery operation fails and the code does not return to its original state. A non-trivial string operator commutes with the stabilizer operators and acts non-trivially on the code space. As we saw before, we can obtain the ground state using equation (32). Applying a non-trivial string $X_{\mathcal{L}}$ on $|0\rangle^{\otimes N}$, we still have a $+1$ eigenvalue of vertex operators. Projecting this onto the $+1$ subspace of plaquettes, we obtain a different ground state. Hence, non-trivial strings are the logical operators of the code. Logical operators are not unique, since deforming string operators using stabilizer operators yields another string with the same effect on the code space. Thus, homologically equivalent strings have the same effect on the code space. This same discussion applies to Z strings in the dual lattice. Since the code has two logical qubits, we can define two pairs of logical operators satisfying the Pauli algebra, as is shown in figure 1b.

Therefore, the information is stored in global degrees of freedom (the homology classes), and in order to measure or modify the information encoded, we need to use these global properties of the code. In an $L\times L$ lattice the shortest non-trivial loop going around the system has distance $d=L$, this is the distance of the code.

Although we have defined the toric code on a square lattice, it is also possible to define it analogously for other lattice geometries, such as the hexagonal lattice with three-valent vertices and hexagonal plaquettes [FT12].

2. The semion code

The semion code is an error correcting code based on the double semion model. This model was developed in the search for new topological orders [Fre+04, LW05] and shares the same gauge group as the Kitaev model. It is defined on a hexagonal lattice, with periodic boundary conditions (forming a torus) and qubits placed at the edges. Vertex operators, Q_v, are the same as in the toric code, applying Z-Pauli operators on the edges associated with a given vertex. Plaquette operators apply X-Pauli operators at the edges of a given plaquette, and additionally, some phases acting on the *legs* coming out of the hexagon:

$$\tilde{B}_p = \prod_{i\in\partial p} X_i \prod_{j\in o(p)} \mathrm{i}^{(1-Z_j)/2}, \tag{34}$$

where $o(p)$ is the set of outgoing edges of plaquette p. The support of these operators is shown in figure 2. The Hamiltonian takes the form

$$H = -\sum_v Q_v + \sum_p \tilde{B}_p. \tag{35}$$

Note the positive sign of the plaquette term, in contrast to the Kitaev Hamiltonian (31). The ground state is the $+1$ eigenstate of vertex operators and -1 eigenstate of plaquette operators. It can be obtained by projecting the empty state on the -1

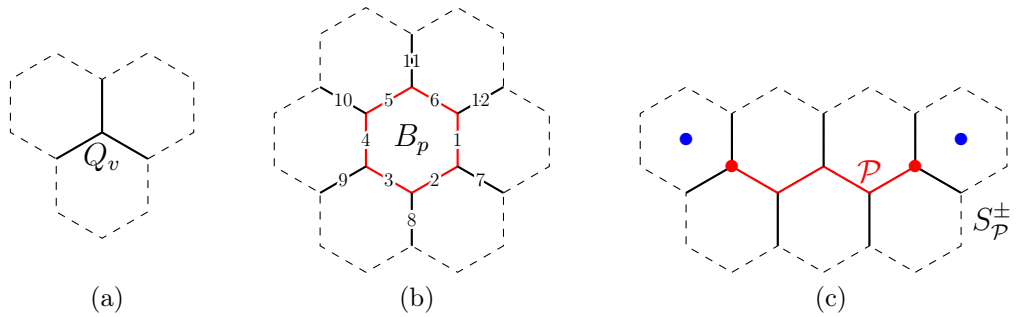

(a) (b) (c)

Figure 2. The support of (a) the vertex operator Q_v and (b) plaquette operator B_p. The qubits are placed on the edges. (c) Positive- or negative-chirality string operator $S^{\pm}_{\mathcal{P}}$. The path $\mathcal{P}$ is indicated by the full red edges where the X operators are applied. The support of $S^{\pm}_{\mathcal{P}}$, Conn($\mathcal{P}$), is indicated with continuous lines. $S^{\pm}_{\mathcal{P}}$ creates a pair of vertex excitations at the at the endpoints of the path $\mathcal{P}$ (red dots). Additionally, the negative-chirality string creates plaquette excitations at the endpoints (blue dots).

subspace of plaquettes, $|\Omega_0\rangle = \prod_p (1-\tilde{B}_p)/2\ |0\rangle^{\otimes N}$. For the Kitaev model, we saw that a similar expression (32) produced a linear superposition of all possible loop configurations in the lattice. For the double semion model, we also have a linear superposition, but as a consequence of the phases in the plaquette, the phase of each state is +1 if the number of loops is even and -1 if odd.

Despite the similarities between the double semion model and the Kitaev code, defining a stabilizer code using the double semion model is not straightforward. Plaquette operators do not square to one and neighboring plaquettes do not commute. They only fulfill these requirements in a certain subspace, where $Q_v|\psi\rangle = |\psi\rangle$. We need to modify the plaquette operators with some additional phases so that they commute and square to one in the whole Hilbert space. Finally, we have

$$B_p = \prod_{j\in\partial p} X_j \sum_{\vec{i}} b_p(\vec{i})|\vec{i}\rangle\langle\vec{i}|, \tag{36}$$

where $\vec{i}$ is a bit string representing the state of the qubits in the computational basis. b_p takes values in $\{\pm 1, \pm \mathrm{i}\}$ and is given explicitly by

$$\sum_{\vec{i}} b_p(\vec{i})|\vec{i}\rangle\langle\vec{i}| = \prod_{j\in\partial p} (-1)^{n^-_{j-1} n^+_j} \prod_{v\in p} \beta_v, \tag{37}$$

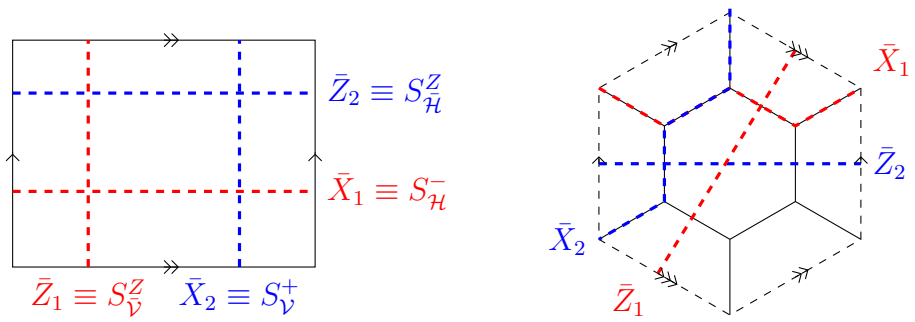

(a) (b)

Figure 3. (a) Schematic picture of the torus with logical operators. (b) Torus with 12 qubits placed at the edges of the hexagonal lattice, 4 plaquettes (3 independent) and 8 vertices (7 independent). $\bar{Z}_L$ distance 2, $\bar{X}_L$ distance 4. Error detecting.

where $n_i^{\pm} = \frac{1}{2}(1 \pm Z_i)$ and subscript v runs over the vertices belonging to plaquette p. $\prod_{v\in p} \beta_v$ is

$$\prod_{v\in p} \beta_v = \mathrm{i}^{n_{12}^-\left(n_1^- n_6^- - n_1^+ n_6^+\right)} \mathrm{i}^{n_7^-\left(n_1^+ n_2^+ - n_1^- n_2^-\right)}\ \mathrm{i}^{n_8^+\left(n_2^- n_3^+ - n_2^+ n_3^-\right)} \times \mathrm{i}^{n_9^-\left(n_3^- n_4^- - n_3^+ n_4^+\right)}\ \mathrm{i}^{n_{10}^-\left(n_4^+ n_5^+ - n_4^- n_5^-\right)} \mathrm{i}^{n_{11}^+\left(n_5^- n_6^+ - n_5^+ n_6^-\right)}, \tag{38}$$

following the labeling of figure 2b. In the subspace where $Q_v|\psi\rangle = |\psi\rangle$, equation (36) reduces to the original plaquette of the double semion model (34).

Plaquette excitations are generated by strings of Z-Pauli operators, as we found for the toric code. These operators commute with every stabilizer except the plaquettes at the endpoints of the string and will be denoted by S^Z. The string operators generating plaquette vertex excitations are more complex than a string of X-Pauli operators. Since plaquette operators (36) have some additional phases, we also need to add some phases to the string of X to make them commute with plaquette operators. For a string on a path $\mathcal{P}$ we have

$$S^+_{\mathcal{P}} = \prod_{j\in\mathcal{P}} X_j \sum_{\vec{i}} F(\vec{i})|\vec{i}\rangle\langle\vec{i}|. \tag{39}$$

The support of $S^+_{\mathcal{P}}$ is $\mathrm{Conn}(\mathcal{P})$, which can be seen in figure 2c. This means that the operator $S^+_{\mathcal{P}}$ acts non-trivially only on the set of qubits $\mathrm{Conn}(\mathcal{P})$. Thus, $F(\vec{i}) = F(\vec{i} \oplus \vec{j})$ for any $\vec{j}$ whose qubits in $\mathrm{Conn}(\mathcal{P})$ are zero. Here, $\oplus$ denotes the sum mod 2 of the bitstrings. $F(\vec{i})$ can be determined by solving the linear system of equations obtained as the result of imposing that $S^+_{\mathcal{P}}$ must commute with plaquettes and square to one. The positive chirality string $S^+_{\mathcal{P}}$ generates vertex excitations at the endpoints. The negative chirality string, $S^-_{\mathcal{P}}$, can be

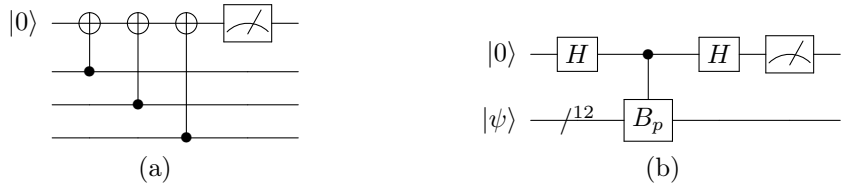

(a) (b)

Figure 4. Measurement circuits for (a) vertex and (b) plaquette operators.

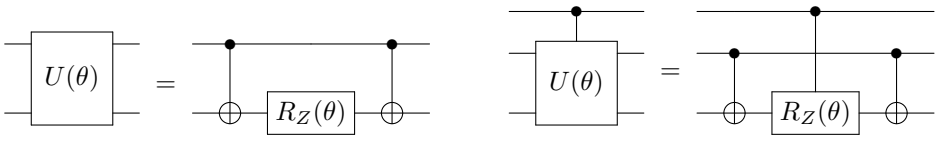

(a) (b)

Figure 5. Decomposition of (a) $U(\theta)$ and (b) controlled $U(\theta)$ into CNOTs and $R_Z(\theta)$.

obtained by multiplying $S^+_{\mathcal{P}}$ and $S^Z_{\mathcal{P}}$. Two strings with the same chirality crossing once anticommute, while strings of opposite chirality commute. S^Z strings crossing once with $S^\pm$ anticommute.

Analogously to what is done for the toric code, non-trivial strings of the torus are related to logical operators of the code. A schematic picture showing two pairs of logical operators in the torus can be seen in figure 3a. Logical operators satisfy the Pauli algebra. Note that X-logical operators are two times longer than Z, as a consequence of the hexagonal lattice, which is not self-dual. Therefore, we will be better protected against certain kind of errors. Similar effects can be observed in the Kitaev code when embedded in hexagonal or non-self-dual lattices [FT12].

2.1. Implementation

A minimal version of the semion code is presented in figure 3b. This code has error detection capabilities, since the code distance is two. To implement this code in a quantum computer, we need to decompose the stabilizer operators into basic gates. Vertex operators work the same way as in Kitaev toric code and can be measured with the circuit shown in figure 4a. The top qubit is an ancilla, which is the target of the three CNOTs coming from the qubits belonging to a given vertex.

The plaquette phases given in equation (37) can be expressed as a product of operators of the form $U(\theta) \equiv \exp\left(-\mathrm{i}\frac{\theta}{2} Z \otimes Z\right)$. In particular we have 6 operators of the form $U(\frac{\pi}{2}) = \exp\left(-\mathrm{i}\frac{\pi}{4} Z \otimes Z\right)$ coming from $\prod_{j\in\partial p} (-1)^{n^-_{j-1} n^+_j}$ and 12 operators of the form $U(\pm\frac{\pi}{4})$ coming from $\prod_{v\in p} \beta_v$. These operators can be realized using the

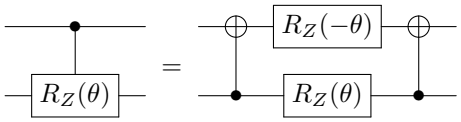

Figure 6. Decomposition of a controlled $R_Z(\theta)$.

circuit of figure 5a, where $R_Z(\theta) = \exp\left(-\mathrm{i}\frac{\theta}{2}Z\right)$. A controlled version of this circuit, useful when measuring the plaquette, is given in figure 5b. Plaquette operators are then measured using the circuit presented in figure 4b. The controlled plaquette operator is given by (following the same labelling as the one given in figure 2b):

- 6 CNOTs, where the ancilla is the control and qubits 1 to 6 the targets.
- 6 controlled $U(\frac{\pi}{2})$, where the ancilla is the control and the pairs (1,2), (2,3), ..., (6,1) are the target.
- 12 controlled $U(\pm\frac{\pi}{4})$, where the ancilla is the control and the target is one qubit at the leg of the hexagon and one of the adjacent qubits, for instance the pair (1,7).

In the IBM quantum computer,[7] basic gates are one-qubit rotations and CNOTs. Therefore the controlled $R_Z(\theta)$ must be decomposed as shown in figure 6. The connectivity limitations of the computer make the circuit even deeper, since, for instance, CNOTs between two neighboring qubits can only be performed in a certain direction. Given the depth of the circuit, it is a very challenging task for current computers.

3. Neural network decoders

Decoders are algorithms that receive as input an error syndrome and output a recovery operation. In this section, we will review the decoding problem in topological codes and then introduce some machine learning concepts that can help us build neural decoders.

3.1. Decoding topological codes

As we saw earlier for the toric code and the semion code, correcting the errors amounts to bringing the quasiparticle excitations back together in such a way that the total operator applied on the system is a trivial loop, equivalent to a multiplication of stabilizer operators. Since the code space is the simultaneous $+1$ eigenstate of stabilizers, applying stabilizer operators to the code space leaves it invariant. While this may seem an easy task, it can become quite tricky in the

[7] See the specifications of some devices at https://github.com/Qiskit/ibmq-device-information/tree/master/backends.

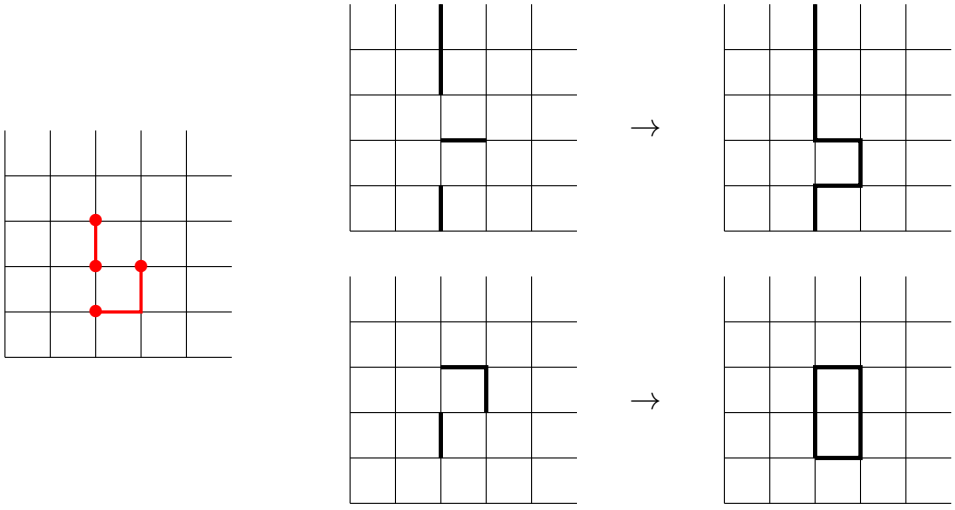

Figure 7. (a) X errors on some links of the lattice. Red dots indicate the vertices flipped by the error, the vertex excitations. (b) Two possible error recovery operations. (c) Total operation applied on the code.

presence of multiple errors and long error strings. Indeed, it is in general computationally hard to find an optimal recovery operation given an error syndrome [Pou06].

An example of a simple decoding problem is illustrated in figure 7, where the syndrome measurement and the recovery process is shown for some X-error chain in the toric code. The decoder is given the syndrome measurements of figure 7a. The actual error that occurred (red links) is not known. Figure 7b shows two possible recovery operations that annihilate the excitations. The total operator applied in the top figure forms a non-trivial loop and the information encoded is damaged. The recovery is not successful and produces a logical error. The other figure shows a successful recovery, since the loop is trivial.

Let us consider X errors to be independent of each other and to occur with probability p. An error chain $\mathcal{E}$ is characterized by the function $n_{\mathcal{E}}(l)$, which is one if edge l belongs to $\mathcal{E}$ and vanishes otherwise. Given an error syndrome s, the probability that error chain $\mathcal{E}$ occurs is

$$P(\mathcal{E}|\, s) = \prod_l (1-p)^{1-n_{\mathcal{E}}(l)} p^{n_{\mathcal{E}}(l)} = N \prod_l \left(\frac{p}{1-p}\right)^{n_{\mathcal{E}}(l)}, \tag{40}$$

where l runs over all the links in the lattice, the endpoints of $\mathcal{E}$ are those vertices where the syndrome is -1 and N is a normalization factor [Den+02]. One may

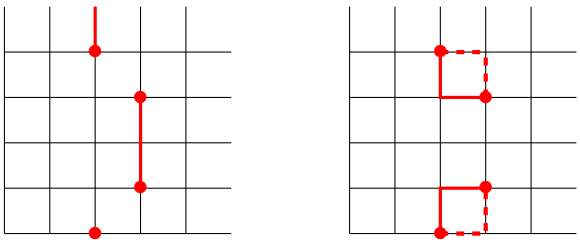

(a) (b)

Figure 8. Different error chains causing the same vertex excitation syndrome. The matching given in (a) is minimum weight and proportional to p^3, while (b) is proportional to $4p^4$, since it is four-fold degenerate. It may happen that (b) is the most likely error.

obtain a recovery operation by maximizing the probability [Fuj15]

$$\mathcal{R} = \arg\max_{\mathcal{E}} P(\mathcal{E}|\, s) = \arg\min_{\mathcal{E}} \sum_{l} n_{\mathcal{E}}(l), \tag{41}$$

where we have again that the endpoints of $\mathcal{E}$ must be the vertices with -1 syndrome. Thus, this decoding procedure assumes that the error that occurred is the one with minimum length. In this way, we can select the bottom recovery operation in figure 7b, since it has length 3 instead of length 4 of the recovery at the top. This choice is intuitively better, because the probability of the former chain is proportional to p^3 whereas the latter is proportional to p^4. As a matter of fact, decoding based on equation (41) can be efficiently implemented by an algorithm called minimum-weight perfect matching (MWPM) [Edm65, Kol09]. This algorithm runs in polynomial time $O(L^6)$, where L is the linear size of the lattice. MWPM receives as input a weighted fully connected graph, where each node is a vertex excitation and each weight is the minimum Manhattan distance between each two vertices. The algorithm matches the excitations so that the sum of weights is minimized.

The above decoding procedure is quite powerful, but it is not the optimal solution. MWPM ignores the fact that there are several error chains producing the same syndrome and that can be corrected with the same recovery $\mathcal{R}$. If recovery $\mathcal{R}$ is successful $\mathcal{E}+\mathcal{R}$ forms a trivial loop. But any error $\mathcal{E}'$ such that $\mathcal{E}' = \mathcal{E}+\mathcal{C}$, where $\mathcal{C}$ is a trivial loop, could have also been successfully corrected with $\mathcal{R}$. This error degeneracy needs to be taken into account in an optimal decoder. The example illustrated in figure 8 shows clearly the effect of degeneracy.

In order to obtain an optimal recovery, we need to sum over all error chains belonging to the same homology class. We use $\mathcal{E} \sim \mathcal{E}'$ to denote that $\mathcal{E}'$ and $\mathcal{E}$ differ only in a trivial loop, $\mathcal{E}' = \mathcal{E}+\mathcal{C}$, and therefore belong to the same homology

class. The probability for a homology class is

$$P(h_{\mathcal{E}}) = \sum_{\mathcal{E}' : \mathcal{E}' \sim \mathcal{E}} P(\mathcal{E}' | \, s), \tag{42}$$

where $\mathcal{E}$ is an error chain compatible with the syndrome and chosen arbitrarily as a reference frame. The sum goes over all $\mathcal{E}'$ in the same homology class as $\mathcal{E}$. Since there are two inequivalent non-trivial loops in the torus, $\mathcal{L}_1$ and $\mathcal{L}_2$, we have four homology classes: $h_{\mathcal{E}}$, $h_{\mathcal{E}+\mathcal{L}_1}$, $h_{\mathcal{E}+\mathcal{L}_2}$ and $h_{\mathcal{E}+\mathcal{L}_1+\mathcal{L}_2}$. The optimal recovery is given by the homology class with maximum probability. Any chain in that class is an optimal recovery operation.

The above discussion applies also to Z errors and plaquette operators. We have considered here independent X and Z errors (bit- and phase-flip), this gives us a general idea of the decoding problem in topological codes. However, we may have noise models (e.g., depolarizing noise) in which both errors are correlated and treating vertex and plaquette syndromes separately yields suboptimal results. Additionally, Pauli noise on non-Pauli codes causes this kind of vertex and plaquette correlations, as is the case of the semion code in publication [P4].

Once we have a decoding strategy, we can simulate how the code performs under a certain noise model. In principle, increasing the size of the code should make it more resistant against errors. In other words, increasing the code distance should reduce the logical error rate. Nevertheless, there is a certain error rate beyond which this does not happen any more. This behavior is pictured in figure 9, where the logical error rate is plotted against the physical error rate for independent bit-flip and phase-flip noise with a MWPM decoder. Explicitly, the noise model is given by the expression $\rho \to (1-p)\rho + p_X X\rho X + p_Y Y\rho Y + p_Z Z\rho Z$, with $p_X = p_Z = p_0 - p_0^2$ and $p_Y = p_0^2$. Each qubit is independently acted on by an X error with probability p_0 and by a Z error with same probability p_0. The threshold value is observed at $p_0 = 0.064$ and separates two regimes, one where error correction is feasible and another where not.

3.2. Neural networks

Machine learning has been applied to many different physical problems in recent years, among them, decoding topological codes [Car+19]. The first example of this was presented by Torlai and Melko [TM17] and many more studies would follow, as we will see in section 3.3. Most of the decoders built for this purpose use neural networks and supervised learning and this is also the approach we will take in publication [P4]. Let us now review these concepts before introducing neural decoders.

Supervised learning involves input and output pairs. The goal is to predict the desired output given an input. A dataset of input and output pairs is provided to the model, which learns by minimizing a cost function. This cost function can take very different forms and is related to the incorrect predictions of the model.

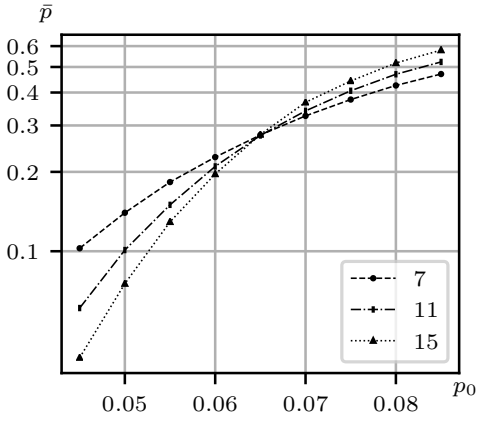

Figure 9. Logical error rate, $\bar{p}$, against physical error rate, p_0, for the hexagonal Kitaev toric code with a MWPM decoder and three different code distances.

For instance, in a regression problem, where we have pairs (x_i, y_i) with $x_i, y_i \in \mathbb{R}$, and we want to predict y given x, we can pick the mean-squared error as the cost function,

$$\text{MSE} = \frac{1}{N}\sum_{i=1}^{N}(y_i - \hat{y}_i)^2, \tag{43}$$

where $\hat{y}_i$ are the predictions of the model and the sum runs over the dataset. The model is a function f, with some trainable parameters $\boldsymbol{w}$, and predictions are given by $\hat{y}_i = f(x_i; \boldsymbol{w})$. Computing the derivative of the cost function with respect to the weights, we can minimize the cost function by gradient descent and train the model. Other problem types require other cost functions. For instance, in a classification task with a discrete set of labels (e.g., predicting if the image contains a cat or a dog), we can use categorical cross entropy,

$$\text{CCE} = -\frac{1}{N}\sum_{i=1}^{N}\sum_{j=1}^{M} y_{i,j}\log \hat{y}_{i,j}. \tag{44}$$

Here, we have M possible categories. If the categories are mutually exclusive, the label $y_{i,j}$ is zero for all j except for one, where we have $y_{i,j} = 1$. $\hat{y}_{i,j}$ is the probability given by the model of element i belonging to category j.

We have presented supervised learning, we now need a learning model. Artificial neural networks [Agg18] are learning algorithms loosely inspired by biological neural networks. They are made out of neurons. Each neuron receives some input, performs a linear operation on this input and then a non-linear function is

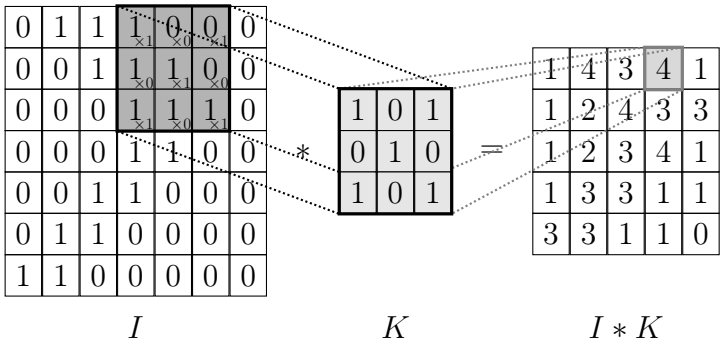

Figure 10. The kernel, K, sweeps the input data, I, and produces at each position an element of the output, $I * K$.

applied yielding an output. The linear operation is characterized by some trainable parameters: weights $\boldsymbol{w}$ and a bias term b. The non-linear operation, known as activation function, is usually chosen to be the rectified linear unit (ReLU): $f(z) = \max(0, z)$.[8] The output of a neuron provided with some input $\boldsymbol{x}$ is

$$y = f(\boldsymbol{w} \cdot \boldsymbol{x} + b). \tag{45}$$

The network is formed by interconnected neurons. Each neuron receives the input from the output of other neurons. One of the simplest neural networks is the multilayer perceptron (MLP). In a MLP neurons are distributed in layers. Each layer is fully connected to the next, meaning that each neuron receives as input all the outputs of the neurons in previous layers. It can be divided in three parts: an input layer, some hidden layers and an output layer. The input layer provides some input from the outside world to the next layer. No computation is performed in these neurons. The hidden layers receive the information from the input layer, perform computations and transfer the information to the output layer. The output layer performs computations and yields the network output. This simple structure is actually very powerful. The universal approximation theorem states that this type of neural networks can approximate any continuous function to any degree of accuracy [Cyb89, Hor91, Les+93].

A specialized type of neural network are convolutional neural networks. These networks can be used with data distributed on a grid-like pattern and are good at learning spatially correlated data. Examples of this are images, spectrograms or the syndrome measurements of a topological error correcting code. The central part of convolutional neural networks are convolutional layers. The convolution

[8]For the output neurons, i.e., those neurons computing the final output of the network, other functions are chosen depending on the problem. If we have a classification task, we can use the softmax activation function, $f_i(\boldsymbol{z}) = e^{z_i} / \sum_j e^{z_j}$. This ensures that the sum of components of the output is one, $\sum_i f_i(\boldsymbol{z}) = 1$, representing a probability. For a regression problem with an unbounded solution, we may choose a linear activation function.

operation performed by one of these layers is shown in figure 10. Each input to the next layer is computed from a small local region of the preceding layer using some trainable parameters called kernels (or filters). The kernel is moved with a certain stride along the input and produces an output at each position by summing the element-wise multiplication. If the stride is higher than one, the size of the output data is reduced, since the kernel moves several steps at a time. For instance, if we have a stride of two, the size along each dimension is halved. Also the concept of padding is important when speaking about the output size. As we can see in figure 10, the output size is reduced by two because of the size of the kernel. However, we can add extra columns and rows at the side of the matrix so that the output has the same shape as the input. If these rows and columns contain zeros, we have what is called zero padding. In publication [P4], since the data has periodic boundary conditions, periodic padding is used.

By stacking the convolutional layers and/or the fully connected layers presented above, we can build very powerful models. In fact, deeper models, i.e., models with many layers stacked on top of each other, seem to be able to tackle more complex tasks [GBC16]. However, for many years training deep networks was nearly impossible and their performance was not much better than that of shallow networks. One of the most significant issues is the vanishing gradient problem, where the gradient computed during the training process tends to vanish or explode. New techniques developed in recent years, such as initialization of weights [GB10, He+15] or batch normalization [IS15], have enabled us to successfully train deep models. For a more detailed explanation of deep learning and neural networks, we refer the reader to [Nie15, GBC16, Agg18].

3.3. Decoding with neural networks

There are very different approaches to the construction of decoders with neural networks. Let us mention briefly a few of the implementations we can find in the literature. In [SJG19], several decoders are chosen. These decoders have different characteristics and can perform differently on the same syndrome. A neural network is then trained to choose which decoder is better to decode a given syndrome. [Ni18] builds a decoder based on the renormalization group decoder [DP10], where the belief propagation process is approximated by a neural network. References [TM17, KJ17, BN18] use neural networks to predict which qubits suffered an error. Other studies [VCB17, Bai+18] use a neural network for classification task where the neural network tries to predict the logical error associated with the final logical operator measured. Likewise, in [MKJ19] the logical error made by a simple rudimentary decoder is predicted by a neural network.

Publication [P4] uses the same approach as [MKJ19] and turns the decoding process into a classification task. A simple decoder, which just takes all excitations to the same point of the lattice, is first given an error syndrome and produces a rudimentary correction. This rudimentary correction causes a logical error in the

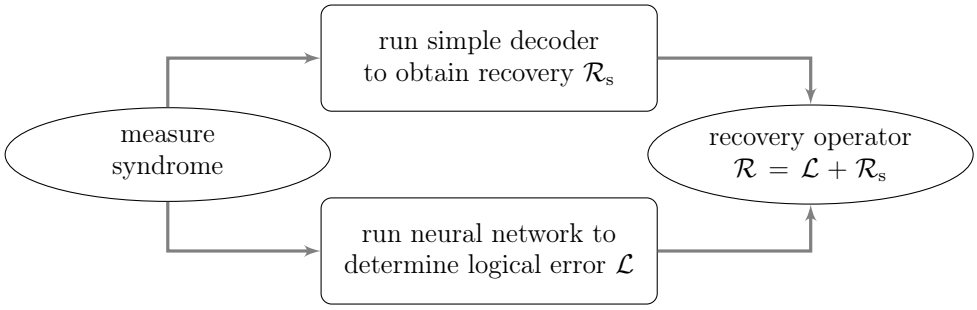

Figure 11. Decoding process. The neural network is trained to predict the logical error made by a simple decoder.

code. If we have one encoded qubit, there are four possibilities: $\bar{I}$ (successful recovery), $\bar{X}$, $\bar{Y}$ or $\bar{Z}$. The neural network is trained to predict which of these four occurred given the error syndrome. Once we have the recovery from the simple decoder and the logical error from the neural network, we can apply a suitable recovery to the code by combining both. A diagram showing this process is depicted in figure 11.

4. Summary and main results of publication 3

The Kitaev code is the simplest topological code yielding a quantum memory. It can also be thought of as a two-dimensional lattice gauge theory with gauge group $\mathbb{Z}_2$. In two spatial dimensions, there is another lattice gauge theory with the same gauge group but different topological properties: the double semion model. Whereas the properties of the Kitaev code have been extensively studied in quantum computation and condensed matter, barely nothing is known about the quantum error correcting properties of the double semion model. In this work we remedy this situation by introducing a new formulation of the double semion model that is suitable for a complete treatment as a quantum memory with topological properties. We build a code which is characterized by the following key properties: it is topological, it satisfies the stabilizer formalism, it is non-CSS, non-Pauli and additive. What is remarkable of the double semion code is that, to our knowledge, this is the first non-CSS topological quantum memory that being a stabilizer code, it is also a topological code throughout the whole Hilbert space of states of the system. In a sense, this was a missing link in the theory of topological quantum error correction codes and we have filled this gap with the tools introduced in our work. Below, the main results obtained in publication [P3] are presented.

1. **Off-shell formulation of the double semion model.** We perform a thorough analysis of a formulation of the plaquette operators which commute in the whole Hilbert space. This construction consists in adding extra phases to the plaquette operators which act on excited states, and

which depend on the configuration of the three edges at each vertex. When the vertex-free condition is imposed, we recover the standard definition of the double semion model.

2. **Explicit construction for string operators along arbitrary paths.** The new string operators are complete in the sense that any operator acting on the system can be decomposed as a linear superposition of such operators. Additionally, the string operators can be constructed efficiently despite the complex structure of the plaquette operators.
3. **Analytical proof that the excitations of the system behave as semions.** We construct strings operators which create excitations called semions. Remarkably, a microscopic formulation to create semions was not proven until now. This is achieved via the detailed study of the constructed string operators, which allows us to explicitly calculate the topological S-matrix. Interestingly enough, most of the string operator properties rely on very generic arguments about the structure of the local operators making up the Hamiltonian, namely that they commute and square to the identity.
4. **Construction of logical operators needed for a quantum memory.** Closed-string operators are constructed, which allow us to perform logical operations on the quantum memory built from the semion code. Homologically non-trivial closed string operators act non-trivially on the degenerate ground space, which is our code space.

New Journal of Physics
The open access journal at the forefront of physics

Deutsche Physikalische Gesellschaft DPG
IOP Institute of Physics

Published in partnership with: Deutsche Physikalische Gesellschaft and the Institute of Physics

OPEN ACCESS

RECEIVED
23 December 2018

REVISED
19 April 2019

ACCEPTED FOR PUBLICATION
2 May 2019

PUBLISHED
29 May 2019

PAPER

Quantum error correction with the semion code

G Dauphinais, L Ortiz, S Varona and M A Martin-Delgado

Departamento de Física Teórica, Universidad Complutense, E-28040 Madrid, Spain

E-mail: gdauphin@ucm.es

Keywords: quantum information, quantum error correction, topological codes, double semion model

Abstract

We present a full quantum error correcting procedure with the semion code: an off-shell extension of the double-semion model. We construct open-string operators that recover the quantum memory from arbitrary errors and closed-string operators that implement the basic logical operations for information processing. Physically, the new open-string operators provide a detailed microscopic description of the creation of semions at their end-points. Remarkably, topological properties of the string operators are determined using fundamental properties of the Hamiltonian, namely, the fact that it is composed of commuting local terms squaring to the identity. In all, the semion code is a topological code that, unlike previously studied topological codes, it is of non-CSS type and fits into the stabilizer formalism. This is in sharp contrast with previous attempts yielding non-commutative codes.

1. Introduction

Topological properties of quantum systems have become a resource of paramount importance to construct quantum memories that are more robust to external noise and decoherence [1–7] than standard quantum error correcting codes [8–15]. The latter are based on a special class of codes—concatenated codes—which enable us to perform longer quantum computations reliably, as we increase the block size.

The Kitaev code is the simplest topological code yielding a quantum memory [1]. It can be thought of as a simple two-dimensional lattice gauge theory with gauge group $G = \mathbb{Z}_2$. In $D = 2$ spatial dimensions, there is another lattice gauge theory with the same gauge group but different topological properties: the double semion (DS) model [16–18, 22–25]. Although the Kitaev and the DS models are lattice gauge theories sharing the same gauge group, $G = \mathbb{Z}_2$, the braiding properties of their quasiparticle excitations are radically different. For example, whereas braiding two elementary quasiparticle excitations (either an electric or a magnetic charge) gives a $+1$ phase in the Kitaev code, doing so in the DS model yields $\pm i$ phase factors.

The DS model was introduced in the context of the search of new topological orders in strongly correlated systems, gapped, non-chiral and based on string-net mechanisms in $D = 2$ dimensions [16, 17]. Generalizations of the DS model to $D = 3$ and to higher dimensions have appeared recently [18]. While the properties of the Kitaev code has been extensively studied in quantum computation and condensed matter, barely nothing is known about the quantum error correcting properties of the DS model despite recent efforts towards realizing such models [19–21]. In this work we remedy this situation by introducing a new formulation of the DS model that is suitable for a complete treatment as a quantum memory with topological properties.

The first obstacle to tackle the DS model as a quantum memory is the original formulation as a string-net model [16]. In this formulation, the Hamiltonian is only Hermitian and exactly solvable in a particular subspace, where plaquette operators are Hermitian and commute. Only linear combinations of closed-string configurations, implying the absence of vertex excitations, are allowed in this subspace [16, 26, 27]. The microscopic formulation of the original DS model starts with a hexagonal lattice Λ with qubits placed at links e. Vertex operators Q_v are attached to the three links meeting at a vertex $v \in \Lambda$. Plaquette operators $\tilde{B}_p$ are attached to hexagons $p \in \Lambda$ with the novel feature that their outer links carry additional phase factors that are missing in the corresponding Kitaev model. Explicitly

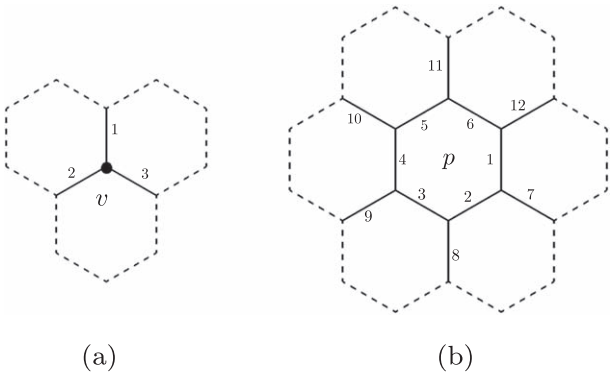

Figure 1. The support of the vertex operator $Q_v = \sigma_1^z\sigma_2^z\sigma_3^z$ and plaquette operator $\tilde{B}_p$. The qubits are placed on the edges.

$$Q_v \coloneqq \sigma_i^z\sigma_j^z\sigma_k^z, \tag{1}$$

with i, j, k, being the three qubits belonging to vertex v (see figure 1(a)) and

$$\tilde{B}_p \coloneqq \left(\prod_{i\in\partial p}\sigma_i^x\right)\prod_{j\in o(p)} i^{\frac{1}{2}(1-\sigma_j^z)}, \tag{2}$$

where ∂p are the six links of the hexagon and $o(p)$ is the set of six edges outgoing from each plaquette p, as it is shown in figure 1(b). Unlike the Kitaev code, these plaquette operators $\tilde{B}_p$ are Hermitian and commute among themselves only in a subspace of the whole Hilbert space, defined by the so-called zero-flux rule [16, 26, 27]. This is given by a vertex-free condition on states

$$\mathcal{H}_v \coloneqq \{|\psi\rangle\colon Q_v|\psi\rangle = +|\psi\rangle, \forall\, v \in \Lambda\}. \tag{3}$$

The set of vertex and plaquette operators defines a Hamiltonian

$$\tilde{H}_{\mathrm{DS}} \coloneqq -\sum_{v\in\Lambda} Q_v + \sum_{p\in\Lambda}\tilde{B}_p. \tag{4}$$

Due to the involved structure of phases that plaquette operators in equation (2) have, it was aforementioned that these operators do not commute out of the vertex-free subspace. This implies that the model is only well-defined when there are no vertex excitations.

Therefore, in order to treat the DS model as a quantum error correcting code [11, 28–31], it is necessary to have a formulation of the model that is valid in the whole Hilbert space and not just for the vertex-free subspace (3), since generic noise processes will make the system leave the mentioned subspace. To this end, we introduce an off-shell DS model that we call the semion code. This new model is achieved by making a deformation of the original plaquette operators (2) such that they become commuting and Hermitian operators without imposing the vertex-free condition [27]. In addition, we are able to develop the complete program of quantum error correction with the semion code.

1.1. Summary of main results

In order to summarize the main contributions that we present in this paper, we hereby advance a list of some of our most relevant results.

(i) We perform a thorough analysis of a formulation of the plaquette operators which commute in the whole Hilbert space [27]. This construction consists in adding extra phases to the plaquette operators, which depend on the configuration of the three edges at each vertex. When the vertex-free condition is imposed, we recover the standard definition of the DS model.

(ii) We give an explicit construction for string operators along arbitrary paths. They are complete in the sense that any operator acting on the system can be decomposed as a linear superposition of such operators. Additionally, the string operators can be constructed efficiently despite the complex structure of the plaquette operators. Remarkably, a microscopic formulation to create semions was not proven until now.

(iii) We analytically show that the excitations of the system behave as semions, via the detailed study of the constructed string operators, which allows us to explicitly calculate the topological S-matrix. Interestingly

enough, most of the string operator properties rely on very generic arguments about the structure of the local operators making up the Hamiltonian, namely that they commute and square to the identity.

(iv) Closed-string operators are constructed, which allow us to perform logical operations on the quantum memory built from the semion code. Logical operators are closed-string operators whose paths are homologically non-trivial and act non-trivially on the degenerate ground space.

(v) Given the above properties, we define a topological quantum error correcting code based on a non-trivial extension of the DS model. We build a code, which is characterized by the following key properties: is topological, satisfies the stabilizer formalism, is non-CSS, non-Pauli and additive.

The topological nature of the code becomes apparent through the fact that global degrees of freedom are used to encode information and only local interactions are considered [1, 4]. Another remarkable feature of the semion code is that is of non-CSS type since in the plaquette operators both Pauli X and Z operators enter in the definition [9, 28]. Consequently, errors in an uncorrelated error model such as independent bit-flip and phase-flip errors cannot be treated separately. However, they can be decomposed as a linear superpositions of fundamental *anyonic* errors (string operators creating pairs of anyons) with a known effect on the Hilbert space. Moreover, the semion code is not a subgroup of the Pauli group since the complex phases entering its definition (see equation (2)) makes impossible to express its generators in terms of tensor products of Pauli matrices [32, 33]. Nevertheless, the semion code is still an additive code: the sum of quantum codewords is also a codeword [34]. This last fact is intimitely related to the abelian nature of the semionic excitations [35, 36].

1.2. Outline

The article is organized as follows. In section 2 we introduce the off-shell DS model, which is suitable for quantum error correction. In section 3 we build string operators creating vertex excitations at their endpoints. Section 4 is devoted to logical operators and quantum error correction. We conclude in section 5. Appendices deserve special attention since they contain the detailed explanations of all the constructions used throughout the text. Specifically, appendix A presents an explicit example of a string operator, appendix B gives the detailed proof of theorem 1, which presents a systematic way to construct string operators, as well as several key properties of the string operators and finally appendix C is devoted to the proof of theorem 2, which gives the commutation relations among string operators.

2. Off-shell DS: microscopic model

We begin by considering a microscopic description of the DS model on the entire Hilbert space of states, since it is much better suited for quantum error correction. We call this an off-shell DS code by borrowing the terminology from quantum field theory and other instances in physics where a shell condition amounts to a constraint on the phase space of a system. For instance, the equation of motion is a shell condition for quantum particles but the phase space is more general. In our case, the shell condition is the vertex-free subspace or zero-flux rule introduced in equation (3).

2.1. DS model in the vertex-free subspace

Let us start by introducing the DS model in a new presentation that is more suitable for building an off-shell formulation of it. We consider the same hexagonal lattice Λ with qubits attached to the edges $e \in \Lambda$. The vertex operators Q_v will remain the same as in equation (1), but the plaquette operators in the zero-flux subspace can be rewritten in an equivalent form to that shown in equation (2), i.e.

$$\tilde{B}_p = \left(\prod_{j=1}^{6} \sigma_j^x\right)\left(\prod_{j=1}^{6} (-1)^{n_{j-1}^- n_j^+}\right), \tag{5}$$

in which $n_i^\pm := \frac{1}{2}(1 \pm \sigma_i^z)$ is the projector on the state $|0\rangle$ (n^+) or $|1\rangle$ (n^-) of qubit i, qubits are labeled as shown in figure 1 and we use the convention that $n_0^\pm$ refers to qubit '6' for simplicity. Remarkably, this expression avoids any reference to the outgoing links of hexagonal plaquettes p. One readily sees that the vertex operators fulfill the following relations:

$$Q_v^2 = 1, \quad [Q_v, Q_{v'}] = 0, \quad [Q_v, \tilde{B}_p] = 0; \tag{6}$$

$\forall\, v, v', p \in \Lambda$. As for the plaquette operators $\tilde{B}_p$, they also satisfy

$$\tilde{B}_p^2 = 1, \quad \tilde{B}_p^\dagger = \tilde{B}_p, \quad [\tilde{B}_p, \tilde{B}_{p'}] = 0; \tag{7}$$

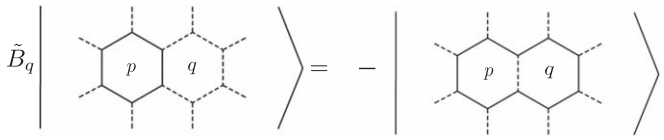

Figure 2. Applying plaquette operator $\tilde{B}_q$ adds a closed loop around plaquette q and multiply the wave function by a -1 phase. Each qubit in a given configuration is represented by a filled link of the lattice if it is in state $|1\rangle$, whereas links in $|0\rangle$ are left empty (dashed line).

$\forall\, p,\, p' \in \Lambda$, but only in the vertex-free subspace (3). Furthermore, the product of all the vertex and plaquette operators is the identity. A simple counting argument reveals that the ground space is 4^g degenerate[1], which g being the genus of the orientable compact surface onto which the lattice is placed.

An explicit unnormalized wavefunction belonging to the ground space is obtained in the following way: we start from the vacuum, i.e. $|0\rangle^{\otimes N}$, which has $+1$ eigenvalue for all vertex operators. Then, plaquette operators are used to build projectors and apply them onto the vacuum

$$|\Omega\rangle = \prod_{p\in\Lambda} \frac{1-\tilde{B}_p}{2}\, |0\rangle^{\otimes N}. \tag{8}$$

It is straightforward to check that this state fulfills the lowest energy condition for the Hamiltonian (4) within the vertex-free subspace. Expanding the product in equation (8), one can see that the ground state is a superposition of closed loops configurations. Due to the condition $\tilde{B}_p = -1$ for the ground state, the coefficients of this superposition of closed loops alternate sign. Thus, we can write the ground state in a different way:

$$|\Omega\rangle = \sum_{\vec{i}\ \in\{\text{C-S conf.}\}} (-1)^{N_L(\vec{i})} |\vec{i}\rangle, \tag{9}$$

where $\vec{i}$ is a bitstring representing a qubit configuration and $\{\text{C-S conf.}\}$ is the set of all possible closed-string configurations. Each configuration in this set has a certain number of closed loops, $N_L(\vec{i})$, whose parity determines the sign of the coefficient in the ground state superposition.

Of course the above construction only gives rise to one of the ground states. To find the other ones, the starting configuration can simply be replaced by a configuration containing an homologically non-trivial closed loop (which necessarily belongs to the vertex-free subspace), and proceed with the same construction. Every different homological class for the closed loop corresponds to a different ground state.

Applying the $\tilde{B}_p$ operator on a specific loop configuration flips the string occupancy of the interior edges of plaquette p while acquiring a phase that depends on the specific configuration under consideration. Applying $\tilde{B}_p$ on the vacuum simply adds a closed loop around plaquette p, while applying $\tilde{B}_p$ next to a closed loop either enlarges (or shrinks) the existing loop to include (exclude) plaquette p, while multiplying the wave function by -1 factor (see figure 2).

Due to the lack of commutativity of the plaquette operators and the fact that they are not Hermitian, the original DS model is only well-defined when there are no vertex excitations. Moreover, the strings creating vertex excitations are not properly defined either. A naive attempt to construct these strings as a chain of σ^x operators, following the similarities with the Kitaev code, resoundingly fails. As a consequence of the phases on the external legs of plaquette operators, σ^x operators create vertex excitations but also plaquette excitations. In order to get a string that creates only two vertex excitations at the endpoints but commutes with all the plaquette operators along the path $\mathcal{P}$, it is necessary to add some extra phases to the chain of σ^x on the outer legs. An approach to this problem is described in [27] but it is not successfully solved since the strings are only well-defined in the vertex-free subspace.

The DS model gives rise to quasiparticle excitations behaving like anyons. They are called semions, due to the fact that their topological charge is 'half' of that of a fermion, i.e. $\pm i$. There exist two types of semions in the model, one corresponding to a vertex excitation, while the other corresponds to both vertex and adjacent plaquettes excitations. From now on, we name these two different possibilities as *chiralities*, positive chirality for the former kind, and negative chirality for the latter one. We warn the reader that this choice has been made arbitrarily, and does not necessarily reflect the topological charge of a given specie.

[1] This is strictly true only if the total number of plaquettes of the system is even. If it is odd, then the ground state must contain a single flux excitation, which can be placed in any of the plaquettes. In that latter case the ground space degeneracy is an extensive quantity. However, any given flux configuration is 4^g-degenerate. For simplicity, we assume in this work that the system contains an even number of plaquettes.

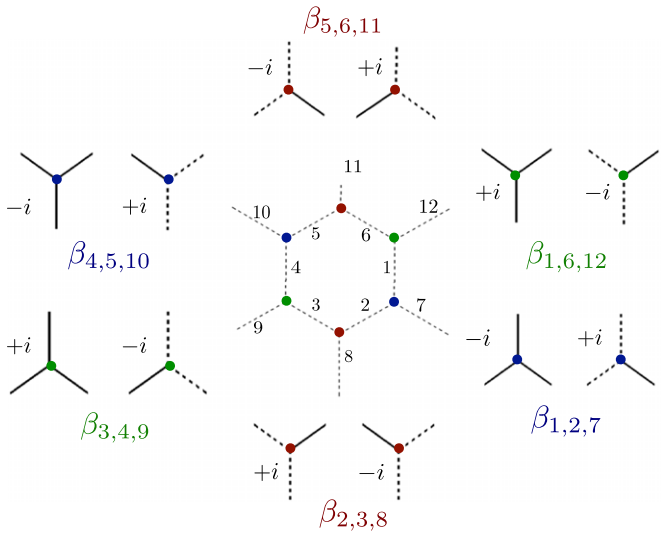

Figure 3. A graphical representation of the various non-trivial phase factors of the form $\beta_{(i,j,k)}$. A trivial phase of $+1$ is applied for any configuration not shown on this picture. The labeling of the edges have been omitted for simplicity, and corresponds to the same as the one on figure 1.

Taking into account all these caveats, we present in the following a formulation of the DS model which gives a microscopic approach to this interesting topological order, fulfilling all the necessary properties in the whole Hilbert space.

2.2. Exactly solvable model in the whole Hilbert space

If we want to consider encoding quantum information in the degenerate ground-state manifold of the standard (on-shell) DS model in equation (4), we immediately run into major problems: X Pauli errors make the state of the system leave the vertex-free subspace. The non-commutativity of the $\tilde{B}_p$ operators poses difficulties when interpreting the DS model as a stabilizer code.

To avoid such difficulties, we consider a modified version of the plaquette operators in equation (2), which we call the off-shell DS model or semion code

$$H_{\mathrm{DS}} = -\sum_{v} Q_v + \sum_{p} B_p, \tag{10}$$

where the *generalized* plaquette operator B_p is a modification of $\tilde{B}_p$ obtained by multiplying it by a phase factor that depends on the configuration on which it is applied. More specifically, we have

$$B_p \coloneqq \tilde{B}_p \times \tilde{\beta}_p, \tag{11}$$

with

$$\tilde{\beta}_p \coloneqq \sum_{\vec{i}} \tilde{b}_p(\vec{i})|\vec{i}\rangle\langle\vec{i}|, \tag{12}$$

where the sum runs over all possible configurations of edges 1 through 12 shown in figure 1. $\tilde{b}_p(\vec{i})$ is the phase factor corresponding to the string configuration $\vec{i}$. $\vec{i}$ represents a state in the computational basis. A qubit in the state $|0\rangle$ is interpreted as the absence of a string on its corresponding edge, while the state $|1\rangle$ reflects the presence of a string. The phase operator β_p can be decomposed as

$$\tilde{\beta}_p = \beta_{(6,1,12)}\,\beta_{(1,2,7)}\,\beta_{(2,3,8)}\,\beta_{(3,4,9)}\,\beta_{(4,5,10)}\,\beta_{(5,6,11)}, \tag{13}$$

where $\beta_{(i,j,k)}$ is a function of the string configuration of edges i, j and k connected to vertex $v(i, j, k)$. The specific values for each factor $\beta_{(i,\,j,\,k)}$ are shown graphically in figure 3. Note that their specific form differ depending on their position on the plaquette.

For future reference, notice that the generalized plaquette operator B_p can be written as

$$B_p = \prod_{i\in\partial p} \sigma_i^x \left(\prod_{j\in\partial p} (-1)^{n_{j-1}^- n_j^+} \right) \prod_{v\in p} \beta_v, \tag{14}$$

where we use the notation $j \in \partial p$ to indicate the qubit associated to edge j in plaquette p. $v \in p$ identify the vertices belonging to plaquette p. Notice that this last expression clearly shows that the phase factor appearing in B_p is a product of phases, β_v, depending on the string configuration of the three edges connected to each vertex of

plaquette p. The complete algebraic expression of the product of all β_v in a plaquette p is [27]

$$\prod_{v\in p}\beta_v = i^{n_{12}^-(n_1^-n_6^- - n_1^+n_6^+)} i^{n_7^-(n_1^+n_2^+ - n_1^-n_2^-)} \times i^{n_8^+(n_2^-n_3^+ - n_2^+n_3^-)} i^{n_9^-(n_3^-n_4^- - n_3^+n_4^+)} \times i^{n_{10}^-(n_4^+n_5^+ - n_4^-n_5^-)} i^{n_{11}^+(n_5^-n_6^+ - n_5^+n_6^-)}. \tag{15}$$

We can easily check that in the zero-flux rule the factors in equation (15) reduce to 1, recovering expression (5) for the plaquette operators.

The crucial point now is that the new generalized plaquette operators, B_p, satisfy the desired properties needed by the stabilizer formalism of quantum error correction. Namely,

$$B_p^2 = 1,\ \ B_p^\dagger = B_p,\ \ [B_p, B_{p'}] = 0,\ \ [Q_v, B_p] = 0; \tag{16}$$

$\forall\, p,\, p',\, v \in \Lambda$, regardless of the vertex-free condition (3). The study of $H_{\rm DS}$ is rendered much simpler than that of $\tilde{H}_{\rm DS}$ on the whole Hilbert space of the qubits by the fact that the new plaquette operators commute.

3. String operators

We seek open-string operators creating excitations at their endpoints without affecting the rest of vertex and plaquette operators, as well as closed-string operators that commute with vertex and plaquette operators. In our case, excited states correspond to states in a -1 eigenstate for a vertex operator or a $+1$ eigenstate of a plaquette operator. We say that an excitation is present at vertex v (plaquette p) if the state of the system is in a -1 ($+1$) eigenstate of Q_v (B_p). Since we have that $\prod_{v\in\Lambda} Q_v = \prod_{p\in\Lambda} B_p = 1$, excitations are always created in pairs.

In order to find such string operators, it is convenient to reexpress the generalized plaquette operators as

$$B_p = \prod_{i\in p}\sigma_i^x \sum_{\vec{i}} b_p(\vec{i})|\vec{i}\rangle\langle\vec{i}|, \tag{17}$$

where p denotes the interior edges of a plaquette (edges 1 through 6 in figure 1) and the string configurations in the sum are taken on edges 1 through 12. $b_p(\vec{i})$ denotes the complex phase picked up when applying operator B_p to the configuration $\vec{i}$. Note that $\sum_{\vec{i}} b_p(\vec{i})|\vec{i}\rangle\langle\vec{i}|$ differs from the product of the β_p's in the -1 factors appearing in equation (14). $\sum_{\vec{i}} b_p(\vec{i})|\vec{i}\rangle\langle\vec{i}|$ includes the -1 factors as well as the product of β_v.

Given two string configurations $\vec{i}$ and $\vec{\alpha}$ on a set of edges, it is useful to define the string configuration $\vec{i}\,\oplus\,\vec{\alpha}$ to be the configuration $\vec{i}\,'$ where the edges occupied in configuration $\vec{\alpha}$ has been flipped. It is equivalent to sum (mod 2) the two bitstrings. Additionally, we define the configuration $\vec{\alpha}^p$ of plaquette p as the string configuration which is empty everywhere except for the six edges in the interior of plaquette p, corresponding to edges 1 through 6 in figure 1. Likewise, $\vec{\alpha}^{\mathcal{P}}$, will be the configuration which is only occupied for edges of path $\mathcal{P}$.

Given a path $\mathcal{P}$, we construct string operators $S_{\mathcal{P}}^+$ creating vertex excitations at its endpoints and commuting with every other operators in Hamiltonian (10). Negative chirality strings are defined as $S_{\mathcal{P}}^- := S_{\mathcal{P}}^+ S_{\mathcal{P}'_{\rm dual}}^z$, where $S_{\mathcal{P}'_{\rm dual}}^z$ is a product of σ^z operators forming a path $\mathcal{P}'_{\rm dual}$ in the dual lattice which is contained in the support of $S_{\mathcal{P}}^+$. If $\mathcal{P}$ is open, $S_{\mathcal{P}'_{\rm dual}}^z$ creates excitations at plaquettes containing the vertices at the endpoints of $\mathcal{P}$ and opposite to the first and last edges of $\mathcal{P}$ (p_1 and p_9 in figure 4), while if $\mathcal{P}$ is closed, $S_{\mathcal{P}'_{\rm dual}}^z$ forms a closed path in the same homological class as $\mathcal{P}$. Note that for a given path $\mathcal{P}$, various paths $\mathcal{P}'_{\rm dual}$ are possible, and each one gives rise to a different string operator $S_{\mathcal{P}}^-$.

3.1. An algorithm to generate string operators

In order to find these string operators, we consider the following ansatz:

$$S_{\mathcal{P}}^+ := \prod_{i\in\mathcal{P}}\sigma_i^x \sum_{\vec{i}\in{\rm Conn}(\mathcal{P})} F_{\mathcal{P}}(\vec{i})|\vec{i}\rangle\langle\vec{i}|, \tag{18}$$

where $F_{\mathcal{P}}(\vec{i})$ is a phase factor acquired when $S_{\mathcal{P}}^+$ is applied on configuration $\vec{i}$. $F_{\mathcal{P}}(\vec{i})$ only depends on qubits belonging to ${\rm Conn}(\mathcal{P})$, defined as:

$${\rm Conn}(\mathcal{P}) := \{\text{links of } \mathcal{P} \text{ and its external legs}\}. \tag{19}$$

It is also useful to define the set of plaquettes

$$\mathcal{B}_{\mathcal{P}} := \{p\colon \partial p \cap {\rm Conn}(\mathcal{P}) \neq \varnothing\}, \tag{20}$$

which is the set of plaquettes that have at least one of their interior edges contained in ${\rm Conn}(\mathcal{P})$. Equivalently, one can define $\mathcal{B}_{\mathcal{P}}$ to be the set of plaquettes such that for at least one string configuration $\vec{i}$, $b_p(\vec{i}\,\oplus\,\vec{\alpha}^{\mathcal{P}}) \neq b_p(\vec{i})$. The structure of $S_{\mathcal{P}}^+$ is illustrated in figure 4. Note that depending on the context, a configuration $\vec{i}$ is

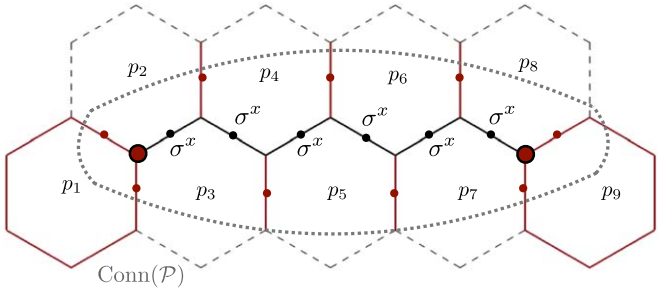

Figure 4. The structure of $S^+_{\mathcal{P}}$, where the path $\mathcal{P}$ is indicated by the full black edges where the σ^x operators are applied. The phase factors $F^+_{\mathcal{P}}$ depend on the configuration of all the edges identified with a dot, which are collectively denoted by Conn($\mathcal{P}$). The effect of $S^+_{\mathcal{P}}$ on the ground state of the system is to create a pair of vertex excitations at the vertices located at the endpoints of the path $\mathcal{P}$, which are identified by big red dots. Plaquettes p_1 to p_9 constitute the set $\mathcal{B}_{\mathcal{P}}$.

either understood to be on the full system, or is the configuration restricted to Conn($\mathcal{P}$). The specific case considered is explicitly stated in each case.

Ansatz (18) should satisfy the following properties.

(i) Anticommutes with vertex operators at the endpoints of $\mathcal{P}$ if it is open, while it commutes with every other vertex and plaquette operators.

(ii) Acts trivially on edges outside Conn($\mathcal{P}$).

Operators satisfying (i) and (ii) are called *string operators*. Additionally, we may be interested in the properties:

Squares to the identity.

Hermitian.

If these are satisfied, they will be called *canonical* string operators.

Properties (iii) and (iv) are satisfied (see lemmas 5 and 6 in appendix B) if

$$F_{\mathcal{P}}(\vec{i} \oplus \vec{\alpha}^{\mathcal{P}}) = [F_{\mathcal{P}}(\vec{i})]^*. \tag{21}$$

Since we want $S^+_{\mathcal{P}}$ to commute with all plaquettes in $\mathcal{B}_{\mathcal{P}}$ (for the rest of plaquettes, it commutes by construction), we impose that the commutator vanishes, $[S^+_{\mathcal{P}}, B_p] = 0$, which yields the equation

$$F_{\mathcal{P}}(\vec{i} \oplus \vec{\alpha}^{p}) = \frac{b_p(\vec{i} \oplus \vec{\alpha}^{\mathcal{P}})}{b_p(\vec{i})} F_{\mathcal{P}}(\vec{i}). \tag{22}$$

It is useful to define the function $\theta_{\mathcal{P}}(\vec{i}, p) \coloneqq b_p(\vec{i} \oplus \vec{\alpha}^{\mathcal{P}})/b_p(\vec{i})$, which relates $F_{\mathcal{P}}(\vec{i} \oplus \vec{\alpha}^{p})$ to $F_{\mathcal{P}}(\vec{i})$. We can generalize equation (22) and function $\theta_{\mathcal{P}}(\vec{i}, p)$ for an arbitrary number of plaquettes, namely

$$F_{\mathcal{P}}(\vec{i} \oplus \vec{\alpha}^{p_1} \oplus \ldots \oplus \vec{\alpha}^{p_m}) = \theta_{\mathcal{P}}(\vec{i}, p_1, \ldots, p_m) F_{\mathcal{P}}(\vec{i}), \tag{23}$$

where $\theta_{\mathcal{P}}(\vec{i}, p_1, \ldots, p_m)$ can be expressed as

$$\theta_{\mathcal{P}}(\vec{i}, p_1, \ldots, p_m) = \prod_{i=1}^{m} \frac{b_{p_i}\left(\vec{i} \oplus \vec{\alpha}^{\mathcal{P}} \bigoplus_{j=1}^{i-1} \vec{\alpha}^{p_j}\right)}{b_{p_i}\left(\vec{i} \bigoplus_{j=1}^{i-1} \vec{\alpha}^{p_j}\right)}. \tag{24}$$

Note that while we use the same symbol for the configurations $\vec{i}$ in $\theta_{\mathcal{P}}$ and in $F_{\mathcal{P}}$, the one in $\theta_{\mathcal{P}}$ is over the whole system in order for equation (24) to be well-defined. The specific way that the configuration $\vec{i}$ is extended over the whole system (i.e. which configuration on the rest of the system is appended to it) does not matter, since as a consequence of the structure of the plaquette operators, it does not affect the value of $\theta_{\mathcal{P}}$. As a consequence of the fact that plaquette operators commute, the order of the plaquettes $p_1, \ldots, p_m$ in $\theta_{\mathcal{P}}(\vec{i}, p_1, \ldots, p_m)$ does not matter (see lemma 1). The function $\theta_{\mathcal{P}}(\vec{i}, p_1, \ldots, p_m)$ relates the value of $F_{\mathcal{P}}$ for configuration $\vec{i}$ to that of configuration $\vec{i} \oplus \vec{\alpha}^{p_1} \oplus \ldots \oplus \vec{\alpha}^{p_m}$. These two configurations differ by a sum of plaquettes and may be considered part of the same configuration class $\mathcal{C}_{\mathcal{P}}(\vec{i})$, defined as

$$\mathcal{C}_{\mathcal{P}}(\vec{i}) \coloneqq \left\{ \vec{j} : \vec{j} = \vec{i} \bigoplus_{p \in \text{subset}(\mathcal{B}_{\mathcal{P}})} \vec{\alpha}^{p} \right\}, \tag{25}$$

where the configurations are restricted to Conn($\mathcal{P}$). These configurations can be regarded as the set of configurations related to $\vec{i}$ by adding loops associated with plaquettes in $\mathcal{B}_{\mathcal{P}}$, only in the region where $S^{+}_{\mathcal{P}}$ acts non-trivially. Taking all this into account, one can obtain an algorithm to compute the phases $F^{+}_{\mathcal{P}}$ of the ansatz in equation (18). This is given by algorithm 1.

Algorithm 1. Determination of the $F_{\mathcal{P}}$ functions for a path $\mathcal{P}$. $e^{i\phi(\vec{i})}$ are initial phases that can take any value.

for every configuration class $\mathcal{C}_{\mathcal{P}}$ **do**
  Pick a class representative $\vec{i} \in \mathcal{C}_{\mathcal{P}}$
  Set $F_{\mathcal{P}}(\vec{i}) = e^{i\phi(\vec{i})}$
  for every subset $(p_1, \ldots, p_m) \subseteq \mathcal{B}_{\mathcal{P}}$ **do**
    $F_{\mathcal{P}}(\vec{i} \bigoplus_{i=1}^{m} \vec{\alpha}^{p_i}) = \theta_{\mathcal{P}}(\vec{i}, p_1, \ldots, p_m) F_{\mathcal{P}}(\vec{i})$
  end for
end for

Algorithm 1 begins by picking up a configuration $\vec{i}$, which we call its class representative, and by setting its value to an arbitrary phase $e^{i\phi(\vec{i})}$. Any phase picked up by the algorithm yields a valid string operator. Once the value for the class representative $\vec{i}$ is fixed, the algorithm assigns values to the rest of the configurations in the same configuration class by making use of equation (23). Afterwards, a configuration, belonging to a different configuration class, where the values have not yet been fixed, is chosen and the same procedure is repeated until $F_{\mathcal{P}}$ has been fixed for all possible configurations. An explicit example of this can be seen in appendix A.

As it is shown in appendix B, it is always possible to determine $F_{\mathcal{P}}$ using algorithm 1 such that the resulting $S^{+}_{\mathcal{P}}$ is a string operator. Furthermore, it is also possible to enforce the constraint given in equation (21) such that we obtain canonical string operators. Those important results are summarized in the following theorem:

Theorem 1. *Let $\mathcal{P}$ be a path. Any function $F_{\mathcal{P}}$ defined by algorithm 1 is such that $S^{+}_{\mathcal{P}}$ is a string operator. Furthermore, it is possible to choose the phases $e^{i\phi}$ such that the string operator is canonical.*

Note that the open-string operators generated by algorithm 1, $S^{+}_{\mathcal{P}}$, have positive chirality, because they anticommute with vertex operators at the endpoints of $\mathcal{P}$ and commute with every other vertex and plaquette operators, satisfying property (i). However, the same does not apply to closed-string operators, since closed strings do not have endpoints. Algorithm 1 produces, in general, closed-string operators without a definite chirality.

3.1.1. Concatenation of open-string operators

It is very useful to build strings as a concatenation of smaller strings. This is specially relevant for constructing non-trivial closed strings, since, as it was mentioned before, algorithm 1 yields, in general, closed strings which have no definite chirality. By building these closed strings out of a multiplication of open strings, which have definite chirality, we obtain positive- and negative-chirality closed strings. Observe that given two paths, $\mathcal{P}_1$ and $\mathcal{P}_2$, meeting at one endpoint or forming a closed path, the multiplication of both $S^{+}_{\mathcal{P}_1 \# \mathcal{P}_2} = S^{+}_{\mathcal{P}_2} S^{+}_{\mathcal{P}_1}$ is a string operator satisfying properties (i) and (ii). In this way we can build long string operators by concatenating short ones.

3.2. Crossing string operators

In order to understand the algebra of the string operators of the semion code that we build in section 4.1, it is essential to know the commutation relations between them acting on different paths.

The notion of crossing paths need to be precisely defined since the region on which the string operators act non-trivially, Conn($\mathcal{P}$), has a finite thickness. Heuristically, in order to consider that two paths are crossing, the commun edges to both paths must not contain the first nor last vertex of neither of the paths. Note that two paths can cross more than once.

We further need to define the notions of *self-crossing* and *self-overlapping* paths. Essentially, a path is self-crossing if an observer moving on the path passes more than once on any given edge. A path is said to be *self-overlapping* if some regions of the support of the string operator but not the path itself overlap and connect some distant parts of the paths. Figure 5 illustrates the previous concepts. We refer the reader to appendix C for rigorous definitions, as well as the proof of theorem 2. This theorem summarizes the commutation relations among the string operators.

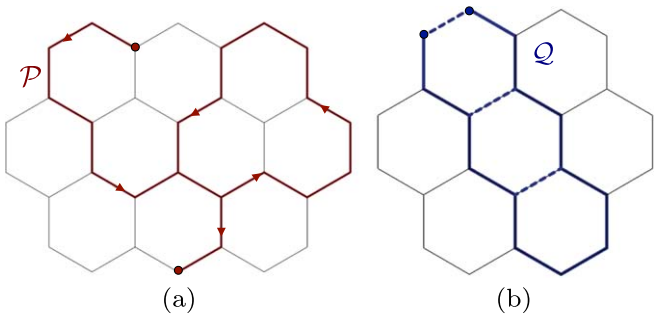

Figure 5. Examples of (a) a self-crossing path $\mathcal{P}$ and of (b) a self-overlapping path $\mathcal{Q}$. The dashed blue edges indicate the links where the string $\mathcal{Q}$ self-overlaps, since some distant parts of the path are connected.

Theorem 2. *Let $\mathcal{P}$ and $\mathcal{Q}$ be two paths crossing n times, composed of non self-overlapping nor self-crossing individual open paths, i.e. $\mathcal{P} = \mathcal{P}_1\#...\#\mathcal{P}_m$ and $\mathcal{Q} = \mathcal{Q}_1\#...\#\mathcal{Q}_{m'}$ for some integers m and m′. We have that*

$$[S^+_{\mathcal{P}}, S^+_{\mathcal{Q}}] = 0 \text{ if} n \text{ is even},$$
$$\{S^+_{\mathcal{P}}, S^+_{\mathcal{Q}}\} = 0 \text{ if} n \text{ is odd}. \tag{26}$$

Given the definition of negative chirality string operators, and using the above results, we find that $[S^-_{\mathcal{P}}, S^-_{\mathcal{Q}}] = 0$ if n is even, while $\{S^-_{\mathcal{P}}, S^-_{\mathcal{Q}}\} = 0$ if n is odd. We also find $[S^\pm_{\mathcal{P}}, S^\mp_{\mathcal{Q}}] = 0$ for any n.

Interpreting a vertex (in the case of $S^+_{\mathcal{P}}$) or the combination of a vertex and plaquette excitations (in the case of $S^-_{\mathcal{P}}$) as the presence of a quasiparticle labeled by s^+ and s^- respectively, the topological S matrix [35], written in the basis $(1, s^+, s^-, s^+s^-)$ where 1 denotes the vacuum, i.e. the absence of excitation, and s^+s^- the composite object excitation, is found to be

$$S = \frac{1}{2}\begin{pmatrix} 1 & 1 & 1 & 1 \\ 1 & -1 & 1 & -1 \\ 1 & 1 & -1 & -1 \\ 1 & -1 & -1 & 1 \end{pmatrix}. \tag{27}$$

We can thus interpret the string operators $S^+_{\mathcal{P}}$ and $S^-_{\mathcal{P}}$ as creating pairs of semions of different chirality at their endpoints.

3.2.1. The need for path concatenation

Notice that theorem 2 does not state anything about closed paths (homologically trivial or not) which are composed of a single path. One can check that when such a path crosses another one, in general they do not commute nor anti-commute. Such paths thus cannot be considered as 'fundamental' string operators in the sense that they do not possess a definite chirality.

Algorithm 1 enforces that the $\sum_{\vec{i}} F_{\mathcal{P}}(\vec{i})|\vec{i}\rangle\langle\vec{i}|$ operator does not contain any open $S^z_{\mathcal{P}'_{\text{dual}}}$ operator for an open path, since by construction, Algortihm 1 builds a string operator which commutes with every plaquette operator. For a closed path however, one can add $S^z_{\mathcal{P}'_{\text{dual}}}$ to $\sum_{\vec{i}} F_{\mathcal{P}}(\vec{i})|\vec{i}\rangle\langle\vec{i}| \rightarrow (\sum_{\vec{i}} F_{\mathcal{P}}(\vec{i})|\vec{i}\rangle\langle\vec{i}|)S^z_{\mathcal{P}'_{\text{dual}}}$, which is also a valid output of algorithm 1. In fact, such a $S^z_{\mathcal{P}'_{\text{dual}}}$ operator can be added selectively to only a subset of configuration classes, causing a 'mixing' of the chiralities. This is explained in detail in appendix C.3.

By producing closed paths starting from smaller open paths as their basic constituents, one can enforce the production of strings of a definite chirality. This is caused by the fact that the individual components cannot carry flux excitations by construction, and so neither can their concatenation. The physical intuition is that each small open string operator creates a pair of semions of positive chirality at their endpoints. Since the created semions are their own anti-particles, they subsequently all fuse to the vacuum, returning the system to the ground space.

3.3. Completeness of the string operators

In this section, we seek to decompose a string of σ^x operators into the strings operators defined in our model, S^+ and S^z.

We first note that any matrix ρ of size $2^n \times 2^n$ can be written as a linear combination of Pauli operators, i.e.

$$\rho = \sum_{P_x, P_z} c(P_x, P_z) P_x P_z, \tag{28}$$

where P_x (P_z) are Pauli operators acting on n qubits and formed of products of identities and σ^x (σ^z) operators only and where c (P_x, P_z) are non-zero complex numbers. Given the matrix ρ, one can recover the coefficients $c(P_x, P_z)$ using the formula

$$c(P_x, P_z) = \frac{1}{2^n}\mathrm{Tr}(P_x P_z \rho). \tag{29}$$

In our case, a chain of σ^x operators on path $\mathcal{P}$, denoted by $X_\mathcal{P}$, can be written as

$$X_\mathcal{P} = S_\mathcal{P}^+ \times \sum_{\vec{i}} [F_\mathcal{P}(\vec{i})]^* |\vec{i}\rangle\langle\vec{i}|. \tag{30}$$

Given the form of $\sum_{\vec{i}} [F_\mathcal{P}(\vec{i})]^* |\vec{i}\rangle\langle\vec{i}|$, we can write

$$X_\mathcal{P} = S_\mathcal{P}^+ \times \sum_{P_z \in \mathrm{Conn}(\mathcal{P})} c(P_z) P_z, \tag{31}$$

where P_z are Pauli operators containing only identities and σ^z and where we write $P_z \in \mathrm{Conn}(\mathcal{P})$ in an abuse of notation to signify that P_z acts non-trivially only on the qubits in $\mathrm{Conn}(\mathcal{P})$. The coefficients $c(P_z)$ are given by

$$c(P_z) = \frac{1}{2^{|\mathrm{Conn}(\mathcal{P})|}} \sum_{\vec{i}} \langle\vec{i}|P_z|\vec{i}\rangle [F_\mathcal{P}(\vec{i})]^*, \tag{32}$$

where $|\mathrm{Conn}(\mathcal{P})|$ is the number of edges in $\mathrm{Conn}(\mathcal{P})$. Chains of σ^z operators form valid string operators S^z, which create flux excitations at their endpoints. This clearly shows that any Pauli operator acting on the system can be written in terms of string operators. Since any operator acting on the system can be decomposed as a linear combination of Pauli operators, we find that the string operators are complete in the sense that any operator can be expressed in terms of them.

4. The semion code

The tools we have developed in previous sections can be used to build a quantum error correction code using as code space the ground space of the off-shell DS model, given by Hamiltonian (4). The information encoded is topologically protected since we are using global degrees of freedom that cannot be affected by local errors. Additionally, we perform quantum error correction using the DS model as a stabilizer code, where plaquette and vertex operators are our stabilizers.

4.1. Logical operators

Recalling that a surface of genus g can be seen as the connected sum of g tori [37], we can define two pairs of anti-commutating logical operators for every torus in the connected sum [38]. One pair consists of string operators S_V^+ and S_H^+, with $V(H)$ any homologically non-trivial path along the vertical (horizontal) direction,while the other pair consists of S_V^- and S_H^-, Both pairs are made up of open non self-crossing nor self-overlapping individual paths, as prescribed by theorem 2. Figure 6 illustrates two such pairs for a genus 1 torus.

4.2. Quantum error correction

The stabilizer operators, vertices and plaquette defined in equations (1) and (11), can be periodically measured to detect any errors occurring in the system. Once the syndrome pattern is obtained, assuming a given noise model, it is fed into a decoder. It outputs a recovery operation using the string operators developed in this work in order to bring the system back to the encoded subspace, where the probability of applying a non-trivial logical operation is minimized. While we leave the development of decoders specifically designed for the semion code for future work, one could imagine adapting some of the various existing decoders developed for topological codes [2, 39–61].

Table 1 shows the probabilities of measuring a given flux configurations after applying a single σ^x on the ground state for the three possible edge orientations shown in figure 7. Note that as equations (30) and (31) suggest, the probabilities in table 1 do not depend of the phases used to initialize the $F_{\{e\}}$ function in algorithm 1. More details giving a deeper understanding on the structure of the string operators $S_\mathcal{P}^+$ can be found in appendix B.3.

A distinctive feature of the probability distributions in table 1 is that there is a directionality in the error pattern. A σ^x error affecting a vertical edge (orientation (b)) is much more likely to leave flux excitations behind than for the other two orientations. This is clearly due to the specific structure of the plaquette operators, and could be used advantageously when dealing with asymmetric noise [62, 63]. Another major difference with the toric code is the fact that chains of σ^x errors are likely to leave flux excitations along their path. This additional information could be used by the decoder and may lead to a higher threshold value.

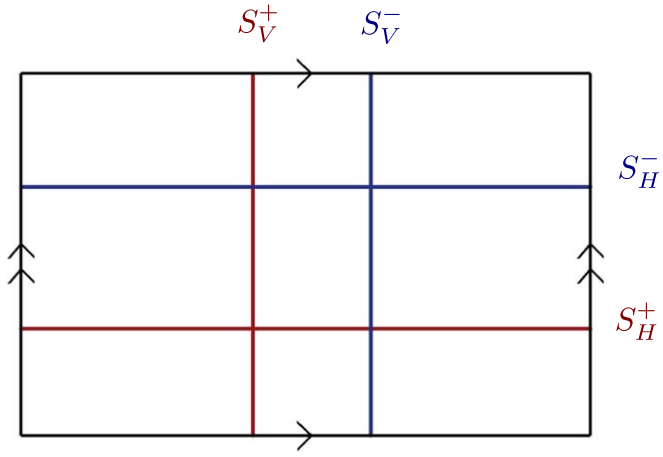

Figure 6. A cartoon example of 2 sets of logical operators on a 1-torus. $\{S_V^+, S_H^+\} = \{S_V^-, S_H^-\} = 0$, while $[S_V^+, S_H^-] = [S_V^-, S_H^+] = 0$. Arrows indicate identified boundaries.

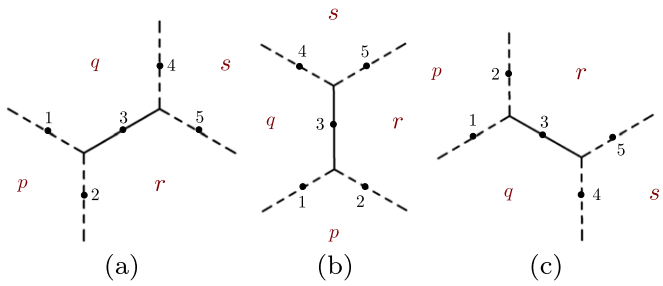

Figure 7. The three possible edge orientations on which the σ^x operator can be applied. Qubit 3 is affected in all cases, and may leave flux excitations on the four surrounding plaquettes labeled by p, q, r and s. The probabilities of measuring a given flux pattern are given in table 1.

Table 1. The various probabilities of getting a given flux excitation configuration after the application of the operator σ^x on a qubit, for the three possible orientations. The plaquettes label correspond to the ones in figure 7.

	Probability		
(b_p, b_q, b_r, b_s)	Orientation (a)	Orientation (b)	Orientation (c)
(0, 0, 0, 0)	9/16	1/16	9/16
(1, 1, 0, 0)	1/16	1/16	1/16
(1, 0, 1, 0)	1/16	1/16	1/16
(0, 1, 1, 0)	1/16	9/16	1/16
(1, 0, 0, 1)	1/16	1/16	1/16
(0, 1, 0, 1)	1/16	1/16	1/16
(0, 0, 1, 1)	1/16	1/16	1/16
(1, 1, 1, 1)	1/16	1/16	1/16

5. Conclusions and outlook

One of the key features of the off-shell DS model developed here for error correction is that it is a non-CSS code [64, 65]. This is not novel in the theory of quantum error correcting codes. In fact, the answer to the important question of what is the minimal complete error correction code that is able to encode one logical qubit and correct for an arbitrary error was precisely a non-CSS code of five qubits [64, 65]. This is consistent with the quantum Hamming bound [32], and is in sharp contrast with the classical case where the solution is the repetition code of three bits. However, what is peculiar of the off-shell DS code is that, to our knowledge, this is

the first non-CSS topological quantum memory that being a stabilizer code, it is also a topological code throughout the whole Hilbert space. In a sense, this was a missing link in the theory of topological quantum error correction codes and we have filled this gap with the tools introduced in our work.

We notice that a previous study [33] attempted to construct a quantum error correction code using the DS model as the starting point. The main difference with our work is that they construct a non-commuting quantum correcting code, whereas we have succeeded in constructing an extension that belongs to the stabilizer formalism. As a consequence of this, the whole error correction procedure of the off-shell DS code is topological. On the contrary, the topological nature of the non-commuting code in [33] is unproven. Both constructions share the feature of using non-Pauli operators to construct the basic string operators of the model.

The outcome of our work is a complete characterization of the error correction procedure for a quantum memory based on a topological non-CSS stabilizer code. This is a major step for the reason explained above. However, a fully-fledged quantum computer will demand more, namely, a universal gate set and a fault-tolerant procedure to battle errors dynamically [66]. With the tools deployed here, it is conceivable that this goal will be achieved elsewhere.

A new way of constructing quantum codes opens up with this work. The tools introduced here for models like the DS based on Abelian lattice gauge theories can be generalized to other Levin–Wen models [16, 67, 68], like doubled Fibonacci models, or twisted versions of fracton models [69]. This is the subject of further study.

Acknowledgments

We thank Fiona Burnell and Juan Miguel Nieto for helpful discussions. We acknowledge financial support from the Spanish MINECO grants FIS2012-33152, FIS2015-67411, and the CAM research consortium QUITEMAD +, Grant No. S2013/ICE-2801. The research of MAM-D has been supported in part by the US Army Research Office through Grant No. W911N F-14-1-0103. SV thanks FPU MECD Grant.

Appendix A. Example of an open-string operator

It is instructive to illustrate the workings of algorithm 1 to find string operators $S^+_{\mathcal{P}}$ in order to gain a more intuitive understanding. Consider the very simple path $\mathcal{P} = \{e\}$, consisting only of edge e shown in figure A1. Any given configuration on the five edges included in Conn($\{e\}$) is represented by a bit string of length 5, for which a 0 indicates the absence of a string, while a 1 indicates that it is occupied. One can also interpret the bit string as a state in the computational basis, a 0 indicating a $+1$ eigenstate of the corresponding σ^z, while a 1 indicates a -1 eigenstate of σ^z. We compute the function $F^+_{\{e\}}$ so that $S^+_{\{e\}}$ is a canonical string operator, i.e. it also fulfills equation (21). Following algorithm 1, the configuration (0, 0, 0, 0, 0) is first chosen and we set $F^+_{\{e\}}(0,\ 0,\ 0,\ 0,\ 0) = 1$. Noting that $\mathcal{B}_{\{e\}}$ contains the 4 plaquettes identified as p, q, r and s in figure A1, we find the following values for $F^+_{\{e\}}$:

$$
\begin{aligned}
&F_{\{e\}}(0,\ 0,\ 0,\ 0,\ 0) = 1, \quad F_{\{e\}}(1,\ 1,\ 0,\ 0,\ 0) = -i,\\
&F_{\{e\}}(1,\ 0,\ 1,\ 1,\ 0) = -i, \quad F_{\{e\}}(0,\ 0,\ 0,\ 1,\ 1) = -i,\\
&F_{\{e\}}(0,\ 0,\ 1,\ 0,\ 0) = 1, \quad F_{\{e\}}(1,\ 1,\ 1,\ 0,\ 0) = i,\\
&F_{\{e\}}(1,\ 0,\ 0,\ 1,\ 0) = i, \quad F_{\{e\}}(0,\ 0,\ 1,\ 1,\ 1) = i,\\
&F_{\{e\}}(0,\ 1,\ 1,\ 0,\ 1) = -i, \quad F_{\{e\}}(1,\ 1,\ 1,\ 1,\ 1) = -1,\\
&F_{\{e\}}(0,\ 1,\ 1,\ 1,\ 0) = -i, \quad F_{\{e\}}(1,\ 0,\ 0,\ 0,\ 1) = i,\\
&F_{\{e\}}(0,\ 1,\ 0,\ 0,\ 1) = i, \quad F_{\{e\}}(1,\ 1,\ 0,\ 1,\ 1) = -1,\\
&F_{\{e\}}(0,\ 1,\ 0,\ 1,\ 0) = i, \quad F_{\{e\}}(1,\ 0,\ 1,\ 0,\ 1) = -i.
\end{aligned}
$$

Here we are not only computing the values for configuration class $\mathcal{C}_{\{e\}}(\vec{0})$, but also for configuration class $\mathcal{C}_{\{e\}}(\vec{\alpha}^{\{e\}})$, since these two are related by equation (21)and therefore algorithm 1 makes the assignment $F_{\{e\}}(i_1,\ i_2,\ i_3 \oplus 1,\ i_4,\ i_5) = [F_{\{e\}}(i_1,\ i_2,\ i_3,\ i_4,\ i_5)]^*$.

Choosing next the configuration (0, 0, 0, 0, 1) and setting $F_{\{e\}}(0,\ 0,\ 0,\ 0,\ 1) = 1$, we can fix the following values of $F_{\{e\}}$:

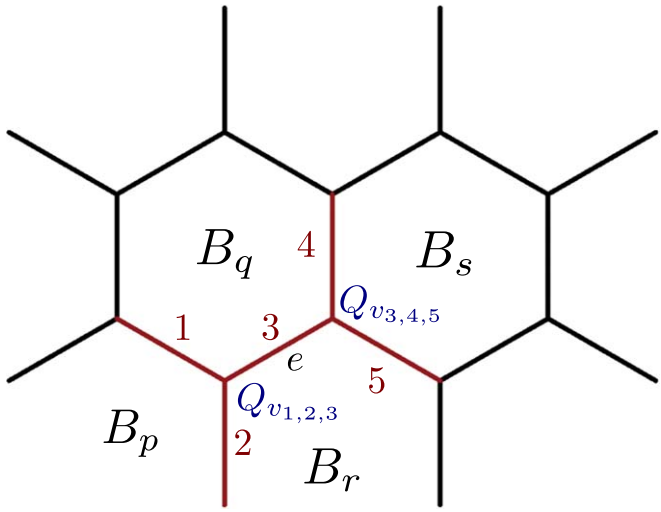

Figure A1. The layout we consider to find a possible string operator S_e^+ creating a pair of vertex excitations at $v_{1,2,3}$ and $v_{3,4,5}$. The red edges correspond to the qubits in Conn(e), the ones on which S_e^+ acts non-trivially, with edge e corresponding to qubit 3. S_e^+ anti commutes with both vertex operators $Q_{v_{1,2,3}} = \sigma_1^z\sigma_2^z\sigma_3^z$ and $Q_{v_{3,4,5}} = \sigma_3^z\sigma_4^z\sigma_5^z$, while commuting with every other vertex operators as well as every generalized plaquette operators.

$$
\begin{aligned}
&F_{\{e\}}(0,0,0,0,1) = 1, \quad F_{\{e\}}(0,0,0,1,0) = 1,\\
&F_{\{e\}}(1,1,0,0,1) = -i, \quad F_{\{e\}}(1,1,0,1,0) = -i,\\
&F_{\{e\}}(0,0,1,0,1) = 1, \quad F_{\{e\}}(0,0,1,1,0) = 1,\\
&F_{\{e\}}(1,1,1,0,1) = i, \quad F_{\{e\}}(1,1,1,1,0) = i,\\
&F_{\{e\}}(1,0,1,1,1) = -1, \quad F_{\{e\}}(0,1,1,1,1) = -1,\\
&F_{\{e\}}(0,1,1,0,0) = i, \quad F_{\{e\}}(1,0,1,0,0) = i,\\
&F_{\{e\}}(1,0,0,1,1) = -1, \quad F_{\{e\}}(0,1,0,1,1) = -1,\\
&F_{\{e\}}(0,1,0,0,0) = -i, \quad F_{\{e\}}(1,0,0,0,0) = -i.
\end{aligned}
$$

Again, two class of configurations are fixed due to the fact that the string is canonical. We keep doing this till all configuration classes have been fixed. As a result, we obtain $S_{\{e\}}^+$, which commutes with the four neighboring plaquette operators B_p, B_q, B_r and B_s shown in figure A1, as well as all the other plaquette operators which are farther away.

Appendix B. Proofs regarding string operators produced by algorithm 1

In order to prove theorem 1, we begin by stating several technical results in the following section.

B.1. Useful technical lemmas

Lemma 1. *Let $\{p_1, p_2, \ldots, p_n\}$ an ordered set of plaquettes and let $\{q_1, q_2, \ldots, q_n\}$ be a permutation of it. For any configuration $\vec{i}$, we have that $\theta_{\mathcal{P}}(\vec{i}, p_1, p_2, \ldots, p_n) = \theta_{\mathcal{P}}(\vec{i}, q_1, q_2, \ldots, q_n)$.*

Proof. According to equation (24), we have that

$$
\begin{aligned}
\theta_{\mathcal{P}}(\vec{i}, p_1, \ldots, p_m) &= \frac{\left\langle \vec{i} \bigoplus_{i=1}^m \vec{\alpha}^{p_i} \oplus \vec{\alpha}^{\mathcal{P}} | B_{p_m} \ldots B_{p_1} | \vec{i} \oplus \vec{\alpha}^{\mathcal{P}} \right\rangle}{\left\langle \vec{i} \bigoplus_{i=1}^m \vec{\alpha}^{p_i} | B_{p_m} \ldots B_{p_1} | \vec{i} \right\rangle}\\
&= \frac{\left\langle \vec{i} \bigoplus_{i=1}^m \vec{\alpha}^{q_i} \oplus \vec{\alpha}^{\mathcal{P}} | B_{q(p_m)} \ldots B_{q(p_1)} | \vec{i} \oplus \vec{\alpha}^{\mathcal{P}} \right\rangle}{\left\langle \vec{i} \bigoplus_{i=1}^m \vec{\alpha}^{q_i} | B_{q(p_m)} \ldots B_{q(p_1)} | \vec{i} \right\rangle} = \theta_{\mathcal{P}}(q_1, \ldots, q_m),
\end{aligned} \tag{B1}
$$

where $q(p_i)$ denotes the permutation of plaquettes that exchange $\{p_1, \ldots, p_m\}$ to $\{q_1, \ldots, q_m\}$, and where we used the fact that the plaquette operators all commute. □

Lemma 2. *Let $\{p_1, p_2, \ldots, p_m\}$ and $\{q_1, q_2, \ldots, q_k\}$ be two different set of plaquettes in $\mathcal{B}_{\mathcal{P}}$ such that $\bigoplus_{i=1}^m \vec{\alpha}^{p_i} = \bigoplus_{i=1}^k \vec{\alpha}^{q_i}$ on the string configuration of* Conn($\mathcal{P}$). *Then, for any configuration $\vec{i}$, we find that*

$$\theta_{\mathcal{P}}(\vec{i}, p_1, p_2, \ldots, p_m) = \theta_{\mathcal{P}}(\vec{i}, q_1, q_2, \ldots, q_k). \tag{B2}$$

Proof. First notice that given the structure of the plaquette operators, $\bigoplus_{i=1}^{m} \vec{\alpha}^{p_i} = \bigoplus_{i=1}^{k} \vec{\alpha}^{q_i}$ on $\mathrm{Conn}(\mathcal{P})$ implies that $\prod_{i=1}^{m} B_{p_i} \prod_{j=1}^{k} B_{q_j} \prod_{l=1}^{s} B_{r_l} = 1$, where $\{r_1, \ldots, r_s\}$ are all the plaquettes outside of $\mathcal{B}_{\mathcal{P}}$. We also have that $\bigoplus_{i=1}^{m} \vec{\alpha}^{p_i} = (\bigoplus_{j=1}^{k} \vec{\alpha}^{q_j}) \oplus (\bigoplus_{l=1}^{s} \vec{\alpha}^{r_l})$, where the configurations are taken over the whole system. Using those facts, we find

$$\begin{aligned}
\theta_{\mathcal{P}}(\vec{i}, p_1, \ldots, p_m) &= \frac{\left\langle \vec{i} \bigoplus_{i=1}^{m} \vec{\alpha}^{p_i} \oplus \vec{\alpha}^{\mathcal{P}} | B_{p_m} \ldots B_{p_1} \prod_{i=1}^{m} B_{p_i} \prod_{j=1}^{k} B_{q_j} \prod_{l=1}^{s} B_{r_l} | \vec{i} \oplus \vec{\alpha}^{\mathcal{P}} \right\rangle}{\left\langle \vec{i} \bigoplus_{i=1}^{m} \vec{\alpha}^{p_i} | B_{p_m} \ldots B_{p_1} \prod_{i=1}^{m} B_{p_i} \prod_{j=1}^{k} B_{q_j} \prod_{l=1}^{s} B_{r_l} | \vec{i} \right\rangle} \\
&= \frac{\left\langle \vec{i} \bigoplus_{i=1}^{m} \vec{\alpha}^{p_i} \oplus \vec{\alpha}^{\mathcal{P}} | \prod_{j=1}^{k} B_{q_j} \prod_{l=1}^{s} B_{r_l} | \vec{i} \oplus \vec{\alpha}^{\mathcal{P}} \right\rangle}{\left\langle \vec{i} \bigoplus_{i=1}^{m} \vec{\alpha}^{p_i} | \prod_{j=1}^{k} B_{q_j} \prod_{l=1}^{s} B_{r_l} | \vec{i} \right\rangle} \\
&= \frac{\left\langle \vec{i} \bigoplus_{i=1}^{m} \vec{\alpha}^{p_i} \oplus \vec{\alpha}^{\mathcal{P}} | \prod_{l=1}^{s} B_{r_l} \left(\sum_{\vec{j}} |\vec{j}\rangle\langle\vec{j}| \right) \prod_{j=1}^{k} B_{q_j} | \vec{i} \oplus \vec{\alpha}^{\mathcal{P}} \right\rangle}{\left\langle \vec{i} \bigoplus_{i=1}^{m} \vec{\alpha}^{p_i} | \prod_{l=1}^{s} B_{r_l} \left(\sum_{\vec{j}} |\vec{j}\rangle\langle\vec{j}| \right) \prod_{j=1}^{k} B_{q_j} | \vec{i} \right\rangle} \\
&= \frac{\left\langle \vec{i} \bigoplus_{j=1}^{k} \vec{\alpha}^{q_j} \oplus (\bigoplus_{l=1}^{s} \vec{\alpha}^{r_l}) \oplus \vec{\alpha}^{\mathcal{P}} | \prod_{l=1}^{s} B_{r_l} | \vec{i} \bigoplus_{j=1}^{k} \vec{\alpha}^{q_j} \oplus \vec{\alpha}^{\mathcal{P}} \right\rangle}{\left\langle \vec{i} \bigoplus_{j=1}^{k} \vec{\alpha}^{q_j} \oplus (\bigoplus_{l=1}^{s} \vec{\alpha}^{r_l}) | \prod_{l=1}^{s} B_{r_l} | \vec{i} \bigoplus_{j=1}^{k} \vec{\alpha}^{q_j} \right\rangle} \\
&\quad \times \frac{\left\langle \vec{i} \bigoplus_{j=1}^{k} \vec{\alpha}^{q_j} \oplus \vec{\alpha}^{\mathcal{P}} | \prod_{j=1}^{k} B_{q_j} | \vec{i} \oplus \vec{\alpha}^{\mathcal{P}} \right\rangle}{\left\langle \vec{i} \bigoplus_{j=1}^{k} \vec{\alpha}^{q_j} | \prod_{j=1}^{k} B_{q_j} | \vec{i} \right\rangle} \\
&= \frac{\left\langle \vec{i} \bigoplus_{j=1}^{k} \vec{\alpha}^{q_j} \oplus (\bigoplus_{l=1}^{s} \vec{\alpha}^{r_l}) | X_{\mathcal{P}} \prod_{l=1}^{s} B_{r_l} X_{\mathcal{P}} | \vec{i} \bigoplus_{j=1}^{k} \vec{\alpha}^{q_j} \right\rangle}{\left\langle \vec{i} \bigoplus_{j=1}^{k} \vec{\alpha}^{q_j} \oplus (\bigoplus_{l=1}^{s} \vec{\alpha}^{r_l}) | \prod_{l=1}^{s} B_{r_l} | \vec{i} \bigoplus_{j=1}^{k} \vec{\alpha}^{q_j} \right\rangle} \theta_{\mathcal{P}}(\vec{i}, q_1, \ldots, q_k), \\
&= \theta_{\mathcal{P}}(\vec{i}, q_1, \ldots, q_k),
\end{aligned} \tag{B3}$$

where we used the fact that $X_{\mathcal{P}}$ commutes with the plaquette operators B_{r_l}, since the plaquettes in $\{r_1, \ldots, r_s\}$ are not in $\mathrm{Conn}(\mathcal{P})$. $X_{\mathcal{P}}$ is the string of σ_x corresponding to the string operator defined on $\mathcal{P}$. □

Lemma 3. *The functions $F_{\mathcal{P}}$ constructed by algorithm 1 are well-defined.*

Proof. First note that lemma 1 states that the order in which the plaquettes $\{p_1, \ldots, p_n\}$ appear in a specific subset of $\mathcal{B}_{\mathcal{P}}$ and the order into which the subsets are chosen do not affect its value.

Next, we show that if there are two different sets of plaquettes $\{p_1, \ldots, p_m\} \subset \mathcal{B}_{\mathcal{P}}$ and $\{q_1, \ldots, q_k\} \subset \mathcal{B}_{\mathcal{P}}$ such that $\vec{\alpha}^{p_1} \oplus \ldots \oplus \vec{\alpha}^{p_m} = \vec{\alpha}^{q_1} \oplus \ldots \oplus \vec{\alpha}^{q_k}$, where it is understood that the configurations are equal on $\mathrm{Conn}(\mathcal{P})$ (as opposed to the whole lattice), then algorithm 1 ensures that $F_{\mathcal{P}}(\vec{i} \oplus \vec{\alpha}^{p_1} \oplus \ldots \oplus \vec{\alpha}^{p_n}) = F_{\mathcal{P}}(\vec{i} \oplus \vec{\alpha}^{q_1} \oplus \ldots \oplus \vec{\alpha}^{q_m})$, for any configurations $\vec{i}$ (and for configuration $\vec{i} \oplus \vec{\alpha}^{\mathcal{P}}$ as well). This is a simple consequence of lemma B2, which tells us that $\theta_{\mathcal{P}}(\vec{i}, p_1, \ldots, p_m) = \theta_{\mathcal{P}}(\vec{i}, q_1, \ldots, q_k)$, and of the way that the $F_{\mathcal{P}}$ functions are built;

$$\begin{aligned}
F_{\mathcal{P}}(\vec{i} \oplus \vec{\alpha}^{p_1} \oplus \ldots \oplus \vec{\alpha}^{p_m}) &= \theta_{\mathcal{P}}(\vec{i}, p_1, \ldots, p_m) F_{\mathcal{P}}(\vec{i}) \\
&= \theta_{\mathcal{P}}(\vec{i}, q_1, \ldots, q_k) F_{\mathcal{P}}(\vec{i}) \\
&= F_{\mathcal{P}}(\vec{i} \oplus \vec{\alpha}^{q_1} \oplus \ldots \oplus \vec{\alpha}^{q_k}).
\end{aligned}$$

□

Lemma 4. *Let $F_{\mathcal{P}}$ be a function determined by algorithm 1. Then $F_{\mathcal{P}}$ simultaneously satisfies all the constraints (22).*

Proof. Consider an arbitrary configuration $\vec{i}$ for which the value of $F_{\mathcal{P}}(\vec{i})$ has been determined using algorithm 1. Two possible cases need to be analyzed:

1. If $\vec{i}$ is one of the configuration picked to set an unknown value of $F_{\mathcal{P}}(\vec{i})$, then we find that for any plaquette p,

$$F_{\mathcal{P}}(\vec{i} \oplus \vec{\alpha}^{p}) = \frac{b_p(\vec{i} \oplus \vec{\alpha}^{\mathcal{P}})}{b_p(\vec{i})} F_{\mathcal{P}}(\vec{i}), \tag{B4}$$

by definition of $\theta_{\mathcal{P}}$.

2. If $\vec{i}$ is not one of the configurations picked, then there is another configuration $\vec{i}\,'$ which was picked as a class representative and a set of plaquettes $\{p_1, \ldots, p_m\} \subset \mathcal{B}_{\mathcal{P}}$ such that $\vec{i} = \vec{i}\,' \oplus \vec{\alpha}^{p_1} \oplus \ldots \oplus \vec{\alpha}^{p_m}$. For any plaquette p, according to algorithm 1, we find that

$$\frac{F_{\mathcal{P}}(\vec{i} \oplus \vec{\alpha}^{p})}{F_{\mathcal{P}}(\vec{i})} = \frac{\theta_{\mathcal{P}}(\vec{i}\,', p_1, \ldots, p_m, p)}{\theta_{\mathcal{P}}(\vec{i}\,', p_1, \ldots, p_m)}. \tag{B5}$$

By using definition (24), we find

$$\frac{\theta_{\mathcal{P}}(\vec{i}\,', p_1, \ldots, p_m, p)}{\theta_{\mathcal{P}}(\vec{i}\,', p_1, \ldots, p_m)} = \frac{b_p(\vec{i}\,' \oplus \vec{\alpha}^{p_1} \oplus \ldots \oplus \vec{\alpha}^{p_m} \oplus \vec{\alpha}^{\mathcal{P}})}{b_p(\vec{i}\,' \oplus \vec{\alpha}^{p_1} \oplus \ldots \oplus \vec{\alpha}^{p_m})} = \frac{b_p(\vec{i} \oplus \vec{\alpha}^{\mathcal{P}})}{b_p(\vec{i})}.$$

We thus have that in both cases, all the constraints (22) are satisfied. □

Lemma 5. *(Canonical strings)* $F_{\mathcal{P}}(\vec{i} \oplus \vec{\alpha}^{\mathcal{P}}) = [F_{\mathcal{P}}(\vec{i})]^*$ *for any string configuration* $\vec{i}$ *if and only if* $[S_{\mathcal{P}}^{+}]^2 = 1$.

Proof. Explicit calculation of $[S_{\mathcal{P}}^{+}]^2$ gives

$$\begin{aligned}
[S_{\mathcal{P}}^{+}]^2 &= \left(\prod_{i \in \mathcal{P}} \sigma_i^x \sum_{\text{String conf.}\vec{i}} F_{\mathcal{P}}(\vec{i}) |\vec{i}\rangle \langle \vec{i}| \right) \\
&\quad \times \left(\prod_{i' \in \mathcal{P}} \sigma_{i'}^x \sum_{\text{String conf.}\vec{i}\,'} F_{\mathcal{P}}(\vec{i}\,') |\vec{i}\,'\rangle \langle \vec{i}\,'| \right) \\
&= \sum_{\text{String conf.}\vec{i}} F_{\mathcal{P}}(\vec{i}) |\vec{i} \oplus \vec{\alpha}^{\mathcal{P}}\rangle \langle \vec{i} \oplus \vec{\alpha}^{\mathcal{P}}| \\
&\quad \times \sum_{\text{String conf.}\vec{i}\,'} F_{\mathcal{P}}(\vec{i}\,') |\vec{i}\,'\rangle \langle \vec{i}\,'| \\
&= \sum_{\text{String conf.}\vec{i}} F_{\mathcal{P}}(\vec{i} \oplus \vec{\alpha}^{\mathcal{P}}) F_{\mathcal{P}}(\vec{i}) |\vec{i}\rangle \langle \vec{i}|.
\end{aligned}$$

Clearly, $F_{\mathcal{P}}(\vec{i} \oplus \vec{\alpha}^{\mathcal{P}}) = [F_{\mathcal{P}}(\vec{i})]^*$ implies that $[S_{\mathcal{P}}^{+}]^2 = 1$, since $F_{\mathcal{P}}(\vec{i})$ is a complex number lying on the unit circle. On the other hand, $[S_{\mathcal{P}}^{+}]^2 = 1$ implies that $F_{\mathcal{P}}(\vec{i}) F_{\mathcal{P}}(\vec{i} \oplus \vec{\alpha}^{\mathcal{P}}) = 1$, which means that $F_{\mathcal{P}}(\vec{i} \oplus \vec{\alpha}^{\mathcal{P}}) = [F_{\mathcal{P}}(\vec{i})]^*$, once again because $F_{\mathcal{P}}(\vec{i})$ is a complex number lying on the unit circle. □

Lemma 6. *(Canonical strings)* $[S_{\mathcal{P}}^{+}]^{\dagger} = S_{\mathcal{P}}^{+}$ *if and only if* $F_{\mathcal{P}}(\vec{i} \oplus \vec{\alpha}^{\mathcal{P}}) = [F_{\mathcal{P}}(\vec{i})]^*$ *for any configuration* $\vec{i}$.

Proof. Explicit calculation of $[S_{\mathcal{P}}^{+}]^{\dagger}$ gives

$$\begin{aligned}
[S_{\mathcal{P}}^{+}]^{\dagger} &= \sum_{\text{String conf.}\vec{i}} [F_{\mathcal{P}}(\vec{i})]^* |\vec{i}\rangle \langle \vec{i}| \prod_{i \in \mathcal{P}} \sigma_i^x \\
&= \sum_{\text{String conf.}\vec{i}} [F_{\mathcal{P}}(\vec{i})]^* \left(\prod_{j \in \mathcal{P}} \sigma_j^x \right)^2 |\vec{i}\rangle \langle \vec{i}| \prod_{i \in \mathcal{P}} \sigma_i^x \\
&= \prod_{i \in \mathcal{P}} \sigma_i^x \sum_{\text{String conf.}\vec{i}} [F_{\mathcal{P}}(\vec{i})]^* |\vec{i} \oplus \vec{\alpha}^{\mathcal{P}}\rangle \langle \vec{i} \oplus \vec{\alpha}^{\mathcal{P}}|,
\end{aligned}$$

Suppose that $[S_{\mathcal{P}}^{+}]^{\dagger} = S_{\mathcal{P}}^{+}$. In that case, it is clear that $[F_{\mathcal{P}}(\vec{i})]^* = F_{\mathcal{P}}(\vec{i} \oplus \vec{\alpha}^{\mathcal{P}})$.

It is also clear that $[F_{\mathcal{P}}(\vec{i})]^* = F_{\mathcal{P}}(\vec{i} \oplus \vec{\alpha}^{\mathcal{P}})$ implies that $[S_{\mathcal{P}}^{+}]^{\dagger} = S_{\mathcal{P}}^{+}$. □

Lemma 7. *(Canonical strings) Suppose that for any set of plaquettes* $\{p_1, p_2, \ldots, p_m\} \subset \mathcal{B}_{\mathcal{P}}$ *and for a string configuration* $\vec{i}$, *we have that* $F_{\mathcal{P}}(\vec{i} \oplus \vec{\alpha}^{p_1} \oplus \ldots \oplus \vec{\alpha}^{p_m}) = \theta_{\mathcal{P}}(\vec{i}, p_1, \ldots, p_m) F_{\mathcal{P}}(\vec{i})$ *and* $F_{\mathcal{P}}(\vec{i} \oplus \vec{\alpha}^{\mathcal{P}} \oplus \vec{\alpha}^{p_1} \oplus \ldots \oplus \vec{\alpha}^{p_m}) = \theta_{\mathcal{P}}(\vec{i} \oplus \vec{\alpha}^{\mathcal{P}}, p_1, \ldots, p_m) F_{\mathcal{P}}(\vec{i} \oplus \vec{\alpha}^{\mathcal{P}})$. *If* $F_{\mathcal{P}}(\vec{i} \oplus \vec{\alpha}^{\mathcal{P}}) = [F_{\mathcal{P}}(\vec{i})]^*$, *then for any set of plaquettes* $\{q_1, \ldots, q_k\} \subset \mathcal{B}_{\mathcal{P}}$, *we have that* $F_{\mathcal{P}}(\vec{i} \oplus \vec{\alpha}^{\mathcal{P}} \oplus \vec{\alpha}^{q_1} \oplus \ldots \oplus \vec{\alpha}^{q_k}) = [F_{\mathcal{P}}(\vec{i} \oplus \vec{\alpha}^{q_1} \oplus \ldots \oplus \vec{\alpha}^{q_k})]^*$.

Proof. By hypothesis, we have that

$$F_{\mathcal{P}}(\vec{i} \oplus \vec{\alpha}^{q_1}) = \theta_{\mathcal{P}}(\vec{i}, q_1) F_{\mathcal{P}}(\vec{i}), \tag{B6}$$

as well as

$$F_{\mathcal{P}}(\vec{i} \oplus \vec{\alpha}^{\mathcal{P}} \oplus \vec{\alpha}^{q_1}) = [\theta_{\mathcal{P}}(\vec{i}, q_1)]^{-1} F_{\mathcal{P}}(\vec{i} \oplus \vec{\alpha}^{\mathcal{P}}), \tag{B7}$$

where we took advantage of the fact that $\theta_{\mathcal{P}}(\vec{i} \oplus \vec{\alpha}^{\mathcal{P}}, q_1) = [\theta_{\mathcal{P}}(\vec{i}, q_1)]^{-1}$, as is clear from equation (21).

Using the fact that $F_{\mathcal{P}}(\vec{i} \oplus \vec{\alpha}^{\mathcal{P}}) = [F_{\mathcal{P}}(\vec{i})]^*$ in equation (B6), we find

$$\begin{aligned}[F_{\mathcal{P}}(\vec{i} \oplus \vec{\alpha}^{\mathcal{P}})]^* &= [\theta_{\mathcal{P}}(\vec{i}, q_1)]^{-1} F_{\mathcal{P}}(\vec{i} \oplus \vec{\alpha}^{q_1}) \\ &= \frac{F_{\mathcal{P}}(\vec{i} \oplus \vec{\alpha}^{\mathcal{P}} \oplus \vec{\alpha}^{q_1})}{F_{\mathcal{P}}(\vec{i} \oplus \vec{\alpha}^{\mathcal{P}})} F_{\mathcal{P}}(\vec{i} \oplus \vec{\alpha}^{q_1}).\end{aligned} \tag{B8}$$

Since $F_{\mathcal{P}}$ lies on the unit circle, we find that

$$F_{\mathcal{P}}(\vec{i} \oplus \vec{\alpha}^{\mathcal{P}} \oplus \vec{\alpha}^{q_1}) F_{\mathcal{P}}(\vec{i} \oplus \vec{\alpha}^{q_1}) = 1, \tag{B9}$$

which in turn implies that

$$F_{\mathcal{P}}(\vec{i} \oplus \vec{\alpha}^{\mathcal{P}} \oplus \vec{\alpha}^{q_1}) = [F_{\mathcal{P}}(\vec{i} \oplus \vec{\alpha}^{q_1})]^*. \tag{B10}$$

The same reasoning can be recursively employed to show that

$$F_{\mathcal{P}}(\vec{i} \oplus \vec{\alpha}^{\mathcal{P}} \oplus \vec{\alpha}^{q_1} \oplus \ldots \oplus \vec{\alpha}^{q_k}) = [F_{\mathcal{P}}(\vec{i} \oplus \vec{\alpha}^{q_1} \oplus \ldots \oplus \vec{\alpha}^{q_k})]^*. \tag{B11}$$

□

Lemma 8. *(Canonical strings) Let $F_{\mathcal{P}}$ be a function determined by algorithm 1. If the phases $e^{i\phi}$ are assigned to the class representatives $\vec{i}$ in such a way that $F_{\mathcal{P}}(\vec{i}) = [F_{\mathcal{P}}(\vec{i} \oplus \vec{\alpha}^{\mathcal{P}})]^*$, then $F_{\mathcal{P}}$ simultaneously satisfies all the constraints in equation (21).*

Proof. As it was done before, two possible cases are considered.

1. If $\vec{i}$ is one of the configuration picked as a class representative to set the value of $F_{\mathcal{P}}(\vec{i})$, then we trivially have that $F_{\mathcal{P}}(\vec{i} \oplus \vec{\alpha}^{\mathcal{P}}) = [F_{\mathcal{P}}(\vec{i})]^*$.
2. If $\vec{i}$ is not one of the configurations picked, then once again we find that $\vec{i} = \vec{i}\,' \oplus \vec{\alpha}^{p_1} \oplus \ldots \oplus \vec{\alpha}^{p_m}$, as mentioned above. We find

$$F_{\mathcal{P}}(\vec{i} \oplus \vec{\alpha}^{\mathcal{P}}) = F_{\mathcal{P}}(\vec{i}\,' \oplus \vec{\alpha}^{\mathcal{P}} \oplus \vec{\alpha}^{p_1} \oplus \ldots \oplus \vec{\alpha}^{p_m}). \tag{B12}$$

Using algorithm 1, we find that

$$\begin{aligned}F_{\mathcal{P}}(\vec{i}\,' \bigoplus_{j=1}^{m} \vec{\alpha}^{p_j}) &= \theta_{\mathcal{P}}(\vec{i}\,', p_1, \ldots, p_m) F^{\pm}_{\mathcal{P}}(\vec{i}\,'), \\ F_{\mathcal{P}}(\vec{i}\,' \oplus \vec{\alpha}^{\mathcal{P}} \bigoplus_{j=1}^{m} \vec{\alpha}^{p_j}) &= \theta_{\mathcal{P}}(\vec{i}\,' \oplus \vec{\alpha}^{\mathcal{P}}, p_1, \ldots, p_m) F^{\pm}_{\mathcal{P}}(\vec{i}\,' \oplus \vec{\alpha}^{\mathcal{P}}).\end{aligned}$$

Since all the conditions of lemma 7 are satisfied, we have that

$$F_{\mathcal{P}}(\vec{i}\,' \oplus \vec{\alpha}^{\mathcal{P}} \oplus \vec{\alpha}^{p_1} \oplus \ldots \oplus \vec{\alpha}^{p_m}) = [F_{\mathcal{P}}(\vec{i}\,' \oplus \vec{\alpha}^{p_1} \oplus \ldots \oplus \vec{\alpha}^{p_m})]^* = [F_{\mathcal{P}}(\vec{i})]^*. \tag{B13}$$

□

B.2. Proof of theorem 1

Given all the previous technical results, it is straightforward to give the proof of theorem 1, which we restate here for ease of reading:

Theorem 1. *Let $\mathcal{P}$ be a path. Any function $F_{\mathcal{P}}$ defined by algorithm 1 is such that $S^{\pm}_{\mathcal{P}}$ is a string operator. Furthermore, it is possible to choose the phases $e^{i\phi(i)}$ such that the string operator is canonical.*

Proof. First note that according to lemma 3, $F_{\mathcal{P}}$ is well-defined. By construction, $F_{\mathcal{P}}$ has non-trivial support only in Conn($\mathcal{P}$),thus any operator $S_{\mathcal{P}}^{\pm}$ built from it satisfies condition (ii). Furthermore,lemma 4 states that $S_{\mathcal{P}}^{+}$ satisfies conditions (22). We thus have that condition (i) is satisfied as well,proving that $S_{\mathcal{P}}^{\pm}$ is a string operator.

In order to show that it is always possible to choose the phases $e^{i\phi(\vec{i})}$'s so that $S_{\mathcal{P}}^{\pm}$ is canonical,we must consider two cases,depending on whether $\mathcal{P}$ is open or close.

Suppose first that the path $\mathcal{P}$ is open. In that case,we have that configurations $\vec{i}$ and $\vec{i} \oplus \vec{\alpha}^{\mathcal{P}}$ are in two distinct configuration classes. Given the class representative $\vec{i}$ for which we set $F_{\mathcal{P}}(\vec{i}) = e^{i\phi}$,we simply pick class representative $\vec{i} \oplus \vec{\alpha}^{\mathcal{P}}$ as representative for its corresponding class, and set $F_{\mathcal{P}}(\vec{i} \oplus \vec{\alpha}^{\mathcal{P}}) = e^{-i\phi}$.

If $\mathcal{P}$ is close, then we find that $\vec{i}$ and $\vec{i} \oplus \vec{\alpha}^{\mathcal{P}}$ belong to the same class of configurations, since there exists a set of plaquettes $\{p_1, \ldots, p_m\} \subseteq \mathcal{B}_{\mathcal{P}}$ such that on Conn($\mathcal{P}$), $\vec{i} \oplus \vec{\alpha}^{\mathcal{P}} = \vec{i} \oplus \vec{\alpha}^{p_1} \oplus \ldots \oplus \vec{\alpha}^{p_m}$. Setting $F_{\mathcal{P}}(\vec{i}) = [\theta_{\mathcal{P}}(\vec{i}, p_1, \ldots, p_m)]^{-\frac{1}{2}}$, we find that $F_{\mathcal{P}}(\vec{i} \oplus \vec{\alpha}^{\mathcal{P}}) = [F_{\mathcal{P}}]^*$.

In both cases, we can use lemma 8 to find that all constraints of equation (21) are fulfilled and therefore, conditions (iii) and (iv) are also satisfied. □

B.3. Consistency of the probability of measuring an excitation configuration

The decomposition of $X_{\mathcal{P}}$ in terms of string operators given by equation (31) is not unique given that in algorithm 1, we are free to choose different initial phases for the various class representatives. However, we show here that the probabilities associated with finding a given excitation pattern after the application $X_{\mathcal{P}}$ are insensitive to those initial phases. For simplicity, we assume that $\mathcal{P}$ is a single non-overlapping and non-crossing open path. The arguments below generalize in a straightforward manner to the case where we need to consider $\mathcal{P} = \mathcal{P}_1 \# \ldots \# \mathcal{P}_m$ for some $m > 1$. First note that

$$|\vec{i}\rangle\langle\vec{i}| = \prod_i \frac{1}{2}(1 + (-1)^{\alpha_i}\sigma_i^z), \tag{B14}$$

where $\vec{i} = (\alpha_1, \ldots, \alpha_n)$. We can thus write $F_{\mathcal{P}}(\vec{i})|\vec{i}\rangle\langle\vec{i}| = \sum_{P_z} c_{P_z}(\vec{i})P_z$, where P_z are all the possible Pauli operators acting on the qubits in Conn($\mathcal{P}$) and composed of σ^z and identities only, and where $c_{P_z}(\vec{i})$ are complex coefficients given by equation (B14) multiplied by $F_{\mathcal{P}}(\vec{i})$. Given $\tilde{F}_{\mathcal{P}}$ differing of $F_{\mathcal{P}}$ by the choice of phases associated with the different class representatives, we have that $\tilde{F}_{\mathcal{P}}(\vec{i})|\vec{i}\rangle\langle\vec{i}| = \sum_{P_z} c_{P_z}(\vec{i})e^{i\varphi(\vec{j})}P_z$, where $\vec{j}$ is the representative of the configuration class into which $\vec{i}$ belongs, and $\varphi(\vec{j})$ is the phase difference used between $F_{\mathcal{P}}$ and $\tilde{F}_{\mathcal{P}}$ to initialize algorithm 1.

We define the orthonormal basis $\{|L, C\rangle\}$ where C labels the vertex and flux excitations configuration while L is a label for the 4^g degenerate states corresponding to a given configuration. The probability of the transition $|L, C\rangle \to |L', C'\rangle$ caused by the application of $X_{\mathcal{P}}$ is given by

$$\begin{aligned} P(|L, C\rangle \to |L', C'\rangle) &= |\langle L', C'|S_{\mathcal{P}}^{+}\sum_{\vec{j}}\sum_{\vec{i}\in\mathcal{C}_{\mathcal{P}}(\vec{j})}\sum_{P_z} c_{P_z}^*(\vec{i})e^{-i\varphi(\vec{j})}P_z|L, C\rangle|^2 \\ &= \sum_{\substack{\vec{j},\vec{j}'}}\sum_{\substack{\vec{i}\in\mathcal{C}_{\mathcal{P}}(\vec{j}) \\ \vec{i}'\in\mathcal{C}_{\mathcal{P}}(\vec{j}')}}\sum_{\substack{P_z \text{ s.t.} |\langle L', C'|S_{\mathcal{P}}^{+}P_z|L, C\rangle|=1 \\ P_z' \text{ s.t.} |\langle L', C'|S_{\mathcal{P}}^{+}P_z'|L, C\rangle|=1}} c_{P_z}^*(\vec{i})c_{P_z'}(\vec{i}')e^{i(\varphi(\vec{j})-\varphi(\vec{j}'))}. \end{aligned} \tag{B15}$$

Clearly, P_z and P_z' share the same endpoints and belong to the same homological class, i.e. P_zP_z' form a trivial closed loop. Given the decomposition in equation (B14), we find that for $\vec{j} \neq \vec{j}'$

$$\sum_{\substack{P_z \text{ s.t.} |\langle L', C'|S_{\mathcal{P}}^{+}P_z|L, C\rangle|=1 \\ P_z' \text{ s.t.} |\langle L', C'|S_{\mathcal{P}}^{+}P_z'|L, C\rangle|=1}} c_{P_z}^*(\vec{i})c_{P_z'}(\vec{i}') = 0. \tag{B16}$$

To see this, we rewrite equation (B16) as

$$\sum_{P_z \text{ s.t.} |\langle L', C'|S_{\mathcal{P}}^{+}P_z|L, C\rangle|=1}\sum_{Q_z\subseteq\{Q_\nu\}} c_{P_z}^*(\vec{i})c_{P_z\cdot Q_z}(\vec{i}'), \tag{B17}$$

where $\{Q_\nu\}$ denotes the set of all subsets of products of charge operators associated with the vertices in path $\mathcal{P}$. Noting that since $\vec{i}$ and $\vec{i}'$ belongs to different configuration classes, there exists a vertex ν' such that $c_{P_z}(\vec{i}') = -c_{P_z\cdot Q_{\nu'}}(\vec{i}')$. Using this last fact, we get

$$\sum_{P_z \text{ s.t.} |\langle L', C'|S_{\mathcal{P}}^{+}P_z|L, C\rangle|=1}\sum_{Q_z\subseteq\{Q_\nu\}\setminus Q_{\nu'}} [c_{P_z}^*(\vec{i})c_{P_z\cdot Q_z}(\vec{i}') + c_{P_z}^*(\vec{i})c_{P_z\cdot Q_zQ_{\nu'}}(\vec{i}')], \tag{B18}$$

which clearly equals 0.

The probability transition is thus given by

$$P(|L,\,C\rangle \to |L',\,C'\rangle) = \sum_{j} \sum_{i,i'\in\mathcal{C}_{\mathcal{P}}(\vec{j})} \sum_{\substack{P_z \text{s.t.}\,|\langle L',C'|P_z|L,C\rangle|=1 \\ P'_z \text{s.t.}\,|\langle L',C'|P'_z|L,C\rangle|=1}} c^{*}_{P_z}(\vec{i}\,')\, c_{P'_z}(\vec{i})\, \langle L,\,C|P_z P'_z|L,\,C\rangle, \tag{B19}$$

which is independent of the phases $e^{i\varphi(\vec{j})}$.

Appendix C. Topological properties of strings operators

Before presenting various technical results, we begin by precisely defining what we mean by *crossing paths*.

Definition 1. Let a path $\mathcal{P} = \{e_1, e_2, \ldots, e_n\}$ be a sequence of edges such that edge e_i connects vertices v_{i-1} to v_i. If $v_0 = v_n$, we say that the path $\mathcal{P}$ is closed; otherwise it is open. If there exists $0 < i < n$ and $j \neq i$, $0 \leqslant j \leqslant n$ such that $v_i = v_j$ in the sequence of vertices it contains, $v_{\mathcal{P}} = \{v_0, v_1, \ldots, v_n\}$, then $\mathcal{P}$ is said to be *self-crossing*. If there exists a plaquette containing two or more vertices of $v_{\mathcal{P}}$ that cannot form a single consecutive sequence, then path $\mathcal{P}$ is said to be self-overlapping. Note that the notions of self-overlapping and self-crossing do not imply each other (see figure 5).

Definition 2. Consider two paths $\mathcal{P} = \{e_1^{\mathcal{P}}, \ldots, e_n^{\mathcal{P}}\}$ and $\mathcal{Q} = \{e_1^{\mathcal{Q}}, \ldots, e_{n'}^{\mathcal{Q}}\}$ connecting vertices $\{v_0^{\mathcal{P}}, \ldots, v_n^{\mathcal{P}}\}$ and $\{v_0^{\mathcal{Q}}, \ldots, v_{n'}^{\mathcal{Q}}\}$ respectively. Consider a sequence of edges in common of both paths $\mathcal{P}$ and $\mathcal{Q}$, and consider the largest (possibly empty) such sequence (supposing for now that it is unique), $E_{\mathcal{P},\mathcal{Q}} = \{e_i^{\mathcal{P}} = e_j^{\mathcal{Q}}, \ldots, e_{i'}^{\mathcal{P}} = e_{j'}^{\mathcal{Q}}\}$ (with both se-quences ordered in increasing order of simplicity, i.e. $i' > i$ and $j' > j$) connecting the common vertices in $\mathcal{P}$ and $\mathcal{Q}$, denoted by $\Lambda_{\mathcal{P},\mathcal{Q}} = \{v_{i-1}^{\mathcal{P}} = v_{j-1}^{\mathcal{Q}}, \ldots, v_{i'}^{\mathcal{P}} = v_{j'}^{\mathcal{Q}}\}$. Consider the following properties:

(i) (in the case where both paths open) none of the vertices $v_0^{\mathcal{P}}$, $v_n^{\mathcal{P}}$, $v_0^{\mathcal{Q}}$ and $v_{n'}^{\mathcal{Q}}$ are in $\Lambda_{\mathcal{P},\mathcal{Q}}$,

(ii) (in the case where one path is open ($\mathcal{P}$), the other is closed ($\mathcal{Q}$)) none of the vertices $v_0^{\mathcal{P}}$ and $v_n^{\mathcal{P}}$ are in $\Lambda_{\mathcal{P},\mathcal{Q}}$,

(iii) both pairs of edges $(e_{i-1}^{\mathcal{P}}, e_{j-1}^{\mathcal{Q}})$ and $(e_{i'+1}^{\mathcal{P}}, e_{j'+1}^{\mathcal{Q}})$ have the same relative orientation, i.e. clockwise or counter-clockwise.

If condition (i) is satisfied, we say that paths $\mathcal{P}$ and $\mathcal{Q}$ cross over the edges $E_{\mathcal{P},\mathcal{Q}}$. Note that for the case of two closed paths, we always say that they cross. If condition (ii) is not satisfied (including the case where $E_{\mathcal{P},\mathcal{Q}}$ is the empty set), we say that $\mathcal{P}$ and $\mathcal{Q}$ cross 0 times, otherwise we say that paths $\mathcal{P}$ and $\mathcal{Q}$ cross once. Finally, if there is more than one pair of sequences $E^{i}_{\mathcal{P},\mathcal{Q}}$ and $\Lambda^{i}_{\mathcal{P},\mathcal{Q}}$ where i runs from 1 through m which *all* satisfy conditions (i), we say that paths $\mathcal{P}$ and $\mathcal{Q}$ cross. For all the regions $E^{i_1}_{\mathcal{P},\mathcal{Q}}, \ldots, E^{i_{m'}}_{\mathcal{P},\mathcal{Q}}$ and $\Lambda^{i_1}_{\mathcal{P},\mathcal{Q}}, \ldots, \Lambda^{i_{m'}}_{\mathcal{P},\mathcal{Q}}$ for which (ii) is satisfied, with $m' \leqslant m$, we say that paths $\mathcal{P}$ and $\mathcal{Q}$ cross over the relevant region, and we additionally say that paths $\mathcal{P}$ and $\mathcal{Q}$ cross m' times. See figure C1 for explicit examples.

Note that in the previous definition, paths $\mathcal{P}$ and $\mathcal{Q}$ can be formed of smaller paths, i.e. $\mathcal{P} = \mathcal{P}_1\#...\#\mathcal{P}_m$ and $\mathcal{Q} = \mathcal{Q}_1\#...\#\mathcal{Q}_n$. Notice that when $\mathcal{P}$ and $\mathcal{Q}$ cross, we may define a reference frame such that one of the paths plays the role of the horizontal and the other the vertical. In the following, we consider that path $\mathcal{P}$ is the horizontal and $\mathcal{Q}$ the vertical.

It is useful to define $\mathcal{B}^{\mathcal{Q},\text{left}}_{\mathcal{P}} = \{p_1^{\text{left}}, \ldots, p_m^{\text{left}}\}$, the set of plaquettes in $\mathcal{B}_{\mathcal{P}}$ such that $\vec{\alpha}^{p_1^{\text{left}}} \oplus ... \oplus \vec{\alpha}^{p_m^{\text{left}}} = \vec{\alpha}^{\mathcal{Q}}$ when restricted to Conn($\mathcal{P}$) and containing the left-most plaquette of $\mathcal{B}_{\mathcal{P}}$. In a complementary way, we define $\mathcal{B}^{\mathcal{Q},\text{right}}_{\mathcal{P}} = \mathcal{B}_{\mathcal{P}} \backslash \mathcal{B}^{\mathcal{Q},\text{left}}_{\mathcal{P}}$. In a similar way, $\mathcal{B}^{\mathcal{P},\text{up}}_{\mathcal{Q}}$ and $\mathcal{B}^{\mathcal{P},\text{down}}_{\mathcal{Q}}$ can be defined for a suitable path $\mathcal{Q}$. The nomenclature of *left* versus *right* is an arbitrary choice (just as is the case for *up* versus *down*).

Note that we implicitly used the fact that paths $\mathcal{P}$ and $\mathcal{Q}$ cross, are open, and that they are not self-overlapping nor self-crossing in the above definition. If it were not the case, then it would not be possible to find a set of plaquettes such that the associated configuration corresponds to the configuration of the other path on its connected region.

Furthermore, for a general path $\mathcal{P} = \mathcal{P}_1\#...\#\mathcal{P}_m$ with every path $\{\mathcal{P}_i\}$ open, not self-crossing nor self-overlapping, but for which it is not necessarily true for the *whole* path $\mathcal{P}$, and for a path $\mathcal{Q}$ such that $\mathcal{P}$ and $\mathcal{Q}$ are crossing, it is always possible to similarly define $\mathcal{B}^{\mathcal{Q},\text{left (right)}}_{\mathcal{P}_i}$ for $i \in \{1, \ldots, m\}$.

Consider two crossing paths $\mathcal{P} = \mathcal{P}_1\#...\#\mathcal{P}_m$ and $\mathcal{Q} = \mathcal{Q}_1\#...\#\mathcal{Q}_n$ such that every individual path $\mathcal{P}_i$ and $\mathcal{Q}_j$ is open, is not self-crossing nor self-overlapping, and we are interested in computing the commutation relations between $S^{+}_{\mathcal{P}_1\#...\#\mathcal{P}_m}$ and $S^{+}_{\mathcal{Q}_1\#...\#\mathcal{Q}_n}$. Explicit calculations give

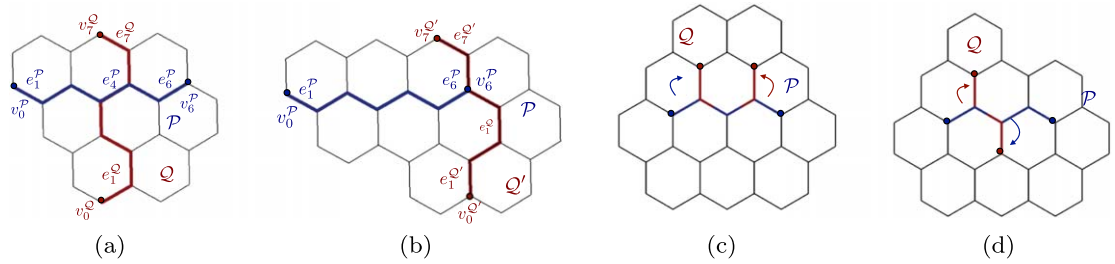

Figure C1. Example of two open paths $\mathcal{P}$ and $\mathcal{Q}$ which, according to criteria (i) of definition 2 are crossing over the edge $E_{\mathcal{P},\mathcal{Q}} = \{e_4^{\mathcal{P}} = e_4^{\mathcal{Q}}\}$(a), as well as paths $\mathcal{P}$ and $\mathcal{Q}'$ which are not crossing (b), since path $\mathcal{Q}$ contains vertex $v_6^{\mathcal{P}}$. The two open paths $\mathcal{P}$ and $\mathcal{Q}$ cross 0 times in (c), according to criteria (ii), while they cross once in (d). The arrows indicate the relative orientation among the strings.

$$S^+_{\mathcal{P}_1\#\ldots\#\mathcal{P}_m} S^+_{\mathcal{Q}_1\#\ldots\#\mathcal{Q}_n} = \prod_{i\in\mathcal{P}} \sigma_i^x \prod_{j\in\mathcal{Q}} \sigma_j^x \sum_{\text{string conf.}\vec{i}} \prod_{i=1}^{m} F_{\mathcal{P}_i}\left(\vec{i} \oplus \vec{\alpha}^{\mathcal{Q}} \bigoplus_{j=1}^{i-1} \vec{\alpha}^{\mathcal{P}_j}\right) \prod_{i'=1}^{n} F_{\mathcal{Q}_{i'}}\left(\vec{i} \bigoplus_{j'=1}^{i'-1} \vec{\alpha}^{\mathcal{Q}_{j'}}\right) |\vec{i}\rangle\langle\vec{i}|, \quad \text{(C1)}$$

where the product over the small strings are taken in the reverse order, and where the string configurations are considered over the whole system.

Similarly computing the product of the string operators in the reverse order, we get

$$S^+_{\mathcal{Q}_1\#\ldots\#\mathcal{Q}_n} S^+_{\mathcal{P}_1\#\ldots\#\mathcal{P}_m} = \prod_{i\in\mathcal{P}} \sigma_i^x \prod_{j\in\mathcal{Q}} \sigma_j^x \sum_{\text{string conf.}\vec{i}} \prod_{i=1}^{m} F_{\mathcal{P}_i}\left(\vec{i} \bigoplus_{j=1}^{i-1} \vec{\alpha}^{\mathcal{P}_j}\right) \prod_{i'=1}^{n} F_{\mathcal{Q}_{i'}}\left(\vec{i} \oplus \vec{\alpha}^{\mathcal{P}} \bigoplus_{j'=1}^{i'-1} \vec{\alpha}^{\mathcal{Q}_{j'}}\right) |\vec{i}\rangle\langle\vec{i}|. \quad \text{(C2)}$$

Considering equations (C1) and (C2), we define the quantity

$$\mathcal{R}_{\mathcal{P}_1\#\ldots\#\mathcal{P}_m,\mathcal{Q}_1\#\ldots\#\mathcal{Q}_n}(\vec{i}) = \frac{\prod_{i=1}^{m} F_{\mathcal{P}_i}\left(\vec{i} \oplus \vec{\alpha}^{\mathcal{Q}} \bigoplus_{j=1}^{i-1} \vec{\alpha}^{\mathcal{P}_j}\right) \prod_{i'=1}^{n} F_{\mathcal{Q}_{i'}}\left(\vec{i} \bigoplus_{j'=1}^{i'-1} \vec{\alpha}^{\mathcal{Q}_{j'}}\right)}{\prod_{i=1}^{m} F_{\mathcal{P}_i}\left(\vec{i} \bigoplus_{j=1}^{i-1} \vec{\alpha}^{\mathcal{P}_j}\right) \prod_{i'=1}^{n} F_{\mathcal{Q}_{i'}}\left(\vec{i} \oplus \vec{\alpha}^{\mathcal{P}} \bigoplus_{j'=1}^{i'-1} \vec{\alpha}^{\mathcal{Q}_{j'}}\right)}, \quad \text{(C3)}$$

which gives the commutation relations between $S^+_{\mathcal{P}_1\#\ldots\#\mathcal{P}_m}$ and $S^+_{\mathcal{Q}_1\#\ldots\#\mathcal{Q}_n}$.The quantity defined in equation (C3) is independent on the specific string configuration $\vec{i}$, which is shown in lemmas 9 and 10, and that it does not depend on the specific way that the paths $\mathcal{P}$ and $\mathcal{Q}$ are partitioned in the smaller paths $\{\mathcal{P}_i\}$ and $\{\mathcal{Q}_j\}$, as long as those are not self-crossing nor self-overlapping. It can also be shown that if paths $\mathcal{P}$ and $\mathcal{Q}$ are transformed to paths $\mathcal{P}'$ and $\mathcal{Q}'$ using a series of elongations, reductions and valid deformations such that none of the elementary step makes a path crossing an endpoint of the other path, then we find $\mathcal{R}_{\mathcal{P},\mathcal{Q}} = \mathcal{R}_{\mathcal{P}',\mathcal{Q}'}$. This is done in lemmas 11 through 15 as well as in corollary 1. If paths $\mathcal{P}$ and $\mathcal{Q}$ cross an odd number of times, one can then proceed to transforms paths $\mathcal{P}$ and $\mathcal{Q}$ to minimal configurations $\mathcal{P}_{\min}$ and $\mathcal{Q}_{\min}$ such that $\mathcal{R}_{\mathcal{P},\mathcal{Q}} = \mathcal{R}_{\mathcal{P}_{\min},\mathcal{Q}_{\min}}$ (see figure C4). Explicitly computing this last quantity for a given string configuration yields $\mathcal{R}_{\mathcal{P},\mathcal{Q}} = -1$. If, on the other hand, $\mathcal{P}$ and $\mathcal{Q}$ cross an even number of times, one can consider the deformed paths $\mathcal{P}_0$ and $\mathcal{Q}_0$ such that $\mathcal{R}_{\mathcal{P},\mathcal{Q}} = \mathcal{R}_{\mathcal{P}_0,\mathcal{Q}_0}$ and such that $\mathcal{P}_0$ and $\mathcal{Q}_0$ supports are disjoint, showing that $\mathcal{R}_{\mathcal{P},\mathcal{Q}} = +1$. Remarkably, all those previous results are essentially due to the fact that the plaquette operators commute and square to the identity.

C.1. Useful technical lemmas

Lemmas mentioned before are introduced here. They are necessary to show theorem 2.

Lemma 9. *Let* $\{p_1^i, \ldots, p_{m^i}^i\} = \mathcal{B}_{\mathcal{P}_i}^{\mathcal{Q},a_i}$ *and* $\{q_1^j, \ldots, q_{n^j}^j\} = \mathcal{B}_{\mathcal{Q}_j}^{\mathcal{P},b_j}$ *with* $a_i =$ left *or* $a_i =$ right *and* $b_j =$ up *or* $b_j =$ down, *as it is shown in figure C2. Then,* $\mathcal{R}_{\mathcal{P}_1\#\ldots\#\mathcal{P}_m,\mathcal{Q}_1\#\ldots\#\mathcal{Q}_n}(\vec{i})$ *can be written as:*

$$\mathcal{R}_{\mathcal{P}_1\#\ldots\#\mathcal{P}_m,\mathcal{Q}_1\#\ldots\#\mathcal{Q}_n}(\vec{i}) = \prod_{i=1}^{m} \frac{\left\langle \vec{i} \bigoplus_{j=1}^{i} \vec{\alpha}^{\mathcal{P}_j} \bigoplus_{k=1}^{m^i} \vec{\alpha}^{p_k^i} | \prod_{j=1}^{m^i} B_{p_j^i} | \vec{i} \bigoplus_{j=1}^{i} \vec{\alpha}^{\mathcal{P}_j} \right\rangle}{\left\langle \vec{i} \bigoplus_{j=1}^{i-1} \vec{\alpha}^{\mathcal{P}_j} \bigoplus_{k=1}^{m^i} \vec{\alpha}^{p_k^i} | \prod_{j=1}^{m^i} B_{p_j^i} | \vec{i} \bigoplus_{j=1}^{i-1} \vec{\alpha}^{\mathcal{P}_j} \right\rangle} \times \prod_{i=1}^{n} \frac{\left\langle \vec{i} \bigoplus_{j=1}^{i-1} \vec{\alpha}^{\mathcal{Q}_j} \bigoplus_{k=1}^{n^i} \vec{\alpha}^{q_k^i} | \prod_{j=1}^{n^i} B_{q_j^i} | \vec{i} \bigoplus_{j=1}^{i-1} \vec{\alpha}^{\mathcal{Q}_j} \right\rangle}{\left\langle \vec{i} \bigoplus_{j=1}^{i} \vec{\alpha}^{\mathcal{Q}_j} \bigoplus_{k=1}^{n^i} \vec{\alpha}^{q_k^i} | \prod_{j=1}^{n^i} B_{q_j^i} | \vec{i} \bigoplus_{j=1}^{i} \vec{\alpha}^{\mathcal{Q}_j} \right\rangle}. \quad \text{(C4)}$$

Proof. We begin by considering the quantity

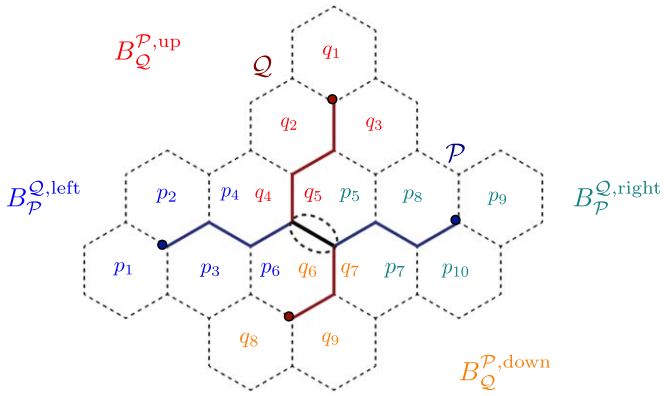

Figure C2. An example of the structure of string operators $S_{\mathcal{P}}^{+}$ and $S_{\mathcal{Q}}^{+}$ on crossing paths $\mathcal{P}$ and $\mathcal{Q}$, shown in dark blue and red, respectively. The various sets of plaquettes $\mathcal{B}_{\mathcal{P}}^{\mathcal{Q},\mathrm{left\ (right)}}$ and $\mathcal{B}_{\mathcal{Q}}^{\mathcal{P},\mathrm{up\ (down)}}$ are presented in various matching colors. The edge over which both paths $\mathcal{P}$ and $\mathcal{Q}$ are overlapping is circled by a dashed line.

$$\frac{F_{\mathcal{P}_i}\left(\vec{i} \oplus \vec{\alpha}^{\mathcal{Q}} \bigoplus_{j=1}^{i-1} \vec{\alpha}^{\mathcal{P}_j}\right)}{F_{\mathcal{P}_i}\left(\vec{i} \bigoplus_{j=1}^{i-1} \vec{\alpha}^{\mathcal{P}_j}\right)}, \tag{C5}$$

which appears in equation (C3). Using the definition of $\mathcal{B}_{\mathcal{P}_i}^{\mathcal{Q},a_i}$, we find

$$\frac{F_{\mathcal{P}_i}\left(\vec{i} \oplus \vec{\alpha}^{\mathcal{Q}} \bigoplus_{j=1}^{i-1} \vec{\alpha}^{\mathcal{P}_j}\right)}{F_{\mathcal{P}_i}\left(\vec{i} \bigoplus_{j=1}^{i-1} \vec{\alpha}^{\mathcal{P}_j}\right)} = \frac{F_{\mathcal{P}_i}(\vec{i} \bigoplus_{j=1}^{m^i} \vec{\alpha}^{p_j^i} \bigoplus_{j=1}^{i-1} \vec{\alpha}^{\mathcal{P}_j})}{F_{\mathcal{P}_i}\left(\vec{i} \bigoplus_{j=1}^{i-1} \vec{\alpha}^{\mathcal{P}_j}\right)}. \tag{C6}$$

Using the structure of the $F_{\mathcal{P}_i}$ as defined by algorithm 1, we find that there exists a configuration $\vec{i}\,'$ and a set of plaquettes $\{p_1', \ldots, p_{m'}'\}$ (possibly empty) such that $\vec{i} \bigoplus_{j=1}^{i-1} \vec{\alpha}^{\mathcal{P}_j} = \vec{i}\,' \bigoplus_{j=1}^{m'} \vec{\alpha}^{p_j'}$ when restricted to $\mathrm{Conn}(\mathcal{P}_i)$. We can thus write

$$\frac{F_{\mathcal{P}_i}\left(\vec{i} \oplus \vec{\alpha}^{\mathcal{Q}} \bigoplus_{j=1}^{i-1} \vec{\alpha}^{\mathcal{P}_j}\right)}{F_{\mathcal{P}_i}\left(\vec{i} \bigoplus_{j=1}^{i-1} \vec{\alpha}^{\mathcal{P}_j}\right)} = \frac{\theta_{\mathcal{P}_i}(\vec{i}\,', p_1', \ldots, p_{m'}', p_1^i, \ldots, p_{m^i}^i)}{\theta_{\mathcal{P}_i}(\vec{i}\,', p_1', \ldots, p_{m'}')} = \theta_{\mathcal{P}_i}(\vec{i}, p_1^i, \ldots, p_{m^i}^i), \tag{C7}$$

where we made use of equation (24). Note that using lemma 2, we are free to choose the values for $a_i = \mathrm{left/right}$ and $b_j = \mathrm{up/down}$, as we please. This will turn out to be very useful later on.

Using equation (24), we find

$$\frac{F_{\mathcal{P}_i}^{+}\left(\vec{i} \oplus \vec{\alpha}^{\mathcal{Q}} \bigoplus_{j=1}^{i-1} \vec{\alpha}^{\mathcal{P}_j}\right)}{F_{\mathcal{P}_i}^{+}\left(\vec{i} \bigoplus_{j=1}^{i-1} \vec{\alpha}^{\mathcal{P}_j}\right)} = \frac{\left\langle \vec{i} \bigoplus_{j=1}^{i} \vec{\alpha}^{\mathcal{P}_j} \bigoplus_{k=1}^{m^i} \vec{\alpha}^{p_k^i} \middle| \prod_{j=1}^{m^i} B_{p_j^i} \middle| \vec{i} \bigoplus_{j=1}^{i} \vec{\alpha}^{\mathcal{P}_j} \right\rangle}{\left\langle \vec{i} \bigoplus_{j=1}^{i-1} \vec{\alpha}^{\mathcal{P}_j} \bigoplus_{k=1}^{m^i} \vec{\alpha}^{p_k^i} \middle| \prod_{j=1}^{m^i} B_{p_j^i} \middle| \vec{i} \bigoplus_{j=1}^{i-1} \vec{\alpha}^{\mathcal{P}_j} \right\rangle}. \tag{C8}$$

A similar reasoning holding for the quantity

$$\left(\frac{F_{\mathcal{Q}_{i'}}^{+}\left(\vec{i} \bigoplus_{j'=1}^{i'-1} \vec{\alpha}^{\mathcal{Q}_{j'}}\right)}{F_{\mathcal{Q}_{i'}}^{+}(\vec{i} \oplus \vec{\alpha}^{\mathcal{P}} \bigoplus_{j'=1}^{i'-1} \vec{\alpha}^{\mathcal{Q}_{j'}})} \right)^{-1}, \tag{C9}$$

this completes the proof. □

The precedent lemma stipulates that $\mathcal{R}_{\mathcal{P},\mathcal{Q}}(\vec{i})$ can be written in terms of the phases acquired by the product of the plaquette operators of the plaquettes contained in $\mathcal{B}_{\mathcal{P}}^{\mathcal{Q},a}$ and $\mathcal{B}_{\mathcal{Q}}^{\mathcal{P},b}$, on the appropriate string configurations.

Lemma 10. *The quantity $\mathcal{R}_{\mathcal{P}_1\#\ldots\#\mathcal{P}_m,\mathcal{Q}_1\#\ldots\#\mathcal{Q}_n}(\vec{i})$ is independent of the string configuration $\vec{i}$.*

Proof. Consider an arbitrary edge e and its associated canonical string operator S_e^{+}, which we can always find according to theorem 1. Further let $\{p_1^i, \ldots, p_{m^i}^i\} = \mathcal{B}_{\mathcal{P}_i}^{\mathcal{Q},a_i}$ and $\{q_1^j, \ldots, q_{n^j}^j\} = \mathcal{B}_{\mathcal{Q}_j}^{\mathcal{P},b_j}$ with $a_i =$ left or $a_i =$ right and $b_j =$ up or $b_j =$ down, and which we are always free to choose according to lemma 2. Using lemma 9 and the fact that S_e^{+} is canonical and therefore squares to one, the quantity $\mathcal{R}_{\mathcal{P}_1\#\ldots\#\mathcal{P}_m,\mathcal{Q}_1\#\ldots\#\mathcal{Q}_m}(\vec{i})$ is given by

$$\mathcal{R}_{\mathcal{P}_1\#\ldots\#\mathcal{P}_m,\mathcal{Q}_1\#\ldots\#\mathcal{Q}_n}(\vec{i}) = \prod_{i=1}^{m}\left(\frac{\left\langle \vec{i}\bigoplus_{j=1}^{i}\vec{\alpha}^{\mathcal{P}_j}\bigoplus_{k=1}^{m^i}\vec{\alpha}^{p_k^i}|S_e^+\prod_{j=1}^{m^i}B_{p_j^i}S_e^+|\vec{i}\bigoplus_{j=1}^{i}\vec{\alpha}^{\mathcal{P}_j}\right\rangle}{\left\langle \vec{i}\bigoplus_{j=1}^{i-1}\vec{\alpha}^{\mathcal{P}_j}\bigoplus_{k=1}^{m^i}\vec{\alpha}^{p_k^i}|S_e^+\prod_{j=1}^{m^i}B_{p_j^i}S_e^+|\vec{i}\bigoplus_{j=1}^{i-1}\vec{\alpha}^{\mathcal{P}_j}\right\rangle}\right)$$
$$\times\prod_{i=1}^{n}\left(\frac{\left\langle \vec{i}\bigoplus_{j=1}^{i-1}\vec{\alpha}^{\mathcal{Q}_j}\bigoplus_{k=1}^{n^i}\vec{\alpha}^{q_k^i}|S_e^+\prod_{j=1}^{n^i}B_{q_j^i}S_e^+|\vec{i}\bigoplus_{j=1}^{i-1}\vec{\alpha}^{\mathcal{Q}_j}\right\rangle}{\left\langle \vec{i}\bigoplus_{j=1}^{i}\vec{\alpha}^{\mathcal{Q}_j}\bigoplus_{k=1}^{n^i}\vec{\alpha}^{q_k^i}|S_e^+\prod_{j=1}^{n^i}B_{q_j^i}S_e^+|\vec{i}\bigoplus_{j=1}^{i}\vec{\alpha}^{\mathcal{Q}_j}\right\rangle}\right)$$
$$=\prod_{i=1}^{m}\left(\frac{\left\langle \vec{i}\bigoplus_{j=1}^{i}\vec{\alpha}^{\mathcal{P}_j}\bigoplus_{k=1}^{m^i}\vec{\alpha}^{p_k^i}\oplus\vec{\alpha}^{e}|\prod_{j=1}^{m^i}B_{p_j^i}|\vec{i}\bigoplus_{j=1}^{i}\vec{\alpha}^{\mathcal{P}_j}\oplus\vec{\alpha}^{e}\right\rangle}{\left\langle \vec{i}\bigoplus_{j=1}^{i-1}\vec{\alpha}^{\mathcal{P}_j}\bigoplus_{k=1}^{m^i}\vec{\alpha}^{p_k^i}\oplus\vec{\alpha}^{e}|\prod_{j=1}^{m^i}B_{p_j^i}|\vec{i}\bigoplus_{j=1}^{i-1}\vec{\alpha}^{\mathcal{P}_j}\oplus\vec{\alpha}^{e}\right\rangle}\right)$$
$$\times\prod_{i=1}^{n}\left(\frac{\left\langle \vec{i}\bigoplus_{j=1}^{i-1}\vec{\alpha}^{\mathcal{Q}_j}\bigoplus_{k=1}^{n^i}\vec{\alpha}^{q_k^i}\oplus\vec{\alpha}^{e}|\prod_{j=1}^{n^i}B_{q_j^i}|\vec{i}\bigoplus_{j=1}^{i-1}\vec{\alpha}^{\mathcal{Q}_j}\oplus\vec{\alpha}^{e}\right\rangle}{\left\langle \vec{i}\bigoplus_{j=1}^{i}\vec{\alpha}^{\mathcal{Q}_j}\bigoplus_{k=1}^{n^i}\vec{\alpha}^{q_k^i}\oplus\vec{\alpha}^{e}|\prod_{j=1}^{n^i}B_{q_j^i}|\vec{i}\bigoplus_{j=1}^{i}\vec{\alpha}^{\mathcal{Q}_j}\oplus\vec{\alpha}^{e}\right\rangle}\right)$$
$$\times\prod_{i=1}^{m}\left(\frac{F_e(\vec{i}\bigoplus_{j=1}^{i}\vec{\alpha}^{\mathcal{P}_j}\bigoplus_{k=1}^{m^i}\vec{\alpha}^{p_k^i}\oplus\vec{\alpha}^{e})F_e(\vec{i}\bigoplus_{j=1}^{i}\vec{\alpha}^{\mathcal{P}_j})}{F_e(\vec{i}\bigoplus_{j=1}^{i-1}\vec{\alpha}^{\mathcal{P}_j})F_e(\vec{i}\bigoplus_{j=1}^{i-1}\vec{\alpha}^{\mathcal{P}_j}\bigoplus_{k=1}^{m^i}\vec{\alpha}^{p_k^i}\oplus\vec{\alpha}^{e})}\right)$$
$$\times\prod_{i=1}^{n}\left(\frac{F_e(\vec{i}\bigoplus_{j=1}^{i-1}\vec{\alpha}^{\mathcal{Q}_j}\bigoplus_{k=1}^{n^i}\vec{\alpha}^{q_k^i}\oplus\vec{\alpha}^{e})F_e(\vec{i}\bigoplus_{j=1}^{i-1}\vec{\alpha}^{\mathcal{Q}_j})}{F_e(\vec{i}\bigoplus_{j=1}^{i}\vec{\alpha}^{\mathcal{Q}_j})F_e(\vec{i}\bigoplus_{j=1}^{i}\vec{\alpha}^{\mathcal{Q}_j}\bigoplus_{k=1}^{n^i}\vec{\alpha}^{q_k^i}\oplus\vec{\alpha}^{e})}\right). \tag{C10}$$

Carefully looking at the right-hand side of the equality, we find that

$$\mathcal{R}_{\mathcal{P}_1\#\ldots\#\mathcal{P}_m,\mathcal{Q}_1\#\ldots\#\mathcal{Q}_n}(\vec{i}) = \mathcal{R}_{\mathcal{P}_1\#\ldots\#\mathcal{P}_m,\mathcal{Q}_1\#\ldots\#\mathcal{Q}_n}(\vec{i}\oplus\vec{\alpha}^{e})$$
$$\times\prod_{i=1}^{m}\left(\frac{F_e(\vec{i}\bigoplus_{j=1}^{i}\vec{\alpha}^{\mathcal{P}_j}\bigoplus_{k=1}^{m^i}\vec{\alpha}^{p_k^i}\oplus\vec{\alpha}^{e})F_e(\vec{i}\bigoplus_{j=1}^{i}\vec{\alpha}^{\mathcal{P}_j})}{F_e(\vec{i}\bigoplus_{j=1}^{i-1}\vec{\alpha}^{\mathcal{P}_j})F_e(\vec{i}\bigoplus_{j=1}^{i-1}\vec{\alpha}^{\mathcal{P}_j}\bigoplus_{k=1}^{m^i}\vec{\alpha}^{p_k^i}\oplus\vec{\alpha}^{e})}\right)$$
$$\times\prod_{i=1}^{n}\left(\frac{F_e(\vec{i}\bigoplus_{j=1}^{i-1}\vec{\alpha}^{\mathcal{Q}_j}\bigoplus_{k=1}^{n^i}\vec{\alpha}^{q_k^i}\oplus\vec{\alpha}^{e})F_e(\vec{i}\bigoplus_{j=1}^{i-1}\vec{\alpha}^{\mathcal{Q}_j})}{F_e(\vec{i}\bigoplus_{j=1}^{i}\vec{\alpha}^{\mathcal{Q}_j})F_e(\vec{i}\bigoplus_{j=1}^{i}\vec{\alpha}^{\mathcal{Q}_j}\bigoplus_{k=1}^{n^i}\vec{\alpha}^{q_k^i}\oplus\vec{\alpha}^{e})}\right). \tag{C11}$$

Note that it is always possible to choose the a_i's and the b_j's so that, in case of need, we can add some additional plaquettes in $\mathcal{B}_{\mathcal{P}_i}^{\mathcal{Q},a_i}$ and $\mathcal{B}_{\mathcal{Q}_j}^{\mathcal{P},b_j}$ respectively without affecting $\mathcal{R}_{\mathcal{P}_1\#\ldots\#\mathcal{P}_m,\mathcal{Q}_1\#\ldots\#\mathcal{Q}_n}(\vec{i})$, in order to have that on $\mathrm{Conn}(\{e\})$, we find $\vec{\alpha}^{p_1^i}\oplus\ldots\oplus\vec{\alpha}^{p_{m^i}^i}=\vec{\alpha}^{\mathcal{Q}}$ for any i, and $\vec{\alpha}^{q_1^j}\oplus\ldots\oplus\vec{\alpha}^{q_{n^j}^j}=\vec{\alpha}^{\mathcal{P}}$ for any j. Using this, we find

$$\prod_{i=1}^{m}\left(\frac{F_e(\vec{i}\bigoplus_{j=1}^{i}\vec{\alpha}^{\mathcal{P}_j}\bigoplus_{k=1}^{m^i}\vec{\alpha}^{p_k^i}\oplus\vec{\alpha}^{e})F_e(\vec{i}\bigoplus_{j=1}^{i}\vec{\alpha}^{\mathcal{P}_j})}{F_e(\vec{i}\bigoplus_{j=1}^{i-1}\vec{\alpha}^{\mathcal{P}_j})F_e(\vec{i}\bigoplus_{j=1}^{i-1}\vec{\alpha}^{\mathcal{P}_j}\bigoplus_{k=1}^{m^i}\vec{\alpha}^{p_k^i}\oplus\vec{\alpha}^{e})}\right)$$
$$\times\prod_{i=1}^{n}\left(\frac{F_e(\vec{i}\bigoplus_{j=1}^{i-1}\vec{\alpha}^{\mathcal{Q}_j}\bigoplus_{k=1}^{n^i}\vec{\alpha}^{q_k^i}\oplus\vec{\alpha}^{e})F_e(\vec{i}\bigoplus_{j=1}^{i-1}\vec{\alpha}^{\mathcal{Q}_j})}{F_e(\vec{i}\bigoplus_{j=1}^{i}\vec{\alpha}^{\mathcal{Q}_j})F_e(\vec{i}\bigoplus_{j=1}^{i}\vec{\alpha}^{\mathcal{Q}_j}\bigoplus_{k=1}^{n^i}\vec{\alpha}^{q_k^i}\oplus\vec{\alpha}^{e})}\right)$$
$$=\frac{F_e(\vec{i}\oplus\vec{\alpha}^{\mathcal{P}}\oplus\vec{\alpha}^{\mathcal{Q}}\oplus\vec{\alpha}^{e})F_e(\vec{i}\oplus\vec{\alpha}^{\mathcal{P}})}{F_e(\vec{i})F_e(\vec{i}\oplus\vec{\alpha}^{\mathcal{Q}}\oplus\vec{\alpha}^{e})}\times\frac{F_e(\vec{i}\oplus\vec{\alpha}^{\mathcal{P}}\oplus\vec{\alpha}^{e})F_e(\vec{i})}{F_e(\vec{i}\oplus\vec{\alpha}^{\mathcal{Q}})F_e(\vec{i}\oplus\vec{\alpha}^{\mathcal{Q}}\oplus\vec{\alpha}^{\mathcal{P}}\oplus\vec{\alpha}^{e})}=1, \tag{C12}$$

where we used that $F_e(\vec{i}\,'\oplus\vec{\alpha}^{e})=[F_e(\vec{i}\,')]^{-1}$ for any string configuration $\vec{i}\,'$, since S_e^+ is canonical. □

Lemma 11. *Let $\mathcal{P}=\mathcal{P}_1\#\ldots\#\mathcal{P}_i\#\mathcal{P}_{i+1}\#\ldots\#\mathcal{P}_m$ and $\mathcal{Q}=\mathcal{Q}_1\#\ldots\#\mathcal{Q}_n$ be two crossing paths. For any $i\in\{1,\ldots,m-1\}$, we denote $\mathcal{P}_i=\{e_1^{\mathcal{P}_i},\ldots,e_{|\mathcal{P}_i|}^{\mathcal{P}_i}\}$, we define $\mathcal{P}_i^+=\{e_1^{\mathcal{P}_i},\ldots,e_{|\mathcal{P}_i|}^{\mathcal{P}_i},e_1^{\mathcal{P}_{i+1}}\}$, ${}^+\mathcal{P}_i=\{e_{|\mathcal{P}_{i-1}|}^{\mathcal{P}_{i-1}},e_1^{\mathcal{P}_i},\ldots,e_{|\mathcal{P}_i|}^{\mathcal{P}_i}\}$, and similarly for $\mathcal{P}_i^-$ and ${}^-\mathcal{P}_i$, this time* removing *the first or last edge, depending on the case. If the paths $\mathcal{P}_i^{\pm}$ and ${}^{\pm}\mathcal{P}_{i+1}$ are not self-overlapping nor self-crossing, we have that*

$$\begin{aligned}\mathcal{R}_{\mathcal{P}_1\#\ldots\#\mathcal{P}_i\#\mathcal{P}_{i+1}\#\ldots\#\mathcal{P}_m,\mathcal{Q}_1\#\ldots\#\mathcal{Q}_n} &= \mathcal{R}_{\mathcal{P}_1\#\ldots\#\mathcal{P}_i^+\#^-\mathcal{P}_{i+1}\#\ldots\#\mathcal{P}_m,\mathcal{Q}_1\#\ldots\#\mathcal{Q}_n}\\ &= \mathcal{R}_{\mathcal{P}_1\#\ldots\#\mathcal{P}_i^-\#^+\mathcal{P}_{i+1}\#\ldots\#\mathcal{P}_m,\mathcal{Q}_1\#\ldots\#\mathcal{Q}_n}.\end{aligned} \tag{C13}$$

Proof. Consider the edge $e_1^{\mathcal{P}_{x+1}}$ and the corresponding *canonical* string operator, written as S_e^+. We then have that

$$\begin{aligned}\mathcal{R}_{\mathcal{P}_1\#\ldots\#\mathcal{P}_x\#\mathcal{P}_{x+1}\#\ldots\mathcal{P}_m,\mathcal{Q}_1\#\ldots\#\mathcal{Q}_n} &= \prod_{i=1}^{m}\frac{\left\langle\vec{i}\bigoplus_{j=1}^{i}\vec{\alpha}^{\mathcal{P}_j}\bigoplus_{k=1}^{m^i}\vec{\alpha}^{p_k^i}|[S_e^+]^{\delta_{x,i}}\prod_{j=1}^{m^i}B_{p_j^i}[S_e^+]^{\delta_{x,i}}|\vec{i}\bigoplus_{j=1}^{i}\vec{\alpha}^{\mathcal{P}_j}\right\rangle}{\left\langle\vec{i}\bigoplus_{j=1}^{i-1}\vec{\alpha}^{\mathcal{P}_j}\bigoplus_{k=1}^{m^i}\vec{\alpha}^{p_k^i}|[S_e^+]^{\delta_{x,i+1}}\prod_{j=1}^{m^i}B_{p_j^i}[S_e^+]^{\delta_{x,i+1}}|\vec{i}\bigoplus_{j=1}^{i-1}\vec{\alpha}^{\mathcal{P}_j}\right\rangle}\\ &\times\prod_{i=1}^{n}\frac{\left\langle\vec{i}\bigoplus_{j=1}^{i-1}\vec{\alpha}^{\mathcal{Q}_j}\bigoplus_{k=1}^{n^i}\vec{\alpha}^{q_k^i}|\prod_{j=1}^{n^i}B_{q_j^i}|\vec{i}\bigoplus_{j=1}^{i-1}\vec{\alpha}^{\mathcal{Q}_j}\right\rangle}{\left\langle\vec{i}\bigoplus_{j=1}^{i}\vec{\alpha}^{\mathcal{Q}_j}\bigoplus_{k=1}^{n^i}\vec{\alpha}^{q_k^i}|\prod_{j=1}^{n^i}B_{q_j^i}|\vec{i}\bigoplus_{j=1}^{i}\vec{\alpha}^{\mathcal{Q}_j}\right\rangle}.\end{aligned} \tag{C14}$$

We thus get

$$\begin{aligned}\mathcal{R}_{\mathcal{P}_1\#\ldots\#\mathcal{P}_x\#\mathcal{P}_{x+1}\#\ldots\#P_m,\mathcal{Q}_1\#\ldots\#\mathcal{Q}_n} &= \mathcal{R}_{\mathcal{P}_1\#\ldots\#\mathcal{P}_x^+\#^-P_{x+1}\#\ldots\#P_m,\mathcal{Q}_1\#\ldots\#\mathcal{Q}_n}\\ &\times\frac{F_e(\vec{i}\bigoplus_{j=1}^{x}\vec{\alpha}^{\mathcal{P}_j})F_e(\vec{i}\bigoplus_{j}^{x}\vec{\alpha}^{\mathcal{P}_j}\bigoplus_{k=1}^{m^x}\vec{\alpha}^{p_k^x}\oplus\vec{\alpha}^{e})}{F_e(\vec{i}\bigoplus_{j=1}^{x}\vec{\alpha}^{\mathcal{P}_j})F_e(\vec{i}\bigoplus_{j}^{x}\vec{\alpha}^{\mathcal{P}_j}\bigoplus_{k=1}^{m^{x+1}}\vec{\alpha}^{p_k^{x+1}}\oplus\vec{\alpha}^{e})}.\end{aligned} \tag{C15}$$

As in the reasoning of the proof of lemma 10, we used our freedom to add some plaquettes to $\mathcal{B}_{\mathcal{P}_x}^{\mathcal{Q},a_x}$ and $\mathcal{B}_{\mathcal{P}_{x+1}}^{\mathcal{Q},a_{x+1}}$, so that we have $\mathcal{B}_{\mathcal{P}_x^+}^{\mathcal{Q},a_x}\subset\mathcal{B}_{\mathcal{P}_x}^{\mathcal{Q},a_x}$ and $\mathcal{B}_{^-\mathcal{P}_{x+1}}^{\mathcal{Q},a_{x+1}}\subset\mathcal{B}_{\mathcal{P}_{x+1}}^{\mathcal{Q},a_{x+1}}$. Additionally, when can choose them such that when restricted to $\mathrm{Conn}(\{e\})$, we have that $\bigoplus_{k=1}^{m^x}\vec{\alpha}^{p_k^x}=\bigoplus_{k=1}^{m^{x+1}}\vec{\alpha}^{p_k^{x+1}}=\mathcal{Q}$. We thus find that

$$\mathcal{R}_{\mathcal{P}_1\#\ldots\#\mathcal{P}_x\#\mathcal{P}_{x+1}\#\ldots\mathcal{P}_m,\mathcal{Q}_1\#\ldots\#\mathcal{Q}_n} = \mathcal{R}_{\mathcal{P}_1\#\ldots\#\mathcal{P}_x^+\#^-P_{x+1}\#\ldots\#\mathcal{P}_m,\mathcal{Q}_1\#\ldots\#\mathcal{Q}_n}. \tag{C16}$$

A similar reasoning shows that

$$\mathcal{R}_{\mathcal{P}_1\#\ldots\#\mathcal{P}_x\#\mathcal{P}_{x+1}\#\ldots\mathcal{P}_m,\mathcal{Q}_1\#\ldots\#\mathcal{Q}_n} = \mathcal{R}_{\mathcal{P}_1\#\ldots\#\mathcal{P}_x^-\#^+P_{x+1}\#\ldots\#\mathcal{P}_m,\mathcal{Q}_1\#\ldots\#\mathcal{Q}_n}. \tag{C17}$$

□

Corollary 1. *Let $\mathcal{P}=\mathcal{P}_1\#\ldots\#\mathcal{P}_m$ and $\mathcal{Q}=\mathcal{Q}_1\#\ldots\#\mathcal{Q}_n$ be two crossing paths. For any $i\in\{1,\ldots,n-1\}$, we have that*

$$\begin{aligned}\mathcal{R}_{\mathcal{P}_1\#\ldots\#\mathcal{P}_m,\mathcal{Q}_1\#\ldots\#\mathcal{Q}_i\#\mathcal{Q}_{i+1}\#\ldots\#\mathcal{Q}_n} &= \mathcal{R}_{\mathcal{P}_1\#\ldots\#\mathcal{P}_m,\mathcal{Q}_1\#\ldots\#\mathcal{Q}_i^+\#^-\mathcal{Q}_{i+1}\#\ldots\#\mathcal{Q}_n}\\ &= \mathcal{R}_{\mathcal{P}_1\#\ldots\#\mathcal{P}_m,\mathcal{Q}_1\#\ldots\#\mathcal{Q}_i^-\#^+\mathcal{Q}_{i+1}\#\ldots\#\mathcal{Q}_n}.\end{aligned} \tag{C18}$$

Proof. To see that equation (C18) holds, it suffices to use the same reasoning than in lemma 11, this time for the appropriate path $\mathcal{Q}_x$. □

Given the fact that the quantity $\mathcal{R}_{\mathcal{P}_1\#\ldots\#\mathcal{P}_m,\mathcal{Q}_1\#\ldots\#\mathcal{Q}_n}$ is insensitive to the specific decomposition of the paths $\mathcal{P}$ and $\mathcal{Q}$ as long as they are composed of simple paths which are not self-crossing nor self-overlapping, from now on we will simply write $\mathcal{R}_{\mathcal{P},\mathcal{Q}}$.

Lemma 12. *Consider the paths $\mathcal{P}$, $\mathcal{P}'=\mathcal{P}_0\#\mathcal{P}\#\mathcal{P}_{m+1}$, $\mathcal{Q}$ and $\mathcal{Q}'=\mathcal{Q}_0\#\mathcal{Q}\#\mathcal{Q}_{n+1}$, such that $\mathcal{P}$ and $\mathcal{Q}$ are crossing, and such that $\mathcal{P}_0$, $\mathcal{P}_{m+1}$ do not contain edges in* $\mathrm{Conn}(\mathcal{Q}')$*, as well as $\mathcal{Q}_0$, $\mathcal{Q}_{n+1}$ do not contain edges in* $\mathrm{Conn}(\mathcal{P}')$*. Then, we have that*

$$\mathcal{R}_{\mathcal{P},\mathcal{Q}} = \mathcal{R}_{\mathcal{P}',\mathcal{Q}'}. \tag{C19}$$

Proof. We begin by considering $\mathcal{R}_{\mathcal{P}_0\#\mathcal{P},\mathcal{Q}}$, given by

$$\mathcal{R}_{\mathcal{P}_0\#\mathcal{P},\mathcal{Q}} = \prod_{i=0}^{m} \frac{\left\langle \vec{i} \bigoplus_{j=0}^{i} \vec{\alpha}^{\mathcal{P}_j} \bigoplus_{k=1}^{m^i} \vec{\alpha}^{p_k^i} \middle| \prod_{j=1}^{m^i} B_{p_j^i} \middle| \vec{i} \bigoplus_{j=0}^{i} \vec{\alpha}^{\mathcal{P}_j} \right\rangle}{\left\langle \vec{i} \bigoplus_{j=0}^{i-1} \vec{\alpha}^{\mathcal{P}_j} \bigoplus_{k=1}^{m^i} \vec{\alpha}^{p_k^i} \middle| \prod_{j=1}^{m^i} B_{p_j^i} \middle| \vec{i} \bigoplus_{j=0}^{i-1} \vec{\alpha}^{\mathcal{P}_j} \right\rangle} \times \prod_{i=1}^{n} \frac{\left\langle \vec{i} \bigoplus_{j=1}^{i-1} \vec{\alpha}^{\mathcal{Q}_j} \bigoplus_{k=1}^{n^i} \vec{\alpha}^{q_k^i} \middle| \prod_{j=1}^{n^i} B_{q_j^i} \middle| \vec{i} \bigoplus_{j=1}^{i-1} \vec{\alpha}^{\mathcal{Q}_j} \right\rangle}{\left\langle \vec{i} \bigoplus_{j=1}^{i} \vec{\alpha}^{\mathcal{Q}_j} \bigoplus_{k=1}^{n^i} \vec{\alpha}^{q_k^i} \middle| \prod_{j=1}^{n^i} B_{q_j^i} \middle| \vec{i} \bigoplus_{j=1}^{i} \vec{\alpha}^{\mathcal{Q}_j} \right\rangle}. \tag{C20}$$

Inserting $[S_{\mathcal{P}_0}^{+}]^2$ at various appropriate locations, with $S_{\mathcal{P}_0}^{+}$ a canonical string operator, and rearranging the terms, we find

$$\begin{aligned}\mathcal{R}_{\mathcal{P}_0\#\mathcal{P},\mathcal{Q}} = \prod_{i=1}^{m} & \frac{\left\langle \vec{i} \oplus \vec{\alpha}^{\mathcal{P}_0} \bigoplus_{j=1}^{i} \vec{\alpha}^{\mathcal{P}_j} \bigoplus_{k=1}^{m^i} \vec{\alpha}^{p_k^i} \middle| \prod_{j=1}^{m^i} B_{p_j^i} \middle| \vec{i} \oplus \vec{\alpha}^{\mathcal{P}_0} \bigoplus_{j=1}^{i} \vec{\alpha}^{\mathcal{P}_j} \right\rangle}{\left\langle \vec{i} \oplus \vec{\alpha}^{\mathcal{P}_0} \bigoplus_{j=1}^{i-1} \vec{\alpha}^{\mathcal{P}_j} \bigoplus_{k=1}^{m^i} \vec{\alpha}^{p_k^i} \middle| \prod_{j=1}^{m^i} B_{p_j^i} \middle| \vec{i} \oplus \vec{\alpha}^{\mathcal{P}_0} \bigoplus_{j=1}^{i-1} \vec{\alpha}^{\mathcal{P}_j} \right\rangle} \\ & \times \prod_{i=1}^{n} \frac{\left\langle \vec{i} \bigoplus_{j=1}^{i-1} \vec{\alpha}^{\mathcal{Q}_j} \bigoplus_{k=1}^{n^i} \vec{\alpha}^{q_k^i} \middle| S_{\mathcal{P}_0}^{+} \prod_{j=1}^{n^i} B_{q_j^i} S_{\mathcal{P}_0}^{+} \middle| \vec{i} \bigoplus_{j=1}^{i-1} \vec{\alpha}^{\mathcal{Q}_j} \right\rangle}{\left\langle \vec{i} \bigoplus_{j=1}^{i} \vec{\alpha}^{\mathcal{Q}_j} \bigoplus_{k=1}^{n^i} \vec{\alpha}^{q_k^i} \middle| S_{\mathcal{P}_0}^{+} \prod_{j=1}^{n^i} B_{q_j^i} S_{\mathcal{P}_0}^{+} \middle| \vec{i} \bigoplus_{j=1}^{i} \vec{\alpha}^{\mathcal{Q}_j} \right\rangle} \\ & \times \frac{\left\langle \vec{i} \oplus \vec{\alpha}^{\mathcal{P}_0} \bigoplus_{k=1}^{m^0} \vec{\alpha}^{p_k^0} \middle| S_{\mathcal{P}_0}^{+} \prod_{j=1}^{m^0} B_{p_j^0} S_{\mathcal{P}_0}^{+} \middle| \vec{i} \oplus \vec{\alpha}^{\mathcal{P}_0} \right\rangle}{\left\langle \vec{i} \bigoplus_{k=1}^{m^0} \vec{\alpha}^{p_k^0} \middle| \prod_{j=1}^{m^0} B_{p_j^0} \middle| \vec{i} \right\rangle}. \end{aligned} \tag{C21}$$

Using the structure of $S_{\mathcal{P}_0}^{+}$, we find that

$$\begin{aligned}\mathcal{R}_{\mathcal{P}_0\#\mathcal{P},\mathcal{Q}} = \prod_{i=1}^{m} & \frac{\left\langle \vec{i} \oplus \vec{\alpha}^{\mathcal{P}_0} \bigoplus_{j=1}^{i} \vec{\alpha}^{\mathcal{P}_j} \bigoplus_{k=1}^{m^i} \vec{\alpha}^{p_k^i} \middle| \prod_{j=1}^{m^i} B_{p_j^i} \middle| \vec{i} \oplus \vec{\alpha}^{\mathcal{P}_0} \bigoplus_{j=1}^{i} \vec{\alpha}^{\mathcal{P}_j} \right\rangle}{\left\langle \vec{i} \oplus \vec{\alpha}^{\mathcal{P}_0} \bigoplus_{j=1}^{i-1} \vec{\alpha}^{\mathcal{P}_j} \bigoplus_{k=1}^{m^i} \vec{\alpha}^{p_k^i} \middle| \prod_{j=1}^{m^i} B_{p_j^i} \middle| \vec{i} \oplus \vec{\alpha}^{\mathcal{P}_0} \bigoplus_{j=1}^{i-1} \vec{\alpha}^{\mathcal{P}_j} \right\rangle} \\ & \times \prod_{i=1}^{n} \frac{\left\langle \vec{i} \oplus \vec{\alpha}^{\mathcal{P}_0} \bigoplus_{j=1}^{i-1} \vec{\alpha}^{\mathcal{Q}_j} \bigoplus_{k=1}^{n^i} \vec{\alpha}^{q_k^i} \middle| \prod_{j=1}^{n^i} B_{q_j^i} \middle| \vec{i} \oplus \vec{\alpha}^{\mathcal{P}_0} \bigoplus_{j=1}^{i-1} \vec{\alpha}^{\mathcal{Q}_j} \right\rangle}{\left\langle \vec{i} \oplus \vec{\alpha}^{\mathcal{P}_0} \bigoplus_{j=1}^{i} \vec{\alpha}^{\mathcal{Q}_j} \bigoplus_{k=1}^{n^i} \vec{\alpha}^{q_k^i} \middle| \prod_{j=1}^{n^i} B_{q_j^i} \middle| \vec{i} \oplus \vec{\alpha}^{\mathcal{P}_0} \bigoplus_{j=1}^{i} \vec{\alpha}^{\mathcal{Q}_j} \right\rangle} \\ & \times \frac{F_{\mathcal{P}_0}\left(\vec{i} \bigoplus_{k=1}^{n^i} \vec{\alpha}^{q_k^i} \oplus \vec{\alpha}^{\mathcal{P}_0}\right) F_{\mathcal{P}_0}(\vec{i})}{F_{\mathcal{P}_0}(\vec{i} \oplus \vec{\alpha}^{\mathcal{Q}} \bigoplus_{k=1}^{n^i} \vec{\alpha}^{q_k^i} \oplus \vec{\alpha}^{\mathcal{P}_0}) F_{\mathcal{P}_0}(\vec{i} \oplus \vec{\alpha}^{\mathcal{Q}})} F_{\mathcal{P}_0}(\vec{i} \oplus \vec{\alpha}^{\mathcal{P}_0}) F_{\mathcal{P}_0}\left(\vec{i} \bigoplus_{k=1}^{m^0} \vec{\alpha}^{p_k^0}\right). \end{aligned} \tag{C22}$$

Since we have that $\mathcal{P}_0 \cap \mathrm{Conn}(\mathcal{Q}) = \varnothing$ and since paths $\mathcal{P}$ and $\mathcal{Q}$ are crossing, we find that for any string configuration $\vec{i}\,'$, $F_{\mathcal{P}_0}(\vec{i}\,' \oplus \vec{\alpha}^{\mathcal{Q}}) = F_{\mathcal{P}_0}(\vec{i}\,')$. We thus conclude that

$$\frac{F_{\mathcal{P}_0}\left(\vec{i} \bigoplus_{k=1}^{n^i} \vec{\alpha}^{q_k^i} \oplus \vec{\alpha}^{\mathcal{P}_0}\right) F_{\mathcal{P}_0}(\vec{i})}{F_{\mathcal{P}_0}\left(\vec{i} \oplus \vec{\alpha}^{\mathcal{Q}} \bigoplus_{k=1}^{n^i} \vec{\alpha}^{q_k^i} \oplus \vec{\alpha}^{\mathcal{P}_0}\right) F_{\mathcal{P}_0}(\vec{i} \oplus \vec{\alpha}^{\mathcal{Q}})} F_{\mathcal{P}_0}(\vec{i} \oplus \vec{\alpha}^{\mathcal{P}_0}) F_{\mathcal{P}_0}\left(\vec{i} \bigoplus_{k=1}^{m^0} \vec{\alpha}^{p_k^0}\right) = 1. \tag{C23}$$

Furthermore, using lemma 10, we see that

$$\begin{aligned}\prod_{i=1}^{m} & \frac{\left\langle \vec{i} \oplus \vec{\alpha}^{\mathcal{P}_0} \bigoplus_{j=1}^{i} \vec{\alpha}^{\mathcal{P}_j} \bigoplus_{k=1}^{m^i} \vec{\alpha}^{p_k^i} \middle| \prod_{j=1}^{m^i} B_{p_j^i} \middle| \vec{i} \oplus \vec{\alpha}^{\mathcal{P}_0} \bigoplus_{j=1}^{i} \vec{\alpha}^{\mathcal{P}_j} \right\rangle}{\left\langle \vec{i} \oplus \vec{\alpha}^{\mathcal{P}_0} \bigoplus_{j=1}^{i-1} \vec{\alpha}^{\mathcal{P}_j} \bigoplus_{k=1}^{m^i} \vec{\alpha}^{p_k^i} \middle| \prod_{j=1}^{m^i} B_{p_j^i} \middle| \vec{i} \oplus \vec{\alpha}^{\mathcal{P}_0} \bigoplus_{j=1}^{i-1} \vec{\alpha}^{\mathcal{P}_j} \right\rangle} \\ & \times \prod_{i=1}^{n} \frac{\left\langle \vec{i} \oplus \vec{\alpha}^{\mathcal{P}_0} \bigoplus_{j=1}^{i-1} \vec{\alpha}^{\mathcal{Q}_j} \bigoplus_{k=1}^{n^i} \vec{\alpha}^{q_k^i} \middle| \prod_{j=1}^{n^i} B_{q_j^i} \middle| \vec{i} \oplus \vec{\alpha}^{\mathcal{P}_0} \bigoplus_{j=1}^{i-1} \vec{\alpha}^{\mathcal{Q}_j} \right\rangle}{\left\langle \vec{i} \oplus \vec{\alpha}^{\mathcal{P}_0} \bigoplus_{j=1}^{i} \vec{\alpha}^{\mathcal{Q}_j} \bigoplus_{k=1}^{n^i} \vec{\alpha}^{q_k^i} \middle| \prod_{j=1}^{n^i} B_{q_j^i} \middle| \vec{i} \oplus \vec{\alpha}^{\mathcal{P}_0} \bigoplus_{j=1}^{i} \vec{\alpha}^{\mathcal{Q}_j} \right\rangle} = \mathcal{R}_{\mathcal{P},\mathcal{Q}}. \end{aligned} \tag{C24}$$

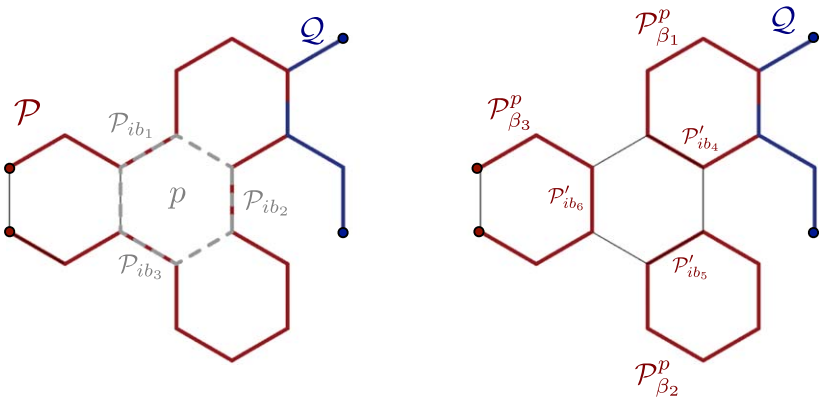

Figure C3. This illustration shows a specific example on path deformation. Three distinct paths ($\{\mathcal{P}_{\beta_1}, \mathcal{P}_{\beta_2}, \mathcal{P}_{\beta_3}\}$, in dark red) are created by applying a plaquette p (in dark blue) to the original path $\mathcal{P}$(dark red). $\mathcal{P}_{ib_1}$, $\mathcal{P}_{ib_2}$, $\mathcal{P}_{ib_3}$ are individual paths which give the parts of path $\mathcal{P}$ that overlaps with plaquette p. $\mathcal{P}'_{ib_4}$, $\mathcal{P}'_{ib_5}$, $\mathcal{P}'_{ib_6}$ are the individual paths which complete plaquette p and are contained in the newly formed paths.

A similar reasoning allows one to add the remaining paths $\mathcal{P}_{m+1}$, $\mathcal{Q}_0$ and $\mathcal{Q}_{n+1}$, to finally find that

$$\mathcal{R}_{\mathcal{P}',\mathcal{Q}'} = \mathcal{R}_{\mathcal{P},\mathcal{Q}}. \tag{C25}$$

□

Lemma 13. *Let $\mathcal{P} = \mathcal{P}_1\#...\#\mathcal{P}_m$ and $\mathcal{Q} = \mathcal{Q}_1\#...\#\mathcal{Q}_n$ be two crossing paths. Assume further that path $\mathcal{P}$ is not self-crossing. Consider a set of distinct paths $\{\mathcal{P}^p_\beta\}$ differing from path $\mathcal{P}$ by a plaquette p, i.e. $\vec{\alpha}^{\mathcal{P}} = \bigoplus_\beta \vec{\alpha}^{\mathcal{P}^p_\beta} \oplus \vec{\alpha}^p$, with the plaquette p not containing the vertices at the endpoint of path $\mathcal{Q}$ and such that every $\mathcal{P}^p_\beta$ is composed of non self-overlapping nor self-crossing individual open paths. Then we have that $\mathcal{R}_{\mathcal{P},\mathcal{Q}} = \prod_\beta \mathcal{R}_{\mathcal{P}^p_\beta,\mathcal{Q}}$.*

Proof. First notice that since paths $\mathcal{P}$ and $\mathcal{Q}$ cross, we have that paths $\mathcal{P}^p_\beta$ and $\mathcal{Q}$ also cross, since the set of paths $\{\mathcal{P}^p_\beta\}$ and $\mathcal{P}$ differs only by a plaquette, which cannot change its endpoints, and since the plaquette p does not contain the endpoints of path $\mathcal{Q}$.

We can decompose the path $\mathcal{P}_p$ of the plaquette in a series of small paths $\mathcal{P}_{b_1}\#...\#\mathcal{P}_{b_k}$ with $k \leqslant 6$ which are not self-overlapping nor self-crossing. Furthermore, using lemma 11, we can assume without loss of generality that the parts of path $\mathcal{P}$ that overlap with plaquette p are given by individuals paths $\mathcal{P}_{i_{b_1}}, \ldots, \mathcal{P}_{i_{b_l}}$, while the rest of the plaquette is given by individual paths $\mathcal{P}'_{b_{l+1}}, \ldots, \mathcal{P}'_{b_k}$ (see figure C3). Note that the various individual paths $\mathcal{P}_{i_{b_1}}, \ldots, P_{i_{b_l}}$ (as well as $\mathcal{P}'_{i_{b_{l+1}}}, \ldots, \mathcal{P}'_{i_{b_k}}$)need not be adjacent to each other. We note that in order for $\{\mathcal{P}^p_\beta\}$ to contain more than one path, the path $\mathcal{P}$ must have at least two different sequences of individual paths in $\{\mathcal{P}_{i_{b_1}}, \ldots, \mathcal{P}_{i_{b_l}}\}$ such that they are separated by some paths in $\{\mathcal{P}'_{i_{b_{l+1}}}, \ldots, \mathcal{P}'_{i_{b_k}}\}$. Given the structure of a plaquette and of the connected region of a path, and using the fact that $\mathcal{P}$ is not self-crossing, we find that the resulting set of paths $\{\mathcal{P}^p_\beta\}$ is such that any path in it does not contain any edge which is in the connected regions of the other ones.

For convenience, we denote the newly formed paths $\mathcal{P}^p_\beta = \mathcal{P}_{\beta,1}\#...\#\mathcal{P}_{\beta,m^\beta}$, and the corresponding paths $\mathcal{P}'_{b_{l+1}}, \ldots, \mathcal{P}'_{b_k}$ that are in $\mathcal{P}^p_\beta$ as $\{\mathcal{P}_{\beta,i_{\beta_1}}, \ldots, \mathcal{P}_{\beta,i_{\beta_{l'}}}\}$, appearing in order. Note that $l' \leqslant k - l$, and its dependance on β has been omitted for the sake of clarity.

We begin by considering $\mathcal{R}^{+,+}_{\mathcal{P},\mathcal{Q}}$ which is given by

$$\mathcal{R}_{\mathcal{P},\mathcal{Q}} = \prod_{i=1}^{m} \frac{\left\langle \vec{i} \bigoplus_{j=1}^{i} \vec{\alpha}^{\mathcal{P}_j} \bigoplus_{k=1}^{m^i} \vec{\alpha}^{p^i_k} | S^+_{\mathcal{P}[i]} \prod_{j=1}^{m^i} B_{p^i_j} [S^+_{\mathcal{P}[i]}]^\dagger | \vec{i} \bigoplus_{j=1}^{i} \vec{\alpha}^{\mathcal{P}_j} \right\rangle}{\left\langle \vec{i} \bigoplus_{j=1}^{i-1} \vec{\alpha}^{\mathcal{P}_j} \bigoplus_{k=1}^{m^i} \vec{\alpha}^{p^i_k} | S^+_{\mathcal{P}[i-1]} \prod_{j=1}^{m^i} B_{p^i_j} [S^+_{\mathcal{P}[i-1]}]^\dagger | \vec{i} \bigoplus_{j=1}^{i-1} \vec{\alpha}^{\mathcal{P}_j} \right\rangle} \times \prod_{i=1}^{n} \frac{\left\langle \vec{i} \bigoplus_{j=1}^{i-1} \vec{\alpha}^{\mathcal{Q}_j} \bigoplus_{k=1}^{n^i} \vec{\alpha}^{q^i_k} | B_p (\prod_{j=1}^{n^i} B_{q^i_j} B_p) | \vec{i} \bigoplus_{j=1}^{i-1} \vec{\alpha}^{\mathcal{Q}_j} \right\rangle}{\left\langle \vec{i} \bigoplus_{j=1}^{i} \vec{\alpha}^{\mathcal{Q}_j} \bigoplus_{k=1}^{n^i} \vec{\alpha}^{q^i_k} | B_p (\prod_{j=1}^{n^i} B_{q^i_j} B_p) | \vec{i} \bigoplus_{j=1}^{i} \vec{\alpha}^{\mathcal{Q}_j} \right\rangle}, \tag{C26}$$

where we have defined

$$S^{+}_{\mathcal{P}[i]} = \begin{cases} 1 & \text{for} \quad i < i_{b_1}, \\ S^{+}_{\mathcal{P}_{i_{b_1}}} \ldots S^{+}_{\mathcal{P}_{i_{b_j}}} & \text{for} \quad i_{b_j} \leqslant i < i_{b_{j+1}},\ j < l \\ S^{+}_{\mathcal{P}_{i_{b_1}}} \ldots S^{+}_{\mathcal{P}_{i_{b_l}}} & \text{for} \quad i \geqslant i_{b_l}, \end{cases} \tag{C27}$$

and where B_p is the plaquette operator associated to plaquette p. We thus get

$$\begin{aligned} \mathcal{R}_{\mathcal{P},\mathcal{Q}} = \prod_{\substack{i=1 \\ i\notin\{i_{b_1},\ldots,i_{b_l}\}}}^{m} & \frac{\left\langle \vec{i} \bigoplus^{i}_{\substack{j=1 \\ j\notin\{i_{b_1},\ldots,i_{b_l}\}}} \vec{\alpha}^{\mathcal{P}_j} \bigoplus_{k=1}^{m^i} \vec{\alpha}^{p^i_k} \middle| \prod_{j=1}^{m^i} B_{p^i_j} \middle| \vec{i} \bigoplus^{i}_{\substack{j=1 \\ j\notin\{i_{b_1},\ldots,i_{b_l}\}}} \vec{\alpha}^{\mathcal{P}_j} \right\rangle}{\left\langle \vec{i} \bigoplus^{i-1}_{\substack{j=1 \\ j\notin\{i_{b_1},\ldots,i_{b_l}\}}} \vec{\alpha}^{\mathcal{P}_j} \bigoplus_{k=1}^{m^i} \vec{\alpha}^{p^i_k} \middle| \prod_{j=1}^{m^i} B_{p^i_j} \middle| \vec{i} \bigoplus^{i-1}_{\substack{j=1 \\ j\notin\{i_{b_1},\ldots,i_{b_l}\}}} \vec{\alpha}^{\mathcal{P}_j} \right\rangle} \\ \times \prod_{i=1}^{n} & \frac{\left\langle \vec{i} \bigoplus^{i-1} \vec{\alpha}^{\mathcal{Q}_j} \bigoplus_{k=1}^{n^i} \vec{\alpha}^{q^i_k} \oplus \vec{\alpha}^{p} \middle| \prod_{j=1}^{n^i} B_{q^i_j} B_p \middle| \vec{i} \bigoplus_{j=1}^{i-1} \vec{\alpha}^{\mathcal{Q}_j} \right\rangle}{\left\langle \vec{i} \bigoplus_{j=1}^{i} \vec{\alpha}^{\mathcal{Q}_j} \bigoplus_{k=1}^{n^i} \vec{\alpha}^{q^i_k} \oplus \vec{\alpha}^{p} \middle| \prod_{j=1}^{n^i} B_{q^i_j} B_p \middle| \vec{i} \bigoplus_{j=1}^{i} \vec{\alpha}^{\mathcal{Q}_j} \right\rangle} \\ \times \prod_{j=1}^{l} & F_{\mathcal{P}_{i_{b_j}}}\left(\vec{i} \oplus \vec{\alpha}^{\mathcal{P}} \oplus \vec{\alpha}^{\mathcal{Q}} \bigoplus_{i=1}^{j-1} \vec{\alpha}^{\mathcal{P}_{i_{b_i}}}\right) F_{\mathcal{P}_{i_{b_j}}}\left(\vec{i} \oplus \vec{\alpha}^{\mathcal{P}} \bigoplus_{i=1}^{j} \vec{\alpha}^{\mathcal{P}_{i_{b_i}}}\right) \\ \times & \frac{b_p(\vec{i} \oplus \vec{\alpha}^{\mathcal{P}})}{b_p(\vec{i} \oplus \vec{\alpha}^{\mathcal{P}} \oplus \vec{\alpha}^{\mathcal{Q}})}, \end{aligned} \tag{C28}$$

where we have implicitly used our freedom in choosing the sets of plaquettes $\mathcal{B}^{\mathcal{Q},a_i}_{\mathcal{P}_i}$, $\mathcal{B}^{\mathcal{P},b_j}_{\mathcal{Q}_j}$ and of adding plaquettes if necessary without affecting the value of $\mathcal{R}_{\mathcal{P},\mathcal{Q}}$ in order to have that on $\mathrm{Conn}(\mathcal{P}_{i_{b_j}})$, we have that $\bigoplus_{k=1}^{m^i} \vec{\alpha}^{p^i_k} = \vec{\alpha}^{\mathcal{Q}}$ for any $i \in \{1, \ldots, m\}$ and for any $j \in \{1, \ldots, l\}$, and where we also have modified the set of plaquettes $\mathcal{B}^{\mathcal{P},b_j}_{\mathcal{Q}_j}$ so that on $\mathrm{Conn}(\mathcal{P}_p)$, $\bigoplus_{k=1}^{n^j} \vec{\alpha}^{q^j_k} = \vec{\alpha}^{\mathcal{P}}$ for any $j \in \{1, \ldots, n\}$ and such that $\bigcup_\beta \mathcal{B}^{\mathcal{P}^p_\beta, b_{\beta,j}}_{\mathcal{Q}_j} = \mathcal{B}^{\mathcal{P},b_j}_{\mathcal{Q}_j} \cup \{p\}$.

We next introduce the various individual paths $\mathcal{P}'_{i_{b_{l+1}}}, \ldots, \mathcal{P}'_{i_{b_k}}$ and rearrange the terms in an appropriate order so as to explicitly make appear the various $\mathcal{P}^p_\beta$'s. Note that in order to do so, we used the fact that the various paths do not have support on the other path's connected regions. We get

$$\begin{aligned} \mathcal{R}_{\mathcal{P},\mathcal{Q}} = \prod_\beta & \left(\prod_{i=1}^{m^\beta} \frac{\left\langle \vec{i} \bigoplus_{j=1}^{i} \vec{\alpha}^{\mathcal{P}^p_\beta j} \bigoplus_{k=1}^{m^{\beta,i}} \vec{\alpha}^{p^{\beta,i}_k} \middle| S^{+}_{\mathcal{P}^p_\beta[i]} \prod_{j=1}^{m^{\beta,i}} B_{p^{\beta,i}_j} [S^{+}_{\mathcal{P}^p_\beta[i]}]^\dagger \middle| \vec{i} \bigoplus_{j=1}^{i} \vec{\alpha}^{\mathcal{P}^p_\beta j} \right\rangle}{\left\langle \vec{i} \bigoplus_{j=1}^{i-1} \vec{\alpha}^{\mathcal{P}^p_\beta j} \bigoplus_{k=1}^{m^{\beta,i}} \vec{\alpha}^{p^{\beta,i}_k} \middle| S^{+}_{\mathcal{P}^p_\beta[i-1]} \prod_{j=1}^{m^{i}} B_{p^{\beta,i}_j} [S^{+}_{\mathcal{P}^p_\beta[i-1]}]^\dagger \middle| \vec{i} \bigoplus_{j=1}^{i-1} \vec{\alpha}^{\mathcal{P}^p_\beta j} \right\rangle} \right) \\ \times \prod_\beta & \left(\prod_{i=1}^{n^\beta} \frac{\left\langle \vec{i} \bigoplus^{i-1} \vec{\alpha}^{\mathcal{Q}_j} \bigoplus_{k=1}^{n^{\beta,i}} \vec{\alpha}^{q^{\beta,i}_k} \middle| \prod_{j=1}^{n^{\beta,i}} B_{q^{\beta,i}_j} \middle| \vec{i} \bigoplus_{j=1}^{i-1} \vec{\alpha}^{\mathcal{Q}_j} \right\rangle}{\left\langle \vec{i} \bigoplus_{j=1}^{i} \vec{\alpha}^{\mathcal{Q}_j} \bigoplus_{k=1}^{n^{\beta,i}} \vec{\alpha}^{q^{\beta,i}_k} \middle| \prod_{j=1}^{n^{\beta,i}} B_{q^{\beta,i}_j} \middle| \vec{i} \bigoplus_{j=1}^{i} \vec{\alpha}^{\mathcal{Q}_j} \right\rangle} \right) \\ \times & \left(\prod_{j=1}^{l} \frac{F_{\mathcal{P}_{i_{b_j}}}\left(\vec{i} \oplus \vec{\alpha}^{\mathcal{P}} \oplus \vec{\alpha}^{\mathcal{Q}} \bigoplus_{i=1}^{j-1} \vec{\alpha}^{\mathcal{P}_{i_{b_i}}}\right)}{F_{\mathcal{P}_{i_{b_j}}}\left(\vec{i} \oplus \vec{\alpha}^{\mathcal{P}} \bigoplus_{i=1}^{j-1} \vec{\alpha}^{\mathcal{P}_{i_{b_i}}}\right)} \right) \frac{b_p(\vec{i} \oplus \vec{\alpha}^{\mathcal{P}})}{b_p(\vec{i} \oplus \vec{\alpha}^{\mathcal{P}} \oplus \vec{\alpha}^{\mathcal{Q}})}, \end{aligned} \tag{C29}$$

where we have defined

$$S^{+}_{\mathcal{P}^p_\beta[i]} = \begin{cases} 1 & \text{for} i < i_{\beta_1} \\ S^{+}_{\mathcal{P}_\beta, i_{\beta_1}} \ldots S^{+}_{\mathcal{P}_\beta, i_{\beta_j}} & \text{for} i_{\beta_j} \leqslant i < i_{\beta_{j+1}},\ j < l' \\ S^{+}_{\mathcal{P}_\beta, i_{\beta_1}} \ldots S^{+}_{\mathcal{P}_\beta, i_{\beta_l}} & \text{for} i \geqslant i_{\beta_{l'}}, \end{cases} \tag{C30}$$

and where we have $\{p^{\beta,i}_j\} = \mathcal{B}^{\mathcal{Q},a_\beta,i}_{\mathcal{P}_\beta,i}$, $\{q^{\beta,i}_j\} = \mathcal{B}^{\mathcal{P}_\beta,i,b_{\beta,i}}_{\mathcal{Q}}$.

Under close inspection, it thus becomes clear that

$$\mathcal{R}_{\mathcal{P},\mathcal{Q}} = \prod_\beta \mathcal{R}_{\mathcal{P}^p_\beta} \times \left(\prod_{j=1}^{k} \frac{F_{\mathcal{P}_{i_{b_j}}}\left(\vec{i} \oplus \vec{\alpha}^{\mathcal{P}} \oplus \vec{\alpha}^{\mathcal{Q}} \bigoplus_{i=1}^{j-1} \vec{\alpha}^{\mathcal{P}_{i_{b_i}}}\right)}{F_{\mathcal{P}_{i_{b_j}}}\left(\vec{i} \oplus \vec{\alpha}^{\mathcal{P}} \bigoplus_{i=1}^{j-1} \vec{\alpha}^{\mathcal{P}_{i_{b_i}}}\right)} \right) \frac{b_p(\vec{i} \oplus \vec{\alpha}^{\mathcal{P}})}{b_p(\vec{i} \oplus \vec{\alpha}^{\mathcal{P}} \oplus \vec{\alpha}^{\mathcal{Q}})}. \tag{C31}$$

We first notice that since all the paths $\mathcal{P}^p_\beta$ and $\mathcal{P}$ cross with path $\mathcal{Q}$, we can define $\mathcal{B}^{\mathcal{Q}}_{\mathcal{P}_p} = \{p_{\mathcal{Q},1}, \ldots, p_{\mathcal{Q},o}\}$, a set of plaquettes in $\mathcal{B}_{\mathcal{P}_p}$ such that on Conn($\mathcal{P}_b$), we have that $\bigoplus_{i=1}^{o} \vec{\alpha}^{p_{\mathcal{Q},i}} = \vec{\alpha}^{\mathcal{Q}}$. Using the same reasoning as in lemma 9, we find that

$$\frac{b_p(\vec{i} \oplus \vec{\alpha}^{\mathcal{P}})}{b_p(\vec{i} \oplus \vec{\alpha}^{\mathcal{P}} \oplus \vec{\alpha}^{\mathcal{Q}})} = \frac{\left\langle \vec{i} \oplus \vec{\alpha}^{\mathcal{P}} \bigoplus_{i=1}^{o} \vec{\alpha}^{p_{\mathcal{Q},i}} \middle| \prod_{i=1}^{o} B_{p_{\mathcal{Q},i}} \middle| \vec{i} \oplus \vec{\alpha}^{\mathcal{P}} \right\rangle}{\left\langle \vec{i} \oplus \vec{\alpha}^{\mathcal{P}} \oplus \vec{\alpha}^{\mathcal{P}_p} \bigoplus_{i=1}^{o} \vec{\alpha}^{p_{\mathcal{Q},i}} \middle| \prod_{i=1}^{o} B_{p_{\mathcal{Q},i}} \middle| \vec{i} \oplus \vec{\alpha}^{\mathcal{P}} \oplus \vec{\alpha}^{\mathcal{P}_p} \right\rangle}. \tag{C32}$$

On the other hand, we find that

$$\begin{aligned} \prod_{j=1}^{k} \frac{F_{\mathcal{P}_{i_{b_j}}}\left(\vec{i} \oplus \vec{\alpha}^{\mathcal{P}} \oplus \vec{\alpha}^{\mathcal{Q}} \bigoplus_{i=1}^{j-1} \vec{\alpha}^{\mathcal{P}_{i_{b_i}}}\right)}{F_{\mathcal{P}_{i_{b_j}}}\left(\vec{i} \oplus \vec{\alpha}^{\mathcal{P}} \bigoplus_{i=1}^{j-1} \vec{\alpha}^{\mathcal{P}_{i_{b_i}}}\right)} &= \prod_{j=1}^{k} \frac{\left\langle \vec{i} \oplus \vec{\alpha}^{\mathcal{P}} \bigoplus_{i=1}^{o} \vec{\alpha}^{p_{\mathcal{Q},i}} \bigoplus_{i=1}^{j} \vec{\alpha}^{\mathcal{P}_{i_{b_i}}} \middle| \prod_{i=1}^{o} B_{p_{\mathcal{Q},i}} \middle| \vec{i} \oplus \vec{\alpha}^{\mathcal{P}} \bigoplus_{i=1}^{j} \vec{\alpha}^{\mathcal{P}_{i_{b_i}}} \right\rangle}{\left\langle \vec{i} \oplus \vec{\alpha}^{\mathcal{P}} \bigoplus_{i=1}^{o} \vec{\alpha}^{p_{\mathcal{Q},i}} \bigoplus_{i=1}^{j-1} \vec{\alpha}^{\mathcal{P}_{i_{b_i}}} \middle| \prod_{i=1}^{o} B_{p_{\mathcal{Q},i}} \middle| \vec{i} \oplus \vec{\alpha}^{\mathcal{P}} \bigoplus_{i=1}^{j-1} \vec{\alpha}^{\mathcal{P}_{i_{b_i}}} \right\rangle} \\ &= \frac{\left\langle \vec{i} \oplus \vec{\alpha}^{\mathcal{P}} \oplus \vec{\alpha}^{\mathcal{P}_p} \bigoplus_{i=1}^{o} \vec{\alpha}^{p_{\mathcal{Q},i}} \middle| \prod_{i=1}^{o} B_{p_{\mathcal{Q},i}} \middle| \vec{i} \oplus \vec{\alpha}^{\mathcal{P}} \oplus \vec{\alpha}^{\mathcal{P}_p} \right\rangle}{\left\langle \vec{i} \oplus \vec{\alpha}^{\mathcal{P}} \bigoplus_{i=1}^{o} \vec{\alpha}^{p_{\mathcal{Q},i}} \middle| \prod_{i=1}^{o} B_{p_{\mathcal{Q},i}} \middle| \vec{i} \oplus \vec{\alpha}^{\mathcal{P}} \right\rangle}. \end{aligned} \tag{C33}$$

Putting equations (C31)–(C33) together, we conclude that

$$\mathcal{R}_{\mathcal{P},\mathcal{Q}} = \prod_{\beta} \mathcal{R}_{\mathcal{P}^p_\beta}. \tag{C34}$$

To finally conclude the proof, we remark that according to lemma 11 we are free to modify the composition in terms of individual paths of the various $\{\mathcal{P}^p_\beta\}$'s as long as the their individual paths remain non self-overlapping nor self-crossing. □

Lemma 14. *Let $\mathcal{P}$ and $\mathcal{Q}$ be two crossing paths such that each of them is made of simple non self-overlapping nor self-crossing open paths, and such that $\mathcal{P}$ is not self-crossing. If they cross an even number of times, then $\mathcal{R}_{\mathcal{P},\mathcal{Q}} = 1$.*

Proof. The idea of the proof is to deform the path $\mathcal{P}$ using the results of lemma 13, as well as path $\mathcal{Q}$ by some elongation and reductions using lemma 12, in order to get a set of paths $\{\mathcal{P}_\beta\}$ and path $\mathcal{Q}'$ such that $\mathcal{R}_{\mathcal{P},\mathcal{Q}} = \prod_\beta \mathcal{R}_{\mathcal{P}_\beta,\mathcal{Q}'}$, and such that all of them are outside of Conn($\mathcal{Q}'$), thus implying that $R_{\mathcal{P}_\beta,\mathcal{Q}} = 1$.

We first note that if $\mathcal{P}$ and $\mathcal{Q}$ do not have any edges in common, then they trivially commute, since by supposition they are crossing each other. This implies that $\mathcal{R}_{\mathcal{P},\mathcal{Q}} = 1$.

Consider the case where $\mathcal{P}$ and $\mathcal{Q}$ have some edges in common. Suppose first that $\mathcal{P}$ and $\mathcal{Q}$ have a single contiguous set of common edges, $\mathcal{E}$. In that case, the path $\mathcal{P}$ can be sequentially deformed along the set of contiguous plaquettes in Conn($\mathcal{Q}$) containing the edges in $\mathcal{E}$ as well as the two edges in $\mathcal{P}\backslash\mathcal{E}$ sharing vertices with the edges in $\mathcal{E}$ in order to give a new sets of paths $\{\mathcal{P}_\beta\}$. Note that since $\mathcal{P}$ and $\mathcal{Q}$ cross 0 times, we can assume that none of the paths in $\{\mathcal{P}_\beta\}$ contains edges in Conn($\mathcal{Q}$). If it is not the case, then we can use lemma 12 to first find a shorter path $\mathcal{Q}'$ such that $\mathcal{R}_{\mathcal{P},\mathcal{Q}} = \mathcal{R}_{\mathcal{P},\mathcal{Q}'}$ and for which it is true. By suitably choosing a decomposition of those plaquettes such that they are non self-overlapping nor self-crossing, we can use lemma 13, to find that $\mathcal{R}_{\mathcal{P},\mathcal{Q}} = \prod_\beta \mathcal{R}_{\mathcal{P}_\beta,\mathcal{Q}} = 1$.

Suppose next that $\mathcal{P}$ and $\mathcal{Q}$ have two or more different contiguous sets of common edges $\{\mathcal{E}_i\}$. In that case, we can deform $\mathcal{P}$ by a subset of plaquettes in $\mathcal{B}_\mathcal{Q}$ so as to form a single contiguous set of common edges $\mathcal{E}$ such that $\mathcal{E} \cup \delta\mathcal{E} \supset \bigcup_i \mathcal{E}_i$, where $\delta\mathcal{E}$ denotes the first and last edges in $\mathcal{Q}$ which are also in $\mathcal{E}$, and such that all newly formed paths $\{\mathcal{P}_\beta\}$ cross $\mathcal{Q}$, where we have again chosen a suitable decomposition of the paths along the plaquettes. Again using lemma 13 and considering a shortened path $\mathcal{Q}'$ using lemma 12 if necessary, we find that $\mathcal{R}_{\mathcal{P},\mathcal{Q}} = \prod_\beta \mathcal{R}_{\mathcal{P}_\beta,\mathcal{Q}'}$, where one of the $\mathcal{P}_\beta$'s have a single set of edges ($\mathcal{E}$) in common with $\mathcal{Q}'$, and where the other paths cross 0 times with $\mathcal{Q}'$. Since modifying the path $\mathcal{P}$ by a set of plaquettes cannot change the parity of the number of crossing, we have that the former path crosses 0 times with $\mathcal{Q}'$ as well. By the previous reasoning, we thus find that $\mathcal{R}_{\mathcal{P},\mathcal{Q}} = 1$. □

Lemma 15. *Let $\mathcal{P}$ and $\mathcal{Q}$ be two crossing paths such that each of them is made of simple non self-overlapping nor self-crossing open paths, and such that $\mathcal{P}$ is not self-crossing. If they cross an* odd *number of times, then $\mathcal{R}_{\mathcal{P},\mathcal{Q}} = -1$.*

Proof. The idea of the proof closely follows that of lemma 14. We begin by sequentially deforming the path $\mathcal{P}$ into a set of paths $\{\mathcal{P}_\beta\}$ such that all of them are crossing with path $\mathcal{Q}$, and such that there is a single set of contiguous edges between one of the path $\mathcal{P}_o \in \{\mathcal{P}_\beta\}$ and $\mathcal{Q}$, and such that $\mathcal{R}_{\mathcal{P},\mathcal{Q}} = \prod_\beta \mathcal{R}_{\mathcal{P}_\beta,\mathcal{Q}'}$, where $\mathcal{Q}'$ may be a shortened path of $\mathcal{Q}$, as described in the proof of lemma 14. Since any path $\mathcal{P}_\beta \neq \mathcal{P}_o$ crosses path $\mathcal{Q}'$ 0 times, we have that $\mathcal{R}_{\mathcal{P}_\beta,\mathcal{Q}} = 1$ for $\beta \neq o$. We thus have that $\mathcal{R}_{\mathcal{P},\mathcal{Q}} = \mathcal{R}_{\mathcal{P}_o,\mathcal{Q}'}$.

In order to calculate $\mathcal{R}_{\mathcal{P}_o,\mathcal{Q}'}$, we note that we can first sequentially deform path $\mathcal{P}_o$ as described previously so that there is a single common edge between the two paths, and we can use lemma 12 to bring the endpoints of the

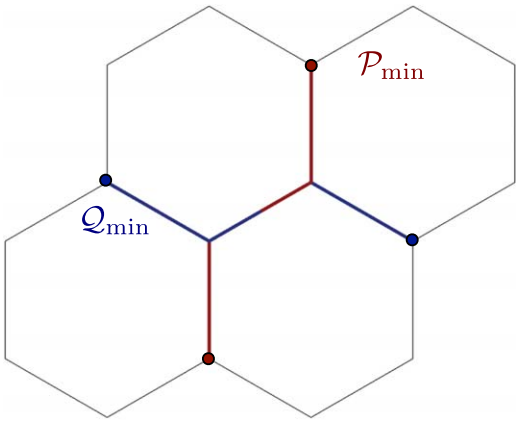

Figure C4. The quantity $\mathcal{R}_{\mathcal{P},\mathcal{Q}}$ for 2 paths $\mathcal{P}$ and $\mathcal{Q}$ crossing an odd number of times is equal to $\mathcal{R}_{\mathcal{P}_{\min},\mathcal{Q}_{\min}}$, for the minimal paths $\mathcal{P}_{\min}$ and $\mathcal{Q}_{\min}$ shown above.

two paths as close as possible in order to minimize the length of the paths. We thus find that computing $\mathcal{R}_{\mathcal{P},\mathcal{Q}}$ reduces to computing this quantity for a single minimal path configurations $\mathcal{P}_{\min}$ and $\mathcal{Q}_{\min}$ illustrated in figure C4. Explicit calculations using equation (C3) for a single underlying string configuration (lemma 10 ensures that its value is independent of the configuration), gives that $\mathcal{R}_{\mathcal{P}_{\min},\mathcal{Q}_{\min}} = -1$. □

C.2. Proof of theorem 2

Having introduced all previous technical lemmas, we are in a position to complete the demonstration of theorem 2.

Theorem 2. *Let $\mathcal{P}$ and $\mathcal{Q}$ be two paths crossing n times, composed of non self-overlapping nor self-crossing individual open paths. We have that*

$$[S^+_{\mathcal{P}},\, S^+_{\mathcal{Q}}] = 0 \text{ if } n \text{ is even},$$
$$\{S^+_{\mathcal{P}},\, S^+_{\mathcal{Q}}\} = 0 \text{ if } n \text{ is odd}. \tag{C35}$$

Proof. Consider first the case where path $\mathcal{P}$ is not self-crossing. Given the definition in equation (C3) of $\mathcal{R}_{\mathcal{P},\mathcal{Q}}$, lemma 14 shows that $[S^+_{\mathcal{P}},\, S^+_{\mathcal{Q}}] = 0$ if n is even, while lemma 15 shows that $\{S^+_{\mathcal{P}},\, S^+_{\mathcal{Q}}\} = 0$ is n is odd.

Consider next the case where $\mathcal{P}$ is self-crossing. Using lemma 11, we can always find paths $\mathcal{P}_1, \ldots, \mathcal{P}_m$ for which $\mathcal{P} = \mathcal{P}_1\#...\#\mathcal{P}_m$, such that none of those are self-crossing, with $\mathcal{R}_{\mathcal{P}_1\#...\#\mathcal{P}_m,\mathcal{Q}} = \mathcal{R}_{\mathcal{P},\mathcal{Q}}$. Suppose that all those paths cross with $\mathcal{Q}$. Since $S^+_{\mathcal{P}_1\#...\#\mathcal{P}_m} = S^+_{\mathcal{P}_m}...S^+_{\mathcal{P}_1}$, it suffices to know the commutation relations between every of the operators $S^+_{\mathcal{P}_1}, \ldots, S^+_{\mathcal{P}_m}$ and $S^+_{\mathcal{Q}}$. Since none of the corresponding paths are self-overlapping, the reasoning of the above paragraph can be used to find the same result.

It may be impossible to decompose path $\mathcal{P} = \mathcal{P}_1\#...\#\mathcal{P}_m$ such that all of its components cross with $\mathcal{Q}$. This happens only in the case where some edges in path $\mathcal{P}$ appear at more than one position. In that case, suppose for simplicity that path $\mathcal{P} = \mathcal{P}_1\#...\#\mathcal{P}_{l-1}\#\mathcal{P}_l\#\mathcal{P}_{l+1}\#...\#\mathcal{P}_{o-1}\#\mathcal{P}_o\#\mathcal{P}_{o+1}\#...\#\mathcal{P}_m$ can be decomposed such that pahts $\mathcal{P}_l = \mathcal{P}_o$ are the only ones with edges in common (possibly in reversed order). The following reasoning works in the same way if there are more than a single pair of such paths. Consider the quantity

$$\begin{aligned}
&\prod_{i=1}^{m} \frac{\left\langle \vec{i} \bigoplus_{j=1}^{i} \vec{\alpha}^{\mathcal{P}_j} \bigoplus_{k=1}^{m^i} \vec{\alpha}^{p^i_k} | S^+_{\mathcal{P}[i]} \prod_{j=1}^{m^i} B_{p^i_j} S^+_{\mathcal{P}[i]} | \vec{i} \bigoplus_{j=1}^{i} \vec{\alpha}^{\mathcal{P}_j} \right\rangle}{\left\langle \vec{i} \bigoplus_{j=1}^{i-1} \vec{\alpha}^{\mathcal{P}_j} \bigoplus_{k=1}^{m^i} \vec{\alpha}^{p^i_k} | S^+_{\mathcal{P}[i-1]} \prod_{j=1}^{m^i} B_{p^i_j} S^+_{\mathcal{P}[i-1]} | \vec{i} \bigoplus_{j=1}^{i-1} \vec{\alpha}^{\mathcal{P}_j} \right\rangle} \\
&= \prod_{\substack{i=1 \\ i\neq l,o}}^{m} \frac{\left\langle \vec{i} \bigoplus_{j=1}^{i} \vec{\alpha}^{\mathcal{P}_j} \bigoplus_{k=1}^{m^i} \vec{\alpha}^{p^i_k} | \prod_{j=1}^{m^i} B_{p^i_j} | \vec{i} \bigoplus_{j=1}^{i} \vec{\alpha}^{\mathcal{P}_j} \right\rangle}{\left\langle \vec{i} \bigoplus_{j=1}^{i-1} \vec{\alpha}^{\mathcal{P}_j} \bigoplus_{k=1}^{m^i} \vec{\alpha}^{p^i_k} | \prod_{j=1}^{m^i} B_{p^i_j} | \vec{i} \bigoplus_{j=1}^{i-1} \vec{\alpha}^{\mathcal{P}_j} \right\rangle} \\
&\quad \times \prod_{i=l}^{o-1} \frac{F_{\mathcal{P}_l}(\vec{i} \bigoplus_{j=1}^{i} \alpha^{\mathcal{P}_j} \bigoplus_{k=1}^{m^i} \vec{\alpha}^{p^i_k} \oplus \vec{\alpha}^{\mathcal{P}_l})}{F_{\mathcal{P}_l}(\vec{i} \bigoplus_{j=1}^{i} \alpha^{\mathcal{P}_j} \bigoplus_{k=1}^{m^{i+1}} \vec{\alpha}^{p^{i+1}_k} \oplus \vec{\alpha}^{\mathcal{P}_l})},
\end{aligned} \tag{C36}$$

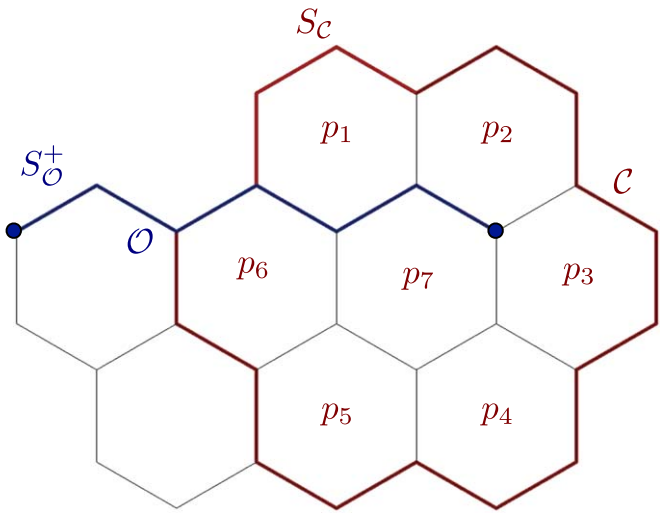

Figure C5. A closed string, $S_{\mathcal{C}}$, and a positive-chirality open string, $S^+_{\mathcal{O}}$, where paths $\mathcal{O}$ and $\mathcal{C}$ cross once. $\vec{\alpha}^{\mathcal{C}}$ can be written in this particular example as $\vec{\alpha}^{\mathcal{C}} = \vec{\alpha}^{p_1} \oplus ... \oplus \vec{\alpha}^{p_6}$, restricted to Conn$(\mathcal{C})$. The multiplication of plaquettes inside $\mathcal{C}$, i.e. $B_{p_1} ... B_{p_7}$ is a negative-chirality string in Conn$(\mathcal{C})$.

where

$$S^+_{\mathcal{P}[i]} = \begin{cases} S^+_{\mathcal{P}_l} & \text{if} l \leqslant i < o \\ 1 & \text{otherwise.} \end{cases} \tag{C37}$$

Using lemma 11, for any $i \in \{l, \ldots, o\}$ it is always possible to find a path decomposition and sets of plaquettes $\mathcal{B}^{\mathcal{Q},a_i}_{\mathcal{P}_i}$ such that on Conn$(\mathcal{P}_l)$, $\bigoplus_{k=1}^{m^i} \vec{\alpha}^{p^i_k} = \vec{\alpha}^{\mathcal{Q}}$. This can simply be achieved by taking individual paths of lenght 1 in the decomposition of path $\mathcal{P}$. We thus find that

$$\prod_{i=l}^{o-1} \frac{F_{\mathcal{P}_l}(\vec{i} \bigoplus_{j=1}^{i} \alpha^{\mathcal{P}_j} \bigoplus_{k=1}^{m^i} \vec{\alpha}^{p^i_k} \oplus \vec{\alpha}^{\mathcal{P}_l})}{F_{\mathcal{P}_l}(\vec{i} \bigoplus_{j=1}^{i} \alpha^{\mathcal{P}_j} \bigoplus_{k=1}^{m^{i+1}} \vec{\alpha}^{p^{i+1}_k} \oplus \vec{\alpha}^{\mathcal{P}_l})} = 1, \tag{C38}$$

which, given equation (C4), leads us to the conclusion that

$$\mathcal{R}_{\mathcal{P}_1\#...\#\mathcal{P}_{l-1}\#\mathcal{P}_l\#\mathcal{P}_{l+1}\#...\#\mathcal{P}_{o-1}\#\mathcal{P}_o\#\mathcal{P}_{o+1}\#...\#\mathcal{P}_m,\mathcal{Q}} = \mathcal{R}_{\mathcal{P}_1\#...\#\mathcal{P}_{l-1}\#\mathcal{P}_{l+1}\#...\#\mathcal{P}_{o-1}\#\mathcal{P}_{o+1}\#...\#\mathcal{P}_m,\mathcal{Q}}. \tag{C39}$$

To complete the proof, it suffices to notice that we can now apply the reasoning of the first two paragraphs of this proof. □

C.3. The need for path concatenation

Each time algorithm 1 picks a configuration representative $\vec{i}$, an initial phase must be chosen. All of these choices yield valid string operators. One may wonder what is the physical difference between different choices. To answer this question, note that two string operators $S^+_{\mathcal{P}}$ and $\tilde{S}^+_{\mathcal{P}}$ obtained by a different choice of phases in algorithm 1 are related through

$$\tilde{S}^+_{\mathcal{P}} = S^+_{\mathcal{P}} \sum_{c \in \mathcal{C}_{\mathcal{P}}} e^{i\theta_c} P_c, \tag{C40}$$

where $\mathcal{C}_{\mathcal{P}}$ denotes the set of all configuration classes of path $\mathcal{P}$, $P_c = \sum_{\vec{i} \in c} |\vec{i}\rangle \langle \vec{i}|$ is the projector on the states of configuration class c, and $e^{i\theta_c}$ is an independent arbitrary complex phase for every class configuration.

Equivalently, given a string operator $S^+_{\mathcal{P}}$, we can obtain another string operator $\tilde{S}^+_{\mathcal{P}}$ multiplying $S^+_{\mathcal{P}}$ by an operator $S^z_{\mathcal{C}_{\text{dual}}}$, where $\mathcal{C}_{\text{dual}}$ is a closed loop in the dual lattice affecting only qubits in Conn$(\mathcal{P})$. Since $S^z_{\mathcal{C}_{\text{dual}}}$ is a loop, it may be expressed as a multiplication of vertex operators (unless it is a non-trivial loop, which may happen for closed strings). Therefore $\tilde{S}^+_{\mathcal{P}}$ still commutes with all plaquette and vertex operators and it is contained in Conn$(\mathcal{P})$, satisfying properties (i) and (ii). It is also possible to obtain another string operator multiplying $S^+_{\mathcal{P}}$ by a linear combination of S^z operators on closed loops, i.e.

$$\tilde{S}^+_{\mathcal{P}} = S^+_{\mathcal{P}}(\mathbb{I} + c(\vec{\alpha}^{\mathcal{C}_1}) S^z_{\mathcal{C}_1} + c(\vec{\alpha}^{\mathcal{C}_2}) S^z_{\mathcal{C}_2} + ...), \tag{C41}$$

where $c(\vec{\alpha}^{\mathcal{C}}_i)$ are coefficients associated with the closed-string operator $S^z_{\mathcal{C}}$ and $\mathcal{C}_1, ..., \mathcal{C}_n$ are closed paths in the dual lattice contained in Conn$(\mathcal{P})$. For any two strings generated by algorithm 1 differing only in the choice of initial phases, we can always find a relation of the form given by equation (C41).

C.3.1. Closed-string operators. If we consider now a closed path, $\mathcal{C}$, and we use algorithm 1 to find a closed-string operator, we will not find in general a positive-chirality nor a negative-chirality string, but some mixing of both. Physically, this is caused by the fact that for a closed string there is no difference in the pattern of plaquette violations between positive- and negative-chirality strings, since there are no endpoints. From equation (C41) we can see that starting from a positive-chirality string, $S_{\mathcal{C}}^{+}$, it is possible to add S^z operators forming a loop which cannot be expressed as the product of vertex operators (which we call a non trivial loop in the remainder of the section) to the linear superposition. Once this is done, the resulting operator, $\tilde{S}_{\mathcal{C}}$, does not have a well-defined chirality. Remember, that for an open string, we may obtain the negative-chirality string by multiplying it by an open string S^z, violating the plaquettes at the endpoints. For closed strings we may proceed analogously to obtain the opposite chirality by multiplying by a non-trivial closed string $S_{\mathcal{C}'}^{z}$. Since we are multiplying $S_{\mathcal{C}}^{+}$ by a linear combination of trivial and non-trivial loops of S^z, the chirality of $\tilde{S}_{\mathcal{C}}$ is no longer positive nor negative. Thus, we drop the '+' superscript in $\tilde{S}_{\mathcal{C}}$.

The mixing of chiralities becomes apparent when computing the commutator between a closed string, $S_{\mathcal{C}}$, and a positive-chirality open string, $S_{\mathcal{O}}^{+}$, where paths $\mathcal{C}$ and $\mathcal{O}$ cross once (see figure C5):

$$\mathcal{R}_{\mathcal{O},\mathcal{C}} = \langle \vec{i} \; | [S_{\mathcal{O}}^{+}, S_{\mathcal{C}}] | \vec{i} \rangle = \frac{F_{\mathcal{O}}(\vec{i} \oplus \vec{\alpha}^{\mathcal{C}}) F_{\mathcal{C}}(\vec{i})}{F_{\mathcal{O}}(\vec{i}) F_{\mathcal{C}}(\vec{i} \oplus \vec{\alpha}^{\mathcal{O}})}, \tag{C42}$$

where here $[\cdot,\cdot]$ is the commutator in the group sense, i.e. $[g,\ h] = g^{-1}h^{-1}gh$. In this case, notice that on $\mathrm{Conn}(\mathcal{C})$, the configurations $\vec{i}$ and $\vec{i} \oplus \vec{\alpha}^{\mathcal{O}}$ do not belong to the same class. Using equation (C40), it is thus clear that $\mathcal{R}_{\mathcal{O},\mathcal{C}}$ can be modified by selecting different phases to initialize $F_{\mathcal{C}}$ in algorithm 1.

References

[1] Kitaev A Y 2003 Fault-tolerant quantum computation by anyons *Ann. Phys.* **303** 2–30
[2] Dennis E, Kitaev A, Landahl A and Preskill J 2002 Topological quantum memory *J. Math. Phys.* **43** 4452–505
[3] Bravyi S B and Kitaev A Y 1998 Quantum codes on a lattice with boundary arXiv:quant-ph/9811052
[4] Bombin H and Martin-Delgado M A 2006 Topological quantum distillation *Phys. Rev. Lett.* **97** 180501
[5] Bombin H and Martin-Delgado M A 2007 Topological computation without braiding *Phys. Rev. Lett.* **98** 160502
[6] Bombin H and Martin-Delgado M A 2007 Homological error correction: classical and quantum codes *J. Math. Phys.* **48** 052105
[7] Bombin H and Martin-Delgado M A 2007 Optimal resources for topological two-dimensional stabilizer codes: comparative study *Phys. Rev.* A **76** 012305
[8] Shor P W 1995 Scheme for reducing decoherence in quantum computer memory *Phys. Rev.* A **52** R2493–6
[9] Steane A M 1996 Error correcting codes in quantum theory *Phys. Rev. Lett.* **77** 793–7
[10] Shor P W 1996 Fault-tolerant quantum computation *37th Symposium on Foundations of Computing* (Piscataway, NJ: IEEE) pp 56–65
[11] Knill W Z E and Laflamme R 1996 Threshold accuracy for quantum computation arXiv:quant-ph/9610011
[12] Kitaev A Y 1997 Quantum computations: algorithms and error correction *Russ. Math. Surv.* **52** 1191–249
[13] Aharonov M B-O D 1999 Fault tolerant quantum computation with constant error *SIAM J. Comp.* **38** 1207–82
[14] Nielsen M A and Chuang I L 2000 *Quantum Computation and Quantum Information* (Cambridge: Cambridge University Press)
[15] Galindo A and Martín-Delgado M A 2002 Information and computation: classical and quantum aspects *Rev. Mod. Phys.* **74** 347–423
[16] Levin M A and Wen X-G 2005 String-net condensation: a physical mechanism for topological phases *Phys. Rev.* B **71** 045110
[17] Freedman M, Nayak C, Shtengel K, Walker K and Wang Z 2004 A class of p,t-invariant topological phases of interacting electrons *Ann. Phys.* **310** 428–92
[18] Freeman M H and Hastings M B 2016 Double semions in arbitrary dimension *Commun. Math. Phys.* **347** 389–419
[19] Furusaki A 2017 Weyl points and Dirac lines protected by multiple screw rotations *Sci. Bull.* **62** 788–994
[20] Li K, Wan Y, Hung L-Y, Lan T, Long G, Lu D, Zeng B and Laflamme R 2017 Experimental identification of non-abelian topological orders on a quantum simulator *Phys. Rev. Lett.* **118** 080502
[21] Syed R, Sirota A and Teo J C Y 2019 From Dirac semimetrals to topological phases in three dimensions: a coupled-wire construction *Phys. Rev.* X **9** 011039
[22] Buerscher O, Morampudi S C and Pollmann F 2014 Double semion phase in an exactly solvable quantum dimer model on the kagome lattice *Phys. Rev.* B **90** 195148
[23] Morampudi S C, von Keyserlingk C and Pollmann F 2014 Numerical study of a transition between $\mathbb{Z}_2$ topologically ordered phases *Phys. Rev.* B **90** 035117
[24] Ors R, Wei T-C, Buerschaper O and Van den Nest M 2014 Geometric entanglement in topologically ordered states *New J. Phys.* **16** 013015
[25] Qi Y, Gu Z-C and Yao H 2015 Double-semion topological order from exactly solvable quantum dimer models *Phys. Rev.* B **92** 155105
[26] Mesaros A and Ran Y 2013 Classification of symmetry enriched topological phases with exactly solvable models *Phys. Rev.* B **87** 155115
[27] von Keyserlingk C W, Burnell F J and Simon S H 2013 Three-dimensional topological lattice models with surface anyons *Phys. Rev.* B **87** 045107
[28] Calderbank A R and Shor P W 1996 Good quantum error-correcting codes exist *Phys. Rev.* A **54** 1098–105
[29] Steane A 1996 Multiple-particle interference and quantum error correction *Proc. R. Soc.* A **452** 2551–77
[30] Preskill J 2004 *Lecture Notes for Physics 219: Quantum Computation*
[31] Terhal B M 2015 Quantum error correction for quantum memories *Rev. Mod. Phys.* **87** 307–46
[32] Gottesman D 1996 Class of quantum error-correcting codes saturating the quantum hamming bound *Phys. Rev.* A **54** 1862–8
[33] Ni X, Buerschaper O and Van den Nest M 2015 A non-commuting stabilizer formalism *J. Math. Phys.* **56** 052201
[34] Calderbank A R, Rains E M, Shor P W and Sloane N J A 1997 Quantum error correction and orthogonal geometry *Phys. Rev. Lett.* **78** 405–8
[35] Kitaev A 2006 Anyons in an exactly solved model and beyond *Ann. Phys.* **321** 2–111

[36] Pfeifer R N, Buerscher O, Trebst S, Ludwig A W W, Troyer M and Vidal G 2012 Translation invariance, topology, and protection of criticality un chains of interacting anyons *Phys. Rev.* B **86** 155111
[37] Nakahara N 2003 *Geometry, Topology and Physics* (London: Taylor and Francis)
[38] Bombin H and Martin-Delgado M A 2007 Homological error correction: classical and quantum codes *J. Math. Phys.* **48** 052105
[39] Wang D S, Fowler A G, Stephens A M and Hollenberg L C L 2010 Threshold error rates for the toric and planar codes *Quantum Inf. Comput.* **10** 456–69
[40] Duclos-Cianci G and Poulin D 2010 Fast decoders for topological quantum codes *Phys. Rev. Lett.* **104** 050504
[41] Bravyi S and Haah J 2013 Quantum self-correction in the 3d cubic code model *Phys. Rev. Lett.* **111** 200501
[42] Fowler A G, Whiteside A C and Hollenberg L C L 2012 Towards practical classical processing for the surface code *Phys. Rev. Lett.* **108** 180501
[43] Anwar H, Brown B J, Campbell E T and Browne D E 2014 Fast decoders for qudit topological codes *New J. Phys.* **16** 063038
[44] Delfosse N and Zmor G 2017 Linear-time maximum likelihood decoding of surface codes over the quantum erasure channel arXiv:1703.01517
[45] Delfosse N and Nickerson N H 2017 Almost-linear time decoding algorithm for topological codes arXiv:1709.06218
[46] Maskara N, Kubica A and Jochym-O'Connor T 2018 Advantages of versatile neural-network decoding for topological codes arXiv:1802.08680
[47] Kubica A and Preskill J 2018 Cellular-automaton decoders with provable thresholds for topological codes arXiv:1809.10145
[48] Herold M, Campbell E T, Eisert J and Kastoryano M J 2015 Cellular-automaton decoders for topological quantum memories *Npj Quantum Inf.* **1** 15010
[49] Wootton J 2015 A simple decoder for topological codes *Entropy* **17** 1946–57
[50] Sarvepalli P and Raussendorf R 2012 Efficient decoding of topological color codes *Phys. Rev.* A **85** 022317
[51] Harrington J 2004 Analysis of quantum error-correcting codes: symplectic lattice codes and toric codes *PhD Thesis* Caltech
[52] Chamberland C and Ronagh P 2018 Deep neural decoders for near term fault-tolerant experiments *Quantum Sci. Technol.* **3** 044002
[53] Herold M, Kastoryano M J, Campbell E T and Eisert J 2017 Cellular automaton decoders of topological quantum memories in the fault tolerant setting *New J. Phys.* **19** 063012
[54] Dauphinais G and Poulin D 2017 Fault-tolerant quantum error correction for non-abelian anyons *Commun. Math. Phys.* **355** 519–60
[55] Sweke R, Kesselring M S, van Nieuwenburg E P L and Eisert J 2018 Reinforcement learning decoders for fault-tolerant quantum computation arXiv:1810.07207
[56] Breuckmann N P, Duivenvoorden K, Michels D and Terhal B M 2017 Local decoders for the 2d and 4d toric code *Quantum Inf. Comput.* **17** 0181
[57] Breuckmann N P and Ni X 2018 Scalable neural network decoders for higher dimensional quantum codes *Quantum* **2** 68
[58] Wootton J R and Loss D 2012 High threshold error correction for the surface code *Phys. Rev. Lett.* **109** 160503
[59] Hutter A, Wootton J R and Loss D 2014 Efficient Markov chain Monte Carlo algorithm for the surface code *Phys. Rev.* A **89** 022326
[60] Bravyi S, Suchara M and Vargo A 2014 Efficient algorithms for maximum likelihood decoding in the surface code *Phys. Rev.* A **90** 032326
[61] Darmawan A S and Poulin D 2018 Linear-time general decoding algorithm for the surface code *Phys. Rev.* E **97** 051302
[62] Bombin H, Andrist R S, Ohzeki M, Katzgraber H G and Martin-Delgado M A 2012 Strong resilience of topological codes to depolarization *Phys. Rev.* X **2** 021004
[63] Tuckett D K, Bartlett S D and Flammia S T 2018 Ultrahigh error threshold for surface codes with biased noise *Phys. Rev. Lett.* **120** 050505
[64] Laflamme R, Miquel C, Paz J P and Zurek W H 1996 Perfect quantum error correcting code *Phys. Rev. Lett.* **77** 198–201
[65] DiVincenzo D P and Shor P W 1996 Fault-tolerant error correction with efficient quantum codes *Phys. Rev. Lett.* **77** 3260–3
[66] Preskill J 1997 Fault-tolerant quantum computation *Introduction to Quantum Computation and Information* ed H-K Lo, T Spiller and S Popescu (Singapore: World Scientific)
[67] Levin M and Gu Z-C 2012 Braiding statistics approach to symmetry-protected topological phases *Phys. Rev.* B **86** 115109
[68] Ortiz L and Martin-Delgado M A 2016 A bilayer double semion model with symmetry-enriched topological order *Ann. Phys.* **375** 193–226
[69] Song H, Prem A, Huang S-J and Martin-Delgado M A 2018 Twisted fracton models in three dimensions *Phys. Rev.* B **99** 155118

5. Summary and main results of publication 4

Little is known about the quantum error correcting properties of topological non-Pauli codes [FTE20] and of the semion code in particular [P3]. In this work, we compute the threshold, a key quantity characterizing the performance and efficiency of an error correcting code. The usual approach taken in order to determine the threshold of topological codes involves mapping the system to a statistical mechanical model. For instance, the Kitaev code is mapped to a two-dimensional random bond Ising model. However, the non-Pauli and non-CSS nature of the code (due to the complex structure of plaquette operators) makes the computation of the threshold very complex with the usual statistical mechanical tools. Thus, we address this problem using machine learning and neural networks. Decoders based on neural networks have proven to have near-optimal performance for topological codes. We will apply two different neural networks to the semion code: a simple multilayer perceptron and a convolutional neural network based on the ResNet architecture. Below, the main results of publication [P4] are presented.

1. **Determination of the semion code threshold.** The threshold is computed for depolarizing and independent bit- and phase-flip Pauli noise, taking advantage of the near-optimal performance of some neural decoders. Threshold values are found to be significantly high despite the non-Pauli nature of the code and the complex structure of the plaquette operators, which are not Pauli operators and whose support involves 12 qubits.
2. **In-detail analysis of the differences between the Kitaev toric code and the semion code.** The same machine learning techniques are applied to the Kitaev toric code in the hexagonal lattice in order to make a detailed comparison with this paradigmatic topological code. The threshold differences found between independent and depolarizing noise for the Kitaev code are not observed in the semion code. This is a consequence of the syndrome correlations between vertex and plaquette operators in the semion code.
3. **Performance comparison of decoders based on multilayer perceptrons and convolutional neural networks.** We use the ResNet architecture, a convolutional neural network allowing the construction of very deep networks. This architecture performs better and requires much less training time and training data than the simple multilayer perceptron.

Determination of the semion code threshold using neural decoders

S. Varona [*] and M. A. Martin-Delgado [†]
Departamento de Física Teórica, Universidad Complutense, 28040 Madrid, Spain

(Received 26 February 2020; accepted 25 August 2020; published 17 September 2020)

We compute the error threshold for the semion code, the companion of the Kitaev toric code with the same gauge symmetry group $\mathbb{Z}_2$. The application of statistical mechanical mapping methods is highly discouraged for the semion code, since the code is non-Pauli and non-Calderbank-Shor-Steane (CSS). Thus, we use machine learning methods, taking advantage of the near-optimal performance of some neural network decoders: multilayer perceptrons and convolutional neural networks (CNNs). We find the values $p_{\text{eff}} = 9.5\%$ for uncorrelated bit-flip and phase-flip noise, and $p_{\text{eff}} = 10.5\%$ for depolarizing noise. We contrast these values with a similar analysis of the Kitaev toric code on a hexagonal lattice with the same methods. For convolutional neural networks, we use the ResNet architecture, which allows us to implement very deep networks and results in better performance and scalability than the multilayer perceptron approach. We analyze and compare in detail both approaches and provide a clear argument favoring the CNN as the best suited numerical method for the semion code.

DOI: 10.1103/PhysRevA.102.032411

I. INTRODUCTION

The robustness of quantum memories to external noise and decoherence is a key aspect along the way to fault-tolerant quantum computing. Topological properties of quantum systems have become a resource of great importance to construct better and more robust quantum error correcting codes. The Kitaev toric code is the simplest topological code yielding a quantum memory [1,2]. It can be regarded as a simple two-dimensional lattice gauge theory with $\mathbb{Z}_2$ gauge group. In two dimensions, there is another lattice gauge theory with the same gauge group but different topological properties: the double semion model. The double semion model has been thoroughly studied in the search for new topological orders in strongly correlated systems, gapped, nonchiral, and based on string-net mechanisms in two dimensions [3–5]. Although the Kitaev and the double semion models share the same gauge group, there are some remarkable differences between both. For instance, braiding two elementary quasiparticle excitations gives a ± 1 phase in the Kitaev toric code, while in the double semion model it yields a $\pm i$ phase factor, showing anyonic statistics.

Topological orders can provide us with a great variety of new topological codes with non-Pauli stabilizers [6]. These new codes might be more appropriate for practical implementation or have smaller overheads when performing, for instance, non-Clifford gates. This strongly motivates the search for new topological codes and their properties beyond the usual toric and color codes. Recently, an error correcting code based on the double semion model, the semion code, was presented [7]. This code is topological and follows the stabilizer formalism. However, in contrast to the Kitaev toric code, it is not a Calderbank-Shor-Steane (CSS) code [8–10], since both Pauli X and Z operators are present in the plaquette operators, and it is not a Pauli code, since plaquette operators cannot be expressed as a tensor product of Pauli matrices.

In order to characterize the performance and efficiency of an error correcting code, the threshold value is one of the most representative quantities quoted [2,11–13]. The threshold represents the physical error rate below which increasing the distance of the code reduces the logical error rate. This error rate separates two different regimes. For error rates below threshold, larger codes translate into longer memory time and lower logical error rate. Therefore, in this regime, it makes sense to use error correction. In this work, we try to shed some light on the threshold properties of the semion code and compare it with the well-known toric code.

In the case of the Kitaev toric code, when considering Pauli noise, the threshold is determined by mapping the system to a statistical model, the random-bond two-dimensional (2D) Ising model [2,11,12,14]. The threshold value corresponds in this new system to the phase transition between the ordered and disordered phases. Nevertheless, this mapping is extremely cumbersome in the semion code because of the complex structure of the plaquette operators. Determining the threshold in the case where Pauli noise affects a non-Pauli code or non-Pauli noise affects a Pauli code needs a new approach. We address this problem using machine learning and neural networks [15–17].

Machine learning, and in particular neural networks, has been proposed in recent years as a solution for efficiently decoding stabilizer codes [18–31]. Although there are different approaches to the decoding problem using neural networks, one of the most common consists in applying a very simple decoder to the code. Afterwards the neural network tries to predict, given the syndrome measurement, the logical error produced by the simple decoder, so that this can be in turn corrected. This approach has been shown to produce near-optimal results for topological codes [32,33]. Thus, the

[*] svarona@ucm.es
[†] mardel@ucm.es

pseudothreshold of these decoders should be very close to the optimal one. This makes neural networks a very suitable way of determining the threshold of a code, and specifically of the semion code.

In this paper, we use two different types of neural networks to build our decoders. First, a multilayer perceptron (MLP), a very simple feedforward neural network. Then, we present a certain type of convolutional neural network (CNN) called ResNet [34], allowing the construction of very deep networks. Since CNNs naturally take into account the spatial structure of the code, we will see that they have multiple scalability and performance advantages in comparison to the MLP. The semion code is an ideal testing ground for the application of CNN methods in order to get the most out of them. The application of CNNs is more justified in the case of the semion code than in the Kitaev [1,2] or color code [35,36] since it allows us to take into account the complex spatial correlation of the syndrome pattern for Pauli noise. This effect is peculiar to the semion code and never studied thus far. The results of the neural network decoders will be benchmarked against the minimal-weight perfect matching (MWPM) decoder [37,38]. While MWPM obtains very good results for the Kitaev code with independent bit-flip and phase-flip noise, it does not perform so well when plaquette and vertex syndromes are correlated, since it does not take these correlations into account. This is where neural networks will make a big difference.

The article is organized as follows. In Sec. II we present a short review of the semion code and the noise model considered. In Sec. III we introduce the neural network decoders, compare their performance, and finally present the threshold values. Section IV is devoted to conclusions.

II. ERROR CORRECTION WITH THE SEMION CODE

The semion code [7] is an error correcting code based on the double semion model. This error correcting code bears similarities to the Kitaev toric code. In particular, it is topological and is a stabilizer code [39]; i.e., plaquette and vertex operators are periodically measured to detect errors. Nevertheless, the semion code is non-CSS and non-Pauli because of the structure of plaquette operators, and is defined in a hexagonal lattice. In the hexagonal lattice, edges will represent the physical qubits and vertices and plaquettes the stabilizer operators.

Vertex operators are equivalent to the ones in the Kitaev toric code $Q_v = Z_i Z_j Z_k$, a Pauli-Z operator applied on each edge of vertex v. Plaquettes are different; their support includes not only a hexagon, but also the outgoing legs of the hexagon (see Fig. 1). We have Pauli-X operators applied on the edges of the hexagon, as in the toric code, but we also have a diagonal operator $\sum_{\vec{j}} b_p(\vec{j})|\vec{j}\rangle\langle\vec{j}|$ acting on the 12 qubits shown in Fig. 1(b). Thus, we have

$$B_p = \prod_{k\in\partial p} X_k \sum_{\vec{j}} b_p(\vec{j})|\vec{j}\rangle\langle\vec{j}|, \tag{1}$$

where $b_p(\vec{j})$ is a function taking values in $\{\pm 1, \pm \mathrm{i}\}$, $\vec{j}$ is a bit string representing a state in the computational basis, and ∂p are the edges belonging to the border of the plaquette. $b_p(\vec{j})$ is

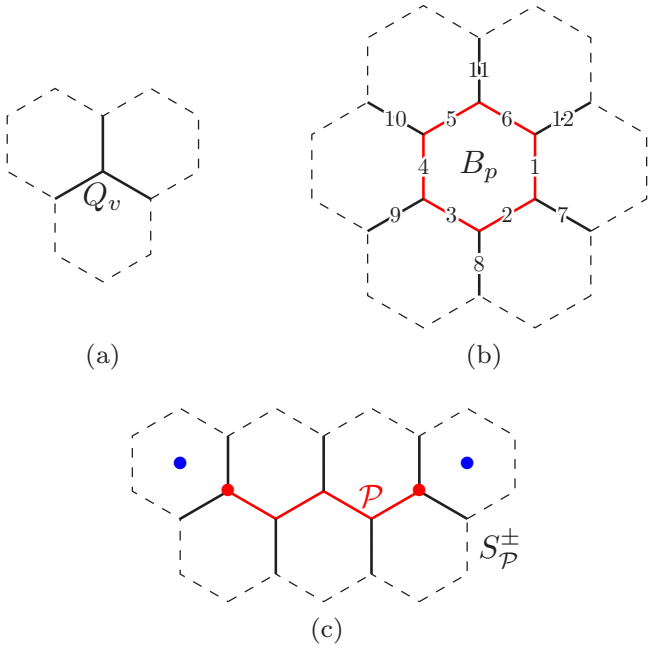

FIG. 1. The support of each of the operators is shown by continuous lines. The qubits are placed on the edges. (a) Vertex operator Q_v. (b) Plaquette operator B_p. Note that the plaquette contains not only the red hexagon (where Pauli-X operators are applied), but also the outgoing legs. (c) Positive- or negative-chirality string operator $S^{\pm}_{\mathcal{P}}$. Path $\mathcal{P}$ is indicated by the solid red edges, where the Pauli-X operators are applied. The support of $S^{\pm}_{\mathcal{P}}$, Conn($\mathcal{P}$), is indicated with continuous lines. The effect of $S^{\pm}_{\mathcal{P}}$ on the ground state of the system is to create a pair of vertex excitations at the vertices located at the endpoints of the path $\mathcal{P}$, which are identified by red dots. Additionally, the negative-chirality string creates a pair of plaquette excitations at the endpoint plaquettes (blue dots).

given explicitly by

$$\sum_{\vec{j}} b_p(\vec{j})|\vec{j}\rangle\langle\vec{j}| = \prod_{k\in\partial p} (-1)^{n^-_{k-1}n^+_k} \prod_{v\in p} \beta_v, \tag{2}$$

where $n^{\pm}_i = \frac{1}{2}(1 \pm Z_i)$, the subscript v runs over the vertices belonging to plaquette p, and $\prod_{v\in p}\beta_v$ is

$$\begin{aligned}\prod_{v\in p}\beta_v = {} & \mathrm{i}^{n^-_{12}(n^-_1 n^-_6 - n^+_1 n^+_6)}\, \mathrm{i}^{n^-_7(n^+_1 n^+_2 - n^-_1 n^-_2)} \\ & \times \mathrm{i}^{n^+_8(n^-_2 n^+_3 - n^+_2 n^+_3)}\, \mathrm{i}^{n^-_9(n^-_3 n^-_4 - n^+_3 n^+_4)} \\ & \times \mathrm{i}^{n^-_{10}(n^+_4 n^+_5 - n^-_4 n^-_5)}\, \mathrm{i}^{n^+_{11}(n^-_5 n^+_6 - n^+_5 n^-_6)},\end{aligned} \tag{3}$$

following the labeling of Fig. 1(b). The Pauli-X operators on the plaquette edges and the (-1) factors of Eq. (2) form the plaquette operator as defined originally in the double semion model topological order,

$$\tilde{B}_p = \prod_{k\in\partial p} X_k \prod_{k\in\partial p} (-1)^{n^-_{k-1}n^+_k}. \tag{4}$$

However, this operator is not Hermitian in the whole Hilbert space. Neighboring plaquettes do not commute either. The local β_v phases added at each vertex to $\tilde{B}_p$ solve these two issues and allow us to define an error correcting code based on the

stabilizer formalism. The code space of the system is formed by states with eigenvalue $+1$ for all vertex operators and -1 for all plaquette operators. Similarly to the Kitaev toric code, when an error occurs, the signs of some of the stabilizers flip. These locations where the stabilizer flipped can be regarded as excitations. The recovery procedure consists in annihilating the excitations with each other in such a way that the total string operator applied (the trajectory of the quasiparticles) forms a trivial loop.

String operators generating plaquette excitations, S^Z, are identical to the ones in the Kitaev toric code, i.e., a string of Z operators. These operators commute with every stabilizer except the plaquettes at the endpoints of the string. String operators generating vertex excitations are formed by a string of X, as in the Kitaev code, and additionally some phases $\sum_{\vec{j}} F(\vec{j})|\vec{j}\rangle\langle\vec{j}|$, where $F(\vec{j})$ takes values in $\{\pm 1, \pm i\}$. For a string on a path $\mathcal{P}$ we have

$$S^+_{\mathcal{P}} = \prod_{k\in\mathcal{P}} X_k \sum_{\vec{j}} F(\vec{j})|\vec{j}\rangle\langle\vec{j}|. \tag{5}$$

The support of $S^+_{\mathcal{P}}$ is $\mathrm{Conn}(\mathcal{P})$, which is shown in Fig. 1(c). This means that the operator $S^+_{\mathcal{P}}$ acts nontrivially only on the set of qubits $\mathrm{Conn}(\mathcal{P})$. Thus, $F(\vec{j}) = F(\vec{j} \oplus \vec{i})$ for any $\vec{i}$ whose qubits in $\mathrm{Conn}(\mathcal{P})$ are zero. Here, $\oplus$ denotes the sum mod 2 of the bit strings. $F(\vec{j})$ can be determined by imposing that the string operator must square to one and that it must commute with the stabilizers (except at the endpoints, where it must anticommute). These constraints give rise to a linear system of equations from which $F(\vec{j})$ can be easily obtained. The quasiparticle vertex excitations generated by $S^+_{\mathcal{P}}$ behave like anyons. They are called semions due to the fact that their topological charge is *half* of that of a fermion, i.e., $\pm i$. The negative-chirality strings can be obtained multiplying S^+ by an S^Z string operator joining both endpoints, $S^- = S^+S^Z$. Since S^+ and S^- create semions at the endpoints, two strings with the same chirality crossing once anticommute, while strings with opposite chirality commute. S^Z commutes with itself and anticommutes with $S^\pm$. Summarizing, we have, for strings crossing once, $\{S^Z, S^\pm\} = 0$, $\{S^\pm, S^\pm\} = 0$, and $[S^\pm, S^\mp] = 0$.

Similarly to what is done in the Kitaev code, we can embed the double semion on a torus to obtain a quantum memory with two logical qubits. An example of this can be seen in Fig. 2. We have a lattice with 16 plaquettes embedded on a torus. Since we have two encoded logical qubits, we need two pairs of logical operators. We can define for one of the logical qubits $\bar{X}_1 \equiv S^-_{\mathcal{H}}$ and $\bar{Z}_1 \equiv S^Z_{\bar{\mathcal{V}}}$, and for the other $\bar{X}_2 \equiv S^+_{\mathcal{V}}$ and $\bar{Z}_2 \equiv S^Z_{\bar{\mathcal{H}}}$. The subscript $\mathcal{H}$ stands for a horizontal path and $\mathcal{V}$ for a vertical one in Fig. 2. It is clear from the commutation rules shown previously that these sets of operators fulfill the necessary anticommutation relations of the Pauli algebra. Note that the distance of $\bar{Z}$ operators is half of the $\bar{X}$, as a consequence of the hexagonal lattice. Therefore, we may be better protected against certain types of errors than against others [7,13,40]. To perform error correction, the stabilizers have to be measured periodically, and the excitations have to be annihilated by bringing them together using the string operators.

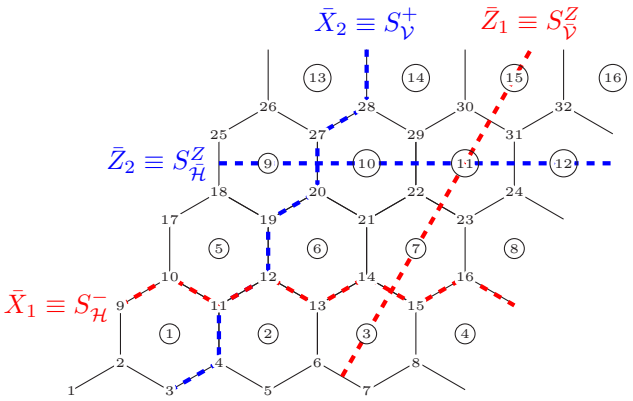

FIG. 2. Semion code embedded on a torus. Top and bottom, and left and right borders are identified. Two pairs of logical string operators (nontrivial loops going around the system) on the torus are shown (red and blue). We have 16 plaquettes, 32 vertices, and 48 physical qubits, resulting into 2 logical qubits (since one vertex and one plaquette operator are not independent). The code has distance 4.

Noise model

We consider Pauli noise models [41], given by the expression

$$\rho \to (1-p)\rho + p_X X\rho X + p_Y Y\rho Y + p_Z Z\rho Z, \tag{6}$$

where $p = p_X + p_Y + p_Z$. In particular we use two error models:

(i) Independent bit-flip and phase errors with $p_X = p_Z = p_0 - p_0^2$ and $p_Y = p_0^2$. Each qubit is independently acted on by an X error with probability p_0 and by a Z error with same probability p_0. The probability of some error happening is $p_{\mathrm{eff}} = 1 - (1-p_0)(1-p_0) = 2p_0 - p_0^2$.

(ii) Depolarizing noise with $p_X = p_Y = p_Z = p_{\mathrm{eff}}/3$. With probability p_{eff} an error occurs in a given qubit. Each error type, X, Y, and Z, is equally likely.

In order to compare the threshold values obtained for both independent and depolarizing noise, we use p_{eff}, defined as the probability of any error occurring on a given qubit.

For these noise models consisting of Pauli operators, it will be important to determine the effect of strings of Pauli-X operators on a path $\mathcal{P}$ acting on the code. We may rewrite a string of X as

$$X_{\mathcal{P}} = \prod_{k\in\mathcal{P}} X_k = S^+_{\mathcal{P}} \sum_{\vec{j}} [F_{\mathcal{P}}(\vec{j})]^* |\vec{j}\rangle\langle\vec{j}|. \tag{7}$$

The diagonal part can be expressed as a sum of strings of Pauli-Z operators,

$$\sum_{\vec{j}} [F_{\mathcal{P}}(\vec{j})]^* |\vec{j}\rangle\langle\vec{j}| = \sum_{\mathcal{Q}\in\mathrm{Conn}(\mathcal{P})} c(Z_{\mathcal{Q}}) Z_{\mathcal{Q}}. \tag{8}$$

Here $Z_{\mathcal{Q}} = \prod_{j\in\mathcal{Q}} Z_j$ is the multiplication of Pauli-Z operators acting on the set of qubits $\mathcal{Q}$, which are contained in $\mathrm{Conn}(\mathcal{P})$. The coefficients $c(Z_{\mathcal{Q}})$ are given by $c(Z_{\mathcal{Q}}) = \frac{1}{2^n}\mathrm{Tr}(Z_{\mathcal{Q}} \sum_{\vec{j}} [F_{\mathcal{P}}(\vec{j})]^* |\vec{j}\rangle\langle\vec{j}|)$, with $n = |\mathrm{Conn}(\mathcal{P})|$.

Now, if we apply $X_{\mathcal{P}}$ to a state in the code space $|L, C\rangle$, with L labeling the logical subspace and C representing the

TABLE I. The various probabilities of getting a given plaquette syndrome pattern after the application of the operator X on a qubit, for the three possible edge orientations [7]. The plaquette labels correspond to the ones in Fig. 3. The + sign represents excitations at a given plaquette.

	Probability		
s(p, q, r, s)	Orientation (a)	Orientation (b)	Orientation (c)
$(----)$	9/16	1/16	9/16
$(++--)$	1/16	1/16	1/16
$(+-+-)$	1/16	1/16	1/16
$(-++-)$	1/16	9/16	1/16
$(+--+)$	1/16	1/16	1/16
$(-+-+)$	1/16	1/16	1/16
$(--++)$	1/16	1/16	1/16
$(++++)$	1/16	1/16	1/16

eigenvalues of the stabilizers (+1 for vertex operators and −1 for plaquette operators), we obtain

$$X_{\mathcal{P}}|L, C\rangle = S^{+}_{\mathcal{P}} \sum_{\mathcal{Q}\in \mathrm{Conn}(\mathcal{P})} c(Z_{\mathcal{Q}}) Z_{\mathcal{Q}}|L, C\rangle. \tag{9}$$

$S^{+}_{\mathcal{P}}$ flips the vertices at the endpoints of $\mathcal{P}$, and $Z_{\mathcal{Q}}$ flips plaquettes at the endpoints of $\mathcal{Q}$, i.e., those plaquettes p where only one Z operator acts on ∂p. When the stabilizer operators are measured, the state in Eq. (9) collapses. The only terms remaining in the sum are those where the $Z_{\mathcal{Q}}$ operator is compatible with the plaquette syndrome measured. This means $Z_{\mathcal{Q}}$ needs to satisfy, for every plaquette involved, $[Z_{\mathcal{Q}}, B_p]_{\mathrm{s}(p)} = 0$, where $\mathrm{s}(p) \in \{\pm 1\}$ is the syndrome of plaquette p, and $[\cdot, \cdot]_-$ denotes the commutator and $[\cdot, \cdot]_+$ the anticommutator. Therefore, we have

$$|L, C'\rangle = N S^{+}_{\mathcal{P}} \sum_{\mathcal{Q}\in G} c(Z_{\mathcal{Q}}) Z_{\mathcal{Q}}|L, C\rangle, \tag{10}$$

where N is some normalization factor and $G = \{\mathcal{Q} \in \mathrm{Conn}(\mathcal{P}) : [Z_{\mathcal{Q}}, B_p]_{\mathrm{s}(p)} = 0 \ \forall p \in \mathcal{B}_{\mathcal{P}}\}$. $\mathcal{B}_{\mathcal{P}}$ represents the set of plaquettes whose support contains some part of $\mathcal{P}$. $|L, C'\rangle$ is a state in which the plaquettes at the endpoints of $Z_{\mathcal{Q}}$ are violated, as well as the vertices at the endpoints of $S^{+}_{\mathcal{P}}$. To get back to the previous state, we need a recovery operation, $Z_{\mathcal{R}}$, that brings us back from $Z_{\mathcal{Q}}|L, C\rangle$ to $|L, C\rangle$, where the multiplication $Z_{\mathcal{R}} Z_{\mathcal{Q}}$ forms a trivial loop of Pauli-Z operators in the dual lattice. Therefore, $Z_{\mathcal{R}}$ corrects plaquette errors. Additionally, applying some $S^{+}_{\mathcal{O}}$ (with $\mathcal{O} + \mathcal{P}$, the symmetric difference of $\mathcal{O}$ and $\mathcal{P}$, a trivial loop), we recover the initial state $|L, C\rangle$.

The probability of obtaining a certain plaquette syndrome when measuring the stabilizers in state (9) is

$$P(\mathrm{s}) = \left| \sum_{\mathcal{Q}\in G} c(Z_{\mathcal{Q}}) \right|^2. \tag{11}$$

The different probabilities of plaquette excitations in the case of a single X operator acting on a qubit can be seen in Table I. Note that the probabilities depend on the orientation of the edge (see Fig. 3), showing that the code has some anisotropy.

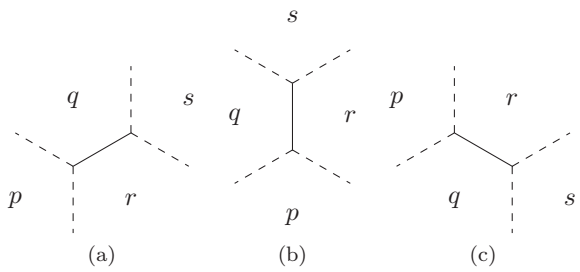

FIG. 3. The three possible edge orientations on which the X operator can be applied. The X operator acts on the central continuous edge, and may leave plaquette excitations on the four surrounding plaquettes labeled by p, q, r, and s. The probabilities of measuring a given plaquette pattern are given in Table I.

Given the complex structure of plaquette operators and the stabilizer syndromes caused by Pauli-X and -Y operators, the error syndromes of plaquette and vertex operators will be highly correlated for Pauli noise models, even for the case of (i) independent bit-flip and phase errors. Mapping the system to a tractable statical mechanical model in the same way it is done with the Kitaev toric code to determine the threshold is extremely difficult. This calls for alternative methods to address this problem and machine learning with neural decoders has remained unexplored for the semion code.

III. NEURAL NETWORK DECODERS

One of the standard practices in neural network decoders is to train a neural network to correct the output of a simple decoder. The simple decoder is given the syndrome measurements and yields a rudimentary correction. When the correction is applied, four different outcomes may occur: the errors are corrected and the code returns to its original state ($\bar{I}$, identity is applied), or a logical error occurs ($\bar{X}$, $\bar{Y}$, or $\bar{Z}$ logical error). The neural network is trained to predict this final outcome, i.e., the logical Pauli operator applied to the code, so that the simple decoder can be corrected. In this way, the decoding process turns into a classification problem where a neural network can be used. This is the approach we adopt here.

In particular, we consider the semion code embedded on a torus, such as the one shown in Fig. 2. Our simple decoder will take all excitations to the same point of the lattice, vertex number 1 or plaquette number 1, using the shortest path, to annihilate all excitations. This recovery operation produces a logical error ($\bar{I}$, $\bar{X}$, $\bar{Y}$, or $\bar{Z}$) which a neural network will try to correct. Note that since the code is embedded on a torus, we have two logical qubits. Thus, we have a total of 16 possible error combinations. Therefore, the input of our neural network will be the syndrome measurements, and the output one of these 16 categories. The input will be given as an array [one-dimensional (1D) or 2D] of bits, with value 1 corresponding to a stabilizer excitation and 0 to no excitation.

Note that one vertex and one plaquette syndrome are redundant, since they can be obtained if we know the rest of the syndromes and error excitations are created in pairs. However, in the presence of measurement errors (when the measurement of syndromes is no longer perfect) this is no longer true, and

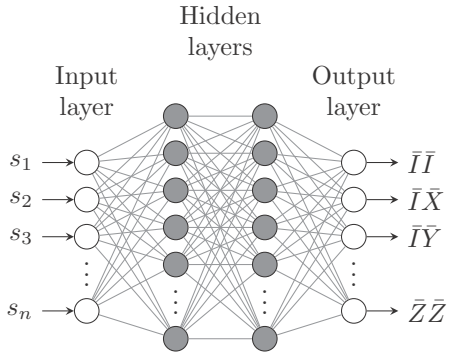

FIG. 4. The MLP receives the syndrome as input, i.e., a bit string with the vertex and plaquette operator measurements, and outputs the predicted error of the two logical qubits encoded in the torus.

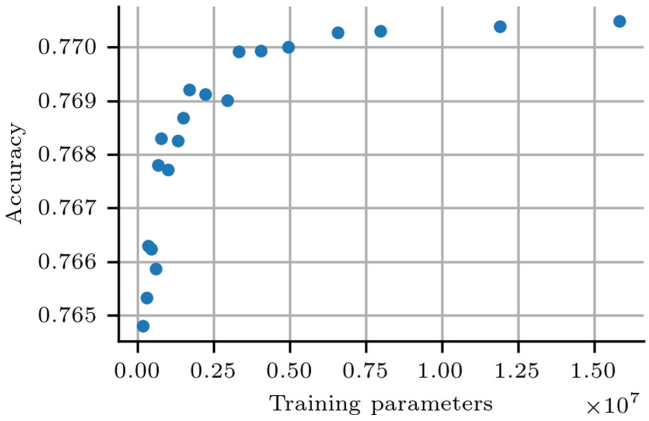

FIG. 5. Accuracy as a function of the number of training parameters for MLPs with different numbers of layers and nodes. Twenty different MLPs considered with the following parameters: hidden layers, $H \in \{4, 6, 8, 10\}$; nodes per layer, $N \in \{266, 400, 600, 900, 1400\}$. Independent bit-flip and phase error at rate $p_0 = 0.045$ for code distance 5.

all syndromes become relevant. While our setup does not consider measurement errors and we could thus omit these two inputs, we have decided to keep them to have a more generalizable model and preserve the spatial structure of the 2D array fed into the CNN.

Training data are generated taking samples of Pauli errors according to the corresponding probability distribution of the noise model and the probability distribution of plaquette syndromes of Eq. (11). The syndrome data are labeled with the logical error produced by the simple decoder. In the training process, the neural network is first trained on a small training set with a low error rate. Then, the network is trained with an error rate near the threshold value to obtain optimal performance. Since the error threshold is not known *a priori*, several error rates are checked. A lower bound can be easily obtained by first using a MWPM decoder. Despite the fact that the model is trained for a certain error rate, it also performs well for lower error rates.

We now present two different neural network decoders. One is based on the MLP and the other is a CNN, in particular a ResNet model.

A. Multilayer perceptron decoder

The MLP is one of the simplest classes of feedforward artificial neural networks. A MLP consists of three different parts: an input layer, hidden layers, and an output layer, as can be seen in Fig. 4. The layers are formed by neurons or nodes, with trainable parameters. Each node is fully connected to all nodes in the neighboring layers. The universal approximation theorem [42,43] states that a finite MLP can approximate any continuous function. Therefore, if trained appropriately, the MLP should be a near-optimal decoder.

The structure of this MLP follows closely the one presented in Ref. [33], where they found near-optimal decoders for other topological codes, the Kitaev code and the color code. All hidden layers have the same number of nodes. The cost function is chosen to be categorical cross entropy [44] and the optimizer is Adam [45], a gradient-based optimization algorithm with better performance than a simple gradient descent. The activation function is ReLU, $f(x) = \max(0, x)$, with He initialization of weights [46]. In order to train deep neural networks and avoid vanishing gradient convergence problems, we make use of batch normalization [47] in each layer.

Instead of computing the gradient of the cost function in the whole data set, an approximation is computed using a small batch of data and then the parameters are updated. The batch size was chosen to be 10^4. The final performance of the MLP is not affected by this number, provided it is not too small. If we have a small data set, and the network is trained several epochs over the same data, it is likely we will suffer overfitting. To avoid this, each batch of data is fed only once into the network during the training process, although this requires larger training sets.

Regarding hyperparameter tuning, a search was done to obtain the optimal number of layers and nodes. In general, for a given code distance, the higher the number of trainable parameters in the model, the better the performance, as can be seen in Fig. 5. However, we found that there is a point beyond which increasing the number of layers or nodes (and consequently increasing the number of parameters) produces very little accuracy improvement while increasing substantially the training time. Beyond that point, there is a broad range of models with very similar performance and different hyperparameters. Among them, we tried to choose the one with the lowest training time. Increasing the code distance by one was roughly observed to require double as many trainable parameters in the MLP model to reach good performance.

B. Convolutional neural network decoder

Despite the very good performance of the MLP in terms of accuracy, this approach is not scalable for error correction in large codes, since the training time increases exponentially with the size of the code. In addition, the information about the spatial distribution of the syndromes was not provided to the MLP, which has to figure this out by itself during training. These two problems suggest using a CNN for the task. In a CNN, the hidden layers are convolutional layers. Each input to the next layer is computed from a small local region of

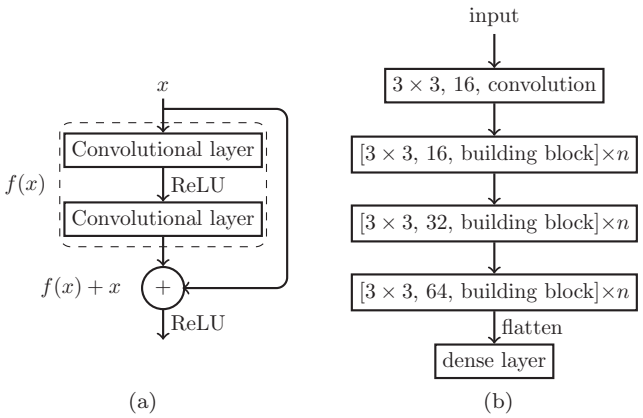

FIG. 6. (a) ResNet building block. A shortcut connection skips the convolutional layers. (b) ResNet model. n building blocks are stacked at each stage. The first stage has 16 filters, the second has 32, and the third 64. The filter size is always 3×3 and stride equals 1. The depth of the model is $d = 6n + 2$.

the preceding layer using some trainable parameters called filters. CNNs have been extensively used for image recognition. Although the information at each position in our lattice is binary, namely, the ± 1 value of the stabilizer measurement (compare this to an RGB image with 256 values per pixel in each channel), we can still see it as an image and feed it into a CNN. A syndrome pattern of errors can be considered as an image to be recognized with machine learning CNN methods. The semion code is very special since the structure of plaquette stabilizers causes complex correlations between X and Z errors produced externally [see Eq. (11)]. This is why we may argue that CNN decoders are especially well suited to the semion code in comparison to other neural network decoders, for CNN models were devised to mitigate the drawbacks posed by the MLP architecture by exploiting the strong spatially local correlation present in natural images.

We base our CNN model on the ResNet architecture. The ResNet architecture allows us to build very deep models, stacking a large number of convolutional layers without learning degradation. This is made possible by introducing residual shortcuts, connections performing the identity mapping and skipping the stacked layers. The shortcut output is added to the output of the stacked layers, as shown in Fig. 6(a), which constitutes the building block of ResNet. Our architecture consists of three stacked stages, where each stage has n building blocks like the one depicted in Fig. 6(a), and the convolutional layers have 3×3 filters. Batch normalization is performed after each convolutional layer. When going from one stage to the next, the number of filters is doubled. When doing image classification, this doubling in the number of filters is usually accompanied by downsampling the data using a convolutional layer of stride 2. However, we found that downsampling reduces noticeably the accuracy of the model, specially when doing two of them (at the end of stage 1 and at the end of stage 2). Therefore, we do not perform any downsamplings. At the beginning of stages 2 and 3, when the number of filters is doubled, the identity shortcut connection of the first block is substituted by a convolutional layer with the corresponding number of 1×1 filters. Finally, the output of these three stages is flattened and fed into a fully connected layer with softmax activation function. The model is shown schematically in Fig. 6(b).

TABLE II. Mapping of syndromes of the hexagonal lattice in Fig. 2 to a square structure suitable for a CNN. The data inside the square contain the stabilizers in the torus of Fig. 2, while the data outside are the periodic padding used in each convolution, indicating the periodic boundary conditions of the torus. × represents some extra values needed to preserve the hexagonal spatial structure in the square lattice; they will always be set to zero. Circled numbers represent plaquettes; the rest are vertices. The 48 stabilizer measurements of a distance $d = 4$ code are fed into the CNN as an 8×8 image. In general a code of distance d will produce an image of size $2d \times 2d$.

4	5	6	7	8	1	2	3	4	5
⑭	×	⑮	×	⑯	×	⑬	×	⑭	×
29	30	31	32	25	26	27	28	29	30
×	⑪	×	⑫	×	⑨	×	⑩	×	⑪
22	23	24	17	18	19	20	21	22	23
⑦	×	⑧	×	⑤	×	⑥	×	⑦	×
15	16	9	10	11	12	13	14	15	16
×	④	×	①	×	②	×	③	×	④
8	1	2	3	4	5	6	7	8	1
⑯	×	⑬	×	⑭	×	⑮	×	⑯	×

In order to perform convolutions, we need to recast our hexagonally distributed data into a square lattice. This is done as presented in Table II for the code of distance 4 in Fig. 2 (this transformation is explained in more detail in Appendix B for a code of arbitrary distance). With this mapping, some extra syndromes are introduced so that the spatial structure is faithful to the original one. These extra syndromes are always set to zero. It is also important to preserve the periodic boundary conditions of the torus. Therefore, before each convolution, the square data are padded periodically, as can be seen in Table II, where one extra row and one extra column is added at each side.

Again, the cost function is the categorical cross entropy and the optimizer is Adam. We also use the ReLU activation

TABLE III. MLP and ResNet figures for code distance 7 and trained with independent noise at $p_{\text{eff}} = 0.048$. The MLP has $H = 8$ and $N = 1400$. The first column shows the number of trainable parameters of each model, the second the number of training steps, and the third the accuracy. This compares to a MWPM accuracy of 58.9%.

	Trainable parameters	Steps	Accuracy
MLP	1.2×10^7	6.9×10^5	74.0%
ResNet14	3.8×10^5	9.1×10^4	73.8%
ResNet50	9.6×10^5	4.3×10^4	74.1%

TABLE IV. Semion code (SC) and hexagonal Kitaev toric code (KTC) p_{eff} threshold values for the different decoders considered: minimal weight perfect matching (MWPM), multilayer perceptron (MLP), and a ResNet50 convolutional neural network. MLP values were not computed for the KTC.

		MWPM	MLP	ResNet50
SC	Bit and phase flip	7.6%	9.4%	9.5%
	Depolarizing	7.5%	10.5%	10.5%
KTC	Bit and phase flip	12.5%		13.2%
	Depolarizing	10.0%		11.9%

function and He initialization. The batch size is chosen to be 1000. For smaller sizes, it is more likely that the model converges to a local minimum during training. During training, when the loss value reaches a plateau, the learning rate is reduced by a factor of 0.3. This is repeated until we observe that reducing the learning rate does not produce any accuracy gains.

These models already have similar performance to the MLP in terms of classification accuracy with $n = 2$, i.e., a depth of 14, and reduce substantially the number of parameters, the training time, and the size of the data set. The optimal performance was found for $n = 8$, depth of 50, for all code distances considered.

Another advantage of CNNs is the possibility of using transfer learning. The parameters learned by the convolutional layers for a given code distance can be reused for another code distance; this applies especially to the initial layers of the model, which tend to learn generic features. These parameters can be used as the starting point of the optimization to reduce the training time of the model. In addition, some of these initial layers can be declared nontrainable so that the learning time is even shorter.

C. Results

Here we present the threshold values obtained for the semion code as well as an analysis of the performance of the different decoders. As was mentioned earlier, ResNet is a much better option than MLP in terms of scalability and computational costs. This is shown in Table III, where we can see that the number of training steps and the number of trainable parameters are, respectively, one and two orders of magnitude lower for the ResNet model. Since the number of training steps is lower, the data set is also smaller for ResNet (the number of training examples is obtained by multiplying the training steps by the batch size), which also reduces the cost of producing the training data.

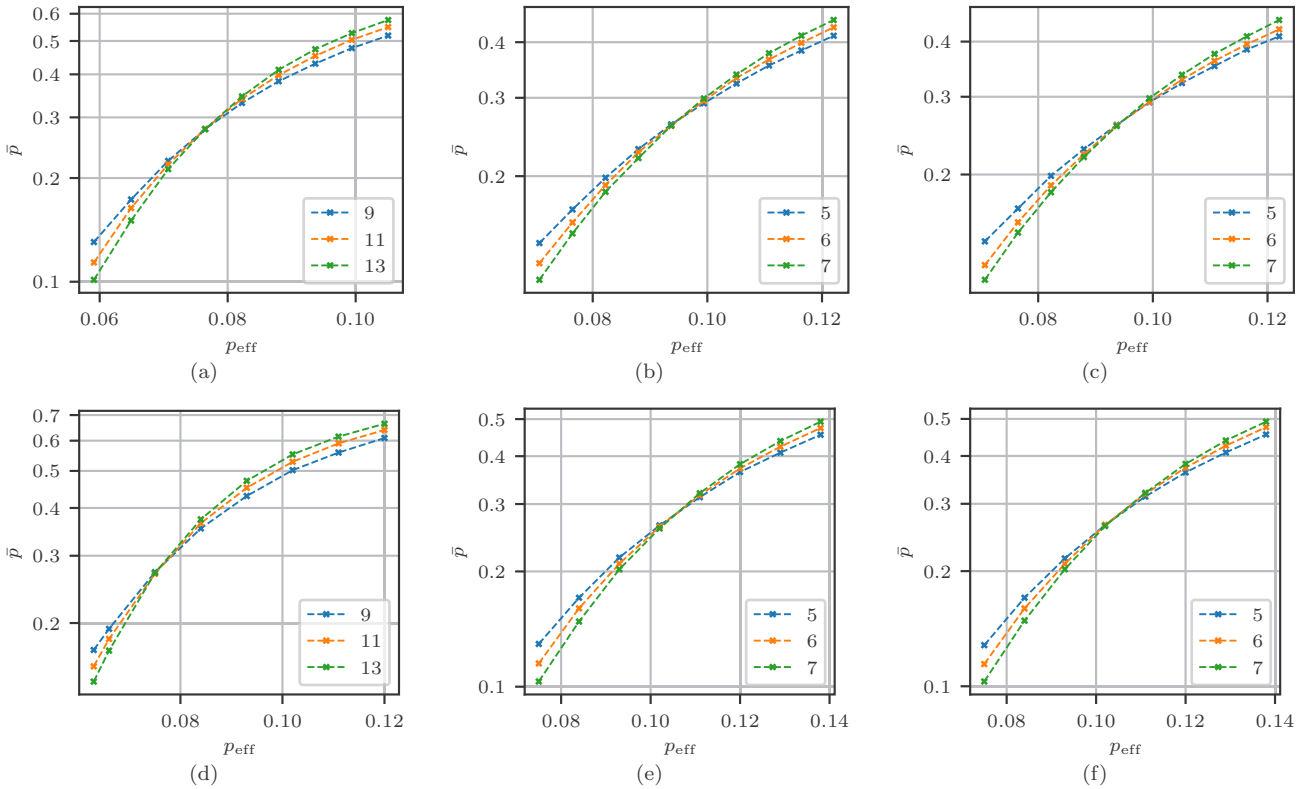

FIG. 7. Logical error rate, $\bar{p}$, as a function of effective error rate, p_{eff}. Independent bit- and phase-flip noise results in (a), (b), and (c). Depolarizing noise in (d), (e), and (f). For the MLP, (b) and (e), the number of hidden layers, H, and number of neurons, N, are $H = 6$ and $N = 900$, for distance 5; $H = 7$ and $N = 1100$, for distance 6; and $H = 8$ and $N = 1400$, for distance 7. (a) MWPM decoder with independent noise. (b) MLP decoder with independent noise. (c) ResNet50 decoder with independent noise. (d) MWPM decoder with depolarizing noise. (e) MLP decoder with depolarizing noise. (e) ResNet50 with depolarizing noise.

In Table IV and Fig. 7, we can see the threshold values for the different decoders. We obtain a threshold of 9.5% in the case of independent bit and phase flip and 10.5% for depolarizing noise. These quantities correspond to the effective error rate, p_{eff}, defined in Sec. II. These values contrast with the ones obtained for the Kitaev toric code in a hexagonal lattice, which we also obtain with neural decoders [48] (see Table IV). We find the depolarizing threshold to be higher than the one for independent bit- and phase-flip noise, suggesting that plaquette and vertex syndrome correlations in the semion code play an important role. Despite the lower threshold results obtained for the semion code, it is important to note that we are considering Pauli noise. Since the stabilizers of the toric code are formed by Pauli operators, Pauli noise results in a simple structure for the errors, while for the double semion we have a much more complex structure [see Eq. (11)]. This is especially so in the case of independent bit- and phase-flip noise, where plaquette and vertex syndromes are not correlated in the Kitaev toric code. We can see that the MWPM threshold gets much closer to the neural decoder threshold for the Kitaev code, since MWPM does not take into account plaquette and vertex correlations, while for the rest of the cases, where correlations contribute significantly, MWPM falls behind and neural decoders perform significantly better. As a consequence of the non-Pauli nature of the semion code, the threshold difference between depolarizing and independent noise is not as high for the semion code, since for both noise cases vertex and plaquette syndromes are correlated.

Despite ResNet being more accurate than the MLP and intrinsically including the spatial information that the MLP lacks, thresholds obtained are nearly the same in both cases. This may suggest that the pseudothresholds achieved are very close to the optimal one, and there is little room for performance enhancements.

IV. CONCLUSION

Quantum error correction is expected to be a fundamental tool to achieve the desired reliable and robust quantum computation and the first proof-of-principle steps towards this goal have been already achieved experimentally [50–53]. Topological quantum error correction with Abelian stabilizer codes has become a mature research field by now, providing one of the most valuable schemes on the road of fault-tolerant quantum computation [10,54,55]. It all begun with the simple Kitaev toric code, whose companion model with the same gauge symmetry group—the double semion model—has remained outside the quantum error correction methods until recently [7].

We have determined a near-optimal threshold for the semion code in the cases of independent bit- and phase-flip noise and depolarizing noise. The fact that neural decoders can have near-optimal performance shows that the pseudothreshold values obtained for the semion code with the ResNet decoder should be very close to the real threshold values. Since for the semion code, the plaquette stabilizer operators are not a simple product of Pauli operators, the usual mapping to a statistical mechanical model becomes a very complex problem, and using deep learning models becomes a nice and efficient way of determining the threshold of the semion code. These same methods could be used for other topological codes with non-Pauli stabilizers or non-Pauli noise models [6,56].

The ResNet architecture has shown a good performance in error correction. Nevertheless, it may still be possible to obtain little performance improvements by, for instance, taking other mappings from the hexagonal lattice to the square lattice (see Table II) or implementing slightly different versions of the ResNet model. In addition, it would be interesting to apply this kind of deep learning model, not only to threshold determination but also to build general purpose scalable decoders. Data augmentation, i.e., taking advantage of the symmetries of the error correcting code to reduce the size of the data set, as was suggested in Ref. [57], and transfer learning, i.e., reusing the weights previously learned for smaller systems, should help us to obtain scalable neural decoders.

The source code of the neural network decoder can be found in Ref. [58].

ACKNOWLEDGMENTS

We thank G. Dauphinais for useful discussions at the early stage of this research. The authors thankfully acknowledge the resources from the supercomputer "Cierzo," HPC infrastructure of the Centro de Supercomputación de Aragón (CESAR), and the technical expertise and assistance provided by BIFI (Universidad de Zaragoza). S.V. especially thanks Héctor Villarrubia Rojo for computational resources and technical assistance. We acknowledge financial support from the Spanish MINECO grants MINECO/FEDER Projects No. FIS2017-91460-EXP and No. PGC2018-099169-B-I00FIS-2018 and from CAM/FEDER Project No. S2018/TCS-4342 (QUITEMAD-CM). The research of M.A.M.-D. has been partially supported by the U.S. Army Research Office through Grant No. W911NF-14-1-0103. S.V. thanks the support of a FPU MECD Grant.

APPENDIX A: EXPONENTIAL SUPPRESSION OF NOISE

To further confirm that what we see is an error correcting threshold, we check here that (i) the noise is exponentially suppressed for larger code distances and (ii) the logical error rate is reduced to values much lower than the physical error rate. In order to show this clearly, we train ResNet50 decoders for code distances up to $d = 13$. Showing this same result for the MLP is very costly given the scaling of the model. Due to memory limitations, the batch size was chosen to be 300 when training the ResNet50 models with $d > 7$. These results are shown in Fig. 8.

APPENDIX B: MAPPING OF THE HEXAGONAL LATTICE INTO A SQUARE LATTICE

In this Appendix, we describe how the 1D array of stabilizer measurements provided as input to the MLP is converted

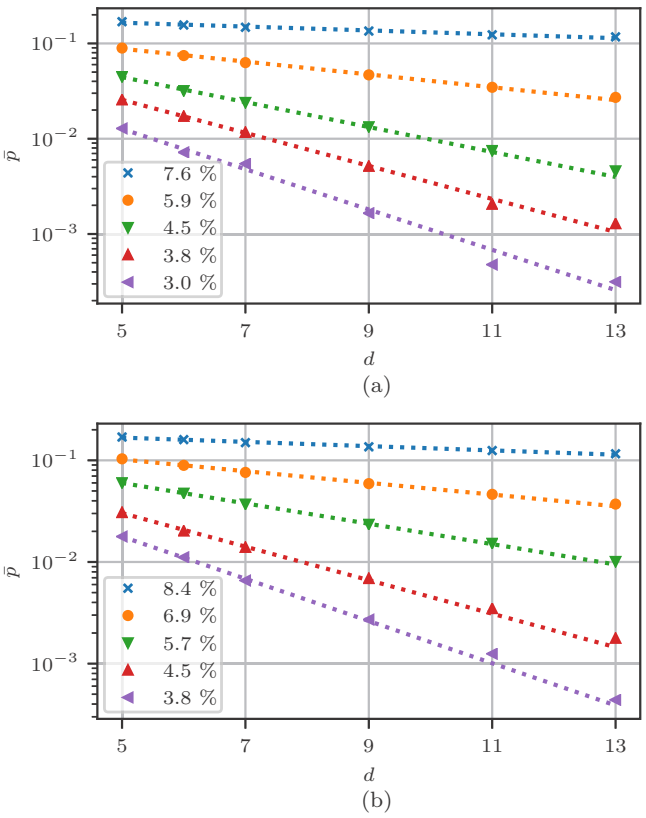

FIG. 8. Logical error rate, $\bar{p}$, as a function of code distance, d, for the ResNet50 decoder. This shows the exponential suppression of noise for (a) independent bit- and phase-flip and (b) depolarizing noise. Each dotted line is an exponential fit of the data points corresponding to a p_{eff} value.

into a 2D array suitable for the CNN and reflecting the spatial structure of the code. Since the semion code is defined on a hexagonal lattice, we need to convert the hexagonally distributed stabilizer measurements into a square distribution, while preserving the spatial structure. This is done as follows. The code of distance d has $n_v = 2d^2$ vertices and $n_p = d^2$ plaquettes, for a total of $n = n_v + n_p = 3d^2$ stabilizers. The 1D array of n stabilizers measurements will be converted into a $2d \times 2d$ image, I. Suppose vertices and plaquettes have been sequentially labeled from left to right and bottom to top, as shown in Fig. 2 for the code of distance 4. The syndrome of vertex v corresponds to the image element $I_{i,j}$, where i and j are

$$i = 2\left\lfloor \frac{v-1}{2d} \right\rfloor + 1, \tag{B1}$$

$$j = \mathrm{mod}\left(v - 1 + (1-2d)\left\lfloor \frac{v-1}{2d} \right\rfloor, 2d\right) + 1. \tag{B2}$$

The syndrome of plaquette p corresponds to the element $I_{i,j}$, with i and j given by

$$i = 2\left\lfloor \frac{p-1}{d} \right\rfloor + 2, \tag{B3}$$

$$j = \mathrm{mod}\left(2p + (1-4d)\left\lfloor \frac{p-1}{d} \right\rfloor, 2d\right) + 1. \tag{B4}$$

Since I has $4d^2$ elements and we have $3d^2$ stabilizers, there are a few elements in I which do not correspond to any stabilizer. These elements are always set to zero. The result of this transformation is shown in Table II for the code of distance 4 of Fig. 2. In Table II, those elements denoted with the symbol "×" represent the elements that do not correspond to any stabilizer measurement.

[1] A. Yu. Kitaev, Fault-tolerant quantum computation by anyons, Ann. Phys. **303**, 2 (2003).

[2] E. Dennis, A. Kitaev, A. Landahl, and J. Preskill, Topological quantum memory, J. Math. Phys. **43**, 4452 (2002).

[3] M. A. Levin and X.-G. Wen, String-net condensation: A physical mechanism for topological phases, Phys. Rev. B **71**, 045110 (2005).

[4] M. Freedman, C. Nayak, K. Shtengel, K. Walker, and Z. Wang, A class of $\mathcal{P}, \mathcal{T}$-invariant topological phases of interacting electrons, Ann. Phys. **310**, 428 (2004).

[5] C. W. von Keyserlingk, F. J. Burnell, and S. H. Simon, Three-dimensional topological lattice models with surface anyons, Phys. Rev. B **87**, 045107 (2013).

[6] Julio Carlos Magdalena de la Fuente, N. Tarantino, and J. Eisert, Non-Pauli topological stabilizer codes from twisted quantum doubles, arXiv:2001.11516.

[7] G. Dauphinais, L. Ortiz, S. Varona, and M. A. Martin-Delgado, Quantum error correction with the semion code, New J. Phys. **21**, 053035 (2019).

[8] A. R. Calderbank and P. W. Shor, Good quantum error-correcting codes exist, Phys. Rev. A **54**, 1098 (1996).

[9] A. M. Steane, Error Correcting Codes in Quantum Theory, Phys. Rev. Lett. **77**, 793 (1996).

[10] B. M. Terhal, Quantum error correction for quantum memories, Rev. Mod. Phys. **87**, 307 (2015).

[11] H. G. Katzgraber, H. Bombin, and M. A. Martin-Delgado, Error Threshold for Color Codes and Random Three-Body Ising Models, Phys. Rev. Lett. **103**, 090501 (2009).

[12] R. S. Andrist, H. G. Katzgraber, H. Bombin, and M. A. Martin-Delgado, Tricolored lattice gauge theory with randomness: Fault tolerance in topological color codes, New J. Phys. **13**, 083006 (2011).

[13] H. Bombin, R. S. Andrist, M. Ohzeki, H. G. Katzgraber, and M. A. Martín-Delgado, Strong Resilience of Topological Codes to Depolarization, Phys. Rev. X **2**, 021004 (2012).

[14] C. T. Chubb and S. T. Flammia, Statistical mechanical models for quantum codes with correlated noise, arXiv:1809.10704.

[15] Z.-A. Jia, Y.-H. Zhang, Y.-C. Wu, L. Kong, G.-C. Guo, and G.-P. Guo, Efficient machine-learning representations of a surface code with boundaries, defects, domain walls, and twists, Phys. Rev. A **99**, 012307 (2019).

[16] H. Chen, M. Vasmer, N. P. Breuckmann, and E. Grant, Machine learning logical gates for quantum error correction, arXiv:1912.10063.

[17] H. Poulsen Nautrup, N. Delfosse, V. Dunjko, H. J. Briegel, and N. Friis, Optimizing quantum error correction codes with reinforcement learning, Quantum **3**, 215 (2019).

[18] G. Torlai and R. G. Melko, Neural Decoder for Topological Codes, Phys. Rev. Lett. **119**, 030501 (2017).

[19] M. Sheth, S. Z. Jafarzadeh, and V. Gheorghiu, Neural ensemble decoding for topological quantum error-correcting codes, Phys. Rev. A **101**, 032338 (2020).

[20] Nikolas P. Breuckmann, and X. Ni, Scalable neural network decoders for higher dimensional quantum codes, Quantum **2**, 68 (2018).

[21] S. Varsamopoulos, B. Criger, and K. Bertels, Decoding small surface codes with feedforward neural networks, Quantum Sci. Technol. **3**, 015004 (2017).

[22] S. Varsamopoulos, K. Bertels, and C. G. Almudever, Comparing neural network based decoders for the surface code, IEEE Trans. Comput. **69**, 300 (2020).

[23] P. Baireuther, T. E. O'Brien, B. Tarasinski, and C. W. J. Beenakker, Machine-learning-assisted correction of correlated qubit errors in a topological code, Quantum **2**, 48 (2018).

[24] P. Andreasson, J. Johansson, S. Liljestrand, and M. Granath, Quantum error correction for the toric code using deep reinforcement learning, Quantum **3**, 183 (2019).

[25] S. Krastanov and L. Jiang, Deep neural network probabilistic decoder for stabilizer codes, Sci. Rep. **7**, 11003 (2017).

[26] D. Fitzek, M. Eliasson, A. F. Kockum, and M. Granath, Deep Q-learning decoder for depolarizing noise on the toric code, Phys. Rev. Research **2**, 023230 (2020).

[27] Y.-H. Liu and D. Poulin, Neural Belief-Propagation Decoders for Quantum Error-Correcting Codes, Phys. Rev. Lett. **122**, 200501 (2019).

[28] P. Baireuther, M. D. Caio, B. Criger, C. W. J. Beenakker, and T. E. O'Brien, Neural network decoder for topological color codes with circuit level noise, New J. Phys. **21**, 013003 (2019).

[29] C. Chamberland and P. Ronagh, Deep neural decoders for near term fault-tolerant experiments, Quantum Sci. Technol. **3**, 044002 (2018).

[30] X. Ni, Neural network decoders for large-distance 2D toric codes, Quantum **4**, 310 (2020).

[31] N. H. Nickerson and B. J. Brown, Analysing correlated noise on the surface code using adaptive decoding algorithms, Quantum **3**, 131 (2019).

[32] A. Davaasuren, Y. Suzuki, K. Fujii, and M. Koashi, General framework for constructing fast and near-optimal machine-learning-based decoder of the topological stabilizer codes, Phys. Rev. Research **2**, 033399 (2020).

[33] N. Maskara, A. Kubica, and T. Jochym-O'Connor, Advantages of versatile neural-network decoding for topological codes, Phys. Rev. A **99**, 052351 (2019).

[34] K. He, X. Zhang, S. Ren, and J. Sun, Deep residual learning for image recognition, in *2016 IEEE Conference on Computer Vision and Pattern Recognition (CVPR), Las Vegas, NV, 2016* (IEEE, New York, 2016), pp. 770–778.

[35] H. Bombin and M. A. Martin-Delgado, Topological Quantum Distillation, Phys. Rev. Lett. **97**, 180501 (2006).

[36] H. Bombin and M. A. Martin-Delgado, Topological Computation without Braiding, Phys. Rev. Lett. **98**, 160502 (2007).

[37] V. Kolmogorov, Blossom V: A new implementation of a minimum cost perfect matching algorithm, Math. Program. Comput. **1**, 43 (2009).

[38] J. Edmonds, Paths, trees, and flowers, Can. J. Math. **17**, 449 (1965).

[39] D. Gottesman, Class of quantum error-correcting codes saturating the quantum hamming bound, Phys. Rev. A **54**, 1862 (1996).

[40] D. K. Tuckett, S. D. Bartlett, and S. T. Flammia, Ultrahigh Error Threshold for Surface Codes with Biased Noise, Phys. Rev. Lett. **120**, 050505 (2018).

[41] S. T. Flammia and J. J. Wallman, Efficient estimation of Pauli channels, arXiv:1907.12976.

[42] M. Leshno, V. Ya. Lin, A. Pinkus, and S. Schocken, Multilayer feedforward networks with a nonpolynomial activation function can approximate any function, Neural Networks **6**, 861 (1993).

[43] K. Hornik, Approximation capabilities of multilayer feedforward networks, Neural Networks **4**, 251 (1991).

[44] I. Goodfellow, Y. Bengio, and A. Courville, *Deep Learning* (MIT Press, Cambridge, MA, 2016), http://www.deeplearningbook.org.

[45] D. P. Kingma and J. Ba, Adam: A method for stochastic optimization, Third International Conference for Learning Representations, San Diego, CA, 2015 (unpublished), arXiv:1412.6980.

[46] K. He, X. Zhang, S. Ren, and J. Sun, Delving deep into rectifiers: Surpassing human-level performance on ImageNet classification, in *2015 IEEE International Conference on Computer Vision (ICCV), Santiago, 2015* (IEEE, New York, 2015), pp. 1026–1034.

[47] S. Ioffe and C. Szegedy, Batch normalization: Accelerating deep network training by reducing internal covariate shift, arXiv:1502.03167.

[48] For independent bit- and phase-flip noise, the error threshold of the Kitaev code in different lattice geometries was computed in Ref. [49] using MWPM.

[49] K. Fujii and Y. Tokunaga, Error and loss tolerances of surface codes with general lattice structures, Phys. Rev. A **86**, 020303(R) (2012).

[50] D. Nigg, M. Mueller, E. A. Martinez, P. Schindler, M. Hennrich, T. Monz, M. A. Martin-Delgado, and R. Blatt, Quantum computations on a topologically encoded qubit, Science **345**, 302 (2014).

[51] M. Müller, A. Rivas, E. A. Martínez, D. Nigg, P. Schindler, T. Monz, R. Blatt, and M. A. Martin-Delgado, Iterative Phase Optimization of Elementary Quantum Error Correcting Codes, Phys. Rev. X **6**, 031030 (2016).

[52] R. Barends, J. Kelly, A. Megrant, A. Veitia, D. Sank, E. Jeffrey, T. C. White, J. Mutus, A. G. Fowler, B. Campbell, Y. Chen, Z. Chen, B. Chiaro, A. Dunsworth, C. Neill, P. O'Malley, P. Roushan, A. Vainsencher, J. Wenner, A. N. Korotkov, A. N. Cleland, and J. M. Martinis, Superconducting quantum circuits at the surface code threshold for fault tolerance, Nature (London) **508**, 500 (2014).

[53] A. D. Córcoles, E. Magesan, S. J. Srinivasan, A. W. Cross, M. Steffen, J. M. Gambetta, and J. M. Chow, Demonstration of a quantum error detection code using a square lattice of four superconducting qubits, Nat. Commun. **6**, 6979 (2015).

[54] D. A. Lidar and T. A. Brun, *Quantum Error Correction* (Cambridge University Press, Cambridge, 2013).

[55] K. Fujii, *Quantum Computation with Topological Codes: From Qubit to Topological Fault-Tolerance* (Springer, 2005).

[56] H. Song, A. Prem, S.-J. Huang, and M. A. Martin-Delgado, Twisted fracton models in three dimensions, Phys. Rev. B **99**, 155118 (2019).

[57] T. Wagner, H. Kampermann, and D. Bruß, Symmetries for a high level neural decoder on the toric code, arXiv:1910.01662.

[58] https://github.com/varona/nn_decoder.

Conclusion

Along this thesis we have explored two main topics: topological superconductors and topological quantum error correction. The former is motivated by the possibility of using Majorana fermions in quantum information processing, and the latter by the necessity of efficient quantum error correcting codes for the long-term goal of fault-tolerant quantum computation.

Realizing topological superconductors in the laboratory requires in general building heterostructures. In this heterostructures, superconductivity is induced in a semiconductor by a parent superconductor in its proximity. While conventional s-wave superconductors are usually considered, we investigate the possibility of using a d-wave superconductor in publication [P1]. Despite the angular dependence of the d-wave pairing, we show that at equal superconducting gap, the localization of the Majorana modes is very similar to the s-wave case. This could translate into much sharper localization for d-wave parent superconductors, since these superconductors correspond to high-temperature superconductors with much larger gaps than conventional ones. Besides, we compute a topological invariant characterizing the system and show the robustness of the Majorana zero modes against static disorder. This analysis can be used for future experiments and proposals using high-temperature superconductors. The possibility of using other exotic superconducting pairings is also considered in publication [P2]. Where we study the phase diagrams of nodeless pairings compatible with tetragonal crystal symmetry and determine the non-Abelian regimes. A similar study could be made for other crystal symmetries.

Regarding topological quantum error correction, topological stabilizer codes have become a mature research field and provide us with of the most viable schemes on the way to fault-tolerant quantum computation. In publication [P3], we exploit the relation between topological orders and topological quantum error correcting codes to construct a new topological code, the semion code, from the double semion model. Remarkably, the semion code is a non-CSS, non-Pauli code, unlike other known topological codes. The tools introduced here for the semion code could be generalized to other topological non-Pauli codes, such as codes based on twisted quantum doubles. Finding new topological codes may help reduce the overhead required to, for instance, perform non-Clifford gates in two-dimensional codes, and is an important research line.

Publication [P4] expands our knowledge of the semion code by computing the threshold value for two different Pauli noise models. The threshold value is quite high, of the same magnitude as the Kitaev toric code. We observe some differences mainly due to the non-Pauli nature of the semion code. These results were obtained using near-optimal neural decoders. The same methods could be used for other topological codes with non-Pauli stabilizers or non-Pauli noise models, where the mapping to a statistical mechanical model becomes difficult. In addition, it would be interesting to apply this kind of deep learning models not only to threshold determination, but also to build general purpose scalable decoders. This specially so in the case of ResNet, the convolutional neural network applied in this work.

Bibliography

[Agg18] Charu C. Aggarwal, *Neural networks and deep learning*, Springer, 2018.

[Alb+16] S. M. Albrecht et al., *Exponential protection of zero modes in Majorana islands*, Nature **531** (2016), no. 7593, 206–209.

[Ali+11] Jason Alicea et al., *Non-Abelian statistics and topological quantum information processing in 1D wire networks*, Nature Physics **7** (2011), no. 5, 412–417.

[Ali10] Jason Alicea, *Majorana fermions in a tunable semiconductor device*, Physical Review B **81** (2010), 125318.

[Ali12] Jason Alicea, *New directions in the pursuit of Majorana fermions in solid state systems*, Reports on Progress in Physics **75** (2012), no. 7, 076501.

[Aru+19] Frank Arute et al., *Quantum supremacy using a programmable superconducting processor*, Nature **574** (2019), no. 7779, 505–510.

[Bac13] Dave Bacon, *Introduction to quantum error correction*, Quantum Error Correction, ed. by Daniel A. Lidar and Todd A.Editors Brun, Cambridge University Press, 2013, 46–77.

[Bai+18] Paul Baireuther et al., *Machine-learning-assisted correction of correlated qubit errors in a topological code*, Quantum **2** (2018), 48.

[BDP12] H. Bombin, Guillaume Duclos-Cianci, and David Poulin, *Universal topological phase of two-dimensional stabilizer codes*, New Journal of Physics **14** (2012), no. 7, 073048.

[Ber+17] A. Bermudez et al., *Assessing the Progress of Trapped-Ion Processors Towards Fault-Tolerant Quantum Computation*, Physical Review X **7** (2017), 041061.

[BH13] B. A. Bernevig and T. L. Hughes, *Topological Insulators and Topological Superconductors*, Princeton University Press, 2013.

[BK05] Sergey Bravyi and Alexei Kitaev, *Universal quantum computation with ideal Clifford gates and noisy ancillas*, Physical Review A **71** (2005), 022316.

[BK13] Sergey Bravyi and Robert König, *Classification of Topologically Protected Gates for Local Stabilizer Codes*, Physical Review Letters **110** (2013), 170503.

[BK98] Sergey Bravyi and Alexei Kitaev, *Quantum codes on a lattice with boundary*, 1998, arXiv: quant-ph/9811052 [quant-ph].

[BM06] H. Bombin and M. A. Martin-Delgado, *Topological Quantum Distillation*, Physical Review Letters **97** (2006), 180501.

[BM07] H. Bombin and M. A. Martin-Delgado, *Topological Computation without Braiding*, Phys. Rev. Lett. **98** (2007), 160502.

[BN18] Nikolas P. Breuckmann and Xiaotong Ni, *Scalable Neural Network Decoders for Higher Dimensional Quantum Codes*, Quantum **2** (2018), 68.

[Bom13] Hector Bombin, *Topological codes*, Quantum Error Correction, ed. by Daniel A. Lidar and Todd A.Editors Brun, Cambridge University Press, 2013, 455–481.

[Bom18] Hector Bombin, *Transversal gates and error propagation in 3D topological codes*, 2018, arXiv: 1810.09575 [quant-ph].

[Bro20] Benjamin J. Brown, *A fault-tolerant non-Clifford gate for the surface code in two dimensions*, Science Advances **6** (2020), no. 21.

[Bru+19] Colin D. Bruzewicz et al., *Trapped-ion quantum computing: Progress and challenges*, Applied Physics Reviews **6** (2019), no. 2, 021314.

[Car+19] Giuseppe Carleo et al., *Machine learning and the physical sciences*, Review of Modern Physics **91** (2019), 045002.

[Chi+16] Ching-Kai Chiu et al., *Classification of topological quantum matter with symmetries*, Review of Modern Physics **88** (2016), 035005.

[Chu+13] H. O. H. Churchill et al., *Superconductor-nanowire devices from tunneling to the multichannel regime: Zero-bias oscillations and magnetoconductance crossover*, Physical Review B **87** (2013), 241401.

[CS96] A. R. Calderbank and Peter W. Shor, *Good quantum error-correcting codes exist*, Physical Review A **54** (1996), 1098–1105.

[Cyb89] G. Cybenko, *Approximation by superpositions of a sigmoidal function*, Mathematics of Control, Signals and Systems **2** (1989), no. 4, 303–314.

[Dav+18] Amarsanaa Davaasuren et al., *General framework for constructing fast and near-optimal machine-learning-based decoder of the topological stabilizer codes*, 2018, arXiv: 1801.04377 [quant-ph].

[Den+02] Eric Dennis et al., *Topological quantum memory*, Journal of Mathematical Physics **43** (2002), no. 9, 4452–4505.

[DP10] Guillaume Duclos-Cianci and David Poulin, *Fast Decoders for Topological Quantum Codes*, Physical Review Letters **104** (2010), 050504.

[DS13] M. H. Devoret and R. J. Schoelkopf, *Superconducting Circuits for Quantum Information: An Outlook*, Science **339** (2013), no. 6124, 1169–1174.

[Edm65] Jack Edmonds, *Paths, trees, and flowers*, Canadian Journal of Mathematics **17** (1965), 449–467.

[EK09] Bryan Eastin and Emanuel Knill, *Restrictions on Transversal Encoded Quantum Gate Sets*, Physical Review Letters **102** (2009), 110502.

[FGG14] Edward Farhi, Jeffrey Goldstone, and Sam Gutmann, *A Quantum Approximate Optimization Algorithm*, 2014, arXiv: 1411.4028 [quant-ph].

[FK08] Liang Fu and C. L. Kane, *Superconducting Proximity Effect and Majorana Fermions at the Surface of a Topological Insulator*, Physical Review Letters **100** (2008), 096407.

[Fow+12] Austin G. Fowler et al., *Surface codes: Towards practical large-scale quantum computation*, Physical Review A **86** (2012), 032324.

[Fre+04] Michael Freedman et al., *A class of P,T-invariant topological phases of interacting electrons*, Annals of Physics **310** (2004), no. 2, 428–492.

[FT12] Keisuke Fujii and Yuuki Tokunaga, *Error and loss tolerances of surface codes with general lattice structures*, Physical Review A **86** (2012), 020303.

[FTE20] Julio Carlos Magdalena de la Fuente, Nicolas Tarantino, and Jens Eisert, *Non-Pauli topological stabilizer codes from twisted quantum doubles*, 2020, arXiv: 2001.11516 [quant-ph].

[Fuj15] Keisuke Fujii, *Quantum computation with topological codes: from qubit to topological fault-tolerance*, Springer, 2015.

[GB10] Xavier Glorot and Yoshua Bengio, *Understanding the difficulty of training deep feedforward neural networks*, Proceedings of the thirteenth international conference on artificial intelligence and statistics, 2010, 249–256.

[GBC16] Ian Goodfellow, Yoshua Bengio, and Aaron Courville, *Deep learning*, MIT press, 2016.

[Got97] Daniel Gottesman, *Stabilizer Codes and Quantum Error Correction*, 1997, arXiv: quant-ph/9705052 [quant-ph].

[GS11] Eytan Grosfeld and Ady Stern, *Observing Majorana bound states of Josephson vortices in topological superconductors*, Proceedings of the National Academy of Sciences **108** (2011), no. 29, 11810–11814.

[He+15] Kaiming He et al., *Delving Deep into Rectifiers: Surpassing Human-Level Performance on ImageNet Classification*, 2015 IEEE International Conference on Computer Vision (ICCV) (2015).

[Hor91] Kurt Hornik, *Approximation capabilities of multilayer feedforward networks*, Neural Networks **4** (1991), no. 2, 251–257.

[HZW05] Alioscia Hamma, Paolo Zanardi, and Xiao-Gang Wen, *String and membrane condensation on three-dimensional lattices*, Phys. Rev. B **72** (2005), 035307.

[IS15] Sergey Ioffe and Christian Szegedy, *Batch Normalization: Accelerating Deep Network Training by Reducing Internal Covariate Shift*, 2015, arXiv: 1502.03167 [cs.LG].

[Kar+17] Torsten Karzig et al., *Scalable designs for quasiparticle-poisoning-protected topological quantum computation with Majorana zero modes*, Physical Review B **95** (2017), 235305.

[KBM09] Helmut G. Katzgraber, H. Bombin, and M. A. Martin-Delgado, *Error Threshold for Color Codes and Random Three-Body Ising Models*, Physical Review Letters **103** (2009), 090501.

[KBS13] C. W. von Keyserlingk, F. J. Burnell, and S. H. Simon, *Three-dimensional topological lattice models with surface anyons*, Physical Review B **87** (2013), 045107.

[Kit01] A. Yu. Kitaev, *Unpaired Majorana fermions in quantum wires*, Physics-Uspekhi **44** (2001), no. 10S, 131–136.

[Kit03] A. Yu. Kitaev, *Fault-tolerant quantum computation by anyons*, Annals of Physics **303** (2003), no. 1, 2–30.

[Kit97] A. Yu. Kitaev, *Quantum Error Correction with Imperfect Gates*, Quantum Communication, Computing, and Measurement, ed. by O. Hirota, A. S. Holevo, and C. M. Caves, Boston, MA: Springer US, 1997, 181–188.

[KJ17] Stefan Krastanov and Liang Jiang, *Deep Neural Network Probabilistic Decoder for Stabilizer Codes*, Scientific Reports **7** (2017), no. 1, 11003.

[Kol09] Vladimir Kolmogorov, *Blossom V: a new implementation of a minimum cost perfect matching algorithm*, Mathematical Programming Computation **1** (2009), no. 1, 43–67.

[Lar+19] Dominique Laroche et al., *Observation of the 4π-periodic Josephson effect in indium arsenide nanowires*, Nature Communications **10** (2019), no. 1, 245.

[Les+93] Moshe Leshno et al., *Multilayer feedforward networks with a nonpolynomial activation function can approximate any function*, Neural Networks **6** (1993), no. 6, 861–867.

[LF12] Martin Leijnse and Karsten Flensberg, *Introduction to topological superconductivity and Majorana fermions*, Semiconductor Science and Technology **27** (2012), no. 12, 124003.

[Lit19] Daniel Litinski, *Magic State Distillation: Not as Costly as You Think*, Quantum **3** (2019), 205.

[LSD10] Roman M. Lutchyn, Jay D. Sau, and S. Das Sarma, *Majorana Fermions and a Topological Phase Transition in Semiconductor-Superconductor Heterostructures*, Physical Review Letters **105** (2010), 077001.

[Lut+18] R. M. Lutchyn et al., *Majorana zero modes in superconductor–semiconductor heterostructures*, Nature Reviews Materials **3** (2018), no. 5, 52–68.

[LW05] Michael A. Levin and Xiao-Gang Wen, *String-net condensation: A physical mechanism for topological phases*, Physical Review B **71** (2005), 045110.

[Mae+12] Yoshiteru Maeno et al., *Evaluation of Spin-Triplet Superconductivity in Sr_2RuO_4*, Journal of the Physical Society of Japan **81** (2012), no. 1, 011009.

[McC+16] Jarrod R McClean et al., *The theory of variational hybrid quantum-classical algorithms*, New Journal of Physics **18** (2016), no. 2, 023023.

[MKJ19] Nishad Maskara, Aleksander Kubica, and Tomas Jochym-O'Connor, *Advantages of versatile neural-network decoding for topological codes*, Physical Review A **99** (2019), 052351.

[Mou+12] V. Mourik et al., *Signatures of Majorana Fermions in Hybrid Superconductor-Semiconductor Nanowire Devices*, Science **336** (2012), no. 6084, 1003–1007.

[Nad+13] S. Nadj-Perge et al., *Proposal for realizing Majorana fermions in chains of magnetic atoms on a superconductor*, Physical Review B **88** (2013), 020407.

[Nad+14] S. Nadj-Perge et al., *Observation of Majorana fermions in ferromagnetic atomic chains on a superconductor*, Science **346** (2014), no. 6209, 602–607.

[Nay+08] Chetan Nayak et al., *Non-Abelian anyons and topological quantum computation*, Review of Modern Physics **80** (2008), 1083–1159.

[Ni18] Xiaotong Ni, *Neural Network Decoders for Large-Distance 2D Toric Codes*, 2018, arXiv: `1809.06640 [quant-ph]`.

[Nie15] Michael A. Nielsen, *Neural networks and deep learning*, Determination Press, 2015.

[ORO10] Yuval Oreg, Gil Refael, and Felix von Oppen, *Helical Liquids and Majorana Bound States in Quantum Wires*, Physical Review Letters **105** (2010), 177002.

[Pou06] David Poulin, *Optimal and efficient decoding of concatenated quantum block codes*, Physical Review A **74** (2006), 052333.

[Pre12] John Preskill, *Quantum computing and the entanglement frontier*, 2012, arXiv: `1203.5813 [quant-ph]`.

[Pre18] John Preskill, *Quantum Computing in the NISQ era and beyond*, Quantum **2** (2018), 79.

[RG00] N. Read and Dmitry Green, *Paired states of fermions in two dimensions with breaking of parity and time-reversal symmetries and the*

fractional quantum Hall effect, Physical Review B **61** (2000), 10267–10297.

[SA17] Masatoshi Sato and Yoichi Ando, *Topological superconductors: a review*, Reports on Progress in Physics **80** (2017), no. 7, 076501.

[SF10] Masatoshi Sato and Satoshi Fujimoto, *Existence of Majorana Fermions and Topological Order in Nodal Superconductors with Spin-Orbit Interactions in External Magnetic Fields*, Physical Review Letters **105** (2010), 217001.

[Sho95] Peter W. Shor, *Scheme for reducing decoherence in quantum computer memory*, Physical Review A **52** (1995), R2493–R2496.

[SJG19] Milap Sheth, Sara Zafar Jafarzadeh, and Vlad Gheorghiu, *Neural ensemble decoding for topological quantum error-correcting codes*, 2019, arXiv: 1905.02345 [quant-ph].

[Sta16] Tudor D. Stanescu, *Introduction to Topological Quantum Matter & Quantum Computation*, CRC Press, 2016.

[Ste96] A. M. Steane, *Simple quantum error-correcting codes*, Physical Review A **54** (1996), 4741–4751.

[Svo+06] Krysta Svore et al., *A flow-map model for analyzing pseudothresholds in fault-tolerant quantum computing*, Quantum Information & Computation **6** (2006), 193–212.

[Tak+13] So Takei et al., *Topological superconductivity and Majorana fermions in hybrid structures involving cuprate high-T_c superconductors*, Physical Review B **87** (2013), 014504.

[Ter15] Barbara M. Terhal, *Quantum error correction for quantum memories*, Review of Modern Physics **87** (2015), 307–346.

[TM17] Giacomo Torlai and Roger G. Melko, *Neural Decoder for Topological Codes*, Physical Review Letters **119** (2017), 030501.

[VBA19] Savvas Varsamopoulos, Koen Bertels, and Carmen G. Almudever, *Decoding surface code with a distributed neural network based decoder*, 2019, arXiv: 1901.10847 [quant-ph].

[VCB17] Savvas Varsamopoulos, Ben Criger, and Koen Bertels, *Decoding small surface codes with feedforward neural networks*, Quantum Science and Technology **3** (2017), no. 1, 015004.

[Wen17a] Xiao-Gang Wen, *Colloquium: Zoo of quantum-topological phases of matter*, Review Modern Physics **89** (2017), 041004.

[Wen17b] G Wendin, *Quantum information processing with superconducting circuits: a review*, Reports on Progress in Physics **80** (2017), no. 10, 106001.

[Zha+18] Hao Zhang et al., *Quantized Majorana conductance*, Nature **556** (2018), no. 7699, 74–79.